Thermal conduction in the high temperature superconductors LSCO and Tl2201: A field and doping dependent study

by

David G. Hawthorn

A thesis submitted in conformity with the requirements
for the degree of Doctor of Philosophy
Graduate Department of Physics
University of Toronto

Your file Votre référence
ISBN: 0-494-02885-8
Our file Notre référence
ISBN: 0-494-02885-8

Abstract

Thermal conduction in the high temperature superconductors LSCO and Tl2201: A field and doping dependent study

David G. Hawthorn
Doctor of Philosophy
Graduate Department of Physics
University of Toronto
2005

We measure the low-temperature thermal conductivity, κ, of single crystals in two high-temperature superconductors, $Tl_2Ba_2CuO_{6+\delta}$ (Tl2201) and $La_{2-x}Sr_xCuO_4$ (LSCO), as a function of carrier density (doping) and magnetic field. Thermal conductivity is a bulk probe of the low-energy ground state excitations. By measuring the thermal conductivity we attempt to distinguish ground states in the cuprates, and gain quantitative information on their properties.

In the superconducting state, the thermal conductivity (in the $T \rightarrow 0$ limit) due to d-wave nodal quasiparticles can be directly related to the superconducting gap maximum, Δ_0, with few assumptions and no free parameters. In Tl2201, along with previous measurements on YBCO and Bi2212, we find Δ_0 from thermal conductivity to be consistent with spectroscopic measurements of the gap. This argues for a simple d-wave BCS-like superconducting state throughout the phase diagram. In addition, following previous measurements in YBCO and BSCCO, we find κ in the mixed state of Tl2201 to increase with applied field, qualitatively consistent with semi-classical theories.

In striking contrast to Tl2201, in underdoped LSCO κ is found to decrease with increasing magnetic field in the $T \rightarrow 0$ limit, unlike all previously measured supercon-

ductors, and most remarkably YBCO at a comparable low doping. In heavily underdoped LSCO, where superconductivity can be entirely suppressed with an applied field, we show that a novel thermal metal-to-insulator transition takes place upon going from the superconducting state to the field-induced normal state. We argue that the doping and field dependence of κ in underdoped LSCO is a signature of competing superconductivity and spin-density wave order.

Finally, we show that the low-temperature ($T < 1$ K) phonon conductivity, κ_{ph}, increases with increasing doping in both LSCO and Tl2201. We argue that κ_{ph} is limited at low temperatures by phonon-electron scattering, which is inversely proportional to the electron-phonon coupling, λ. The doping dependence of κ_{ph} is explained by a decrease in λ with increasing doping, in agreement with the quasiparticle velocity renormalization observed in angle-resolved photoemission. We speculate on relevance of this result to the mechanism of high-temperature superconductivity.

To Kelly

ACKNOWLEDGEMENTS

I goes without saying that the work presented in this thesis could not have been accomplished without the support and inspiration of a number of people.

First, I would like to thank my supervisor Louis Taillefer, whose enthusiasm for physics, masterful writing, and keen eye for the most interesting elements of a given project, continue to inspire.

I thank all of the members of the Taillefer group, Robert Hill, Cyril Proust, Makariy Tanatar, Fil Ronning, Shiyan Li, Andrew MacFarlane, Mike Sutherland, Johnpierre Paglione, Etienne Boaknin and Christian Lupien. I have had the opportunity to work closely with the all members of the group, sharing equipment, ideas and workload (Saturday night Helium transfers). This has been a tremendous benefit, not only in regards to the help I received in completing my own thesis project, but also in the personal interaction with this exceptional group of researchers. Each member of the group has brought at different times a set of skill, knowledge and personality to the group. My hope is that the better qualities of each has rubbed off, at least in part, on myself.

I would also like to thank all those that provided samples for my thesis, Shuichi Wakimoto, Harry Zhang, Nigel Hussey, N. Nohara, Hide Takagi, T. Kimura, Andrew Mackenzie, N. N. Koleshnikov, Ruixing Liang, Darren Peets, Walter Hardy and Doug Bonn. There would be no experiments without the samples. In particular, I would like to thank Shuichi Wakimoto and Harry Zhang for sharing their knowledge of crystal growth and guiding me through the successful growth of the one and only sample I grew.

I thank a number of researchers for performing additional measurements to supplement my work. Specifically, I thank Patrick Fournier for susceptibility measurements, Claudio Cermignani for EPMA measurements and Cyril Proust for pulsed field resistivity measurements.

I thank the staff and faculty of physics department at the University of Toronto, in particular Prof. John Wei and the late Prof. Bryan Statt, Robert Henderson and Shahidul Islam for a steady supply of liquid Helium, and Marianne Khurana and Krystyna Biel for their administrative support.

I would also like thank Mike Smith, Kamran Behnia and Shuichi Wakimoto, amongst many others, for stimulating discussions. I would like to thank Prof. Tom Timusk for the career advice he gave me before I started graduate school that directed me to the University of Toronto and the Taillefer group.

I thank the funding agencies, the National Sciences and Engineering Research Council of Canada (NSERC), the Walter Sumner foundation and the University of Toronto, that

made this research possible. In addition, I would like to thank the Canadian Institute for Advanced Research (CIAR) and the National Science Foundation for funding excellent summer schools and meetings that I have had the opportunity to attend.

Finally, I would like to thank my family and friends for their love and support: My mother and father, Matt, Carolyn, Emma, Nancy, Terry, Chris, Denise, Keith, Andy, Matt, Fraser, Todd, Sarah, Don, Aaron and Jamie. Lastly, I would like to thank Kelly Irwin for being my cheerleader.

Statement of Originality

In this thesis I present results of three main projects on the low-temperature thermal conductivity in the high-temperature superconductors: a study of the low-temperature electronic contributions to the thermal conductivity in the material $La_{2-x}Sr_xCuO_4$ as a function of doping and applied magnetic field, a similar study on the related material $Tl_2Ba_2CuO_{6+\delta}$, and a study of the phonon conductivity as a function of doping in both LSCO and Tl2201. Here I briefly outline the contributions of myself and others to these projects, and make note of similar work by other groups.

Field-Induced Thermal Metal-to-Insulator Transition in Underdoped LSCO

Two papers [1, 2] have been published dealing with the field dependence of the thermal conductivity in LSCO. In underdoped LSCO, we find the thermal conductivity at $T \to 0$ to *decrease* with an applied field, unlike all previously measured superconductors. In a heavily underdoped sample where we are able to suppress superconductivity with an applied field, we show that the decrease in thermal conductivity with applied field is indicative of a novel thermal metal-to-insulator transition. In this thesis we relate this result to measurements of static spin-density wave order by elastic neutron scattering and argue that the behavior of the thermal conductivity is due to competing superconducting and spin-density wave order. All experimental parts of this project were done by myself, with the help of Robert Hill, Cyril Proust, Fil Ronning, Etienne Boaknin, Mike Sutherland, Christian Lupien, Makariy Tanatar and Johnpierre Paglione. The crystal that is the primary focus of this work ($x = 0.06$) was grown by the author, Shuichi Wakimoto and Harry Zhang. Other crystals used in the study were grown by our collaborators Shuichi Wakimoto, Nigel Hussey, N. Nohara, H. Takagi and T. Kimura. The papers detailing this work [1, 2] were written by myself and Louis Taillefer, with participation from the other co-authors. We note that similar work to this has also been reported around the same time as our publication by the Ando group [3]. Although Sun et al. reach similar conclusions, their work does not extend to as low temperature and doping as our study and, as such, is considerably less conclusive.

A third paper [4] has also been published on our thermal conductivity measurements in LSCO. This paper deals with doping evolution of the thermal conductivity in YBCO and LSCO in zero field. The objective was to test how theoretical models of electronic transport in superconductors, shown previously to be successful at optimal doping, holds up at a variety of dopings. The result was a quantitative agreement with theoretical models in YBCO but a non-trivial breakdown of the theory in underdoped LSCO. A quantitative analysis of YBCO allowed important parameters describing the supercon-

ducting state, such as the quasiparticle gap, to be determined. My contributions were to measure all of the LSCO samples presented in the study, in addition to assisting in some measurements on YBCO. The manuscript was written by Mike Sutherland, who performed the measurements on YBCO presented in the manuscript, Louis Taillefer and myself, with additional input from members of our group. In this regard, I wrote initial drafts of the manuscript, which were latter developed considerably by Mike Sutherland and Louis Taillefer. Similar, and consistent, measurements of the low temperature thermal conductivity in 0T on LSCO (not YBCO), again by the Ando group, preceded the publication of our results [5].

In addition, a fourth forthcoming publication [6] (to be submitted to PRL) primarily on underdoped YBCO will also feature data from the study of thermal conductivity in LSCO. This paper was written by Mike Sutherland and Louis Taillefer, with contributions from the author, Robert Hill and Fil Ronning.

The quasiparticle gap in Tl2201 from low temperature thermal conductivity

The second project is to measure the thermal conductivity in overdoped Tl2201. Like YBCO, Tl2201 is a 90 K superconductor at optimal doping. But, unlike YBCO, which may not be heavily overdoped, it may be doped from optimal doping to the heavily overdoped region of the phase diagram. This allows us to extend the measurements of the thermal conductivity in underdoped and optimally doped YBCO from Sutherland et al. [4], where the mean-field theoretical models provide a successful description of the thermal conductivity to the overdoped region of the phase diagram in another 90 K superconductor. Measurements of Tl2201 were first performed by our group by Cyril Proust and Etienne Boaknin [7]. These measurements, however, were only at a single doping. Here we extend these measurements to other dopings and, like YBCO, we find quantitative agreement between theory and experiment. From our thermal conductivity measurements we extract the quasiparticle gap at low energies across the doping phase diagram. Most of the experimental parts of this project were done by myself, with the help of Etienne Boaknin, Mike Sutherland, Shiyan Li, Robert Hill, Makariy Tanatar, Johnpierre Paglione and Fil Ronning. I acknowledge two significant contributions by my collaborators. First, two samples (T_c = 72 K and 76 K) were prepared by the author but measured by Shiyan Li at the University of Sherbrooke. Second, one other sample (T_c = 27 K) was prepared and measured by Etienne Boaknin and Cyril Proust, with little involvement by the author. The crystals used in this study were grown by our collaborators, Darren Peets, Ruixing Liang, Doug Bonn, Walter Hardy, N. N. Koleshnikov and Andrew Mackenzie. This work currently exists in preprint form [8], written by the author, but has yet to be submitted for publication (likely to be submitted to PRB).

A second aspect to the project on Tl2201 is the field dependence of the thermal conductivity. Like previous measurements on YBCO [9] and BSCCO [10], we find agreement with semiclassical models of the field dependence of the thermal conductivity. This work is currently unpublished.

Sub-Kelvin phonon thermal conductivity in Tl2201 and LSCO: novel doping dependence of the electron-phonon coupling

Finally, a last project that has evolved out of the writing of this thesis, is a measurement of the evolution of the phonon contribution to the thermal conductivity in both LSCO and Tl2201 as a function of doping. In LSCO the phonon thermal conductivity, κ_{ph}, at intermediate temperatures has a novel doping dependence: with increasing doping κ_{ph} first decreases at low doping, but with increasing doping, in heavily overdoped samples κ_{ph} anomalously increases, an observation first noted by Nakamura and co-workers [11]. Here we track the phonon thermal conductivity and show, at sub-Kelvin temperatures and in both LSCO and Tl2201, a similar doping evolution as the measurements at higher temperatures in LSCO. We argue that κ_{ph} is limited at low temperatures by phonon-electron scattering, which is inversely proportional to the electron-phonon coupling, λ. The doping dependence of κ_{ph} is explained by a decrease in λ with increasing doping, in agreement with the quasiparticle velocity renormalization observed in angle-resolved photoemission. We speculate on relevance of this result to the mechanism of high-temperature superconductivity. This observation of an intrinsic doping dependence to the low temperature thermal conductivity in the cuprates, and its correlation with the electron phonon coupling, was made by the author. This work is currently unpublished.

The work presented in this thesis is presented in the following papers:

- D. G. Hawthorn, R. W. Hill, C. Proust, F. Ronning, Mike Sutherland, Etienne Boaknin, C. Lupien, M. A. Tanatar, Johnpierre Paglione, S. Wakimoto, H. Zhang, Louis Taillefer, T. Kimura, M. Nohara, H. Takagi, and N. E. Hussey.
  Field-Induced Thermal Metal-to-Insulator Transition in Underdoped $La_{2-x}Sr_xCuO_{4+\delta}$.
  Physical Review Letters **90**, 197004 (2003). [4 pages]

- Mike Sutherland, D. G. Hawthorn, R. W. Hill, F. Ronning, S. Wakimoto, H. Zhang, C. Proust, Etienne Boaknin, C. Lupien, Louis Taillefer , Ruixing Liang, D. A. Bonn, W. N. Hardy, Robert Gagnon, N. E. Hussey, T. Kimura, M. Nohara, and H. Takagi.
  Thermal conductivity across the phase diagram of cuprates: Low-energy quasiparticles and doping dependence of the superconducting gap.
  Physical Review B **67**, 174520 (2003). [11 pages]

- Mike Sutherland, D. G. Hawthorn, R. W. Hill, F. Ronning, M. A. Tanatar, J. Paglione, E. Boaknin, H. Zhang, Louis Taillefer, J. DeBenedictis, Ruixing Liang, D. A. Bonn and W. N. Hardy.
  Nodal Metallic Phase in Underdoped Cuprates.
  unpublished (2004).

- D. G. Hawthorn, S. Li, M. Sutherland, Etienne Boaknin, R. W. Hill, C. Proust, F. Ronning, M. A. Tanatar, Johnpierre Paglione, N. N. Koleshnikov, Ruixing Liang, D. Peets, D. Bonn, W. Hardy and Louis Taillefer.
  The quasiparticle gap in Tl2201 from low temperature thermal conductivity.
  unpublished (2004).

Contents

Figures and Tables

Figures

TABLES

1

INTRODUCTION

High temperature superconductors were first discovered by Bednorz and Muller in 1986 [12] in the material $La_{2-x}Ba_xCuO_4$. Since this time considerable effort has been focused towards understanding the superconductivity and other novel phenomena exhibited by high temperature superconductors. What makes them interesting is that they have a rich doping-temperature phase diagram that combines elements from many active areas of condensed matter physics research, including metal-to-insulator transitions (doped Mott insulators), quantum criticality, unconventional superconductivity, and novel orbital current and stripe ordered phases of matter, which may compete with the superconductivity in the underdoped region of the phase diagram. One area of interest where all of these notions converge is that they all have some impact on low-energy excitations of the cuprates.

In this thesis we attempt to explore the low-energy excitations in the cuprates as a function of carrier doping and magnetic field, by measuring the thermal conductivity at very low temperatures (down to 40 mK). Thermal conductivity is a bulk measurement that is sensitive to all mobile excitations that can carry heat (have entropy), and thereby provides an excellent probe of the low-energy excitations.

We explore the thermal conductivity in two cuprate families, LSCO and Tl2201, as a function of carrier concentration (doping). In Tl2201 we are able to dope the material from optimal doping, where the superconducting transition temperature, T_c, is maximal, to heavily overdoped, where the superconductivity weakens and the material evolves towards a more conventional Fermi liquid ground state. In LSCO, we are able to dope the material from the undoped anti-ferromagnetic insulator all the way to the overdoped, non-superconducting metallic state. In addition to studying these two materials we also compare our measurements to doping dependent measurements of the thermal conductivity by Mike Sutherland in another cuprate material, YBCO [4, 6, 13].

From these studies we aim to achieve a few specific goals. First, we compare our mea-

surements of thermal conductivity as a function of carrier concentration with existing theories of thermal transport in a d-wave superconductor to see how robustly the theory applies as a function of carrier concentration. This comparison is an extension of previous measurements of thermal transport in optimally doped YBCO [14, 15, 4] and BSCCO [15, 16], and to a lesser extent overdoped Tl2201 [7]. At low temperatures the thermal conductivity in the superconducting state of a d-wave superconductor is a "universal" quantity (independent of the quasiparticle scattering rate). Moreover it is dependent only upon the dispersion of the quasiparticles in the superconducting state (plus some well known material dependent properties). Using this property we extract the quasiparticle gap at low energies from the thermal conductivity. We find good agreement with our measurements and spectroscopic measurements of the gap from angle-resolved photoemission and tunneling. Together with the work of Mike Sutherland on YBCO, these results indicate that the superconducting state is well described by as a simple d-wave superconductor at low energies throughout the superconducting region of the phase diagram in Tl2201 and YBCO. This is the subject of chapter 6.

In chapter 7, we apply a magnetic field, H, to the samples of Tl2201 and test the applicability of semiclassical theories of thermal transport in the vortex state. Here the expectation is that the thermal conductivity increases approximately as $\sqrt{H}$ due to a field-induced enhancement of the quasiparticle density of states. This enhancement comes about due to an increase in the quasiparticle energy as it is Doppler shifted with respect to the superfluid that encircles vortices in the mixed state. In Tl2201 we find the thermal conductivity increases with increasing magnetic field in accordance with the expectation of semiclassical models of the field dependence.

Together with previous measurements, the results of these two chapters indicate that the paradigm of a d-wave superconductor describes the low-energy excitations in the class of $\sim$90 K superconductors YBCO, Bi2212 and Tl2201.

However, by also studying LSCO, presented in chapter 8, we uncover qualitatively different behavior that is seemingly inconsistent with a simple d-wave superconductor. In overdoped LSCO we find a sizeable electronic contribution to the thermal conductivity and a field dependence that are roughly consistent with a d-wave superconductor, and similar to YBCO, Tl2201 and BSCCO. In contrast, in underdoped LSCO we find that the thermal conductivity in the superconducting state is too small to be accounted for within the simple mean-field calculations for a d-wave superconductor. Rather the electronic contribution to the thermal conductivity onsets at the non-superconductor-to-

superconductor transition.

More interestingly, we find that with the application of a magnetic field the thermal conductivity *decreases* in underdoped LSCO. This is in striking contrast to the increase in thermal conductivity observed at low temperatures in all previously measured superconductors (at $T \rightarrow 0$). In heavily underdoped LSCO, where superconductivity can be entirely suppressed with an applied field, we show that a novel thermal metal-to-insulator transition takes place upon going from the superconducting state to the field-induced normal state.

The suppression of the thermal conductivity, either with decreasing doping or applied field, is directly contrasted with very recent measurements on underdoped YBCO by Mike Sutherland [6]. Here the thermal conductivity is finite and neither decreases with decreasing doping or applied magnetic field. In other words, the ground state excitations in LSCO and YBCO differ in the underdoped region near the onset of superconductivity. We relate the results in underdoped LSCO to evidence for spin-density wave order from elastic neutron scattering measurements and propose that the suppressed thermal conductivity in LSCO, with either doping or magnetic field, is a signature of the competition between superconductivity and spin-density wave order.

Finally, in chapter 9 we switch gears and discuss the phonon thermal conductivity, κ_{ph}, in both Tl2201 and LSCO. We find that κ_{ph} at low temperatures increases with increasing doping. We argue that κ_{ph} is limited at low temperatures by phonon-electron scattering. Phonon-electron scattering is inversely proportional to the electron-phonon coupling, λ, which in conventional superconductors determines, in part, the superconducting transition temperatures. The doping dependence of κ_{ph} is explained by a decrease in λ with increasing doping, in agreement with the quasiparticle velocity renormalization observed in angle-resolved photoemission. We speculate on the relevance of this result to the mechanism of high-temperature superconductivity.

In addition, to motivate and support the main results of this thesis we provide several chapters of background or supplementary information. In chapter 2 we briefly review high-temperature superconductors. In chapter 3, we review theory of thermal transport starting, including normal metals and insulators, conventional superconductors in the superconducting and mixed states, and d-wave superconductors. In chapter 4, we review some of the experimental details of low temperature thermal conductivity measurements. And finally, in chapter 5 we review some basic properties of LSCO and Tl2201, and discuss the growth, preparation and characterization of the samples used in our study.

Additional details of the samples are given in appendix A.

2

HIGH-TEMPERATURE SUPERCONDUCTORS

In 1986 superconductivity was famously discovered in the material $La_{2-x}Ba_xCuO_4$ with a transition temperature of $\sim$ 35 K by Bednorz and Muller [12]. It was not long after this that superconductivity was realized in related systems, YBCO and Bi2212, with superconducting transition temperatures of $\sim$90 K [17]. To date superconductivity with T_c as high as 160 K has been achieved in the cuprates under pressure (see ref. [18] for a recent listing of cuprates). While the search for superconductors with higher transition temperatures is ongoing, it was realized soon after the discovery of superconductivity in $La_{2-x}Ba_xCuO_4$, that the physics necessary to describe the phenomenology is rich, fascinating and new.

The novelty of the cuprates emerges from a number of important features that distinguish them from conventional superconductors. First, they are quasi-2 dimensional. The quasiparticles reside, for the most part, on CuO_2 layers. As such, part of the problem of high temperature superconductors (HTSC)involves the confinement of quasiparticles into two dimensions, and perhaps how the hop from one quasi-2D layer to the next. Second, they are doped Mott insulators. The electrons in the undoped parent compound are sufficiently repulsed by the Coulomb repulsion so as to localize them onto their lattice sites. As one adds carriers the electronic gridlock is relaxed and the materials eventually behave as Fermi liquids, like conventional metals. At intermediate dopings electronic transport is possible and superconductivity forms. In addition to the superconductivity, however, the strong interaction between electrons may lead to a number of other proposed ordered electronic phases, including orbital ordered [19, 20, 21, 22] and stripe [23, 24] phases that have exciting and important implications. Third, the cuprates are magnetic. The doped Mott insulator is antiferromagnetic. As one dopes carriers, the antiferromagnetism is rapidly suppressed, but magnetism of some form remains into the superconducting state either as some form of static magnetism or in the dynamics of the spin susceptibility. This highlights a important role of magnetism in explaining much

of the phenomenology of the cuprates, and potentially the microscopic mechanism for superconductivity. Perhaps more generally, the cuprates fall into a class of materials, like the manganites, that exhibit important couplings of the charge, spin and lattice degrees of freedom. In addition, quantum criticality [22, 25], another issue at the forefront of condensed matter physics, may also be relevant to the cuprates.

In the following I will review *some* of the phenomenology of the cuprates. In doing so, however, it must be appreciated that, due to the enormity of the field, I have undoubtedly left out important aspects of the cuprate problem. For more detailed reviews of the field I refer readers to two articles by Orenstein and Millis [26] and Norman and Pepin [27].

2.1 The electronic structure

Although there are many variations of the cuprates, they share several generic structural and electronic properties. The basic structure of the HTSC's consists of CuO_2 layers separated by insulating[1] spacer layers (see fig. 2.1). In the CuO_2 layer the Cu atoms are arranged in a square lattice with O atoms arranged between each Cu. By varying the composition of the spacer layers, holes (or electrons) may be doped into the CuO_2 planes.

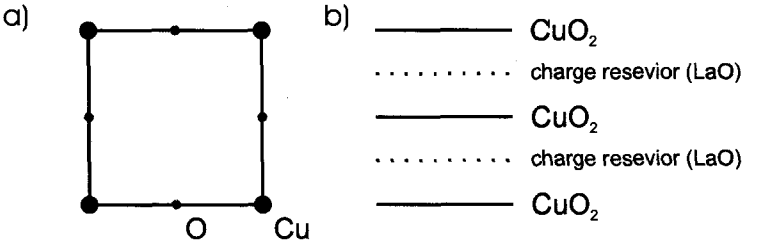

Figure 2.1: The basic structure of the cuprates (single layer). a) The CuO_2 plane. b) The layered structure along the c-axis.

The electronic structure of the cuprates is relatively simple [27]. The tetragonal structure of the stacked CuO_2 planes leads to a single $3d$ hole per Cu atom. The hybridization of the Cu $3d$ orbitals and the O $2p$ orbitals leads to a single half-filled band (the anti-bonding band). At half-filling, this band is split by an onsite Coulomb repulsion into upper and lower Mott-Hubbard bands, with the chemical potential lying somewhere in the gap ($\sim$ 2 eV) between the two bands. The end result is that the electronic structure

[1] In some cuprates, for instance $Y_2Ba_3CuO_{6+\delta}$, the layers between the CuO_2 planes also contain metallic chain layers. It is the common view, however, that these chain layers do not play a central role in the physics of HTSC.

is a Mott insulator at half-filling (1 hole per Cu atom) and is with doping relatively simple with a single two-dimensional band near the Fermi energy.

With hole doping, the electronic structure evolves to form a single hole-like Fermi surface that is, at optimal doping [2], roughly described as a cylinder about the (π, π) position in k-space, with $k_F \simeq 0.7\text{Å}^{-1}$.

The physical realization of the stacked CuO_2 planes is generic to all of the cuprates (see ref. [18] for a listing of materials). In this thesis we will focus entirely on four well studied cuprates: $La_{2-x}Sr_xCuO_4$ (LSCO) and $Tl_2Ba_2CuO_{6+\delta}$ (Tl2201), which are the focus of the thesis, and also $YBa_2Cu_3O_{6+\delta}$ (YBCO) and $Bi_2Sr_2CaCu_2O_{8+\delta}$ (BSCCO).

2.2 The phase diagram

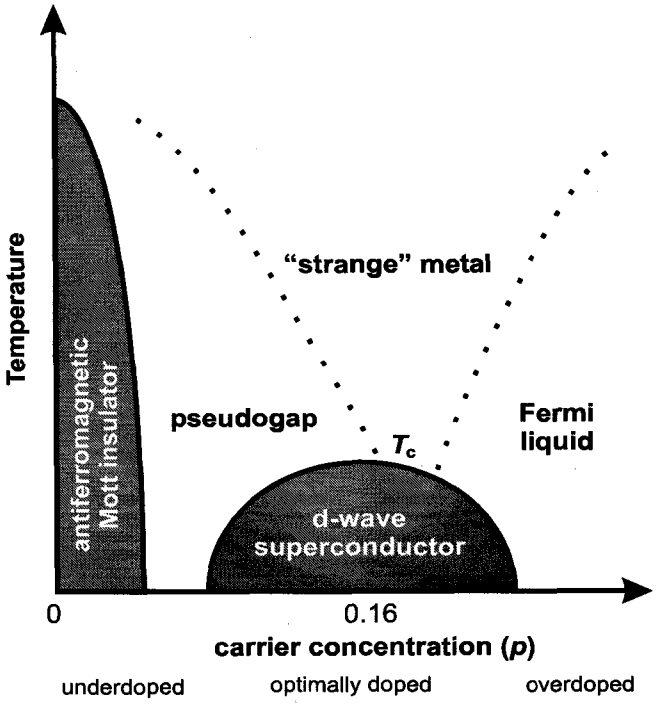

Figure 2.2: The temperature-doping phase diagram of the cuprates.

The doping (p) versus temperature phase diagram that results from doping additional holes into the CuO planes is shown in fig. 2.2. In addition to being a Mott insulator as discussed above, at half-filling the cuprates are anti-ferromagnetic. The anti-ferromagnetism

[2]The evolution of the Fermi surface with hole doping in underdoped cuprates is still being elucidated. At low doping the it is difficult to resolve a Fermi surface away from (π, π). This may indicate that only a Fermi arc or a hole pocket forms about (π, π) in underdoped cuprates.

is well described as a 2D spin 1/2 Heisenberg anti-ferromagnet [28]. With doping the anti-ferromagnetic state is rapidly suppressed. In $La_{2-x}Sr_xCuO_4$ this occurs by a hole doping of $p = 0.02$-0.03 additional holes. At higher doping a d-wave superconductor state forms below of dome centered about $p = 0.16$. At still higher doping, beyond the superconducting dome, the ground state is a Fermi liquid. In addition to these three zero temperature phases there is a pseudogap phase that is reached when ones raises the temperature above the superconducting transition temperature in underdoped cuprates and a strange metal phase in the normal state above optimally doped cuprates.

2.2.1 The superconducting state

The superconducting state in the cuprates is similar in many respects to the superconductivity observed in conventional superconductors. It shares the primary signatures of superconductivity, namely zero resistance and the Meissner effect. One of the striking differences between the superconductivity of the cuprates and that of conventional superconductors is the pairing symmetry of the superconducting order parameter. Conventional BCS superconductivity pairs electrons of with an s-wave (zero spin and orbital angular momentum $S = 0$ and $L = 0$) symmetry of the order parameter. In contrast it is now accepted[3] that the superconducting state of the cuprates has a d-wave symmetry ($S = 0$ and $L = 2$). Moreover, due to the quasi-2D nature of the CuO_2 planes, it has a 2D representation, $d_{x^2-y^2}$.

One of the distinguishing features of the $d_{x^2-y^2}$ order parameter is that it undergoes a sign change along the (0,0) - (π, π) direction in reciprocal space. As such, the superconducting gap, which is proportional to the order parameter in BCS theory, has zeros (nodes) along the (0,0) - (π, π) direction. The nodes (zeros) in the superconducting gap lead to low energy quasiparticles. This is in contrast to the s-wave order parameter of conventional superconductors where an isotropic gap leads to an exponentially small quasiparticle density of states at low energy. The presence of the nodes in the order parameter results in power law temperature dependencies in many transport and thermodynamic properties of the cuprates, including the specific heat, penetration depth [31] and the thermal conductivity [14].

While the symmetry of the order parameter is now agreed upon, several other fundamental aspects of the superconductivity remain controversial. First, while the pair-

[3]Reviews of the cuprates detailing the evidence for d-wave superconductivity can be found in references [29], [26], [30] and [27].

ing mechanism responsible for superconductivity in conventional superconductors is the electron-phonon interaction, it has been argued by many that the pairing mechanism in the cuprates is of electronic origin. In particular it has been argued that anti-ferromagnetic spin-fluctuations provide the pair mechanism in the cuprates. Amongst other reasons for this view are that anti-ferromagnetic spin fluctuations naturally favor a d-wave order-parameter over the isotropic s-wave order parameter. In this view the superconductivity in the cuprates may have much in common with superconductivity observed in several quantum critical heavy Fermion systems, where superconductivity emerges when anti-ferromagnetic order is suppressed.

Second, in conventional superconductors the superconducting order parameter is proportional to the superconducting gap maximum, Δ_0, which in turn is proportional to the superconducting transition temperature, modulo a factor that depends on the strength of electron-phonon coupling. In overdoped cuprates T_c and Δ_0 both decrease with increasing doping, qualitatively consistent with conventional superconductors. In underdoped cuprates, however, angle-resolved photoemission [32] and tunneling measurements [33] have shown that the superconducting gap increases with decreasing doping, opposite to the doping dependence of T_c, which decreases with decreasing doping. In addition, as noted by Uemura and co-workers, while the gap no longer scales with T_c in underdoped cuprates, the superfluid density does [34]. This brings us conveniently to the pseudogap phase.

2.2.2 The pseudogap phase

Above T_c in underdoped cuprates is the so-called pseudogap phase (see review by Timusk and Statt [35]), characterized by a gap-like feature that manifests below a temperature T^*. The first observation of the pseudogap was from spin-lattice relaxation rate measured by NMR [36], where they observed a suppression of the spin lattice relaxation well above the superconducting transition temperature, T_c. The pseudogap has since been observed in ARPES [37, 38, 39], tunneling [33], c-axis infrared conductivity [40], resistivity [41], specific heat [42], NMR Knight shift [43] and as will be discussed in chapter 6, thermal conductivity [4].

Of particular note, as shown by ARPES, tunneling and c-axis infrared conductivity the pseudogap has approximately the same energy both above and below T_c. The gap is filled in, rather than closed in energy with increasing T. In addition, measurements of the pseudogap by ARPES have shown the pseudogap to have approximately the same

angular dependence as the d-wave superconducting gap below T_c [37].

The interpretations of the pseudogap phase in the underdoped region can be loosely classified into two groups represented in figure 2.3, precursor pairing scenarios and competing order scenarios[4].

The precursor pairing scenario of the pseudogap

In precursor pairing scenarios [44] the pseudogap Δ_{pg} and temperature T^* represent mean-field values of the superconducting gap and transition temperature. Superconductivity does not occur at T^*, however, because fluctuations of the phase of the order parameter prevent the development of coherent superconductivity. Between T_c and T^*, the Cooper pairs are present but do not form a superconducting state. It has been argued that the cuprates are amiable to phase fluctuations, particularly in the underdoped regime for a combination of reasons: they are quasi two-dimensional, have low carrier density and have short coherence lengths. The dome shape of the superconductivity in the phase diagram can be understood in this picture as a crossing of a decrease in Δ_{pg} and an increase in phase coherence with increasing doping, as depicted in fig. 2.3a). With sufficient overdoping T_c merges with the mean-field transition, T^*. Although the picture of fig. 2.3a) describes thermal fluctuations of the phase it is also possible that quantum phase fluctuations suppress superconductivity at low doping [45, 46]. In this picture the $T = 0$ ground state intervening the anti-ferromagnetism and the onset of superconductivity can be viewed as a quantum disordered superconductor.

In addition to explaining the persistence of the gap above T_c, the precursor pairing scenario has received support from a number of other experiments. Measurements of the Nernst effect have provided evidence for the vortex-like excitations in the pseudogap phase above the superconducting transition temperature [47] and measurements of the superfluid density at terahertz energies have provided evidence for fluctuating superconductivity above T_c [48]. In both of these cases however, signatures for fluctuating superconductivity do not extend up to T^*, but rather only in a region above T_c.

Competing order scenarios of the pseudogap

An alternate class of scenarios, depicted in figure 2.3 b), is to view the pseudogap state as another ordered state, independent of superconductivity, that competes and in some

[4]I caution against any strict adherence to this classification. They're may be room in many theories to accommodate elements of both competing order and precursor pairing. An example of this is the stripe model, discussed below.

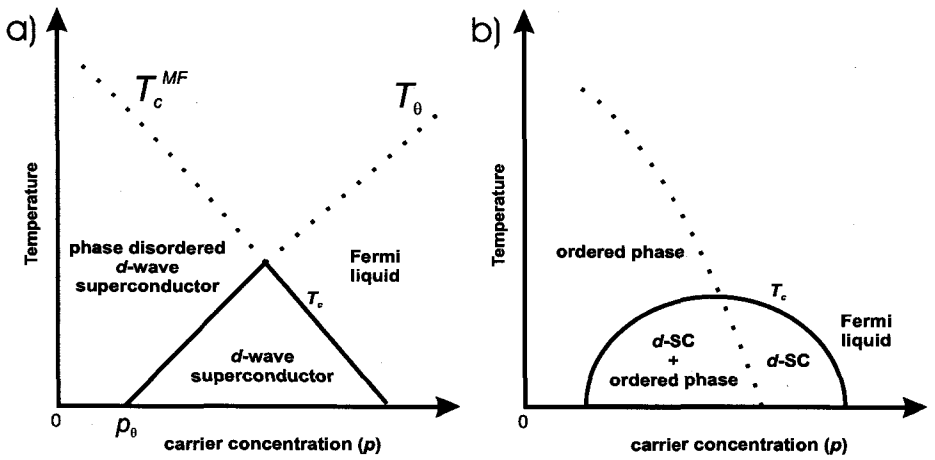

Figure 2.3: Two views of the temperature-doping phase diagram of the cuprates. a) The pre-formed pairing scenario phase diagram. b) The competing-order scenario phase diagram.

instances co-exists with superconductivity. A number of possible states have been proposed along these lines including orbital current phases (d-density wave order [19] and staggered-flux phases [21, 22]) and spin-density wave and charge-density wave phases (stripes) [23, 49, 50, 24, 51].

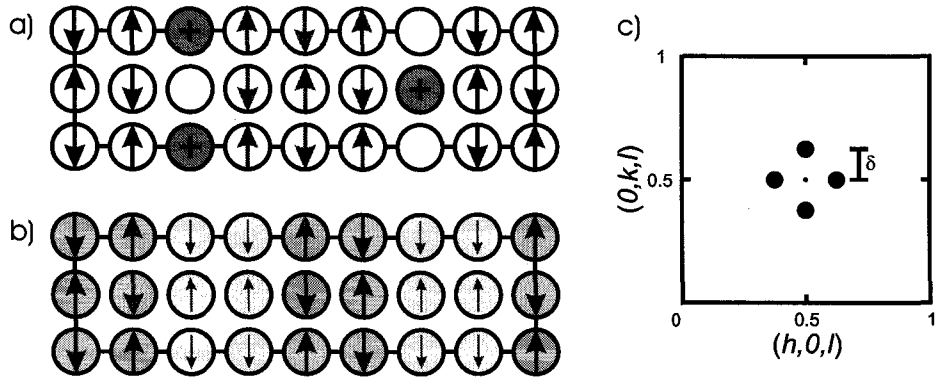

Figure 2.4: a) A proposal for stripe pattern in CuO_2 plane of $La_{1.48}Nd_{0.4}Sr_{0.12}CuO_4$ from Tranquada et al. [52]. The arrows indicate the magnetic moments on the Cu ions (the O ions are not shown). The shaded circles are holes which form 1/2 filled rivers of charge. This depiction microscopic phase separation represents the strong coupling limit of the stripe picture. b) The weak coupling picture of the spin density wave (stripe) order. The magnitude of the spin on each Cu site is modulated. A corresponding modulation of the charge density (CDW) is also expected. c) Reciprocal space showing the location of the magnetic Bragg peaks that are associated with the spin-stripe order depicted in panels a) and b).

The basic phase diagram in these scenarios is one in which the pseudogap phase below T^* is the competing ordered state, and Δ_{pg} observed in the pseudogap phase is the gap associated with the competing order. Below the superconducting transition

temperature there is a region of coexistence between the superconducting and competing orders. Finally, above some critical doping, p_{cr}, there is a quantum phase transition inside the superconducting dome to a state where superconductivity is the only long range order. Interestingly in addition to doping, magnetic field has emerged as a useful parameter to tune the competition between competing orders [51].

Experimentally, evidence for orbital current phases has been reported but remains controversial. However, there is now plenty of evidence for SDW order, and more recently CDW order, in at least some families of the cuprates in the underdoped region of the phase diagram. It is, however, far from clear whether these competing orders are crucial to the broad structure of the phase diagram or merely spectators.

2.2.3 SDW order (stripes)

One brand of competing order, spin-density wave (SDW) order ("stripes"), warrants particular attention due to it's robust experimental demonstration[5,6]. Generally "stripes" refer to a unidirectional spatial density modulation of the charge or the spin and charge [50]. In the strong coupling limit, stripes will be a microscopic phase separation into rivers of holes separated by anti-ferromagnetic domains (see fig. 2.4a for a particular manifestation of stripes relevant to $La_{1.48}Nd_{0.4}Sr_{0.12}CuO_4$ [52]). In the opposite limit of weak coupling, stripes are a density modulation that may arise due to a nested portions of the Fermi surface.

Experimentally, stripe phases are evidenced in neutron or x-ray scattering measurements by Bragg peaks at incommensurate wave vectors given by the period of modulation of the stripe, l. For spin stripes running parallel to the CuO_2 bond in the cuprates the magnetic Bragg peaks are at $2\pi/a(1/2 \pm\delta, 1/2)$ and $2\pi/a(1/2, 1/2 \pm \delta)$, where $\delta = a/l$ (see fig. 2.4b). In the cuprates Bragg peaks at these incommensurate wave vectors have been observed in neutron scattering in a number of materials, although primarily the La_2CuO_4 family of materials, in both inelastic neutron scattering ("dynamic" stripes) and in elastic neutron scattering ("static" stripes). In this thesis we are primarily interested in the low-energy properties of the cuprates, so I will focus on observations of static stripes.

[5]For detailed reviews of theory and experiments related to stripes I refer readers to Kivelson et al. [50] and Carlson et al. [24], Emery et al. [49] and Orenstein and Millis [26].

[6]The relevance of the stripe picture to the competing order scenario of the pseudogap, discussed above and depicted in fig. 2.3b) is unclear. Stripes may in fact have more relevance to a phase fluctuation description of the pseudogap.

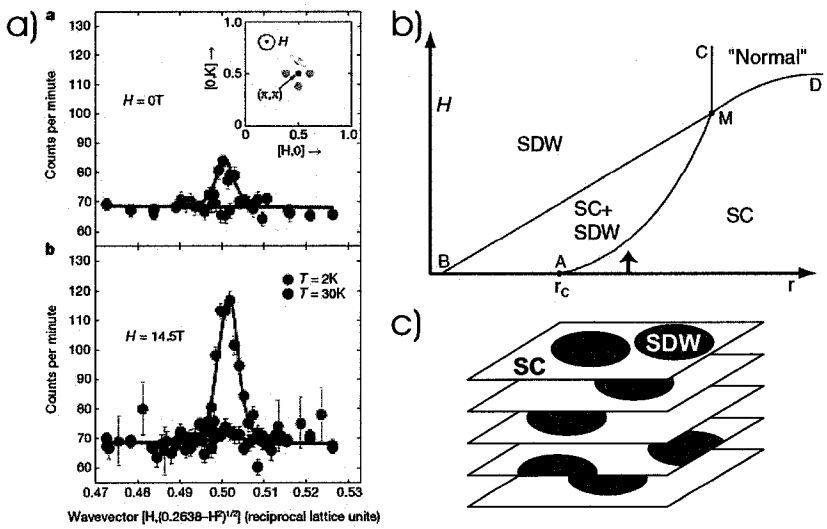

Figure 2.5: Tuning SDW order with an applied magnetic field. a) Incommensurate neutron scattering in $La_{1.9}Sr_{0.1}CuO_4$ in 0T and 14T from Lake et al. [53]. At low temperatures the application of field enhances the intensity of the elastic incommensurate magnetic Bragg peak associated with static stripes by a factor of 3. b) The phase diagram from Demler et al. [54] depicting the competition between superconductivity (SC) and spin-density wave order (SDW). Tuning magnetic field, H, drives one close to SDW order. The parameter r is similar but not equivalent to doping, p (see Demler et al. [54]). c) The mesoscopic phase separation of SDW and SC order proposed by Savici et al. on the basis of μSR measurements of the volume fraction of SDW order [55]. Figure adapted from ref. [55].

The first, and perhaps most compelling, evidence for static stripes in the cuprates is from x-ray and neutron scattering measurements in $La_{1.48}Nd_{0.4}Sr_{0.12}CuO_4$ by Tranquada and co-workers [52]. Here they observe evidence from both charge and spin stripes with incommensurability $\delta = 1/8$. This observation is notable for a number of reasons. First, $\delta = 1/8$ corresponds to half filled stripes for a hole doping $x \simeq 1/8$, as depicted in fig. 2.4a, representing a particularly stable stripe configuration. Second, the doping of $x = 1/8$ corresponds to a local suppression of T_c observed in $La_{1.875}Sr_{0.125}CuO_4$ [56] and $La_{1.875}Ba_{0.125}CuO_4$ [57] (the so-called 1/8 anomaly). In fact, in $La_{1.48}Nd_{0.4}Sr_{0.12}CuO_4$ T_c is driven to zero. This observation suggests a competition between superconductivity and static stripes.

More recently static SDW order has been found to co-exist and compete with superconductivity in LSCO without Nd doping [58, 59, 60, 61] for Sr dopings less than $x = 0.13$, and also for the oxygen doped relative, $La_2CuO_{4.12}$ (T_c= 42 K) [62]. Above this doping a spin-gap opens up, gapping out the low-energy excitations (see [63] and references therein). The competition between superconductivity and static spin stripes can also be

tuned with the application of magnetic field. In field the intensity of the incommensurate magnetic Bragg peak increases with increasing magnetic field [64, 53, 65, 66, 67, 68], as shown in measurements by Lake et al. [53] in fig. 2.5.

These latter observations are consistent with theories suggesting that SDW order should be enhanced not only in the vortex cores, where superconductivity is suppressed, but in the regions surrounding the vortex cores [54]. The phase diagram suggested by Demler et al. [54], given in fig. 2.5b, is one in which the field drives the superconducting state closer to the SDW state.

Two important questions arise regarding these observations of static stripes in LSCO. First, one may ask whether static stripes generic to the cuprates. Unfortunately, this question is, as yet, unsettled. The majority of elastic neutron scattering measurements in underdoped cuprates have been on the LSCO family of materials due to the ability to grow large crystals suitable for neutron scattering measurements. As such, considerably fewer measurements have been done on materials such as YBCO and BSCCO at comparable doping for purely practical reasons. As yet no clear evidence for static spin stripes has surfaced in YBCO [69], although there is evidence for dynamic stripes from inelastic neutron scattering [70]. Evidently, it is speculated that disorder may play a key role in stabilizing static stripes [50]. As LSCO is known to be a more disordered material than YBCO due to the cation substitution (Sr for La) it may be that static stripes are only present in LSCO, or similarly disordered materials.

A second issue is how homogeneous is the stripe order in underdoped LSCO. Do stripes and superconductivity co-exist at a microscopic level or is there mesoscopic phase separation into hole-rich superconducting regions and hole-poor stripe regions? Recent muon spin resonance measurements (μSR) on $La_2CuO_{4.12}$ and $La_{1.88}Sr_{0.12}CuO_4$ [55] suggest the latter view, depicted in the cartoon in fig. 2.5c. From μSR the volume fraction of SDW regions is estimated to be $27-40\%$ for $La_2CuO_{4.12}$ and 10-20 % for $La_{1.88}Sr_{0.12}CuO_4$. In addition, from the μSR lineshape they estimate the size of the magnetic regions to be only 15-30 Å, although this value is seemingly in conflict with the considerably smaller magnetic correlation length (> 400 Å) determined from the width of the magnetic Bragg peaks in neutron scattering [62, 53, 65]. Also, it should be noted that although the μSR measurements show that the SDW order only occupies a faction of the sample volume in a heterogeneous fashion, they cannot exclude the possibility that SDW order and superconductivity co-exist at a microscopic level.

More fundamentally, there is an issue of how essential is the stripe phenomena is

to the mechanism behind HTSC. In other words, are stripes driving HTSC or are they an added complication, (albeit an interesting one, no-doubt worthy of study)? Several theories have predicted that the hopping of holes onto fluctuating stripes is the mechanism for superconductivity [24].

2.2.4 The "normal" state

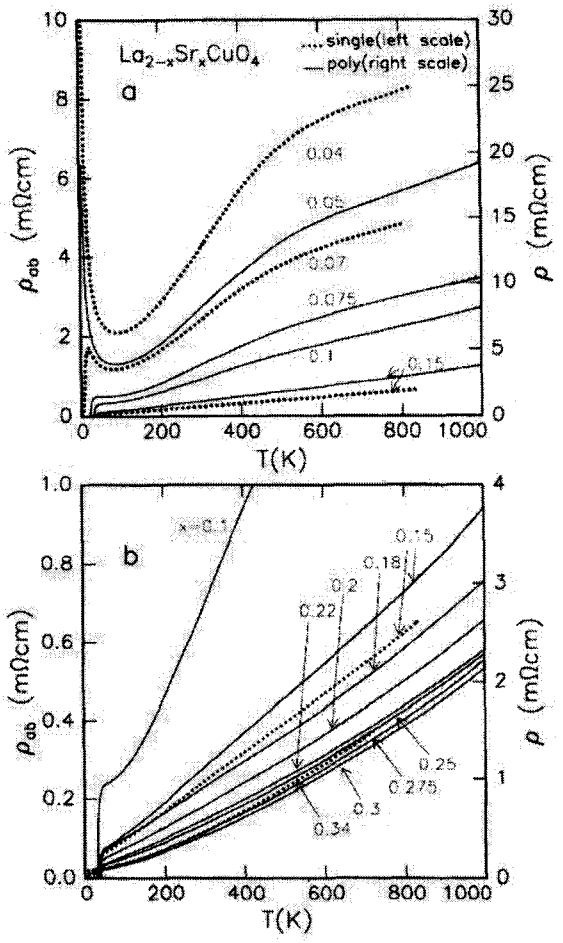

Figure 2.6: The resistivity in LSCO as a function of doping for a) $x < 0.15$ and b) $0.15 < x < 0.35$. Note both polycrystalline (solid) and single crystal (dotted) samples are shown.

In the "normal" state ($T > T_c$) of the cuprates, a number of properties have unusual characteristics, in addition to the pseudogap. This is perhaps most evident in the normal state resistivity as a function of doping. In fig. 2.6 the normal state resistivity, ρ, measured by Takagi [71] on polycrystalline samples of LSCO is shown up to 1000 K as the doping

is increased from the undoped Mott insulator to heavily overdoped Fermi-liquid state[7]. For very low dopings, LSCO is insulating at low temperatures. As noted above, although band structure predicts La_2CuO_4 to be a metal, the strong on-site Coulomb repulsion makes La_2CuO_4 a Mott insulator.

With increasing doping the magnitude of the resistivity decreases, consistent with an increase in carrier density, but the low temperature resistivity remains insulating. By further increasing the doping the resistivity eventually becomes metallic. At optimal doping the resistivity in LSCO, and other cuprates, has an unusual linear in T temperature dependence that persists up to 1000 K [71]. This so-called "strange metal" is very difficult to explain and as yet no consensus has been reached on the origin of the T linear resistivity. Recent measurements by Ando have noted, however, that the T linear resistivity is only observed over a very narrow range of doping about optimal doping [78]. With further increase in doping the resistivity evolves from T linear to T^2. This latter temperature dependence, which has been clearly established in heavily overdoped non-superconducting LSCO with $x = 0.30$ [79], is a hallmark of a Fermi liquid ground state. Other indications that the normal state in overdoped cuprates is a Fermi liquid come from the observation of the Wiedemann-Franz law in the field induced normal state [7].

As doping is varied between the Mott insulator and the Fermi liquid states, a metal-to-insulator transition occurs at low temperature. Precisely, where in the superconducting dome this occurs, however, is obscured by the onset of superconductivity. Measurements by Boebinger and Ando [76, 80] circumvented this problem by using pulsed magnetic fields of 60 T to suppress superconductivity and reveal the resistivity in the field-induced normal state. As a function of doping they find that LSCO undergoes a metal-to-insulator transition at a doping of $x = 0.17$ (see figure 2.7). Note they have adopted a definition for the metal-to-insulator transition as the point where the temperature dependence of the resistivity crosses over from $\delta\rho/\delta T > 0$ to $\delta\rho/\delta T < 0$. Below $x = 0.17$, in the superconducting samples, they report the insulating behavior to have an unusual, and as yet unexplained, $\log(1/T)$ temperature dependence [80].

Note that this logarithmic temperature dependence is notably weaker than the exponential T dependence exhibited at dopings just below the onset of superconductivity where the temperature dependence can be described by a model of 3D variable-range

[7]The normal state resistivity, ρ, in LSCO has also been studied by several other groups [72, 73, 74, 75, 76, 77, 78], and also our own group (see ch. 5)

hopping (VRH): $\rho = \rho_0 \exp(-T_0/T)^{1/2}$[81, 75, 74, 82]. In this model quasiparticles are localized by defects. Transport is via phonon assisted hopping between defect sites that are separated by a variable distance but are close in energy. Unlike the Mott insulator, where strong correlations result in insulating behavior, variable range hopping can occur simply due to disorder. The introduction of strong correlations add a Coulomb gap and change the exponent in the exponential from 1/4 to 1/2. It is difficult to clearly distinguish between these two exponents experimentally. It leaves open the question of the extent to which the insulating behavior in underdoped LSCO is governed by strong correlations versus disorder.

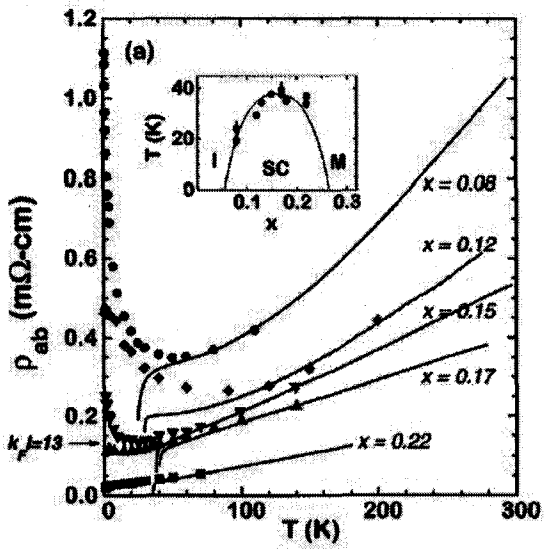

Figure 2.7: ρ vs. T as a function of doping in LSCO in both 0T (solid lines) and 60 T (symbols). The 60 T data is the field-induced "normal" state resistivity. With doping a metal-to-insulator transition occurs at a doping of $x \simeq 0.17$, the doping where $\delta\rho/\delta T$ at low T cross over from -ve to +ve. Figure taken from reference [76].

A number of questions result from this discussion of the resistivity many of which are pertinent to an investigation of the low-temperature thermal conductivity. For instance, how does LSCO evolve from the Mott insulator to the Fermi liquid? What role does disorder play in this? What would the state be at $x = 0.05$ in the absence of disorder, metallic or insulating? If underdoped LSCO is insulating in the normal state, what are the excitations in the superconducting state? Does one have delocalized d-wave nodal quasiparticles or are all the quasiparticles localized in the superconducting state? Can one have delocalized heat carriers and localized charge carriers: ie spin-charge separation?

In this regard it is important to note that much of the information regarding the nor-

mal state in this heavily underdoped region of the phase diagram comes from measurements on LSCO. The answer to this question may be further elucidated by measurements on less disordered materials, such as YBCO, in the same region of the phase diagram.

2.3 What thermal conductivity has to add?

As outlined above there are a number of important outstanding questions in the cuprates. For instance, what is role of competing order in the cuprates? Is it fundamental to the physics HTSC or simply a bystander? And, what is the glue that binds the Cooper pairs in the cuprates? Is it electronic in origin (spin fluctuations) or the electron-phonon interaction, like conventional superconductors?

Before discussing thermal conductivity in the rest of the thesis, we'll first consider what thermal conductivity measurements may be able to add to the answers to these important questions. In general thermal conductivity, as a technique has a number of favorable properties.

- Thermal conductivity is a bulk measurement.
- Thermal conductivity is sensitive to all mobile excitations that can carry heat (have entropy), unlike specific heat which also measures the entropy of localized excitations.
- With thermal conductivity we can potentially distinguish the quantum statistics of the excitations (bosons vs. fermions) at low temperatures by their different characteristic power law temperature dependencies.
- Unlike, DC resistivity, which is shorted by the condensate, thermal conductivity can measure excitations both inside and outside of the superconducting state.
- Thermal conductivity can be employed to measure the quasiparticles down to very low temperatures ($T \simeq 40$ mK), setting an energy scale (resolution) much lower than many other techniques.
- Thermal conductivity can be used to study many different families of the cuprates. It is not sensitive to the surfaces of the samples, like tunneling and ARPES, nor does it require very large sized samples like neutron scattering. This latter feature allows for an important comparison between different families of cuprates using the

same technique, something that we will employ throughout the thesis to attempt to isolate generic features from material specific phenomena.

- Finally, thermal conductivity may be measured in an applied magnetic field, giving us an additional tuning parameter to explore. This is most useful when we are able to suppress superconductivity with an applied field, allowing us to explore quasiparticle transport in both the superconducting and field-induced normal states.

Turning the technique to study the cuprates, the usefulness of many of these features becomes apparent. With well defined theory of d-wave superconductor, which will be reviewed in chapter 3, comparison between experiment and analytic expressions from theory can be used to test the validity of the nodal quasiparticle framework. This has already proven to be successful in the cuprates at optimal doping [14, 16, 15], and to a lesser extent in heavily overdoped Tl2201 [7], but can be put to the test as a function of carrier concentration, in both underdoped and overdoped cuprates.

Perhaps more interestingly, above we have described scenarios to explain aspects of the underdoped region of the cuprate phase diagram based on competing order. These competing order states have different ground states than the d-wave superconductor and, as such, have different ground state excitations. A change in the ground state excitations should, in principal, have a signature in the low temperature thermal transport. For instance, d-density wave order has a nodal structure similar to the d-wave superconductor and hence similar transport, although differs in the details. However, one would expect the stripe order to have a different excitation spectrum than the d-wave superconductor. The limit of 1D non-interacting charge stripes will behave more as a Luttinger liquid with different excitations than the Bogoliubov quasiparticles of a quasi-2D d-wave superconductor.

Finally, the thermal conductivity depends not only on the quasiparticles, but also on the conduction of phonons. In conventional metals, the phonons are scattered at low temperatures primarily by electrons. This interaction depends on the coupling of the electrons and phonons via the same coupling constant, λ, that determines, in part, T_c in conventional superconductors. If an argument can be made that phonons are also scattered by electrons in the cuprates, the phonon conductivity may be used as a measure of the electron-phonon interaction. The results of this investigation, which is discussed in chapter 9, may have important implications for the understanding of the pairing mechanism in high temperature superconductors.

3

THE THEORY OF THERMAL CONDUCTIVITY

The thermal conductivity, κ, of solids is governed primarily by the conduction of electrons and phonons[1] and the effectiveness with which the electrons and phonons are able to conduct heat is limited by multiple scattering mechanisms. In our study of the cuprates we have historically been interested in the electronic contribution to κ and the task has been to extract this contribution from a sizable phonon contribution to κ. As we'll see in chapter 9, however, when the electron-phonon interaction dominates κ_{ph}, the phonon thermal conductivity may also contain important physics. In either case, our interpretation of the experimental results will be aided considerably by the theory outlined in this chapter.

The discussion of thermal conductivity will start with a review of κ_{ph} and κ_{el} in a normal metal using the simple kinetic model of thermal transport. The discussion will then evolve to include κ_{el} in the superconducting state, first in the case of a conventional s-wave superconductor and then in the more relevant case of a d-wave superconductor. In both instances, the theory will be discussed in zero-field and the vortex state. The case of a d-wave superconductor will be discussed in some detail, since as we will show in latter chapters, we find certain instances where the mean-field theory κ in a d-wave superconductor outlined here provides a very successful description of the data. In other instances, where the theory fails, comparison with the expectations presented in this chapter may provide telling clues as to the reason for discrepancies between theory and experiment.

To understand the results of our thermal conductivity measurements on the cuprates we must first review elements of the theoretical understanding of thermal transport. To first order we must find a means to overcome the complication that the thermal conductivity is the sum of two distinct contributions arising from the phonons and the

[1] Nonlocal spin excitations such as magnons may in principle also contribute to the thermal conductivity but this contribution will not be discussed here.

electrons. In the cuprates we are primarily interested in the electronic contribution to κ, but we must first understand something of the phonon thermal conductivity in order to reliably extract our object of interest. This discussion will focus on the kinetic theory of transport, which is conceptually very simple and intuitive, and although not theoretically rigorous suits the aims of this chapter quite well. For more detailed discussions of thermal transport in normal metals and insulators I refer readers to several excellent books and reviews [83, 84, 85, 86].

Finally, the focus of this thesis and concomitantly this chapter is on the low temperature limit of the thermal conductivity. At low temperatures, the physics is in general simplified, as often a single scattering mechanism dominates the transport as $T \rightarrow 0$. At low T the scattering is dominated by elastic quasiparticle-impurity scattering for quasiparticles and phonon-boundary or phonon-electron scattering for phonons.

3.1 Lattice conduction

3.1.1 Kinetic theory

We will begin by describing the phonon thermal conductivity in terms of the simple kinetic theory. The kinetic theory is a classical description of transport where heat is transported ballistically by particles (phonons) travelling at a given velocity, each carrying a quantum of energy over a mean distance. While this description of the conductivity is not rigorous and makes a number of approximations that break down in real materials, particularly at high temperatures, it provides both a conceptually and practically useful description of κ_{ph}. Moreover, it provides an accurate description of κ_{ph} in the limit that a single scattering mechanism dominates κ_{ph}, such as in the low-T limit. For more detailed descriptions of κ_{ph} I refer readers to books by Ziman [83] and Berman [84] and reviews by Klemens [85] and Carruthers [86].

From simple kinetic theory, κ_{ph} is given (for $T \ll$ the Debye temperature, Θ_D) by

$$\kappa_{ph} = \frac{1}{3}\beta < v_{ph} > \Lambda T^3 \tag{3.1}$$

where β is the coefficient of phonon specific heat, Λ is the phonon mean-free-path, and $< v_{ph} >$ is a suitable average of the transverse and longitudinal acoustic sound velocities [87]. The phonon specific heat has the simple Debye T^3 temperature dependence for acoustic phonons and the sound velocities are essentially T independent. The remaining T dependence is contained in the average phonon mean-free-path, Λ. Following

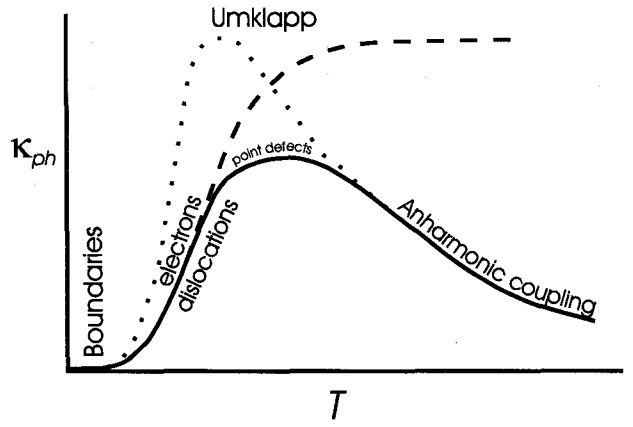

Figure 3.1: The phonon thermal conductivity, κ_{ph}, as a function of temperature depicting the various contributions to phonon scattering. Figure adapted from Ziman [83].

Matthiessen's rule (applied to phonon thermal conductivity) the phonon scattering rate, $\tau_{ph}^{-1} = v_{ph}/\Lambda$, is the sum of the scattering rates from all of the different scattering channels [2]:

$$\tau_{ph}^{-1} = \tau_{BS}^{-1} + \tau_{ph-dis}^{-1} + \tau_{ph-qp}^{-1} + \tau_{iso}^{-1} + \tau_{ump}^{-1}, \tag{3.2}$$

where τ_{BS}^{-1}, τ_{ph-dis}^{-1}, τ_{ph-qp}^{-1}, τ_{iso}^{-1} and τ_{ump}^{-1} are for scattering from the sample boundaries, the strain-field from dislocations, electrons, point defects (isotopes or impurities) and Umklapp scattering of phonons.

These various scattering mechanisms have different dependencies on the wavelength and energy of the phonons. Generally the scattering will be weak when the phonon wavelength becomes much greater than the spatial extent of the scatterer, ie. at low temperatures. In addition, Umklapp scattering between phonons, which requires finite phonon energies, becomes negligible at low T but dominates κ_{ph} in the high T limit. A schematic of κ_{ph} vs. T showing the dominant scattering mechanisms at various temperatures is shown in figure 3.1. In pure materials, a peak in κ, typically between 20 and 80 K, is formed due to the decrease in τ_{ump}^{-1} and/or τ_{iso}^{-1} as temperature is lowered. Below the peak κ_{ph} is governed by any or all of τ_{BS}^{-1}, τ_{ph-dis}^{-1} and τ_{ph-qp}^{-1}.

Point defect scattering

Atomic scale defects responsible for τ_{iso}^{-1}, such as an isotope or chemical substitution, act as point-like scatterers for typical phonons at $T \ll \theta_D$. For point-like defects, phonons will

[2]Here we have ignored "normal" phonon-phonon scattering processes, which do not contribute to the scattering rate directly, but can influence the scattering rate of other scattering mechanisms

undergo Rayleigh scattering and τ_{iso}^{-1} will have an $\omega^4(T^4)$ dependence, giving $\kappa_{ph} \propto 1/T$. The high power law means that this type of scattering is usually only dominant around the peak in the phonon conductivity: at low temperatures Λ will be limited by boundary scattering and at high temperatures the conductivity will be dominated by Umklapp scattering.

It is point like scattering that should be the relevant scattering mechanism for describing the scattering associated with the chemical substitution used for doping in the cuprates (Sr for La substitution in LSCO), interstitial atoms (interstitial O in Tl2201) or a vacancy at a lattice site. As such, although Sr doping, for instance, may contribute to suppressing the peak in the phonon thermal conductivity at intermediate temperatures, as discussed in chapter 5, it should not have a direct impact on scattering in the low temperature limit ($T < 1$ K).

Phonon-dislocation scattering

In contrast to point-like defects, dislocations can cause significant scattering at low temperatures. Unlike point defects, dislocations have linear dimensions and have a larger length scale. With dislocations, the scattering is not primarily from the core of the dislocation as would be naively assumed, but rather from the strain field extending out from the dislocation. This may be understood by analogy to the scattering of light through a region with a changing index of refraction. The scattering rate for scattering from the strain field was deduced by Klemens to be linearly proportional to ω. The resulting thermal conductivity, κ_{ph}, is proportional to T^2 if scattering from dislocations is dominant. This T dependence has been verified in experiments although comparisons between experiment and theory do not agree quantitatively, the actual scattering being 100-1000 times stronger than accounted for by the theory. Resonant scattering from mobile dislocations has been proposed to account for this numerical discrepancy.

In the cuprates, as in all real crystals, there is a certain density of dislocations, whether they be screw or edge dislocations or some more complicated combination of these, will be present in as grown samples. If they are of large enough density they may impact on the low temperature thermal conductivity although they should be removed or reduced by annealing.

3.1.2 Boundary scattering

In the original treatment of phonons scattering from the boundaries of a crystal by Casimir [88], the phonons incident on the surface of a sample are absorbed at the surface and re-radiated with a frequency distribution indicative of the temperature at the surface. The resulting phonon mean-free-path is temperature independent and given by the geometry of the sample, resulting in a phonon thermal conductivity with a T^3 temperature dependence. For rectangular shaped samples, Λ is often given as the geometric mean of the cross-sectional area of the sample $\Lambda_{Casimir} = 2\sqrt{A/\pi}$, although several authors have suggested other, more accurate forms for $\Lambda_{Casimir}$ [89, 87].

The difficulty with Casimir's treatment is that when one examines the mechanism for a phonon scattering from the surface of a crystal it is not clear it should be frequency (temperature) independent process. For instance, for a perfectly smooth surface a phonon should scatter specularly from the surface, resulting in no change in heat flow, or infinite thermal conductivity. Thus, whether or not a phonon is specularly reflected from the surface or diffusely scattered as in Casimir's treatment depends on some way upon the defect structure at the surface of the sample. As the temperature of a crystal is reduced and the average phonon wavelength increases, a surface of a given roughness appears smoother, which increases the occurrence of specular reflection and results in a mean free path which varies in temperature.

It is well established empirically [90, 87, 91] that the phonon thermal conductivity is affected by the boundary for sufficiently abraded samples, but for surfaces with a higher degree of crystalline perfection (polished, etched, annealed) the phonon thermal conductivity exceeds the Casimir limit and empirically follows a power law temperature dependence, so that $\kappa_{ph} \propto T^{\alpha}$. Such an effect has been previously observed in many studies of low-temperature phonon heat transport in high-quality crystals such as Si [87], LiF [90, 92], diamond [93] and Al_2O_3 [91]. The measurements on Al_2O_3 from ref. [91] are reproduced in figure 3.2. They show a T^3 power law for an abraded surface but in the polished sample the phonon thermal conductivity increases and develops a $T^{2.7}$ power law. Note that cuprate samples are always have either polished surfaces or as-grown, mirror like surfaces. As such, similar sub-cubic power laws may be expected for boundary scattered phonons.

Finally, we note that the there is no fundamental reason for a single power law - it is simply an empirical result. The process by which phonons are diffusely scattered at the

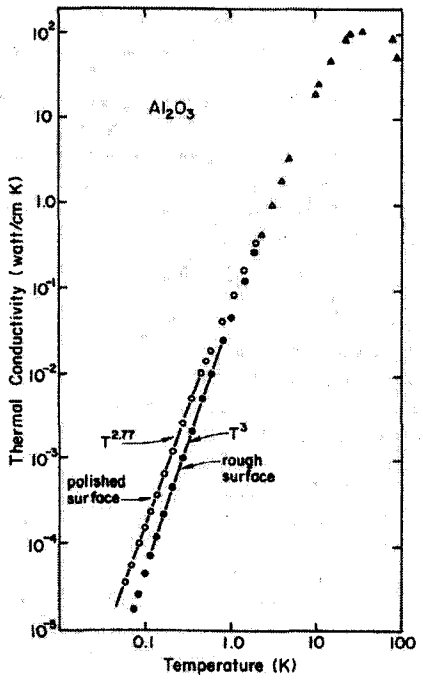

Figure 3.2: Thermal conductivity of sapphire (Al_2O_3) single crystals. The $T^{2.77}$ line through the data for the polished sample is a good fit. The T^3 line through the data for the surface-roughened sample is the Casimir prediction. This figure is reproduced from reference [91].

surface of a crystal remains poorly understood. In particular, is the phonon scattered by the surface roughness or by a damaged layer below the surface. In the latter case the diffuse scattering has a connection to the dislocation scattering in the bulk.

3.1.3 Phonon-electron scattering

In a normal metal phonon-electron is the dominant source of phonon scattering at low temperatures. In clean crystals, such that the electronic mean-free path is longer than the phonon wavelength, the contribution to the phonon thermal resistance from the electron-phonon scattering, W_{ph-el}, is proportional to $1/T^2$ [83, 84, 94]. In the treatment by Butler and Williams [94]

$$W_{ph-el} = 0.42N(E_F)\Omega_a^{1/3}\left(\frac{\Theta_D}{T}\right)^2 \lambda(\text{Kcm/W}), \tag{3.3}$$

where $N(E_F)$ is the electronic density of states at the Fermi energy in (spin states)/eV, Ω_a is the atomic volume in Å^3, Θ_D is the Debye temperature in K, and λ is the electron-phonon coupling parameter. λ determines the electron-phonon mass enhancement and the superconducting transition temperature in conventional superconductors, making it,

in principle, an interesting quantity to study.

This formulation of W_{ph-el} is only strictly valid in the limit that the wavelength of the important phonon is less than the mean-free path of the electrons, l_e. At the sub-Kelvin temperatures relevant to our experiments the phonon wavelength will grow beyond l_e. As discussed by Ziman [83], the phonon interaction in the limit $\lambda_{ph} > l_e$ may be more correctly modeled using theory developed by Pippard [95] for the description of ultrasonic sound attenuation. As shown in measurements of impure Cu [96], W_{ph-el} depends on l_e in the limit $\lambda_{ph} > l_e$ but notably may still vary in temperature as $1/T^2$ and must depend in some manner on the electron-phonon coupling parameter λ.

Whether these theories, devised for normal metals for describing W_{ph-el} in normal metals is appropriate for the cuprates, whose normal state has been described as a "strange metal", is unclear. In addition, we must consider that many of our measurements are conducted in the "universal' limit of the d-wave superconducting state (discussed below) rather than the normal state at all. In a d-wave superconductor W^p_{ph-el}, has, to our knowledge, not been developed theoretically in enough detail to make any quantitative predictions. However, based on the fact that the "universal" limit has a energy independent density of states, like a conventional metal, there is reason to suspect a similar T dependence to W_{ph-el} in a d-wave superconductor at low T as that of the normal metal.

3.2 Normal state electronic thermal conduction

The electronic contribution to κ in a normal metal can be evaluated using the same simple kinetic theory used to interpret the phonon thermal conductivity (eq. 3.1) with the appropriate substitution of the quasiparticle velocity, v_F, heat capacity, C_e, and mean-free-path, l_e. In a normal metal at low temperatures the quasiparticle density of states is constant, which leads to a linear in T heat capacity, and the quasiparticle velocity is the Fermi velocity, v_F, and is T independent. Thus, the T dependence of κ_{el} is largely dependent upon that of the quasiparticle mean-free-path. Like the phonon mean-free-path at low T, l_e is given by the sum of the scattering rates from different scattering mechanisms using Matthiessen's rule.

Although at high temperatures the scattering can be dominated by a number of scattering mechanisms, such as electron-phonon scattering, electron-electron scattering or more exotic scattering mechanisms, at low-temperatures l_e is dominated by quasiparticle-defect scattering. The defects we speak of may be vacancies, impurities or interstitial

atoms. Quasiparticle-defect scattering is elastic and independent of the deBroglie wavelength of the electrons, in other words T independent at low temperatures, resulting in $\kappa_{el}(T \rightarrow 0) \propto T$.

The kinetic theory is only conceptually valid when the mean-free-path exceeds the de Broglie wavelength of the electron, $l_e > \lambda_e = 2\pi/k_F$: the Ioffe-Regel limit [97]. In the case of the cuprates, however, the Ioffe-Regel limit is violated at high temperatures and low dopings if one uses the simple averaging of the kinetic theory [44, 98, 76]. Thus, we will have to exercise caution in applying the kinetic theory formalism to the normal state of the cuprates.

In sufficiently underdoped cuprates the charge conductivity is insulating and described by a variable-range-hopping model of transport [75, 74]. The corresponding thermal conductivity in the VRH model has not been calculated, although by any estimation it's magnitude is too small to be distinguished experimentally from a sizeable phonon contribution to κ.

3.3 Thermal conductivity in conventional superconductors

In a superconductor quasiparticles pair up to form Cooper pairs, which condense to form a superfluid. Naturally, this has a dramatic effect on the thermal conductivity. Viewing the problem in a phenomenological two-fluid model (superfluid + normal fluid) gives us a qualitative sense of the effect on the thermal conductivity. Since the superfluid has no entropy it makes no contribution to the thermal conductivity. This leaves the excitations out of the superconducting state, the normal fluid, as the sole electronic heat carriers. In a clean s-wave superconductor the isotropic gap dictates that the quasiparticle density is exponentially reduced below T_c. Thus, at low enough temperatures electrons make no contribution to the thermal conductivity and the thermal conductivity will be given entirely by the phonons. Bardeen, Rickayzen and Tewordt [99] (BRT) worked out a detailed theory of the electronic thermal conductivity, based on BCS theory, in the limit where quasiparticles are scattered primarily by impurities. Their results, shown in fig. 3.3, predict the reduced electronic thermal conductivity (κ_{sc}/κ_n vs. T/T_c) to depend only on the ratio Δ/k_BT_c and not on the scattering rate. These calculations agree remarkably well with measurements on a variety of conventional superconductors. One example of this agreement on Al is shown in fig. 3.4 a). Notably, the BRT theory gives a relatively smooth evolution of κ through T_c. This will not be the case if the quasiparticle scattering

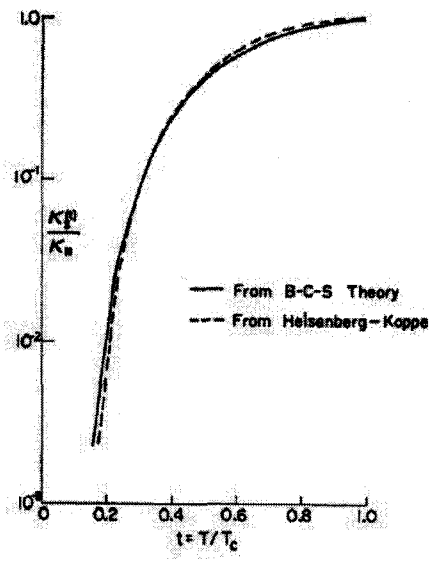

Figure 3.3: The thermal conductivity in the superconducting state as calculated by the theory of Bardeen, Rickayzen and Tewordt [99]. κ_{sc} is plotted normalized to the normal state thermal conductivity κ_n. Figure taken from ref [99].

rate is dominated by inelastic scattering.

In addition to reducing the electronic conductivity, the onset of superconductivity also has an impact on the phonon thermal conductivity. In instances where phonon scattering is dominated by phonon-quasiparticle scattering, the onset of superconductivity will increase the phonon contribution to the thermal conductivity. In some instances this may lead to thermal conductivity in the superconducting state that is greater than that of the normal state. At sufficiently low temperatures, however, the phonon thermal conductivity will be limited by the boundaries of the sample resulting in a peak in the low temperature thermal conductivity, as shown in measurements on Nb by Kes et. al. [100] in fig. 3.4 b). Note in this low T limit, where phonons are scattered from the boundaries of the sample, the total thermal conductivity in the superconducting state should be strictly less than that of the normal state.

3.3.1 Thermal conductivity in the mixed state

The introduction of vortices into a superconductor by the application of magnetic field will have considerable implications on the thermal conductivity. Consider first a single vortex. About the core of the vortex the order parameter $\Delta(r)$ is suppressed over a length scale given by the coherence length ξ. Within the core the density of states is

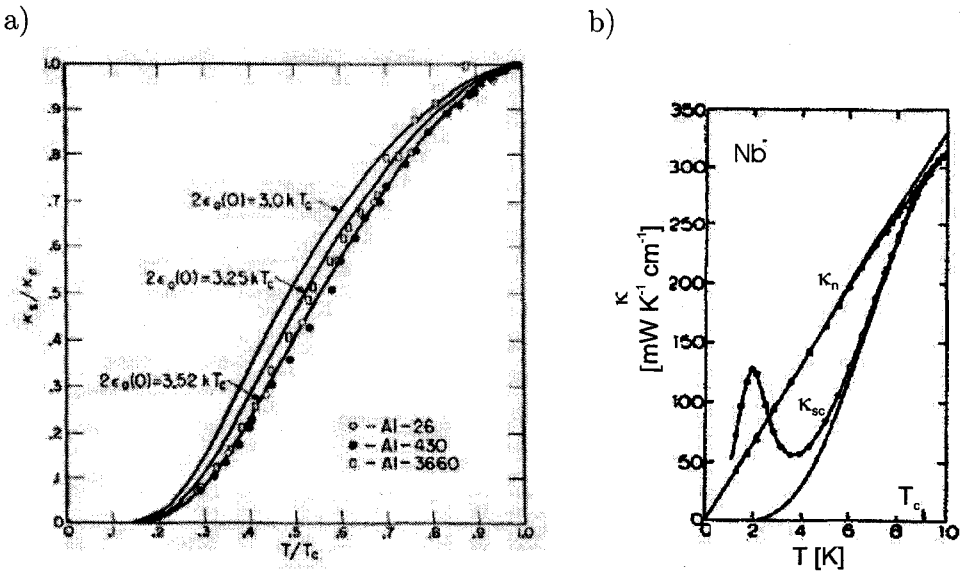

Figure 3.4: a) κ_{sc}/κ_n vs. T/T_c in Al from ref. [101]. The lines are fits to BRT theory [99] using different values of Δ/k_BT_c. The sets of data are for samples with different impurity scattering rate (Al-x, where x is the residual resistivity ratio $R_{273K}/R_{1.2K}$). b) κ vs. T for Nb in both the superconducting and normal states. Figure adapted from ref. [100].

similar to that of the normal state, although the states are localized to the cores (the "bound" states are gapped by a small energy gap) [102]. At low fields these bound states will not contribute to the thermal conductivity. At higher fields, however, the vortex density increases and the core states begin to overlap, allowing transport by tunneling between vortices to occur. As H_{c2} is approached the core states overlap completely and the normal state is recovered.

In addition to the bound states, a vortex will also interact with the delocalized quasiparticles already present via interactions with the magnetic field, the superfluid velocity and the modulation of the order parameter $\Delta(r)$ and in general these interactions will result in quasiparticle vortex scattering [103].

In figure 3.5 we show measurements of κ vs. applied field, H, in Nb from Lowell and Sousa [104] at two temperatures. At 5.54 K the thermal conductivity decreases dramatically at H_{c1}, reaches a minimum and increases to meet up with the normal state value at H_{c2}. At 1.98 K the conductivity also decreases at H_{c1} although with much reduced amplitude. The initial decrease at H_{c1} can be attributed to phonon-vortex scattering or quasiparticle-vortex scattering as soon as vortices enter the sample. The phonon vortex scattering is due to phonons scattering from the normal fluid in the

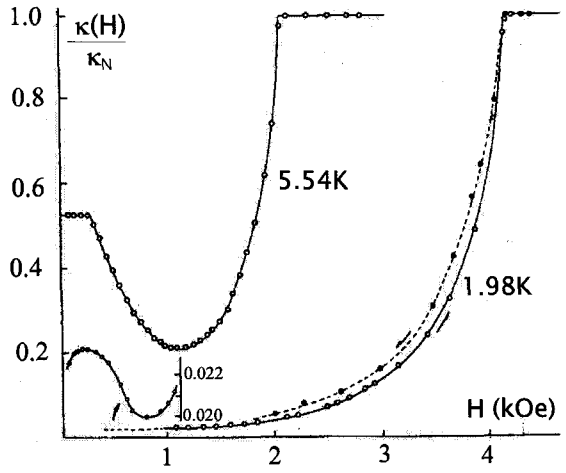

Figure 3.5: Thermal conductivity as a function of field for Nb at 5.54 K and 1.98 K. Figure adapted from ref. [104].

vortex cores. As such it should contribute when phonon scattering in the normal state is dominated by electron-phonon scattering but not in the $T \rightarrow 0$ limit where phonon-boundary scattering sets the phonon mean-free-path. Quasiparticle vortex scattering will be most important to thermal transport at high temperatures where there is still a significant quasiparticle density, but will be relatively unimportant when the density of delocalized quasiparticles is negligible. Finally, at low T and high field, the conductivity will be dominated by the tunneling between core states and will rise monotonically with field towards H_{c2}.

3.4 Thermal conductivity in a d-wave superconductor

3.4.1 d-wave nodal quasiparticles

As discussed in Chapter 2, it is now reasonably well established that, at least at optimal doping, the superconducting state of the cuprates has $d_{x^2-y^2}$ pairing symmetry. The $d_{x^2-y^2}$ order parameter has a gap structure that varies as $\Delta = \Delta_0 \cos(2\phi)$, where the angle ϕ is measured from the Cu-O bonds in the CuO_2 planes (see fig. 3.6). This gap is maximum for $\phi = 0, \pi/2, ...$ (the anti-nodal directions) and zero for $\phi = \pi/4, 3\pi/4, ...$ (the nodal directions). Along the nodes, where Δ vanishes, quasiparticle excitations persist down to $T = 0$ and dominate the low-energy thermodynamic and transport properties of the cuprates. In the following we will focus only on the transport at low-energies ($T < T_c/10$). At these low temperatures inelastic scattering is negligible and the quasiparticle dispersion can safely be linearized about the nodes.

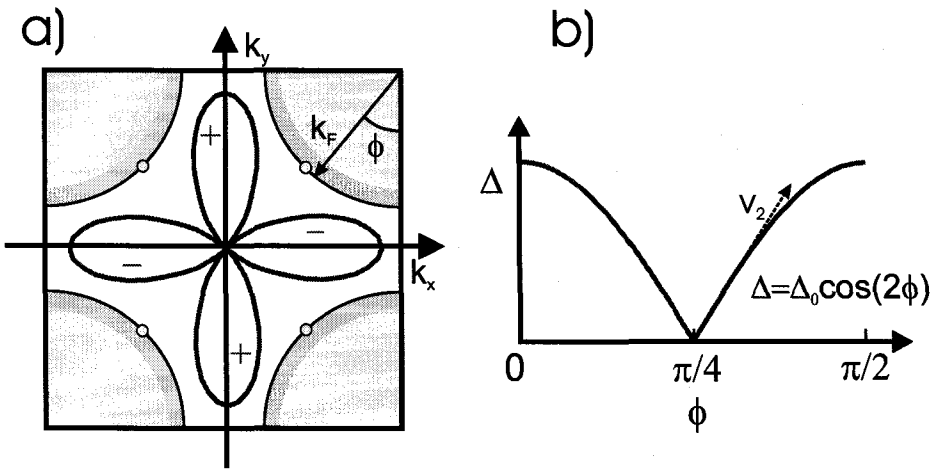

Figure 3.6: a) The cuprate 1st Brillouin zone. The approximately cylindrical hole like Fermi surface is centered about (π, π). The d-wave gap plotted in polar co-ordinates is shown in red. b) The magnitude of the gap, Δ, for the $d_{x^2-y^2}$ gap as a function of the angle relative to the Cu-O bond, ϕ.

The nodal approximation

Following convention, within a single band tight-binding model the Fermi surface (for a tetragonal HTSC) is written as

$$\epsilon_k = -2t(\cos k_x a + \cos k_y a) - \mu, \tag{3.4}$$

where $k_x(k_y)$ is the $\mathbf{k}$ vector along the Cu-O bond, a is the ab plane lattice constant, μ is the chemical potential and t is the in-plane hopping integral. In the same co-ordinate system the $d_{x^2-y^2}$ gap is written as

$$\Delta_k = \frac{\Delta_0}{2}(\cos k_x a - \cos k_y a). \tag{3.5}$$

Using the convenient reparameterization

$$k_1 = \frac{(k_x + k_y)}{\sqrt{2}} - |k_F|, \tag{3.6}$$

$$k_2 = \frac{(k_x - k_y)}{\sqrt{2}} \tag{3.7}$$

with k_1 and k_2 perpendicular and parallel to the Fermi surface respectively, Δ_k and ϵ_k can be linearized about the nodes and written in terms of the quasiparticle velocities perpendicular (the Fermi velocity, v_F) and parallel (v_2) to the Fermi surface:

$$\epsilon_k \simeq k_1 \frac{\delta \epsilon_k}{\delta \mathbf{k}} \equiv \hbar k_1 v_F, \tag{3.8}$$

$$\Delta_k \simeq k_2 \frac{\delta\Delta}{\delta \mathbf{k}} \equiv \hbar k_2 v_2. \tag{3.9}$$

The linearized excitation spectrum close to the nodes is now written as

$$E_k = \sqrt{\epsilon_k^2 + \Delta_k^2} = \hbar\sqrt{(v_F k_1)^2 + (v_2 k_2)^2}. \tag{3.10}$$

The formal equivalence of this dispersion to that of relativistic fermions has led many to refer to the nodal quasiparticles as Dirac quasiparticles. Neglecting impurities the quasiparticle density of states arising from the d-wave dispersion is

$$N_s(E) = \left(\frac{2}{\pi\hbar^2}\right)\left(\frac{1}{v_F v_2}\right) E. \tag{3.11}$$

The linear in E energy dependence results in quasiparticle excitations down to $T = 0$ but not strictly at $T = 0$. Although the "clean" limit density of states can be used to calculate many observed properties of the HTSC, namely a linear in T superfluid density [31] and T^2 electronic specific heat co-efficient, the study of truly low temperature properties of the HTSC's will require the inclusion of impurities.

In the following we will examine 3 ways to populate the low energy states of a d-wave superconductor: by thermally exciting quasiparticles, through the application of magnetic fields and via scattering from impurities. To understand thermal transport, in addition to exciting states, we must also understand the scattering rate and its dependence upon temperature and magnetic field.

3.4.2 *Impurities in a d-wave superconductor*

The addition of impurities in a d-wave superconductor has a significant impact on the low energy transport and thermodynamic properties. Impurities not only impact on the scattering rate, as they do in a normal metal, they also result in a finite zero energy density of states for a superconductor with nodes [105]. Calculations of the zero energy density of states in a d-wave superconductor in the self-consistent T matrix approximation (SCTMA) give [106, 107, 108, 109]

$$N_s(0) = N_n(0)\frac{2\gamma}{\pi\Delta_0}\ln\left(\frac{\Delta_0}{\gamma}\right) \sim N_n(0)\frac{2\gamma}{\pi\Delta_0}, \tag{3.12}$$

where $N_n(0)$ is the normal state density of states and γ is energy scale that depends on the impurity concentration, n_{imp}, and the strength of the scattering potential. γ can be understood as the bandwidth of quasiparticle states bound to impurities (see ref. [109] and references therein) or as the quasiparticle scattering rate [30, 107]. γ also

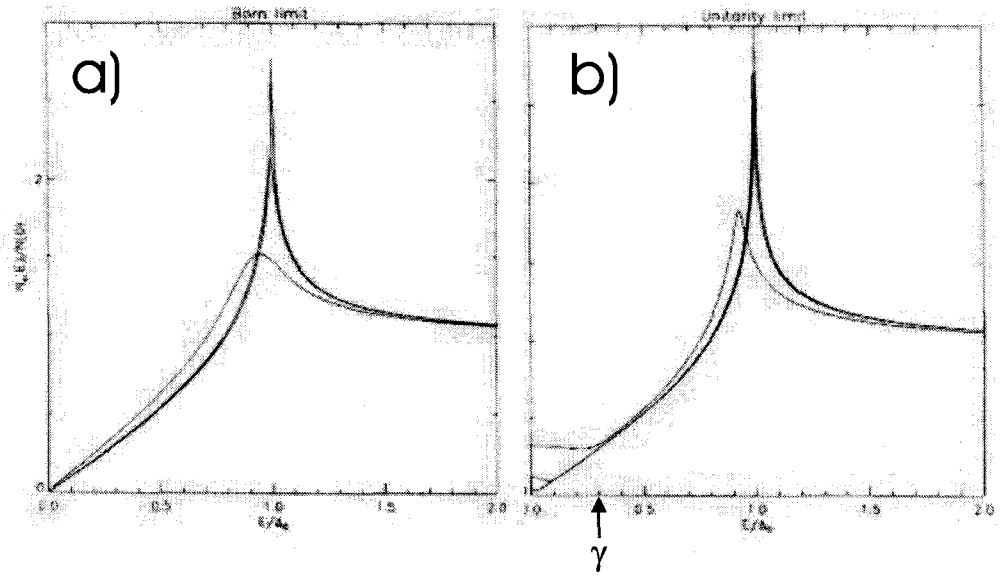

Figure 3.7: The density of states for a d-wave superconductor in the a) Born and b) Unitary scattering limits. Figures taken from Preosti et. al. [106]. $N(E)$ is plotted for three levels of the normal state scattering rate, $\Gamma_N/\Delta \simeq 10^{-3}, 10^{-2}$ and 10^{-1}, with the uppermost curves being for the largest level of disorder.

represents an energy scale over which the density of states crosses over from the "clean" limit (eq. 3.11) to a roughly constant in E density of states with a value given by eq. 3.12 (see fig. 3.7).

γ, and hence $N(E)$, has a significant dependence upon the strength of the scattering potential. For weak scattering (the Born limit) $\gamma \sim \Delta_0 e^{-\Delta_0/\Gamma_N}$ [105], where we have expressed γ in terms of the normal state scattering rate, Γ_N. Note the exponential dependence on Δ_0/Γ_N will give very small values of γ for physically reasonable values of Γ_N. For strong scattering (the unitary limit) $\gamma \simeq 0.63\sqrt{\Gamma_N \Delta_0}$ [108]. Notably the scattering rate here will typically be greater than the normal state scattering rate. For equivalent values of Γ_N, γ will be orders of magnitude smaller in the Born limit than the Unitary limit [106]. This difference echoes the different dependence on density of states between Born and unitary scattering in the metals: $\Gamma_N \propto N(E)$ and $\Gamma_N \propto 1/N(E)$ for Born and unitary scattering respectively. Fig. 3.7 compares the DOS for the same value of Γ_N in both the Born (a) and unitary (b) limits.

Experimentally the cuprates have been suggested to lie in the unitary scattering limit. Amongst other arguments (see the review by Hussey and references therein for additional arguments [30]) unitary scattering is argued by the crossover in penetration depth from $\propto T$ ("clean", $T > \gamma$) to T^2 ("dirty", $T < \gamma$) with the addition of Zn impurities [31, 108].

Also, in the Born approximation, for γ to be on the order of several K would require a very large normal state scattering rate, which would suppress superconductivity due to Abrikosov-Gorkov pair breaking. In contrast reasonable values of Γ are found in the unitary limit[108].

3.4.3 Universal transport

In 1993 Lee calculated the conductivity at low temperatures ($k_BT < \gamma$) and surprisingly found σ_0 to be independent of disorder (universal) [107] and given by:[1]

$$\sigma_0 = \frac{e^2}{2\pi\hbar}\left(\frac{n}{d}\right)\left(\frac{v_F}{v_2}\right). \tag{3.13}$$

Considering the conductivity in the kinetic theory of metals ($\sigma \propto N(0)v_F^2\tau$), Lee's universal conductivity can be understood as an exact cancelation of the increase in $N(0) \propto \gamma$ (from eq. 3.12) induced by disorder and the decrease in the scattering time, $\tau \propto 1/\gamma$, by the same disorder.

In addition to the disorder independence (the universality), σ is only dependent upon the quasiparticle dispersion at the nodal positions in k-space. Thus, although the quasiparticle dispersion away from the nodes exhibits a variety of complexities, σ_0 will be largely unaffected by these complications. Finally, σ is parameterized by v_F and $v_2 \propto \Delta_0$, two important parameters describing the superconducting state. As will be discussed in ch. 6, transport measurements in the universal limit may be used as a determination of these parameters.

Of particular importance to the work presented in this thesis, Graf et. al. [111] showed the universal result of Lee to also applies to thermal transport. As latter calculated by Durst and Lee [109], the thermal conductivity in the universal limit is given by

$$\frac{\kappa_0}{T} = \frac{k_B^2}{3\hbar}\left(\frac{n}{d}\right)\left(\frac{v_F}{v_2} + \frac{v_2}{v_F}\right). \tag{3.14}$$

The universal thermal conductivity includes an additional term $\propto v_2/v_F$ not present in the calculation of charge conductivity (eq. 3.13)[2]. This additional term arises from the fact that κ is proportional to the group velocity $v_G = \delta E_k/\delta k$, as opposed to charge transport which is proportional to $v_F = \delta\epsilon_k/\delta k$. While v_F is essentially constant over the area of the node v_G is not, leading to the additional term $\propto v_2/v_F$ [109]. In practice,

[1] Fradkin [110] had arrived at similar universal conductivity for the case of gapless semiconductors.
[2] This additional term was missed in the original calculation of Graf et. al. [111].

except for very underdoped samples, $v_F/v_2 \gg 1$ ($v_F/v_2 = 14$ in optimally doped YBCO [15], for instance), and the second term in eq. 3.14 can be neglected.

In the original treatment of the universal conductivity of Lee, vertex and Fermi liquid corrections to the conductivity were neglected. Durst and Lee [109] latter included these corrections in their calculations leading to a modification to the result of eq. 3.13:

$$\sigma_0 = \frac{e^2}{2\pi\hbar}\left(\frac{n}{d}\right)\left(\frac{\beta_{vc}\alpha_{fl}^2 v_F}{v_2}\right). \tag{3.15}$$

The vertex correction β_{vc} arises due to the fact that back-scattering degrades the charge current more than forward scattering, resulting in a difference between intranode (predominantly forward scattering) and internode scattering. The Fermi liquid correction accounts for the Fermi-liquid interactions between quasiparticles which induce additional drag on the current. Quite notably, unlike charge transport the thermal conductivity is renormalized by neither Fermi liquid or vertex corrections [109] (eq. 3.14 is correct). As such thermal conductivity is the only truly universal transport co-efficient. In thermal conductivity the absence of the Fermi liquid correction is related to particle-hole symmetry across the Fermi surface. The vertex correction is absent in κ essentially because v_G can vary within the area of a node. As such, unlike the charge current, the thermal current can relax equally well via either internode or intranode scattering.

Graf et. al. also calculated the leading order temperature correction to the universal limit [111]:

$$\frac{\kappa(T)}{T} = \frac{\kappa_0}{T}\left(1 + \frac{7\pi^2}{15}\frac{a^2 k_B^2 T^2}{\gamma^2}\right), \tag{3.16}$$

where the co-efficient a is strongly dependent on the scattering strength ($a = 1/2$ in the unitary limit, $a \gg 1$ in the Born limit). The key point is the finite temperature correction depends strongly on γ and the details of the disorder model.

Summary of nodal quasiparticles in 0T

- With decreasing temperature a crossover occurs between a high energy "clean" limit regime ($N(E) \propto E$) to low-energy impurity dominated regime ($N(E) \propto \gamma$)
- The quasiparticle scattering rate γ depends significantly on the model of disorder (Born vs. unitary). γ also sets crossover temperature separated "clean" and "dirty" behavior.
- Thermal conductivity is universal for $T \ll \gamma$. κ_0/T is dependent only upon the velocity anisotropy ratio, v_F/v_2.

- The leading order temperature correction to κ_0 goes as T^3 and is strongly dependent upon details of the scattering.

3.4.4 Nodal quasiparticles in a magnetic field

In section 3.3 the effect of a magnetic field on thermal conductivity was discussed for a conventional superconductor. In this case the effects of field were two-fold: a decrease in κ_{ph} due to scattering from normal fluid in the vortex cores and an increase in κ_{el} as quasiparticles tunnel between cores. In a d-wave superconductor, although effects in an s-wave superconductor may still occur, the presence of nodal quasiparticles results in additional phenomena that dominates the thermodynamic and transport properties (at least at low fields and low temperatures). Nodal quasiparticles will respond to the vortices in two fashions. First, the average energy of the quasiparticles will be increased due to the Doppler shift by the superfluid encircling the vortices (the Volovik effect [112]). This energy shift results in an increase in the quasiparticle density of states and may also have an impact on the quasiparticle scattering rate, either by changing the impurity induced quasiparticle scattering rate (which in general is also E dependent) or by allowing higher energy inelastic scattering. Second, the quasiparticle scattering rate may also increase due to quasiparticle vortex scattering, the quasiparticles being Andreev scattered by the superfluid encircling the vortices. A third, purely quantum mechanical effect involves the phase winding of a quasiparticle encircling a vortex (the Berry phase).

The Volovik effect

Volovik showed that for a d-wave superconductor the quasiparticles will experience an energy shift, E_H, due to the flow of superfluid about a vortex. This is essentially the classical Doppler shift applied to nodal quasiparticles. The Doppler shift to the quasiparticle spectrum has the form $E(\mathbf{k},\mathbf{r}) = E(\mathbf{k}) - e\mathbf{v_s}(\mathbf{r}) \bullet \mathbf{k}$, where $\mathbf{v_s}$ is the superfluid velocity. $\mathbf{v_s}(\mathbf{r})$ meanwhile simply falls off as one over the distance from the vortex core: $\mathbf{v_s}(\mathbf{r}) = \hbar\hat{\phi}/(2mr)$. Integrating over a vortex lattice unit cell gives an average Doppler shift energy $E_H = a\Delta_0\sqrt{H/H_{c2}}$, where a is a constant of order unity that depends on the geometry of the vortex lattice (a=0.5 (0.465) for square (triangular) vortex lattices [30]). Recalling the linear in E dependence of $N(E)$ in the "clean" limit (eq. 3.11), the Volovik effect naturally leads to $N(0,H) \propto \sqrt{H}$. More precisely,

$$\frac{N(0,H)}{N_n} \simeq \sqrt{\frac{8}{\pi a}}\sqrt{\frac{H}{H_{c2}}}, \tag{3.17}$$

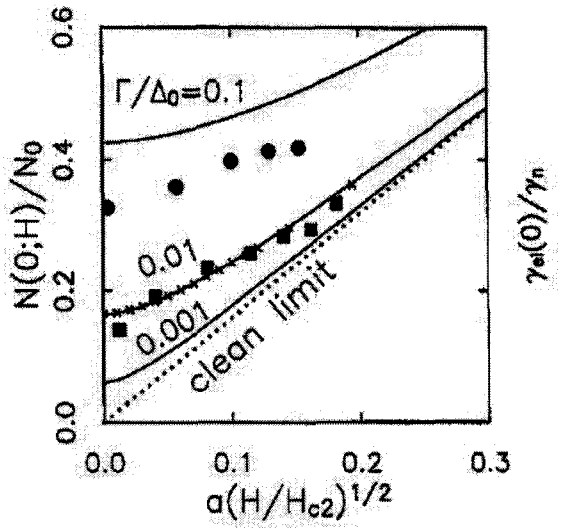

Figure 3.8: The normalized density of states for $\Gamma/\Delta_0 = 0.1$, 0.01 and 0.001 vs. $\sqrt{H}$ from Kübert and Hirschfeld [113]. Calculations in the unitary limit.

for $H_{c1} < H \ll H_{c2}$. The $\sqrt{H}$ increase in $N(H)$ leads to a specific heat co-efficient that also varies as $\sqrt{H}$ [112].

Kübert and Hirschfeld [113] extended Volovik's treatment in the clean limit to explore the dirty limit ($E_H < \gamma$). As already discussed, in the dirty limit $N(E)$ at low energy is dominated by impurity scattering. Instead of the clean limit DOS, $N(E) \propto E$, the leading order energy dependence in the dirty limit is $N(E) \sim N(0) + bE^2$, where $N(0)$ is the zero energy DOS from eq. 3.12 [113]. The Volovik affect on the zero energy DOS in the dirty limit is:

$$\frac{\delta N(0,H)}{N_0} \simeq \frac{\Delta_0}{8\gamma} a^2 \left(\frac{H}{H_{c2}}\right) \log\left[\frac{\pi}{2a^2}\left(\frac{H_{c2}}{H}\right)\right]. \tag{3.18}$$

Thermal conductivity in magnetic field

Kübert and Hirschfeld [114] calculated the electronic thermal conductivity due to the Volovik effect in both the clean and dirty limits[3]. Their calculation neglects the influence of the vortex cores and quasiparticle-vortex scattering, but includes an energy dependence to the quasiparticle scattering rate. At $T = 0$, $\mathbf{J_Q} \perp \mathbf{H}$ and for $H \ll H_{c2}$ they find:

$$\frac{\kappa(H)}{\kappa_0} = \frac{\rho^2}{\rho\sqrt{1+\rho^2} - \sinh^{-1}\rho}, \tag{3.19}$$

[3]Here "clean" and "dirty" refers to E_H, as opposed to k_BT, with respect to γ.

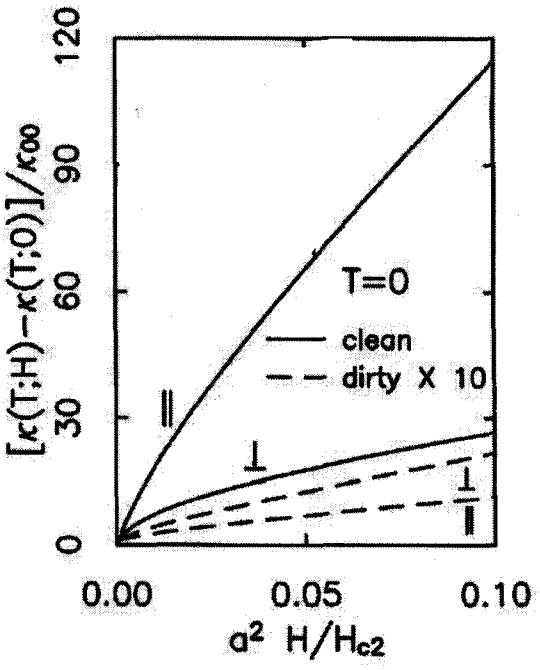

Figure 3.9: The magnetic field dependence of thermal conductivity from Kübert and Hirschfeld [114]. Solid lines: $\Gamma/\Delta_0 = 0.0005$; dashed lines $10 \times \delta\kappa/\kappa_0$ for $\Gamma/\Delta_0 = 0.1$. Calculations in the unitary limit. $\parallel$ and $\perp$ are for $\mathbf{J_Q} \parallel \mathbf{H}$ and $\mathbf{J_Q} \perp \mathbf{H}$ respectively.

where κ_0 is the universal value in zero field (eq. 3.14) and

$$\rho = \sqrt{\frac{8\Gamma H_{c2}}{\pi^2 a^2 \Delta_0 H}} \text{for } \gamma \ll E_H(\text{"clean"}) \tag{3.20}$$

$$\rho = \sqrt{\frac{6\gamma^2 H_{c2}}{\pi a^2 \Delta_0^2 H}} \text{for } \gamma > E_H.(\text{"dirty"}) \tag{3.21}$$

Here Γ is the scattering rate in the unitary limit ($\Gamma = n_i/\pi N_n$).

There are a few comments to make about these results. First, the zero temperature limit has the same functional form in both the dirty and clean limits. Secondly, *the application of field always increases the thermal conductivity*; the increase in the density of states has a greater effect than the decrease in the quasiparticle scattering rate. And thirdly, unlike the zero field case the field dependence of κ is not universal.

Quasiparticle-vortex scattering

The influence of quasiparticle vortex scattering has been included in a number of thermal conductivity calculations of d-wave superconductors [115, 116, 117, 118, 119]. In these calculations the quasiparticle-vortex scattering arises due to Andreev scattering of quasi-

particles from the superfluid flow encircling the vortices, as calculated for an s-wave type II superconductor [103]. For a disordered vortex lattice the effect is to produce an effective QP-vortex mean-free-path ($l_{vor-QP} \propto \sqrt{H_{c2}/H}$ [116]) that will add with QP-impurity scattering via Matthiessen's rule: $l_{QP}^{-1} = l_{imp-QP}^{-1} + l_{vor-QP}^{-1}$. For $l_{vor-QP} > l_{imp-QP}$ the thermal QP-vortex scattering will reduce κ. The overall H dependence of κ will depend on the relative contributions of QP-vortex scattering reducing l_{QP} and the increase QP DOS due to the Volovik effect.

At intermediate T QP-vortex scattering has been used to explain decreases in $\kappa(H)$ observed in several materials [10, 120]. At low energies, however, the QP-vortex scattering cross-section vanishes for low quasiparticle energies [116, 117, 119]. Thus, at low T quasiparticle-vortex scattering may be negligible. This is brought out by $T = 0$ calculations of $\kappa(H)$ including QP-vortex scattering by Vekhter and Houghton [117], which are qualitatively consistent with calculations that neglects QP-vortex scattering by Kübert and Hirschfeld [114]. In contrast, however, other calculations by Kim et. al. show the effect of QP-vortex scattering even at $T = 0$ in clean samples, although their calculation includes no energy dependence to the QP-vortex scattering cross section [118]. Evidently, accurately calculating the quasiparticle vortex scattering is a theoretically challenging problem, due to the extended nature of the vortices. In addition, quantum-mechanical effects associated with the Berry phase factor picked up as a quasiparticle winds about a vortex [121], may also be relevant for quasiparticle-vortex scattering. This advanced topic, however, is beyond the scope of this thesis.

Vortex core contributions

In all of the calculations outlined above the assumption has been that vortex cores have a negligible contribution to scattering and transport. As argued by Franz [116] scattering by vortex cores is proportional to $(\xi/a_v)^2$, where $a_v = \xi\sqrt{H_{c2}/H}$ is the average intervortex spacing and $\xi = v_F/\pi\Delta_0$ is the coherence length [116]. Deep in the superconducting state ($H \ll H_{c2}$), $(\xi/a_v)^2 = H/H_{c2}$ is small and QP-vortex core scattering can be neglected. Similarly tunneling between cores, providing a new channel for electronic transport in the superconducting state, will be negligible for $H/H_{c2} \ll 1$. While no detailed calculations have been performed, in the opposite limit $H \sim H_{c2}$ thermal conductivity due to core states in a d-wave superconductor should be similar to conventional s-wave superconductors. As cores overlap the conductivity should increase as quasiparticles tunnel between cores. This will have an impact when the (density of states per

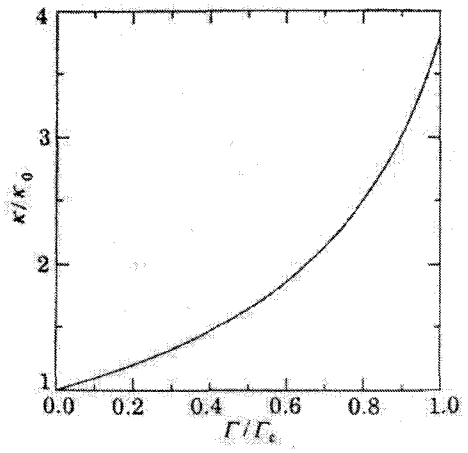

Figure 3.10: The calculated thermal conductivity, $\kappa(\Gamma)$ of a "dirty" d-wave superconductor as a function of the normal state scattering rate, Γ, plotted as $\kappa(\Gamma)/\kappa(0)$ vs. Γ/Γ_c from Sun and Maki [124]. Γ_c is the critical value of Γ ($=0.88k_BT_c$ using a weak-coupling BCS theory) at which superconductivity is suppressed.

core)×(number of cores) is comparable to the nodal QP density of states. For $H = H_{c2}$ the normal state QP density of states and conductivity are recovered as the cores completely overlap. These states may in fact be more relevant in d-wave superconductors due to the extended nature of nodal quasiparticles.

3.4.5 *Strong disorder: Beyond the "universal" limit*

In all of the previous discussion the distinction between "clean" and "dirty" has been made in reference to the energy scales set by temperature or magnetic field relative to γ, the energy scale set by disorder. Implicit in all of the calculations however, has been the assumption that we have been working in the more conventional notion of "clean", namely $\gamma \ll \Delta_0$. For $\gamma \sim \Delta_0$, as in conventional superconductors with magnetic impurities, Abrikosov-Gor'kov pair breaking [122] will modify many of the above results. In particular, for strong disorder the universal limit is no longer universal but dependent upon the scattering rate [123].

Sun and Maki calculated the thermal conductivity as a function of Γ and found an increase in $\kappa(\Gamma)/\kappa(0)$ with increasing Γ (see fig. 3.10). In other words, the creation of quasiparticles by depairing is more significant than the increase in the quasiparticle scattering rate [124]. Sun and Maki treat the effect of Abrikosov-Gor'kov pair-breaking in a mean-field fashion as a renormalization of the spatially averaged gap $\Delta_0(\Gamma)$. In detail, however, an impurity produces Abrikosov-Gor'kov pairbreaking as a local suppression of

the order parameter at the impurity: a "swiss cheese" of non-superconducting regions created by impurities, amongst a superconducting background. As such, mean-field calculations which do not treat the local order parameter may be inadequate for strong disorder.

Recently the literature has attempted to move beyond the mean-field to deal with the effects of order parameter suppression using the Bogoliubov-deGennes equations [125]. Detailed calculations of the low energy density of states are somewhat controversial, however, with various treatments predicting contradictory results, both divergences and low energy gaps in the DOS at E=0. Calculation of transport co-efficients in a B-dG picture have yielded greater than T linear temperature dependencies that have yet to be definitively observed in experiments [126].

4

Experimental Setup

In this chapter I briefly review the instrumentation used in our thermal conductivity and resistivity measurements[1] I will introduce the steady state technique which we employ to measure thermal conductivity and discuss our specific implementation of the technique.

4.1 Cryogenic measurements

The thermal conductivity and resistivity measurements presented in this thesis were performed using a four different cryostats (a ^{4}He cryostat, a ^{3}He cryostat and two dilution refrigerators) and three superconducting magnets. The operating principles behind each of these cryostats, which I will not review here, are discussed in references [128, 129].

^{4}He cryostat

For measurements between room temperature and 1.5 K we used a pumped He^4 cryostat. This cryostat was outfitted for both thermal conductivity, described below, and resistivity measurements with all measurements performed in vacuum within a sealed can. In addition, this cryostat is sufficiently versatile to be run in either in zero field in a ^{4}He transport dewar or in field in either the Oxford 13/15T superconducting Kelvinox magnet or the 16/18T superconducting Heliox magnet discussed below.

^{3}He cryostat and 16/18T superconducting magnet

Resistivity measurements between room temperature and 300 mK could be performed using an Oxford instruments Heliox ^{3}He cryostat. This cryostat is designed to fit into a 16T/18T superconducting magnet system. At 4.2 K the magnet can be run to a magnetic field up to 16T. By pumping on liquid ^{4}He surrounding the magnet (using the lambda plate) to cool the magnet to below ~1.5 K, the magnet may be run up to a field of 18T.

[1] A more extensive review of the same technique and instrumentation may be found in the thesis of Etienne Boaknin [127].

Dilution refrigerator and 13/15T magnet

All of the sub-Kelvin thermal conductivity measurements were performed in a Oxford instruments Kelvinox 400 dilution refrigerator. The base temperature of this dilution refrigerator is $\sim$ 20 mK. In practice, however, measurements were only performed above 40 mK for a variety of technical reasons, some of which will be discussed below. This dilution refrigerator is designed to insert into a 13T/15T magnet (15T is achieved by pumping on the lambda plate as discussed above for the Heliox ^{3}He system). A crucial feature of this magnet system is the addition of a field-compensated region where the coils of the magnet are wound counter to the main magnet coils, creating a region of zero magnetic field. This field compensated region is located to coincide with the mixing chamber of the dilution refrigerator and the experiments reside on a tail that extends from the mixing chamber into the bore of the magnet. In this fashion we are able to place thermometry within the field compensated region, providing a measure of temperature that is unaffected by thermometer magneto resistance.

Dilution refrigerator and 16/18T magnet

Additional resistivity measurements were performed up to 16T and down to 20 mK in an Oxford instruments Kelvinox 400 dilution refrigerator. This dilution refrigerator was designed to insert into a 16T/18T superconducting magnet, also with a field compensated region.

4.2 Steady State Thermal conductivity measurements

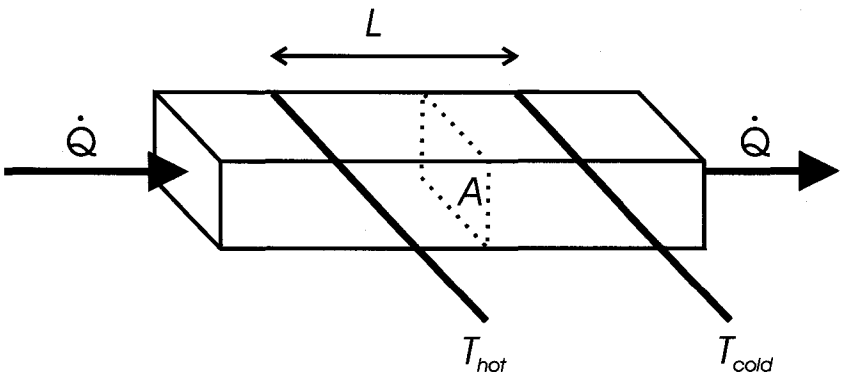

Figure 4.1: The principle of the steady-state thermal conductivity measurement. A heat current, $\dot{Q}$, is applied along the sample and the temperature is measured at two points T_{hot} and T_{cold} along the length of the sample.

To measure the thermal conductivity we employ a longitudinal steady state method, depicted schematically in figure 4.1. With sample of cross-sectional area, A, we apply a known heat current, $\dot{Q}$ to one end of the sample and measured the temperature difference, $\Delta T = T_{hot} - T_{cold}$, created between two points that are a known distance L apart[2]. The thermal conductivity using this technique is given by the expression

$$\kappa = \frac{L}{A}\frac{\dot{Q}}{\Delta T} = \frac{L}{A}\frac{\dot{Q}}{(T_{hot} - T_{cold})}. \tag{4.1}$$

The measured value κ will correspond to the thermal conductivity at temperature that is the average of T_{hot} and T_{cold}[3].

In an actual experiment the heat current is achieved by attaching a resistor to the sample on one end of the sample and anchoring the other end to a cold point that acts as a thermal ground. By applying a current to this resistor, a heat current may be generated by Joule heating and is given simply by $\dot{Q} = I^2_{heater}R_{heater}$. Measurement of the temperatures T_{hot} and T_{cold} is achieved by attaching resistance thermometers to the sample at two points along it's length. Finally, if the sample geometry is known, κ may be deduced.

In practice, this technique is only effective if one can guarantee that all (or at least all but an insignificant fraction) of the heat generated by the heater travels through sample to the thermal ground. Heat may be lost through convection, radiation or conduction of the electrical leads and supports that are attached to the sample heater and thermometer. At dilution refrigerator temperatures radiative heat losses, which vary as T^4, and convective heat losses through any residual gas in the sample chamber is negligible (At higher temperatures (for instance above 100 K), however, they may be significant.). At low temperatures, conductive heat losses are the primary concern, and are avoided by carefully designing the thermal conductivity mount using appropriate materials. A thorough review of heat losses in our experimental setup, at both high and low temperatures, is given in the thesis of Etienne Boaknin [127].

[2]Note the similarity between the steady state thermal conductivity measurement and a 4-wire resistivity measurement.

[3]This correspondence is accurate even for relatively large values of ΔT. For instance even for $\Delta T/T_{avg}$ = 10%, the difference in the measured value of κ and the actual value of κ at T_{avg} is $\sim$ 0.25% for κ vary as T^3 [84]. In our measurements κ always varies at a rate slower than T^3 and $\Delta T/T_{avg} < 10\%$, giving $\Delta\kappa/\kappa < 0.25\%$.

4.3 The low temperature thermal conductivity mount

A schematic of thermal conductivity mount used in our experiments is given in fig. 4.2. In our experiment this mount is located on a Cu tail that extends into the bore of the magnet. The tail holds three such mounts allowing three separate samples to be measured simultaneously. A single mount consists of a strain gauge resistor that we use as the sample heater and two thick film RuO_2 resistance thermometers to measure T_{hot} and T_{cold}. These components are described below.

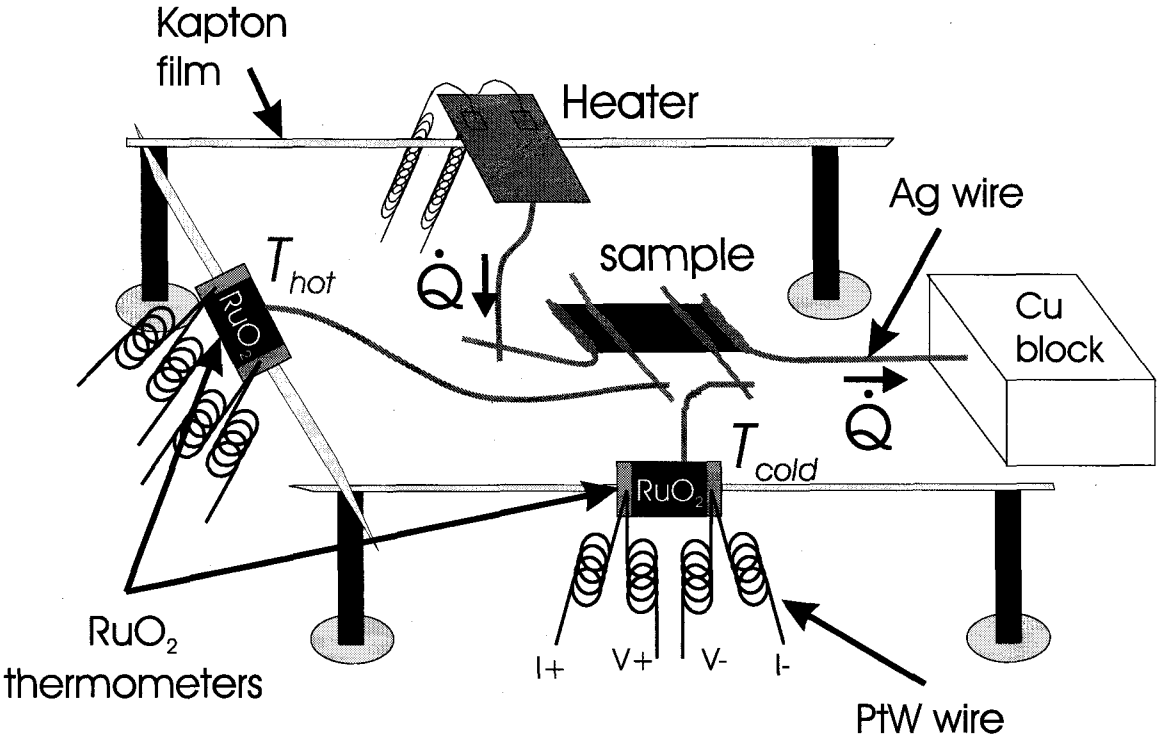

Figure 4.2: A schematic of a mount for low temperature thermal conductivity measurements. The RuO_2 thermometers and the strain gauge heater are suspended on long thin Kapton lines to provide rigid support, yet minimize thermal contact to the ground. Electrical contact to the thermometers and wires is made with long thin coils of PtW wire.

Thermometers

The thermometers are commercial ruthenium oxide (RuO_2) thick films[4] with room temperature resistance of $\sim$1 kΩ ($\sim$ 7 kΩ at 40 mK). They are suspended on 7.5 μm thick Kapton® film[5] that is cut into $\sim$100 μm wide strips that extend $\sim$1 cm from either side

[4]From Dale.
[5]HN gauge 30 polyimide film from Dupont.

of the thermometer to support posts made of Vespel[6]. The Vespel posts are glued to the copper base with low temperature epoxy. The RuO_2 resistors come evaporated on a AlO_2 substrate that we have thinned down by polishing to reduce the heat capacity of the thermometers.

Electrical contact to the thermometers is made through 25 μm diameter PtW wire[7]. Each coil has a room temperature resistance (this does not change much with temperature) of 100-150 Ω, which determines it's thermal conductance.

During the measurements the RuO_2 thermometers are calibrated, with the heat off ($\dot{Q} = 0$), against a principal thermometer (a Ge resistance thermometer[8] or calibrated RuO_2 thermometer) mounted on the mixing chamber of the dilution refrigerator in the field-compensated region of the magnet. This thermometer is used for temperature control, and most importantly, to provide a field-independent measure of the temperature with which we are able to calibrate the sample thermometers against. After calibration with $\dot{Q} = 0$, the heat is applied and the thermometers are remeasured to determine the thermal conductivity.

Heater

The heater was made of two strain gauges[9] wired in series. Each strain gauge has a resistance of 5 kΩ that is independent of temperature from room temperature down to the base temperature of the dilution refrigerator. This characteristic allows us to measure only the current applied through the heater (rather than current and voltage) and still deduce the Joule heating produced by the heater. Like the RuO_2 thermometers, the heater is suspended on Kapton lines and connected electrically by PtW wires.

Electronics

Resistivity measurements to determine the thermometer resistance were performed using either a linear research LR700 AC resistance bridge or two Stanford Research systems SR830 lock-in amplifiers operated at typical frequencies between 8 and 20 Hz. These same instruments were also used for all of the resistivity measurements presented in this thesis.

[6]Vespel SP1 from Dupont.
[7]The wire has 92% Pt and 8% W and is from Sigmund Cohn Corporation (model 479 Pt).
[8]Germanium resistor model GR-200A-30 from Lakeshore which was calibrated by Oxford instruments down to 50 mK.
[9]SR-4 strain gauges from BLH Electronic Inc. (Type FSM-A6306S-500-S13C).

For temperature control of the principal thermometer, located on the mixing chamber, two setups were used. Prior to June 2002, the LR700 resistance bridge was used to measure the thermometer resistance and temperature control was performed from this measurement using an AVS TS530 temperature controller. After June 2002, the LR700 was used to measure the sample thermometers and temperature control was performed using a Lakeshore 370 AC resistance bridge and temperature controller. Keithley 224 (220) high precision current sources provide the current excitation to the sample heaters in increments of 5 nA (0.5pA). Finally, in an effort to screen out RF noise, all of the wires leading to and from the cryostat were filtered using low-pass pi filters located at the top of the cryostat and the measurements are performed in an RF shielded Faraday cage.

4.4 Tests of accuracy: Wiedemann-Franz law

Our experimental setup is now well tested and has proven itself to be very accurate and reproducible. A fine example of this is the observation of agreement between thermal conductivity measurements from this experimental setup and the expected value based on independent measurements of charge transport via the Wiedemann-Franz law, $\kappa_{el}/T = L_0/\rho$. We now observe agreement of the Wiedemann Franz law at $T = 0$ in a number of systems, including Tl2201 [7], $LuNi_2B_2C$ [130], $NbSe_2$ [131], $Sr_3Ru_2O_7$ and $CeCoIn_5$. In fig. 4.3, the Wiedemann-Franz law agreement from measurements in the normal state (4.5T) of $NbSe_2$, a quasi-2D superconductor, is shown as agreement between the symbols (thermal conductivity) and the solid line (residual resistivity).

4.5 Thermal conductivity mount for $T > 1.5$ K

In addition to the thermal conductivity measurements at low temperatures, we performed thermal conductivity between 1.5 K and ~150 K in the ^{4}He cryostat using a thermal conductivity mount similar to the mount used for measurements in the dilution refrigerator [10]. For these higher temperature measurements Lakeshore Cernox thermometers were used both as the sample thermometers (CX-1030) and as the principle thermometer (CX-1050) used for temperature control and sample thermometer calibration. In addition, for these measurements the sample thermometers and strain gauge heater were suspended from a fiberglass frame by 12 μm PtW wire that served the dual purpose of

[10] Details of this mount can be found in ref [127]

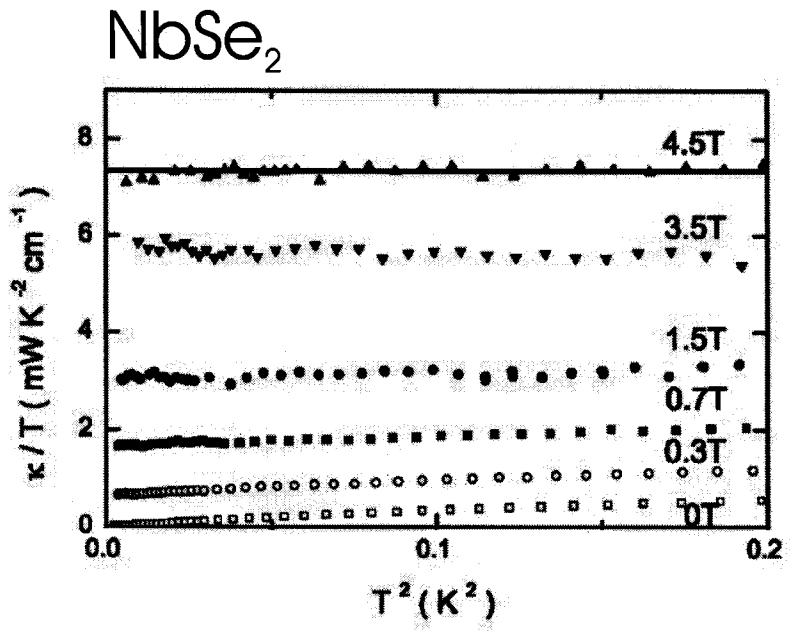

Figure 4.3: Thermal conductivity in $NbSe_2$ as a function of temperature in various magnetic fields from ref. [131], plotted as κ_0/T vs. T^2. This sample is superconducting below $H_{c2} = 4.5$ T. In the normal state (4.5 T), κ_0/T agrees well with the expectation for the thermal conductivity based on the measured resistivity and the Wiedemann-Franz law L_0/ρ, shown as the solid line. Agreement with the Wiedemann-Franz law gives us confidence in the accuracy of our measurements.

providing electrical contact to the sample and providing structural support (rather than the Kapton film and Vespel posts used at low temperatures).

For this measurement temperature control on the principal thermometer was done using a Lakeshore DRC93 temperature controller. The sample thermometer resistance was measured using two Stanford research SR830 (or SR850) lockin amplifiers. The current was applied using a home-made, optically de coupled voltage source. The voltage across the heater was subsequently measured using a Keithley DMM-2000 digital multimeter.

5

THE MATERIALS

In this chapter I cover the some of the basic material properties of $La_{2-x}Sr_xCuO_4$ and $Tl_2Ba_2CuO_{6+\delta}$ such as their crystal structure, growth and doping. In addition, I describe the preparation for transport measurements and characterization of the samples presented in chapters 6, 7, 8 and 9.

5.1 $La_{2-x}Sr_xCuO_4$

5.1.1 *LSCO crystal structure*

By cuprate standards, $La_{2-x}Sr_xCuO_4$ has a relatively simple crystal structure, shown in figure 5.1. The basic structural unit are conductive CuO_2 layers, that along with the apical oxygen atoms form CuO_4 tetrahedra common to many of the hole doped cuprates. Between the CuO_2 planes is a layer of (La,Sr) atoms that forms an insulating charge reservoir.

LSCO has two structural phases, a low-T orthorhombic phase and a high temperature tetragonal phase. The tetragonal-orthorhombic structural phase transition is a soft-phonon driven phase transition that has no apparent relation to the superconductivity [28, 132]. With Sr doping the transition temperature decreases and beyond $x \simeq 0.22$ the tetragonal phase persists to $T = 0$.

In the orthorhombic phase, the CuO_6 octahedra, depicted in fig. 5.1, are alternately tilted out of the plane by $\sim 4°$ along the (110) direction of the tetragonal unit cell, creating a slight zig-zag of the Cu-O bonds [28]. The lattice constants in the tetragonal phase are $a = 3.812$ Å and $c = 13.15$ Å. In the orthorhombic phase the unit cell has unit cell vectors that are shifted 45° from the tetragonal unit cell ($a = 5.35$ Å, $b = 5.40$ Å). Note that there are two CuO_2 planes per unit cell, giving a separation between CuO_2 of $c/2 = 6.57$ Å.

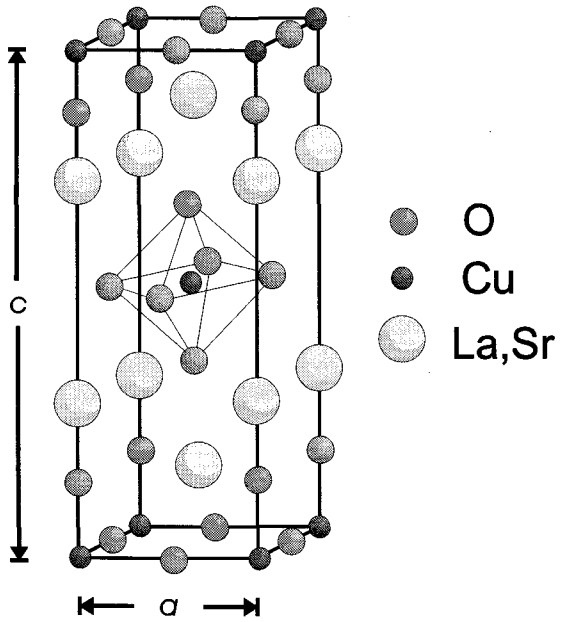

Figure 5.1: The tetragonal representation of the crystal structure of $La_{2-x}Sr_xCuO_4$. The layered perovskite structure consists of CuO_2 planes with (La,Sr)O planes above and below.

Doping

In the parent compound, La_2CuO_4, the valence state of Cu is $3d^9$, one hole per Cu atom. Additional holes may be doped into the CuO_2 planes by either intercalation of additional O^{2-} between the planes, $La_2CuO_{4+\delta}$, or by cation substitution of Ba^{2+} or Sr^{2+} for La^{3+}. In our study the samples were doped using latter method of cation substitution of Sr for La. Sr substitution produces one additional hole in the CuO_2 plane per Sr atom, x, and this simple relation may be used as a convenient measure of the hole concentration in the CuO_2 planes. The phase diagram of LSCO is essentially that of the generic HTSC phase diagram discussed in chapter 2. At $x = 0$ LSCO is a antiferromagnetic Mott insulator with Neel temperature, $T_N = 350$ K. With Sr doping T_N is rapidly suppressed and driven to zero by $x = 0.02$. The onset of superconductivity occurs at $x \simeq 0.055$ and reaches optimal T_c of ~ 39 K at $x = 0.16$. With further doping T_c decreases, becoming non-superconducting at $x \simeq 0.29$ [133].

5.1.2 LSCO crystal growth

All samples studied were grown using the travelling solvent floating zone technique in an image furnace. This technique has become the preferred method of producing large high quality single crystals of LSCO [134, 135, 136, 137, 138, 139]. Samples are grown as large

boules with unknown crystallographic orientation. The samples need to be oriented, cut and polished in order to produce samples suitable for *ab*-plane transport measurements.

The samples studied were grown by several groups throughout the world including Nigel Hussey, Nohara and Takagi from Tokyo ($x = 0.09, 0.20$), Kimura from Tokyo ($x = 0.17$), Shuichi Wakimoto ($x = 0, 0.05, 0.06, 0.07$) and Harry Zhang ($x = 0.06, 0.25, 0.30$) from Toronto, and the author ($x = 0.06$). Samples of $x = 0.06$ were grown using the image furnace of Graeme Luke and Bruce Gaulin at McMaster University with the assistance of Hanna Dabkowska.

The Travelling-Solvent Floating Zone technique

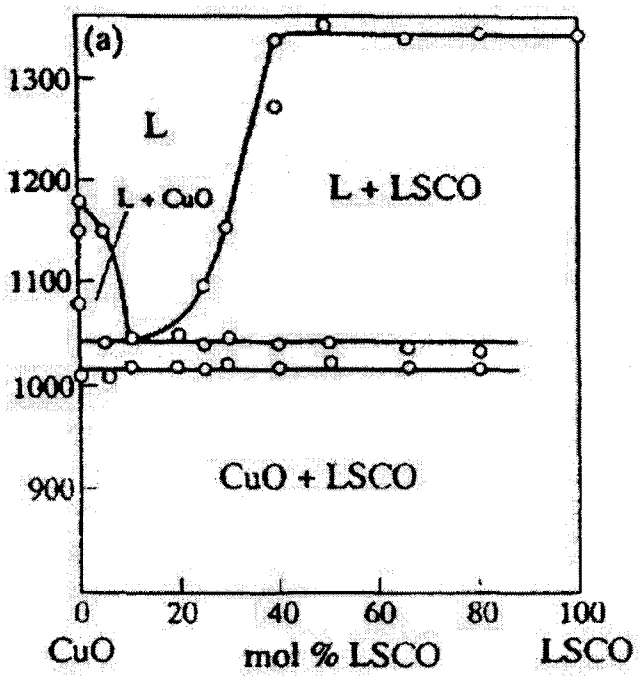

Figure 5.2: The LSCO - CuO growth phase diagram from Chen [135].

LSCO melts incongruently (it decomposes before it melts). Therefore, single crystals of LSCO must be grown from a flux to lower the growth temperature to below the decomposition temperature. In our case single crystal samples of LSCO are grown from a flux of $La_{2-x}Sr_xCuO_4$ and CuO. The growth phase diagram of LSCO is shown in figure 5.2. Using a flux with a relative concentration of CuO to LSCO that passes through the liquidus line separating the liquid phase from the LSCO + liquid phase, single crystal LSCO may be drawn out of the liquid. For other concentrations of LSCO:CuO, impurity phases of La_2O_3, $La_2SrCu_2O_6$ or CuO will be produced.

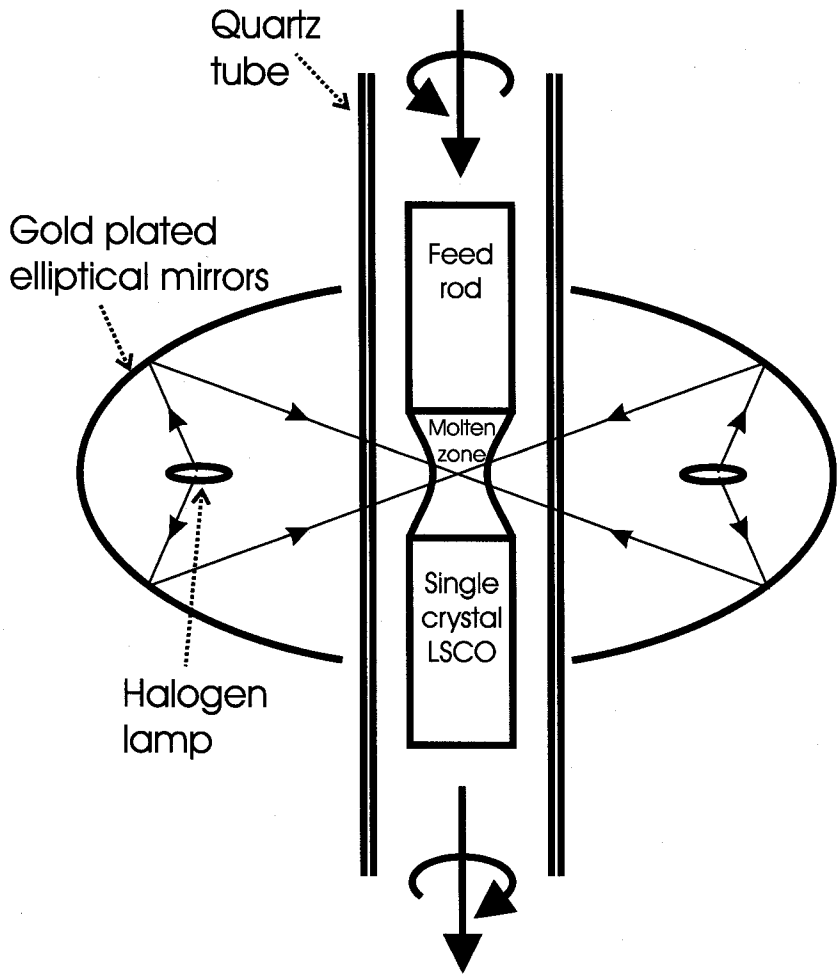

Figure 5.3: A schematic of the growth of LSCO using the travelling solvent floating zone technique in an image furnace.

In our samples, the growth of single crystals is achieved using the travelling solvent floating zone technique using an image furnace. With this technique, a flux of LSCO:CuO is melted using light from halogen lamps focused onto the flux. A schematic of this technique is given in figure 5.3. The distance away from the focus of the light creates the temperature gradient needed for LSCO to crystallize out of the flux (ie pass through the liquidus line in fig. 5.2). As LSCO crystalizes out of the flux, the flux will be depleted of LSCO. In order to keep a stable LSCO:CuO ratio (to keep the zone in the region of the phase diagram where no unwanted phases will crystallize) the zone needs to be fed with a fresh supply of LSCO to replace the LSCO removed as single crystals form. For this a rod of polycrystalline LSCO (the feed rod) is fed into the flux from the direction opposite to where the crystal are forming. A stable molten zone may be maintained by

feeding the molten zone with the feed rod while single crystals are drawn out of the other end.

Initially, this procedure will produce several polycrystals of differing orientation. However, in LSCO the sample grows at a different rate along different crystalographic axes. Approximately, the growth rate is fastest along the a-axis and slowest along the c-axis. Thus, for a polycrystalline sample, as the growth progresses, crystallites with their c-axis along the axis on the feed rod (the growth direction) will be surpassed by crystallites with their a-axis along the growth direction. Eventually, the fastest growing crystals will win out and a single crystal is formed. This procedure depends somewhat on the speed of the growth. If the rate is too fast, no crystallites will be able to propagate. On the other hand, if it is too slow the c-axis grains will be able to propagate better and we will be left with a polycrystalline sample.

In the following I will describe the specific details of the growth of our sample of LSCO with $x = 0.06$. This sample was grown by Shuichi Wakimoto, Harry Zhang and the author at McMaster University.

LSCO $x = 0.06$: Feed-rod preparation

Before growing single crystals of LSCO using the image furnace, the polycrystalline samples LSCO samples that make up the feed rods and molten zone need to be prepared. The starting materials for $La_{1.94}Sr_{0.06}CuO_4$ are La_2CuO_3 (99.99%), $SrCO_3$ (99.95%) and CuO (99.99%), mixed in stoichiometric proportions (La_2CuO_3: 39.07 g, $SrCO_3$: 1.096 g and CuO: 9.834 g to give $\sim$ 50 g of starting material). The $SrCO_3$ and CuO powders were first baked at 600 °C in air overnight in alumina crucibles in order to dry the materials, removing any potential water. The powders were removed from furnace at $\sim$350 °C and placed immediately in the desiccator to keep them dry.

The La_2CuO_3, $SrCO_3$ and CuO were then mixed and ground together in a clean (cleaned with HCl) agate mortar and pestle. The powders were then baked at 850 °C in air for 14 hrs. to create LSCO powder via a solid state reaction. In this reaction the C escapes as CO_2, and the oxygen equilibrates in the air to give approximately the correct oxygen content. The stochiometry of LSCO is set by the relative concentrations of the metal ions, La, Sr and Cu.

After this initial reaction, the LSCO powder was reground using the mortar and pestle and re baked for 15 1/2 hrs. at 950 °C to complete LSCO solid state reaction, after which the LSCO powder was reground once again. The flux was made by taking 10.0034 g of

the LSCO powder and adding 7.9134 g of CuO to give a LSCO:CuO ratio of 20 % mol LSCO to 80 % mol CuO. This flux was then mixed and reground using the mortar and pestle.

The LSCO and flux powders were then prepared into the rods to be used in the image furnace. This involves pressing the powders into an appropriate shape using a hydrostatic press and sintering the rods at high temperature to sinter them.

To make the feed rods we filled thin rubber tubes with powder. These serve as guides for the shape of the feed rods. The tubes were cleaned with ethanol before use[1].

To remove as much air as possible, the rubber tubes were pumped out using a water tap pump and tied off. The tubes were molded into shape and rolled in an acetate overhead transparencies to hold their shape and two brass half cylinders were placed around the sample as guides. The filled tubes were then pressed at 60 psi for ~2 min in a hydrostatic press. 5 feed rods were formed with the longest being 7 cm. In addition, another rod was formed out of the 20 % mol LSCO and 80 % mol CuO mixture to serve as the flux.

The feed rods were annealed at 900 °C overnight in air in an alumina boat to sinter them. To improve the density of the rods, and enhance the stability of the eventual growth in the image furnace, the feed rods are reannealed at a temperature close to the melting temperature of LSCO (1150 °C overnight in air). For this latter annealing a hole was drilled in the top of the feed rods and they were suspended in air from an alumina rod by tantalum wire fed through the hole. In this manner no contamination of the feed rods occurs due to contact with the alumina crucible at these higher annealing temperatures. In addition, a more homogeneous temperature for the feed rod may be achieved. Since we are annealing at close to the melting temperature, the feed rods will warp if there is an inhomogeneous temperature gradient, for instance if they had rested in an alumina boat.

LSCO $x = 0.06$: Image furnace growth

The single crystal growth of $La_{1.94}Sr_{0.06}CuO_4$ took place at McMaster university, with assistance from Hanna Dabkowska, in the lab of Prof. Bruce Gaulin and Prof. Graeme Luke using their CSI image furnace. This furnace has 4 halogen lamps (max power 500 W) and gold-plated mirrors. The seed crystal, in our case just a piece of feed rod, was

[1]There may have been a small amount of Talcum powder lining the tubes. However, as talcum powder is organic, it will burn away during the annealing process and will not contaminate our sample.

mounted on the lower shaft in a alumina hold and tied into place with chromel wire. A 0.5 cm length of the CuO:LSCO solvent rod was placed on top of the seed. A 2 cm feed rod was then suspended above the solvent on a hook from the upper shaft by chromel wire. The rods were then sealed in a quartz tube and flushed with flowing O_2 gas. The atmosphere for the growth was a 1:1 mixture of oxygen and air at $P = 5$ kPa.

To start the growth the lamps are focused on the solvent and the power is slowly increased until the solvent melts ($Power = 57.3\%$). The lower shaft is rotating at 25 rpm to produce a homogeneous temperature. After the zone is melted, the feed rod was lowered into the solvent. The feed rod, connected to the upper shaft, was rotated at 30 rpm counter to the rotation of the lower shaft. This mixes the molten zone, aiding in diffusion and maintaining a homogeneous temperature in the molten zone. The upper and lower shafts were then lowered relative to the lamps at the growth rate of 1 mm/hr. The power of the lamps was slowly raised to a stable value of 71.8 %.

To stop the growth, the slow progression of the upper and lower shafts was stopped. The power of the lamps was slowly reduced (~1hr.) to until the zone starts to shrink. The upper shaft is finally raised when only a small liquidus zone is left[2]. The power was then slowly[3] lowered over 1-2 hr.

The initial sample was grown to a length of 3.15 cm. Of this the final ~1 cm comprised a single crystal. The sample was tested for La_2O_3 inclusions by leaving the sample in water overnight. La_2O_3 reacts with water to form $La_2(OH)_3$ and samples with La_2O_3 inclusions will turn into a grey powder after exposure to water. Fortunately, our sample survived the water, indicating no La_2O_3 inclusions.

A second 5 cm long boule (boule #2) was also produced. For this sample, the middle section of boule #1 was used as the seed crystal.

Post-growth annealing

The as grown crystals of $La_{2-x}Sr_xCuO_{4+\delta}$ have non-stoichiometric O content ($\delta \neq 0$). To produce stoichiometric oxygen O_4, one generally needs to be anneal the samples after the growth. The conditions nessesary for this annealing depend on the Sr doping of the samples. For undoped $La_2CuO_{4+\delta}$, there is excess oxygen in as-grown samples. However, as the Sr content is increased, the reverse is true, as grown overdoped samples are oxygen

[2]Raising the feed rod with too large a liquidus zone will result in the solvent falling off the sides of the crystal. This may cause cracks to form.

[3]Cooling too quickly will cause cracks to form in the sample.

deficient.

In our study we have carefully postannealed some, but not all, of the samples[4]. The heavily overdoped samples ($x = 0.25$ and 0.30) were annealed under 3 atm of oxygen to attempt to fill oxygen vacancies. In the undoped sample ($x = 0$) we annealed in flowing Ar at 800 °C to remove excess oxygen. In the some of the underdoped samples, however, no annealing of the as grown samples was performed ($x = 0.06$ A, 0.07 and 0.09). While this may lead to some broadening of the superconducting transition temperature, it is unlikely to result in significant variation of the sample doping from the nominal Sr content, x, due to the proximity of the samples to the Sr content where the oxygen is stoichiometric in as grown crystals. In this regard it is interesting to compare the properties of sample $x = 0.06$ A, which was not annealed, to another sample ($x = 0.06$ B) at the same Sr content but annealed in flowing oxygen at 800 °C for 12 hrs. As shown in chapter 8, the properties of the two samples are very similar, suggesting little annealing dependent variation in the sample doping at this Sr content. It is noteworthy that, as expected, the annealing results in a higher degree of sample homogeneity, based on the sharper superconducting transition width's observed in the resistivity of sample B relative to the unannealed sample A (see fig. 8.6).

5.1.3 *LSCO sample preparation*

Samples are first oriented using Laue backscattering. Typical Laue patterns along the [100] and [001] (tetragonal unit cell) are shown in figure 5.4. These measurements were done on a Rigaku Geigerflex x-ray machine using a W target and typically operated with a current of 25 mA and a voltage of 25 kV. Using Polariod film (type 57, 4x5"), the images are exposed for 5-15 min with the sample placed a distance 56 mm from the film. The sample is mounted on a triple-axis goniometer so that it may be rotated from a random orientation to a direction of high symmetry. The resulting images are compared to calculations of the Laue pattern made using the known structure of the material and LaueX software. From these images the sample orientation is determined and adjusted.

After orientation, the samples are coated in Crystalbond^{TM} 509[5] to protect their

[4]Details of the annealing of each sample is listed in the appendix.

[5]Crystalbond^{TM}509 is a clear adhesive that is applied to add structural support to the samples during cutting and polishing. At room temperature Crystalbond is solid, but will melt and flow over the sample when heated to 135 °C. It is removed, leaving no residue, with an acetone solvent.

surfaces and cut using a diamond saw[6]. Samples are then reoriented and re cut to produce bar shaped samples with long axis along the [100] direction. Finally samples were carefully polished down to remove surface material damaged during cutting and to produce samples with appropriate dimensions for thermal conductivity measurements. Sheets of silicon carbide film with grit size between 30 and 5 μm was typically used to polish the samples.

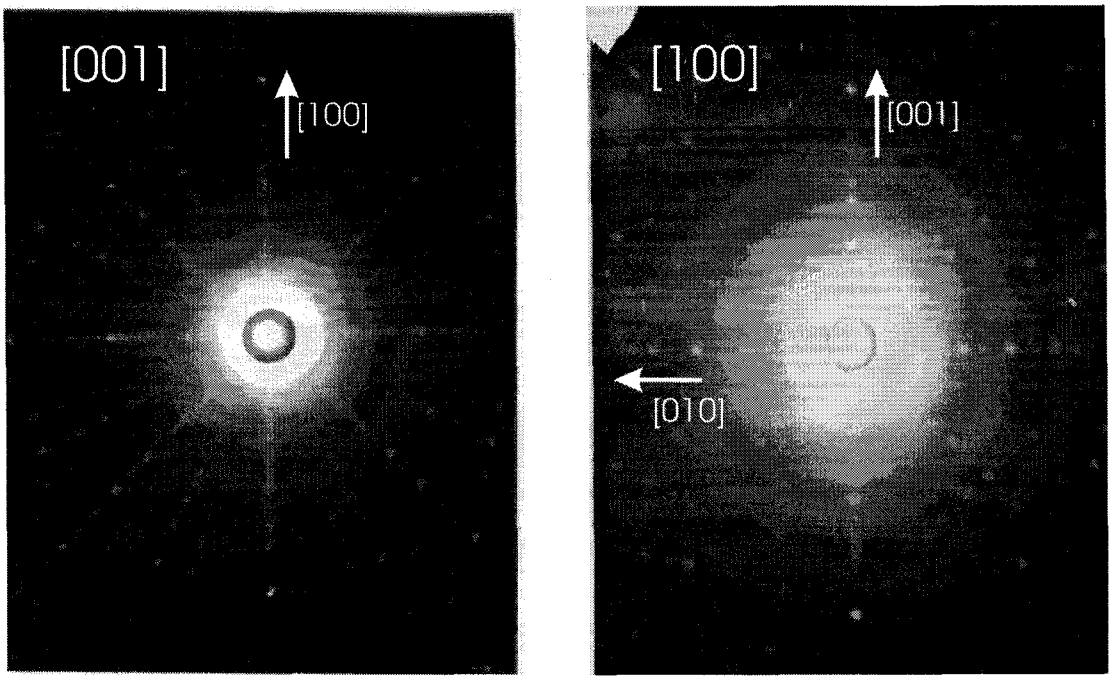

Figure 5.4: Laue patterns for LSCO $x = 0.07$ single crystals grown by the travelling solvent floating zone technique. left: [001] direction. right: [100] direction. Polaroid images were taken with a W x-ray source using I = 25 mA, V = 35 kV, a 15 min. exposure and $\simeq$ 56 mm distance between the sample and the film.

Electrical and thermal contacts were made to the samples using 2-part Epotech H20E Ag epoxy. Contact pads were painted onto the samples and cured at $\sim$ 180°C for 5 - 10 minutes. The contact pads were then annealed at 500 °C in flowing oxygen (Ar gas for undoped La_2CuO_4 sample) for $\sim$1 hr. to allow the Ag to diffuse into the sample, improving the contact resistance [7]. 50 or 100 μm diameter silver wires were then attached to the contact pads using the same Ag epoxy, again cured at $\sim$ 180°C for 5 - 10 minutes. Contact resistances as low as 50 mΩ at room T and 5 mΩ at low T were achieved. In

[6]The goniometer used may be translated from the x-ray machine to the diamond saw while maintaining the sample orientation.

[7]Low contact resistances generally cannot be achieved without annealing.

the appendix the sample and contact resistances are given for all samples.

In some initial resistivity measurements of the samples anomalously large *ab* plane resistivity values, inconsistent with literature, were measured for some samples. The anomalous resistivity is attributed to coupling of *c*-axis conductivity into the measurement due to inhomogeneous current distribution. In order to verify the accuracy of subsequent resistivity measurements a six-wire, as opposed to the standard 4-wire, contact configuration was used. An example of a sample prepared with 6 contact wires is shown in figure 5.5 a). Two pairs of voltage contacts with different spacing between them were painted along the *ab* face of the samples. Comparison of the resistivity measured on either side of the sample can be used to identify extrinsic problems, such as *c*-axis contributions. Agreement between the two sets of voltage contacts implies homogeneous current distribution. The contact pads were also painted down the sides of the samples (the *ac* faces) in an effort to electrically short the *c* axis. A comparison of homogeneous current distribution vs. inhomogeneous current distribution is given in figure 5.5 b). In sample *a*, the resistivity measured with voltage contacts on either face of the sample yield different results. In this sample the voltage contacts were not painted down the *c*-axis of the sample. In contrast, in sample *b*, where the voltage pads were painted down the sides of the sample, coupling the planes, the agreement between the resistivity measured with two sets of voltage contacts is better than 2 %.

5.1.4 *LSCO sample characterization*

Samples were characterized using a variety of techniques. Laue x-ray diffraction was used to orient samples, as discussed above, but also to verify that the samples used were indeed single crystals. In addition, electron probe microanalysis (EPMA) was used to verify that the sample composition agrees with the composition determined from the pre growth starting composition of the material. Finally, resistivity was measured to determine T_c and verify the sample doping, as discussed in the following section.

Electron Probe Microanalysis

Electron probe microanalysis (EPMA) measurements were performed by Dr. Claudio Cermignani in the Department of Geology at the University of Toronto. Electron probe microanalysis measures the x-ray fluorescence from the sample subjected to a beam of electrons. By measuring the spectrum of x-ray fluorescence, EPMA can determine the presence and relative concentrations of specific atoms in a sample.

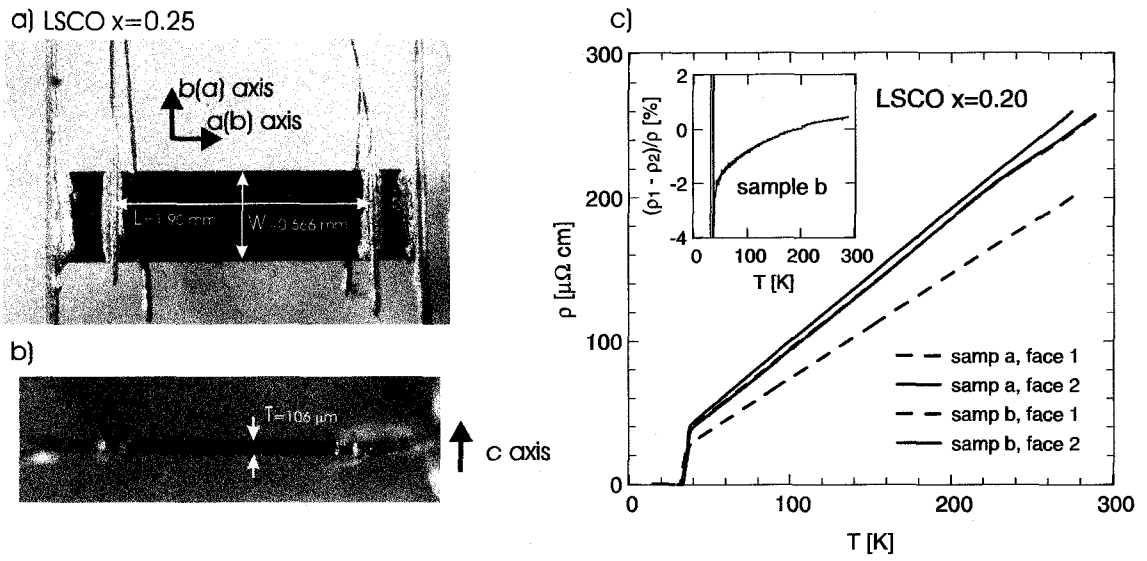

Figure 5.5: a) A image of the *ab* face of a sample of LSCO ($x = 0.25$) taken under an optical microscope. This sample has six contact wires attached: two current leads on either end and two pairs of voltage leads on either face. Contacts pads are made with Epotech H20E Ag epoxy. b) The edge of the same sample under an optical microscope. Note the contact pads are painted along the *c*-axis of the sample. c) The resistivity of LSCO ($x = 0.20$) vs. temperature measured in two samples *a* and *b*, each with two different sets of voltage contacts on either face of the sample. The agreement between the measurements on either face in sample *b* indicates homogeneous current distribution. In contrast, the disagreement between the measurements on either face in sample *a* suggest *c*-axis contributions to the resistivity. Inset: the percentage difference between the resistivities measured on either face of sample *b*. With the exception of very close to the transition temperature, this difference is less than 2 %.

The composition of the samples studied by EPMA is given in table 5.1[8]. Note that the nominal Sr content agrees well with that determined from EPMA within a few standard deviations, however, the EPMA analysis suggests that the samples with nominal Sr content of x=0.09 and 0.07 are in fact both closer to $x = 0.08$.

Finally, EPMA was also used as microscopy to verify that the sample composition did not vary over the size of the sample and that the samples contained no inclusions of secondary phases.

Resistivity measurements of LSCO

The resistivity, ρ, which has been well studied by several groups [72, 71, 73, 74, 75, 76, 77, 78] and was discussed in section 2.2.4, is shown for our samples in figure 5.6. Our

[8]Note that as EPMA is insensitive to oxygen, the oxygen content is determined from the measured stoichiometry of the cations and requiring that the lattice be electrically neutral.

Table 5.1: EPMA determination of the composition[a] of the $La_{2-x}Sr_xCuO_4$ samples.

Nominal Sr	La	Sr	Cu	O
0.06	1.965 ± 0.005	0.065 ± 0.006	1 ± 0.002	4.014 ± 0.001
0.07	1.951 ± 0.005	0.077 ± 0.005	1 ± 0.004	4.004 ± 0.001
0.09	1.947 ± 0.004	0.078 ± 0.004	1 ± 0.005	3.998 ± 0.001
0.25	1.780 ± 0.019	0.255 ± 0.006	1 ± 0.021	3.925 ± 0.005

[a]The relative atomic concentration is written normalized to Cu to express the composition in the familiar formula units of LSCO (La + Sr = 2, Cu = 1, O = 4).

Table 5.2: T_c, p and dimensions of $La_{2-x}Sr_xCuO_4$ samples.

x	T_c (K)	L (mm)	W (mm)	T (μm)	$\alpha = TW/L$ (cm)
0	-	0.98 ± 0.05	0.803 ± 0.008	167 ± 8	1.37×10^{-2} ± 5%
0.05 (#2, face 1)	-	0.697 ± 0.0.50	0.545 ± 0.008	280 ± 8	2.19×10^{-2} ± 8%
0.06 A (#3)	5.5	0.833 ± 0.050	0.758 ± 0.008	180 ± 8	1.65×10^{-2} ± 8%
0.06 B (#4)	8.5	0.659 ± 0.050	0.758 ± 0.008	183 ± 8	2.10×10^{-2} ± 9%
0.07 (#11, face 1)	19	1.28 ± 0.050	0.530 ± 0.008	303 ± 8	1.26×10^{-2} ± 5%
0.09 (#7)	16	0.435 ± 0.050	0.533 ± 0.008	83 ± 8	1.02×10^{-3} ± 15%
0.17	34	0.97 ± 0.05	1.26 ± 0.01	212 ± 8	2.75×10^{-2} ± 6%
0.20 (b, face 1)	33.5	1.175 ± 0.05	0.227 ± 11	167 ± 8	3.22×10^{-3} ± 8%
0.25 (face 1)	13	1.545 ± 0.075	0.666 ± 0.008	106 ±8	4.57×10^{-3} ± 9%
0.30 (face 2)	-	2.13 ± 0.05	0.508 ± 0.008	76 ± 3	1.81×10^{-3} ± 5%

measurements are in agreement with resistivity measurements by other groups, and show the resistivity at low temperatures is at insulating ($\delta\rho/\delta T < 0$) at low dopings, below the onset of superconductivity, and metallic ($\delta\rho/\delta T > 0$) at higher doping.

In addition, from the resistivity we determine the superconducting transition temperature, T_c, listed in table 5.2, for all of the superconducting samples. Here we have adopted a definition of T_c as the point where resistivity is has gone to zero. Note for some of the samples, T_c using this definition is lower than expected for samples with these doping levels. Part of this is due to our definition of T_c. The point where $\rho = 0$ is typically less than the onset of diamagnetism observed in susceptibility measurements and frequently used as a definition of T_c. However, in a few of our samples it may reflect either sample inhomogeneity or a difference in the doping from expectations based on starting sample composition. In particular, we draw attention to two questionable

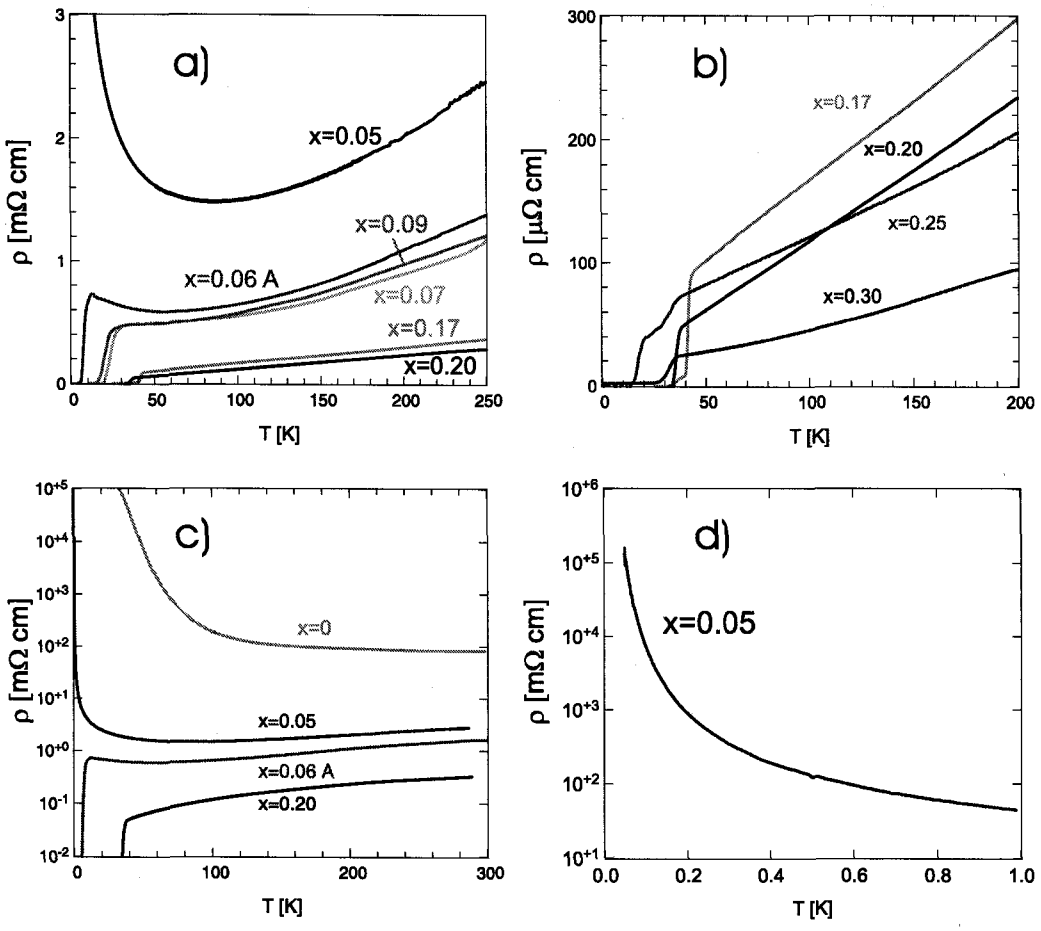

Figure 5.6: The resistivity in LSCO as a function of doping. a) ρ vs. T with $x = 0.05$, 0.06 A, 0.07, 0.09, 0.17 and 0.20. b) ρ vs. T for overdoped LSCO. c) ρ vs. T in LSCO on a semi-log plot for $x = 0$, 0.05, 0.06 A and 0.2. The x=0 sample is strongly insulating below room temperature. d) ρ vs. T on a semi-log scale for $x = 0.05$ below 1 K. The temperature dependence of the low temperature resistivity is consistent with a 3D variable-range-hopping model of localization.

results. First, in the $x = 0.17$ sample ρ finally goes to zero at $T = 33.4$ K, much lower than $T_c \simeq 39$ K often cited for samples of this doping. This may be an indication of either Sr or O inhomogeneity in this sample, resulting in a hole doping less (or greater) than the nominal doping of 0.17. Second, in the $x = 0.09$ sample has a lower T_c than the sample with a nominally lower doping of $x = 0.07$. We note, that these two samples were grown by different sample growers (N. Hussey, N. Nohara and H. Takagi grew the $x = 0.09$ sample, whereas S. Wakimoto grew the $x = 0.07$ sample). In addition, EPMA measurements, discussed above indicate that both samples have actual Sr doping closer to $x = 0.08$.

In addition, in the $x = 0.17$, 0.25 and 0.30 samples there are partial superconducting

transitions at higher temperatures than where ρ finally goes to zero (in the $x = 0.30$ sample ρ does not go to zero, the sample is non-superconducting in the bulk). These partial transitions are evidence for some form of sample inhomogeneity. As the transitions are only partial, however, we suspect that they evidence only a small fraction of the sample volume, and hence will not influence bulk properties such as the thermal conductivity.

5.2 $Tl_2Ba_2CuO_{6+\delta}$

5.2.1 Tl2201 crystal structure

$Tl_2Ba_2CuO_6$ is a single layered tetragonal cuprate with lattice parameters $a = 3.86$ Å and $c = 23.2$ Å. The crystal structure is shown in Fig. 5.7. In some ways Tl2201 is an ideal cuprate. It has the same $T_c(\text{max}) = 90$ K as the well studied systems YBCO and Bi2212, but it lacks the CuO_2 bilayers and CuO chains that tend to complicate some measurements of YBCO and Bi2212.

The layered perovskite structure of Tl2201 consists of CuO_2 planes with BaO planes above and below. A staggered TlO bilayer resides between the BaO-CuO_2-BaO structures. Like LSCO, Tl2201 has two CuO_2 planes per unit cell, giving an a spacing between planes of 11.6 Å. This is notably almost double that of LSCO, resulting in stronger c/a anisotropy ($\sim 1 \times 10^3$ in Tl2201 [140] vs. $\sim 1 \times 10^2$ in overdoped LSCO [73]).

Stoichiometric $Tl_2Ba_2CuO_6$ ($\delta = 0$) has three distinct oxygen sites, O(1), O(2) and O(3) on the CuO_2, BaO and TlO planes, respectively. The excess oxygen ($\delta > 0$) can be forced into an interstitial sites, O(4), between the TlO planes to dope additional holes in the CuO_2 planes [141, 142]. With no excess oxygen ($\delta = 0$) Tl2201 is optimally doped ($T_c \sim 90$ K) and it can be overdoped to completely non-superconducting with $\delta \simeq 0.1$. In practice, the doping is achieved by annealing the as-grown samples under oxygen pressure (for overdoped samples) or vacuum for optimally doped samples [143, 144]. In well ordered samples, the addition of the interstitial O(4) also drives Tl2201 slightly orthorhombic, as depicted by the placement of the O94) atoms in fig. 5.7.

In principle Tl2201 can be grown with low levels of disorder. The oxygenation that results in hole doping into the CuO planes occurs far away from the CuO_2 planes. As such, oxygen disorder should have little effect on in-plane scattering rate of carriers in the CuO_2 planes. In several samples reported in literature, however, a small amount of Cu (5-8 %) is known to substitute for Tl during growth, resulting in disordered TlO planes [142, 141, 145]. The impact of this greater disorder on the scattering rate is unclear. The

Cu substitution does, however, disrupt the oxygen ordering that drives $Tl_2Ba_2CuO_{6+\delta}$ orthorhombic, resulting in tetragonal samples [142, 141].

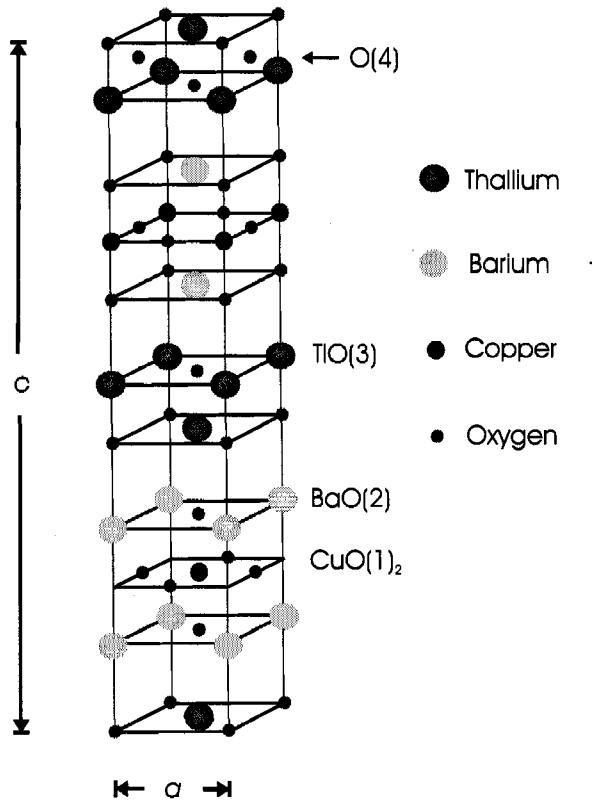

Figure 5.7: The crystal structure of $Tl_2Ba_2CuO_{6+\delta}$. The layered perovskite structure consists of CuO_2 planes with BaO planes above and below. A staggered TlO bilayer resides between the BaO-CuO_2-BaO structures. Stoichiometric $Tl_2Ba_2CuO_6$ ($\delta = 0$) has three distinct oxygen sites. The excess oxygen ($\delta > 0$) to dopes holes into the CuO_2 planes occupy an interstitial site, O(4), between the TlO planes.

Single crystal samples measured in our study were grown by Ruixing Liang and Darren Peets at the University of British Columbia using a self-flux technique described in reference [145]. The resulting crystals are grown as thin platelets with the thin axis along the c-axis. While the UBC group has demonstrated the ability to grow orthorhombic (and hence free of Cu substitution) single crystals the level of Cu for Tl substitution in the samples presented in our study is unknown. Additionally, two samples grown by other crystal growers, Andrew Mackenzie at Cambridge University and N. N. Koleshnikov at Chernagolovka in Russia are presented in this thesis. The sample grown by Andrew Mackenzie has a $T_c = 89$ K and is labeled Mac#15. The sample grown by Koleshnikov has a $T_c = 26$ K (labeled Kol2A) and was prepared and measured by Etienne Boaknin

and Cyril Proust.

Finally, it is worth noting that previous measurements from our group (by Etienne Boaknin and Cyril Proust) on samples grown by Andrew Mackenzie are not included in this thesis. I refer readers to the thesis of Etienne Boaknin [127] for details of these samples and measurements.

5.2.2 Tl2201 sample preparation

Sample contacts

Electrical and thermal contacts to all of the samples, with the exception of the sample with $T_c = 26$ K, were made using gold evaporated contact in a 4-wire contact configuration[9]. To make the gold contacts a mask was first constructed using strips of 7 μm thick Kapton. Three Kapton strips were laid across the sample to cover all of the sample except two narrow strips, to serve as the voltage contacts, and the ends of the sample, to serve as the current contacts. The mask was then glued down using Loctite to keep the mask and sample fixed in place.

The evaporation took place in an Edwards Auto 306 (with FL400 box chamber) thermal evaporator. In the evaporator, the sample is placed on a rotating stage a distance of ~10 cm from the gold, and at an angle such that the plume from the evaporated gold strikes the sample at ~45°. With the sample rotating, this setup ensures that gold covers the edges (*ac*) of the samples as well as the face (*ab*-plane), although the Au layer will undoubtedly be thicker on the face of the samples using this procedure. For the evaporation 90-110 mg's of Au is placed in a tungsten boat. The chamber is then pumped down with a turbo pump to a pressure of $1 - 5\times10^{-6}$ torr. The gold is then evaporated onto the sample by sending a high current through the tungsten boat, heating it until the gold evaporates (power=10). The power is left on until all of the gold evaporates (about 10 min). The resulting contacts are approximately 50-70 nm thick (on the faces), as measured by the Edwards FTM6 film thickness monitor installed in the evaporator and located a similar distance from the tungsten boat as the sample.

After evaporating the gold contacts, the samples annealed to set the oxygen content and diffuse in the gold, as described below. Ag wires were then attached to the samples

[9]Due to small sample size a 6-wire measurement, as done in LSCO, could not be achieved on the Tl2201 samples.

using Dupont 4929N Ag paint[10]. The resulting contact resistances using this procedure varied from 100 mΩ to 5 Ω. In the appendix the contact resistances for all samples is listed.

All but one sample had evaporated gold contacts. The exception is the sample with T_c = 26 K. This sample has contacts prepared by Etienne Boaknin and Cyril Proust using Epotech H20E Ag epoxy, in a similar fashion to the LSCO samples discussed above.

The dimensions of the samples, listed in table 5.3, were measured with an optical microscope (66x mag.) for the length and width and with a scanning electron microscope for the thickness. An example of a sample with Ag wires attached with Ag paint is shown in figure 5.8. These latter measurements were performed by Massimo diCiano in the group of Prof. John Wei. Despite the detailed measurement of the sample dimensions, a sizeable error in the geometric factor, α, of the order of 25 % remains in several samples due to the finite width of the voltage contacts and/or the irregular shape of some samples. This is more so for the sample with T_c = 89 K. SEM images of this sample indicate irregular thickness and possibly sample deterioration. While this impairs quantitative analysis of the magnitude of the thermal conductivity, comparisons of the conductivity as a function of magnetic field (see chapter 7) can still be considered reliable.

Annealing

The sample with contacts was then annealed to both improve the contact resistance and set the oxygen content. The annealing conditions varied greatly depending on the desired doping. The heavily overdoped samples $T_c \sim$ 18 K were annealed by Ruixing Liang at the University of British Columbia at 400-480 °C under 50-60 atm of oxygen for up to 14 days. Optimally doped samples (T_c = 84 K) were annealed here at the University of Toronto at 500 °C for 20 hrs. under a pressure of 5×10^{-7} torr, achieved by pumping on the sample with a turbo pump during the annealing. The other samples were annealed in Ar or O atmospheres to achieve T_c's of 26 - 76 K, as listed in the appendix.

In three cases we were able to measure a single sample at two different dopings, in this way eliminating the error in the geometric factor for the measurements on a single sample. This was achieved by first evaporating Au pads onto the sample and annealing the sample to set the doping, as described above. After measuring the sample, the wires

[10]The Ag paint dries at room temperature in about ten minutes. Additionally, it may be completely removed, leaving no residue with a solvent of 1-acetoxy-2-butoxyethane (from Sigma Aldrich). This solvent is also used to thin the Ag paint in order to achieve an appropriate working consistency.

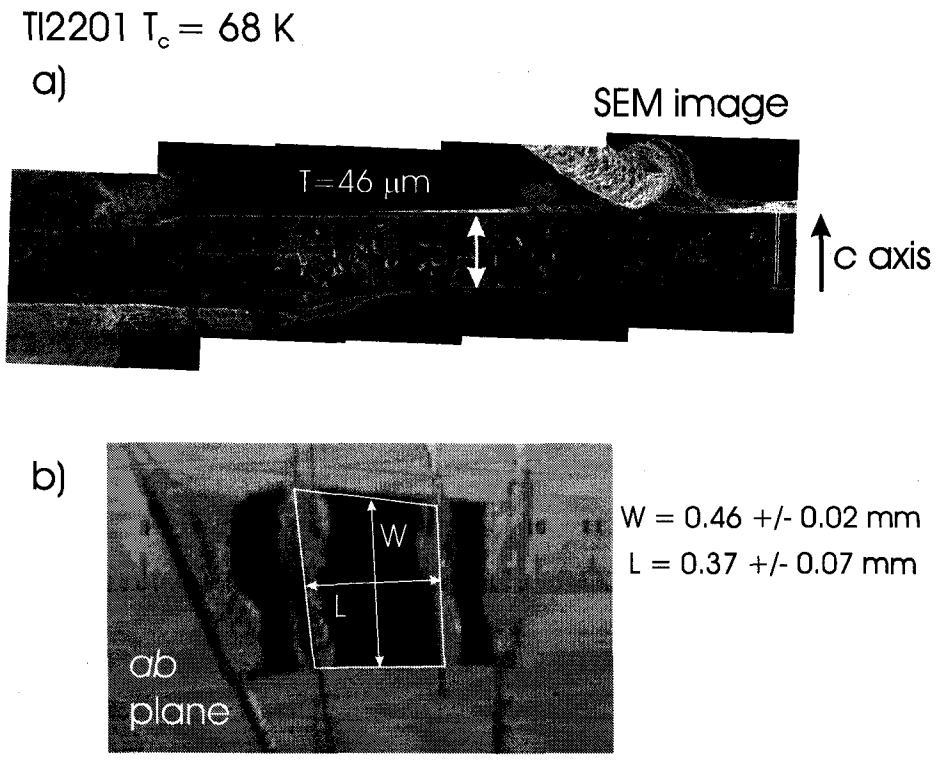

Figure 5.8: Images of a crystal of Tl2201 (T_c = 68 K) with Au contact pads and Ag wires attached with Ag paint. a) an SEM image of the c-axis of the sample to measure the sample thickness. b) an image of the ab-plane of the sample through the optical microscope.

and Ag paint were removed and the sample was reannealed to a different doping. In one case a single sample was measured with T_c = 84 K and then remeasured after being overdoped to T_c = 26 K. A second sample was annealed in reverse order: measured at T_c = 19 K and then remeasured at T_c = 72 K. Finally, in a third sample was measured first at T_c = 4 K and then remeasured at T_c = 76 K.

5.2.3 Tl2201 sample characterization

Resistivity

The ab-plane resistivity measured on all samples is shown in figure 5.9. Unlike the resistivity measurements on LSCO we use the resistivity measurements only as a determination of T_c and caution against detailed interpretation of the magnitude of the charge transport. This is due to possible contamination of ab plane resistivity measurements in Tl2201 by c-axis contributions to the conductivity which may be induced by either inhomogeneity in the sample or contact pads. Note, while this potential error makes the magnitude and T dependence of the charge conductivity suspect, it does not result in an

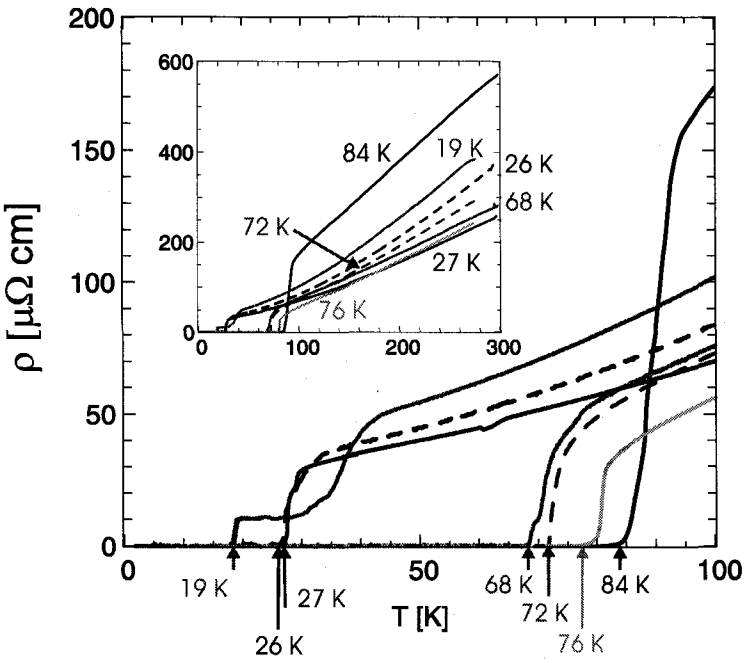

Figure 5.9: ρ vs. T of Tl2201 at various dopings. T_c for all samples is taken as the point where $\rho = 0$. Inset: A blowup of the resistivity to include room T data. The solid and dashed curves of the same color indicate measurements done on the same sample at two different dopings.

error in the thermal transport: in thermal transport, thermalization of heat gradients by nearly isotropic phonons make c-axis contributions negligible.

T_c is determined from these resistivity measurements as the temperature at which $\rho = 0$. The carrier doping in the CuO_2 planes, p, is subsequently determined from T_c using the empirical formula[146]

$$\frac{T_c}{T_c^{max}} = 1 - 82.6(x - 0.16)^2, \tag{5.1}$$

where $T_c^{max} = 89.0$ K is taken as the transition temperature of optimally doped Tl2201. The p values for all samples, along with the geometric factors is given in table 5.3.

Table 5.3: T_c, p and dimensions of Tl2201 samples.

	T_c (K)	p	L (mm)	W (mm)	T (μm)	$\alpha = TW/L$ (cm)
Mac15[a]	89	0.16	0.30 ± 22%	0.40 ± 5%	15.4	2.05×10^{-3}
UBC1A[b]	84	0.186	0.724 ± 7 %	0.377 ± 10 %	36.4 ± 15 %	$1.90\times10^{-3} \pm 17\%$
UBC4B[c]	76	0.202	0.450 ± 15.6 %	0.400 ± 2 %	39 ± 5 %	$3.47 \times10^{-3} \pm 16\%$
UBC3C[d]	72	0.208	0.386 ± 14 %	0.447 ± 2 %	27 ± 5 %	$3.13 \times10^{-3} \pm 15\%$
UBC2	68	0.213	0.374 ± 19 %	0.463 ± 5 %	46.0 ± 15 %	$5.69 \times10^{-3} \pm 25\%$
Kol2A	27	0.253	0.351 ± 18 %	0.313 ± 7 %	64.6 ± 15 %	$5.76 \times10^{-3} \pm 24\%$
UBC1B[b]	26	0.252	0.724 ± 7 %	0.377 ± 10 %	36.4 ± 15 %	$1.90 \times10^{-3} \pm 19\%$
UBC3A[d]	19	0.258	0.386 ± 14 %	0.447 ± 2 %	27 ± 5 %	$3.13 \times10^{-3} \pm 15\%$
UBC4A[c]	4	0.268	0.450 ± 15.6 %	0.400 ± 2 %	39 ± 5 %	$3.47 \times10^{-3} \pm 16\%$

[a]Images of the thickness of this sample indicate potential an irregular, possibly deteriorated sample. As such, an accurate determination of the geometric factor is presently not possible.
[b]The same sample was measured both after annealing to $T_c = 84$ K and reannealing to $T_c = 26$ K.
[c]The same sample was measured both after annealing to $T_c = 4$ K and reannealing to $T_c = 76$ K.
[d]The same sample was measured both after annealing to $T_c = 19$ K and reannealing to $T_c = 72$ K.

6

THERMAL CONDUCTIVITY IN TL2201: A d-WAVE SUPERCONDUCTOR

In chapter 3 we outlined the theory of the low T thermal conductivity in a d-wave superconductor. In this chapter we test out the mean-field theory in the cuprate Tl2201 in a region of the cuprate phase diagram covering from optimal doping to heavily overdoped. This study follows in the same vein as previous work on low T thermal conductivity [14, 16, 15, 7, 4]. We find that the mean-field nodal quasiparticle theory of thermal conductivity provides a successful description of our results. The implications of this are that well-defined delocalized nodal quasiparticles exist down to $T \simeq 0$ throughout the phase diagram and that, at least in YBCO and Tl2201, they are described by a simple d-wave gap.

Our test of the mean-field theory takes the form of measuring the linear in temperature electronic contribution to κ at very low temperatures. Using the formalism outlined in ch. 3 (eq. 3.14) we determine v_2, which is proportional to the slope of the quasiparticle gap at the nodes, $v_2 = \delta\Delta/\delta\mathbf{k}|_{node}$. The gap maximum, Δ_0 can be inferred, as it is in Sutherland et al. [4], by assuming a simple d-wave form for the gap. In this fashion thermal conductivity serves as a novel probe of the quasiparticle gap.

This measure of the gap from thermal conductivity is notable for a number of reasons that make it an excellent complement to conventional measurements of the superconducting gap, for instance from ARPES and tunneling. First, it is a very low energy measurement of the gap, the energy scale being set by temperature (and also the impurity bandwidth, γ). Second, it measures the gap at the nodal positions in k-space (along (π,π)) as opposed to the gap maximum at the anti nodal (π,0) positions. The gap maximum can be interpolated by assuming a simple form for the gap, for instance the simple d-wave gap $\Delta = \Delta_0 \cos(2\phi)$. Thirdly, thermal conductivity provides a bulk measure of the gap, unlike surface sensitive techniques such as ARPES and tunneling. Finally, thermal conductivity is only sensitive to delocalized quasiparticle excitations. Localized excitations that may have a signature in tunneling, APRES and specific heat

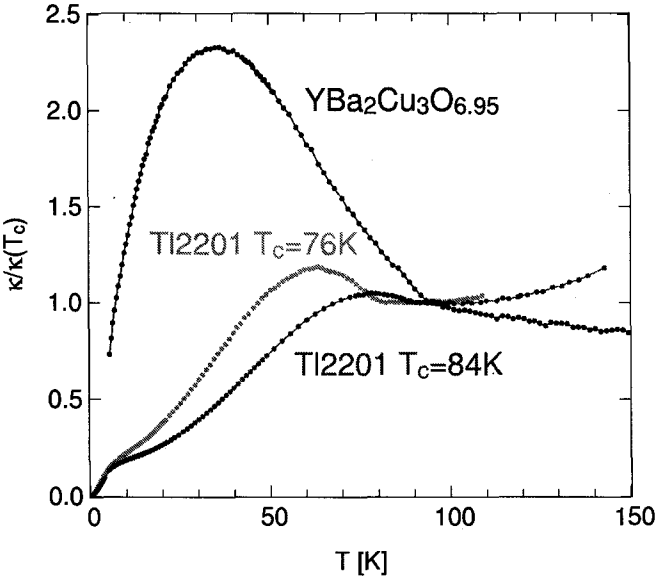

Figure 6.1: κ normalized to $\kappa(T_c)$ vs. T for Tl2201 with T_c = 84 K and 76 K, along with measurements of YBCO from ref. [4]. The YBCO data is from a sample grown in a yttrium-stabilized zirconium crucible.

will not transport heat.

In this chapter we measure Tl2201 a various dopings from optimal doping (T_c = 84 K) to heavily overdoped (T_c = 19 K) to attain a systematic study of the gap in overdoped cuprates[1]. As Tl2201 is a $T_c^{max} \simeq$ 90 K superconductor like YBCO and Bi2212, between the three materials we are able to construct the generic doping dependence of the gap in a 90 K cuprate superconductor. We find agreement with spectroscopic measurements of the gap and find Δ_0 to approximately follow T_c in overdoped Tl2201. Additional measurements of the thermal conductivity in Tl2201 at intermediate temperatures (2 K - 120 K) are also presented in order to comment on the relative disorder levels of the various cuprate materials.

6.1 Thermal conductivity at intermediate temperatures

In figure 6.1 we show our measurements of the thermal conductivity, κ, at around optimal doping in two samples of Tl2201 along with measurements of optimally doped YBCO from ref. [4]. In all three samples the thermal conductivity increases abruptly at $\sim T_c$ and forms a peak at some lower temperature. While the origin of this peak was an open

[1]The sample with T_c = 89 K is not included in this chapter due to excessive uncertainty in the samples geometric factor. Data on this sample is however presented in the following chapter.

question in the early days of HTSC, it is now well established that the peak is largely of electronic origin [147]. The clearest evidence for this interpretation comes from microwave conductivity [148, 149] and thermal hall effect [150] measurements, both of which are insensitive to phonon conductivity and yet observe a large increase in conductivity below T_c. The peak results from a collapse of the inelastic quasiparticle scattering rate as the superconducting state is entered. This collapse has a greater impact on the conductivity than the reduction in the density of states due to the opening of the superconducting gap. As the temperature is decreased the quasiparticle scattering rate continues to decrease until it becomes limited by the elastic, quasiparticle-impurity scattering rate. In this way the height of the peak provides a measure of the relative contributions of elastic and inelastic scattering. Theoretical models have been developed to describe the peak height and relate it to the quasiparticle-impurity scattering rate [151, 152].

In the Tl2201 sample with $T_c = 84$ K the peak height is similar to previous measurements of optimally doped Tl2201 [153] but is smaller than peak in the $T_c = 76$ K sample and significantly smaller than the peak in YBCO. This suggests a different elastic scattering rate in the three samples. This difference in elastic scattering rate echoes the expected differences in level of disorder between the two materials. YBCO can be grown very pure and is considered very stable against cation substitution, giving it a high degree of crystalline perfection. In Tl2201, however, disorder may be introduced in the TlO bilayers due to partial substitution of Cu on the Tl site [142, 141, 145]. The difference in the two Tl2201 samples is indicative of the annealing conditions used to prepare the samples, and perhaps their starting purity level (they come from different growth batches). In the 84 K sample, the sample was annealed at 500 °C, a relatively high temperature that may have resulted in Tl evaporation. In the 76 K sample, however, the sample was annealed at lower temperature, thereby reducing Tl evaporation and leading to a less disordered sample.

6.2 Low temperature thermal conductivity

We now turn to discuss the low temperature data, where a quantitative analysis is possible. The thermal conductivity measured at sub-Kelvin temperatures is shown in Fig. 6.2 as a function of doping. To extract the electronic and phonon contributions to κ the data was fit to

$$\frac{\kappa}{T} = \frac{\kappa_0}{T} + AT, \tag{6.1}$$

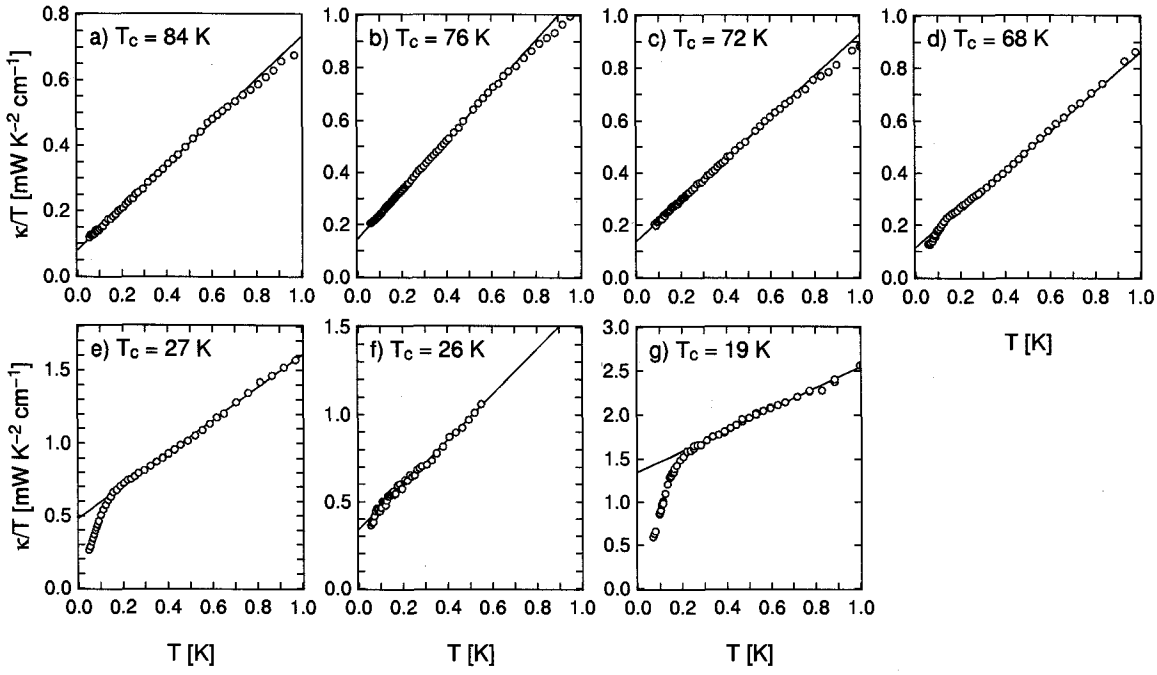

Figure 6.2: κ/T vs. T below 1 K for Tl2201 samples with T_c = 84 K, 76 K, 72 K, 68 K, 27 K, 26 K and 19 K. The lines are fits to eq. 6.1.

where κ_0/T is the electronic contribution to the total thermal conductivity and the second term is the phonon contribution, κ_{ph}. Note, in some samples (T_c = 68, 27 and 19 K) a downturn in the data is observed at $T = 150 - 200$ mK associated with electron-phonon decoupling [154], described below. In these instances we fit the data above the onset of the downturn. κ_{ph} has a T^2 dependence that is described in detail in ch. 9, and that we attribute to the phonon scattering rate being dominated by electron-phonon scattering. Note that this T dependence for κ_{ph} is in contrast to underdoped YBCO and LSCO [4, 1], where boundary scattering dominates κ_{ph} below $\sim$ 0.5 K, having a T dependence, $\kappa_{ph} \propto T^{2.4-3}$. In Tl2201 the boundary scattering limit will presumably also be reached at temperatures lower than those accessible in our measurement and we must consider the impact this may have on our interpretation (our determination of κ_0/T). A crossover to the boundary scattering limit will have the effect of producing an upturn in κ_{ph}. Thus the values of κ_0/T from fits to eq. 6.1 represent the lower limit of κ_0/T. However, the actual values are not expected to differ considerably from the extrapolated values. Also, it is important to note that this uncertainty does not impact on any of the general conclusions drawn in this chapter. The values of κ_0/T and A from fits to eq. 6.1 are listed in table 6.1 and plotted in fig. 6.3.

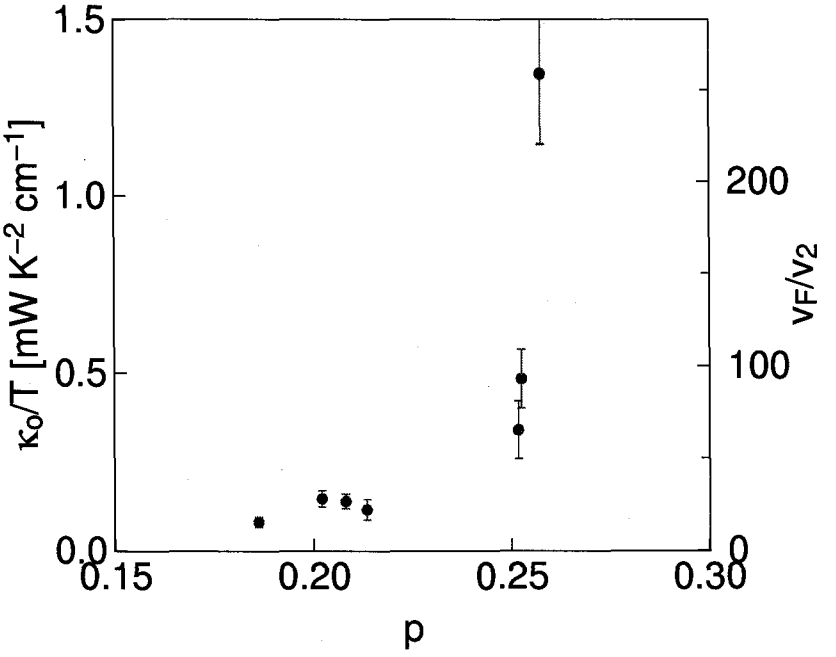

Figure 6.3: κ_0/T and v_F/v_2 vs. hole concentration, p, for Tl2201.

Electron-Phonon decoupling

As noted above, in three of the samples a downturn in the data is observed at 160 to 250 mK in the samples with $T_c = 68$, 27 and 19 K (d, e and g in fig. 6.2). These downturns are believed to be associated with a thermal decoupling of the phonons and the quasiparticles at low T, resulting in the phonons and quasiparticles falling out of thermal equilibrium with each other at low temperatures [154]. In instances where the initial heat current is dominated by phonon conduction, the contribution to the total heat current by the electrons is limited by the electron-phonon heat transfer rate. This falls off as a rapid function of temperature, T^{4-5}, [154] leading to a sharp reduction in κ_{el}. Whether or not a downturn is observed due to electron-phonon decoupling will depend on a number of factors including the nature of the thermal contact between the heater and the sample, which typically varies from sample to sample, and the electron-phonon coupling.

In the event that a downturn occurs due to electron-phonon decoupling, it is appropriate to extrapolate the data from above the downturn[2] in order to gain an intrinsic measure of κ_{el} and κ_{ph}. This procedure is proven to be effective in heavily overdoped

[2]Unlike above the downturn, the data below the onset of the downturn is indicative of electron-phonon decoupling and is not a measure of the sum of the electronic and phononic conductivities as assumed in eq. 6.1.

Table 6.1: κ_0/T and A for Tl2201 samples.

T_c (K)	p	κ_0/T [mW K^{-2} cm^{-1}]	A [mW K^{-3} cm^{-1}]
84 [a]	0.186	0.080 ± 17 %	0.65 ± 17 %
76	0.202	0.145 ± 16 %	0.948 ± 16 %
72 [b]	0.208	0.139 ± 15 %	0.790 ± 15 %
68	0.213	0.115 ± 25 %	0.744 ± 25 %
27	0.253	0.340 ± 24 %	1.29 ± 24 %
26 [a]	0.252	0.48 ± 17 %	1.12 ± 17 %
19 [b]	0.258	1.35 ± 15 %	1.20 ± 15 %

[a]The same sample was measured both after annealing to T_c = 84 K and reannealing to T_c = 26 K.
[b]The same sample was measured both after annealing to T_c = 19 K and reannealing to T_c = 72 K.

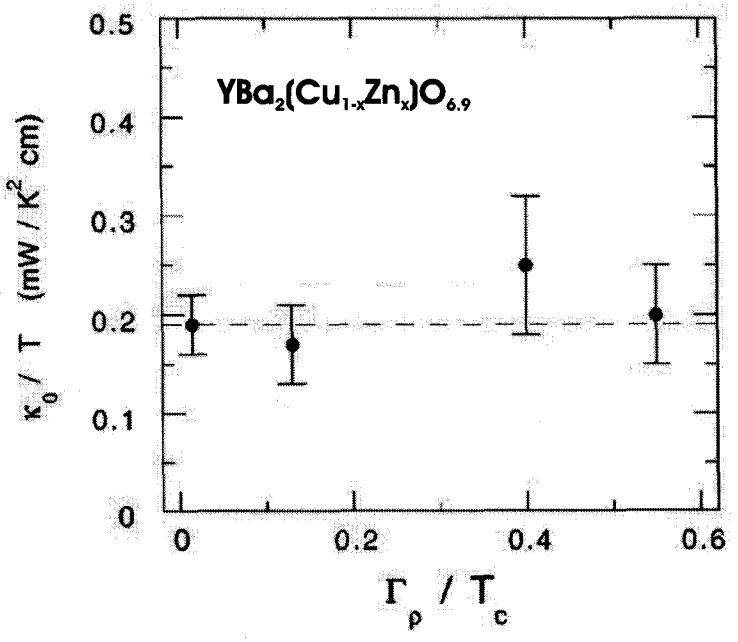

Figure 6.4: κ_0/T vs. scattering rate, Γ for the four crystals of $YBa_2(Cu_{2-x}Zn_x)_3O_{6.9}$ with varied levels of Zn impurities (scattering rates) from ref [14]. κ_0/T is unaffected by large changes in the level of disorder (universal), having a roughly constant value of 0.19 mW K^{-2} cm^{-}1 (dashed line). Figure adapted from reference [14].

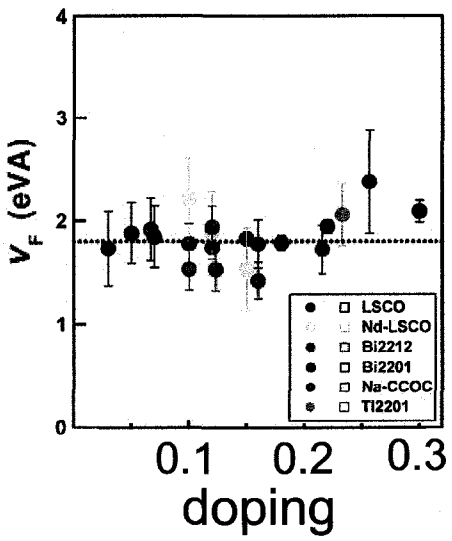

Figure 6.5: The nodal Fermi velocity v_F vs. hole doping, p, for different cuprate systems measured by angle resolved photoemission. Figure adapted from reference [155].

LSCO, where downturns are also observed. By extrapolating from above the downturn the Wiedemann-Franz law is recovered [79] (see fig. 9.5).

Universal thermal conductivity

The T linear electronic contribution to κ is due to transport from d-wave nodal quasiparticles in the universal limit ($T \ll \gamma$, where γ is the impurity band width[3] [107, 111, 14]. In the low T limit, the linear in T conductivity results from a T independent, impurity-induced quasiparticle density of states and a scattering rate that is limited by quasiparticle-impurity scattering. A mean-field calculation of κ_{el} in the universal limit by Durst and Lee [109], given by eq. 3.14, shows that κ_o/T depends only on the velocity anisotropy ratio, v_F/v_2, and *not* on the quasiparticle scattering rate Γ [107, 111, 109]. It has also been shown to be robust to both Fermi liquid and vertex corrections [109].

Experimentally this mean-field theory of thermal conductivity has been validated at optimal doping in YBCO and Bi2212 [14, 16, 15]. In both optimally doped YBCO [14], shown in fig. 6.4, and Bi2212 [16] the thermal conductivity has been shown to be independent of the quasiparticle scattering rate (universal). Additionally, in Bi2212 a direct comparison of v_F/v_2 from thermal conductivity ($v_F/v_2 = 20$) was shown to agree well with measurements from angle-resolved photoemission (ARPES) ($v_F/v_2 = 19$) [15].

Furthermore, with knowledge of v_F (and k_F) from ARPES, thermal conductivity can

[3]Here we assume $T \ll \gamma$. In chapter 7, however, we show this assumption to be warranted.

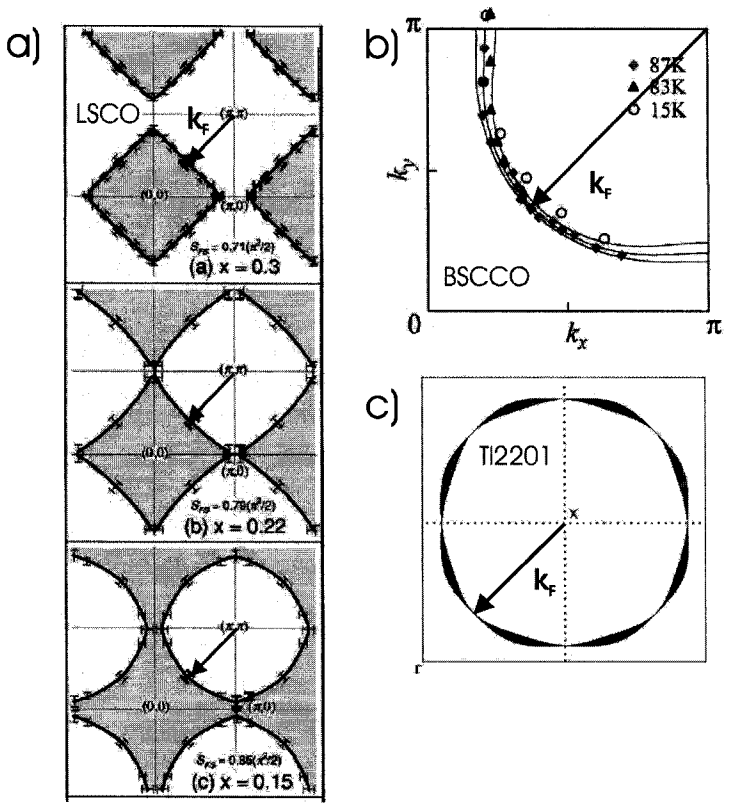

Figure 6.6: a) The Fermi surface in $La_{2-x}Sr_xCuO_4$ from ARPES by Ino et al. [156] for three different dopings $x = 0.15$, 0.22 and 0.30. k_F at along the nodal direction, given by the arrow, is independent of doping and material. b) The Fermi surface in BSCCO from ARPES measurements by Ding et al. [157]. The different symbols are for underdoped samples at different dopings ($T_c = 15$, 83 and 89 K). c) The Fermi surface in overdoped Tl2201 with $T_c \sim 20$ K from angular magneto resistance oscillations (AMRO) by Hussey et al. [158]. Figure adapted from references [156], [157] and [158].

be used to provide a direct measurement of v_2, or the slope of the quasiparticle gap at the nodes. As one dopes away from optimal doping the mean-field nodal quasiparticle theory can be tested by comparing the gap derived from thermal conductivity with more conventional, spectroscopic measurements of the gap. In underdoped YBCO [4] this has been done, with the finding that the gap from thermal conductivity followed the pseudogap as measured by ARPES and tunneling.

Making the assumption that Δ has the $d_{x^2-y^2}$ form $\Delta(\phi) = \Delta_0 \cos(2\phi)$, eq. 3.14 can be rewritten (for $v_F \gg v_2$) as

$$\frac{\kappa_0}{T} = \frac{k_B^2}{3}\frac{n}{c}2k_F\frac{v_F}{\Delta_0}. \tag{6.2}$$

κ_0/T can be related in a straight forward fashion to the gap maximum, Δ_0, by making use

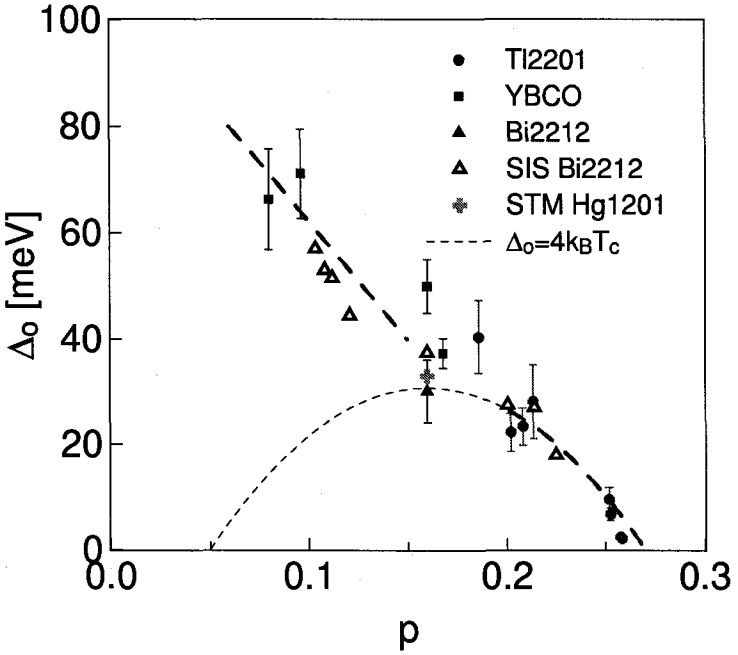

Figure 6.7: The gap maximum, Δ_0, vs. p, from thermal conductivity on Tl2201 (solid circles), YBCO (squares) and Bi2212 (solid triangle). Spectroscopic measurements of Δ_0 from SIS tunneling on Bi2212 (open triangles) and STM on Hg1201 (cross) are also shown. The YBCO and Bi2212 data are taken from ref.'s [4] and [15] respectively, while the SIS tunneling data is taken from ref. [159] and the STM data is from ref. [160]. The thin dashed line gives the BCS doping dependence of the gap based on T_c , $\Delta_0 = \mu k_B T_c$ using a strong coupling value of $\mu = 4$. The thick dashed line is a guide to the eye.

of the fact that at the nodes v_F and k_F are doping independent. ARPES measurements recently showed v_F to be independent of both doping and material, as shown in figure 6.5, and to have a value $v_F = 2.7 \times 10^7 \pm 20\%$ cm/s [155]. k_F is also essentially doping and material independent along the (0,0) - (π, π) direction, yet has significant doping dependence along (0,0) - $(0,\pi)$. As shown in figure 6.6, measurements of the Fermi surface by ARPES in LSCO [156] and BSCCO [157] and angular magneto resistance oscillation (AMRO) measurements [158] in Tl2201, show k_F to have a value $\sim 0.72 - 0.74$ Å along the nodes independent of material or doping.

In figure 6.7 Δ_0 vs. hole doping, p, in Tl2201 is shown along with Δ_0 from thermal conductivity measurements on YBCO [4] and Bi2212 [15]. Δ_0 monotonically decreases with increasing doping and follows the doping dependence of the gap measured by spectroscopic probes such as tunneling [33, 159] and ARPES [32]. In fig. 6.7 we also plot the doping dependence of Δ_0 in Bi2212 measured using SIS tunneling by Miyakawa et. al. [159] and find good quantitative agreement with Δ_0 measured by thermal conductivity.

Given the difference in how the two techniques measure Δ_0, this result has important consequences. It provides compelling evidence for coherent nodal quasiparticle excitations that are correctly described by mean-field d-wave quasiparticle theory, not just at optimal doping but throughout the superconducting region of the phase diagram.

That the gap derived from low energy nodal quasiparticles via thermal conductivity agrees well with the gap derived from higher energy anti-nodal quasiparticles from tunneling or ARPES suggests that the gap structure is not too different from the simple d-wave gap assumed in the analysis of our data. While we cannot strictly rule out an additional, small subdominant order parameter (SDW, is, id) that may result in a fully gapped nodal region [161], we note that the inclusion of one is not necessary to provide a consistent description of the superconducting state.

Additionally, since thermal conductivity is a bulk probe, as opposed to tunneling and ARPES which only probe the surface of a sample, our results argue for bulk superconductivity throughout the phase diagram. This is in contrast to recent arguments for inhomogeneity in overdoped cuprates [162]. The assertion of bulk superconductivity in overdoped Tl2201 is also supported by the $\sim$ 3-fold increase in κ_0/T observed upon driving a sample into the normal state with the application of a magnetic field [7] (see also ch. 7).

Finally, we add that our measurements of Δ_0 in Tl2201 extend to high doping levels that have not been thoroughly explored by tunneling or ARPES. We speculate that the doping dependence of Δ_0 in the overdoped region follows T_c, in line with BCS theory and an approximately doping independent coupling parameter. This would imply that the suppression of T_c in overdoped cuprates is due to a weakening of the pairing interaction. The scaling as $\Delta_0 = 4k_BT_c$ (the dashed line in fig. 6.7) rather than weak coupling result of $\Delta_0 = 2.14k_BT_c$ [163] can perhaps be understood as an indication of strong coupling.

For the heavily overdoped samples with $T_c < 26$ K, however, Δ_0/k_BT_c is lower than the value 4 observed at higher doping, similar to a previously measured sample at higher doping [7]. This may signal the end of the universal regime ($\gamma \ll \Delta_0$), and hence the limits of applicability of our analysis, rather than a change in the intrinsic doping dependence of Δ_0. This interpretation is in line with unitary scattering, where $\gamma \propto \sqrt{\Delta_0\Gamma}$ [108], giving $\gamma/\Delta_0 \propto \sqrt{\Gamma/T_c}$. As T_c is driven to zero, we are by necessity driven into the "dirty" limit: $\gamma/\Delta_0 \sim 1$. In this limit quantitative analysis of κ_0/T is complicated by Abrikosov-Gorkov pair breaking [123, 124, 122], details of the scattering phase-shift and potentially the breakdown of the nodal approximation (ie. variation of Γ and v_F across the Fermi

surface may become relevant). We note, however, that the simplest calculation of the dirty limit [123, 124] (see section 3.4.5) involves a reduction in the gap maximum, and an increase in κ_0/T in line with measurements on the most heavily overdoped samples [7].

In conclusion, we show that the d-wave nodal QP theory provides a consistent description of low temperature thermal conductivity across the entire phase diagram in $T_c^{max} = 90$ K high-temperature superconductors. We find Δ_0 extracted from thermal conductivity agrees well with spectroscopic measurements of the gap.

7

Tl2201: Thermal conductivity in the Vortex state

The application of a magnetic field in the vortex state of a d-wave superconductor has a varied effect on the thermal conductivity. The vortices introduced with an applied field may contribute to quasiparticle scattering, or even phonon scattering, driving the thermal conductivity downwards. In addition, the application of field will result in an increase in the quasiparticle density of states due to the Volovik effect [112, 114] (described in ch 3), driving an increase in the thermal conductivity. Depending on the temperature, the level of disorder and the magnetic field strength, the thermal conductivity may either increase or decrease with application of field.

At sufficiently low temperatures, the thermal conductivity will be largely governed the level of disorder and the field strength, and temperature will not be a relevant energy scale. Here the quasiparticles will be induced by pair-breaking disorder or excited by the magnetic field via the Volovik effect. The application of magnetic fields at low temperatures has the effect of increasing the thermal conductivity as has been observed in the $T \rightarrow 0$ limit at optimal doping in YBCO [9], BSCCO [10] and, as will be discussed in ch. 8, LSCO [1]. In these cases qualitative agreement is achieved with the semi-classical transport theories [114, 117] based upon the Volovik effect.

In this chapter we report measurements of the low temperature thermal conductivity in the vortex state of Tl2201 as a function of doping. At around optimal doping, we find an increase in κ_0/T with increasing field, consistent with previous measurements on YBCO, BSCCO and LSCO and the semi-classical theory of Kübert and Hirschfeld [114]. Moreover, we find that in Tl2201 the H dependence of κ/T at $T = 0$ extends up to ~ 4 K in optimally doped samples.

Finally, using the theory of Kübert and Hirschfeld we perform a quantitative analysis of the field dependence of the thermal conductivity and evaluate the quasiparticle impurity bandwidth, γ, and the normal state quasiparticle scattering rate, Γ, in a similar fashion to Chiao et al. [9]. We find Γ calculated in the Unitary limit to result in

quasiparticle mean-free-paths, l_e of order 10^3 Å, consistent with previous estimations of l_e from normal state charge transport [164].

Before embarking on our presentation of the low temperature measurements we briefly present measurements at intermediate temperatures.

7.1 Thermal conductivity in the vortex state: intermediate temperatures

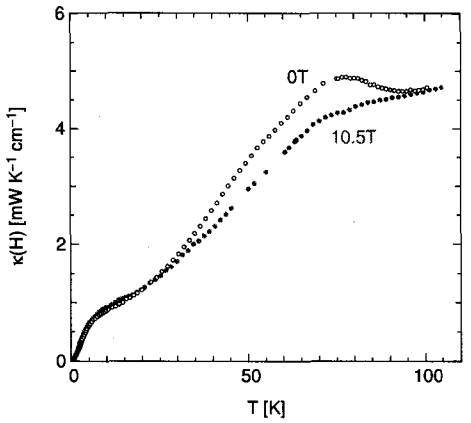

Figure 7.1: $\kappa(H)$ vs. T for Tl2201 ($T_c = 84$ K) up to 110 K in 0T and 10.5T.

In figure 7.1 the thermal conductivity in 0T and 10.5T ($H \perp c$-axis) is shown for Tl2201 with $T_c = 84$ K up to 110 K. The thermal conductivity decreases with increasing field at high temperatures and increases with increasing field at low temperatures, crossing at 20 K. This measurement reproduces earlier work showing the decrease in κ at intermediate temperatures with the application of field [153, 120, 10, 165]. In particular the effect is quantitatively similar to previous measurements on a sample of Tl2201 of approximately the same doping by Yu et al. [153]. The reason for the decrease in κ at these temperatures can be attributed to a number of sources, including scattering of quasiparticles from vortices [115, 103, 116, 119]. Alternately, κ_{el} may decrease at finite T even in the absence of the quasiparticle-vortex scattering due to the energy dependence of the quasiparticle impurity scattering rate, [114]. Finally, although often neglected, it is not clear that phonon-vortex scattering is not also contributing to the decrease in κ at these temperatures.

Typically, the thermal conductivity is difficult to evaluate unambiguously at these temperatures due the difficulty in separating the electronic and phonon contributions

and the difficulty in assigning the T and H dependence of the κ to a number of different possible sources of scattering. At low temperatures, however, κ may reach well defined limiting behavior, where processes that dominate the physics at high temperature no longer contribute.

7.2 Thermal conductivity in the vortex state: low temperatures

In figure 7.2 we show the thermal conductivity at sub-Kelvin temperatures in Tl2201 at several doping levels[1] in 0T and an applied field ($H \perp c$-axis). At low temperatures κ increases with increasing H for all samples. Notably the increase in $\kappa(H)$ with applied field is linear in T. The additional T dependence, that we assigned as the phonon thermal conductivity (see ch. 6 and ch. 9), has no field dependence in the optimally doped samples and only a weak field dependence in heavily overdoped samples (T_c = 27 K and 19 K), as shown in measurements up to 4 K shown in figure 7.3.

This result should be contrasted with recent measurements on ultrapure YBCO [166], shown in fig. 7.4. In high purity YBCO the electronic conductivity, κ_{el}, has a sizeable T^3 contribution in zero field that is suppressed with the application of 0.8 T. This term is understood to be the leading order temperature correction to the universal limit (see eq. 3.16) as calculated by Graf et al. [111]. This correction term is shown to be proportional to $1/\gamma$ and as such will make the largest contribution to κ when γ is small, as it is in very pure YBCO. The rapid suppression of this T^3 contribution to κ_{el} is interpreted as an increase in the quasiparticle scattering rate due to quasiparticle vortex scattering.

The noted absence of this leading order correction term in Tl2201 implies a significantly larger γ consistent with the greater degree of disorder in Tl2201 than YBCO. This observation is consistent with the observation of a smaller peak height in κ(0T) below T_c in Tl2201 (fig. 6.1). Essentially this result shows us that in Tl2201, below ~4 K we enter a regime where κ is governed by the level of disorder and the field strength, and temperature is not be a relevant energy scale. In the following we are able to evaluate γ using a semiclassical theory of the field dependence and, assuming unitary scattering, we are able to estimate the magnitude of the T^3 correction in Tl2201. We find that in

[1]There is some ambiguity about the geometric factor of the sample with T_c = 89 K (fig. 7.2a). As such, the magnitude of κ may vary by a factor of two. This will not, however, effect measurements of $\kappa(H)/\kappa$(0T) or our determination of γ, discussed below.

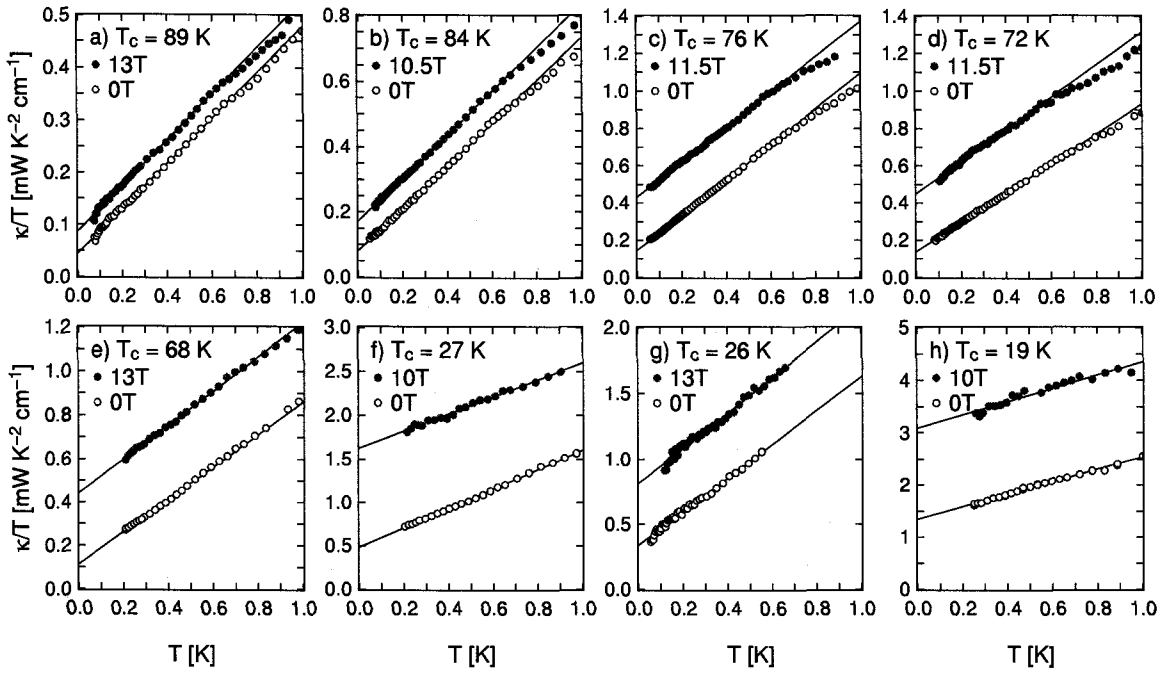

Figure 7.2: $\kappa(H)/T$ vs. T up to 1K for Tl2201 with a) $T_c = 89$ K, b) $T_c = 84$ K, c) $T_c = 76$ K, d) $T_c = 72$ K, e) $T_c = 68$ K, f) $T_c = 27$ K, g) $T_c = 26$ K and h) $T_c = 19$ K. Low temperature downturns (see ch. 6 in the data for the samples with $T_c = 68$ K, 27 K and 19 K have been cut-off for clarity.

Tl2201 it is indeed negligible.

7.2.1 Optimal Doping: the Volovik effect

At optimal doping we have measured the thermal conductivity at several fields and are able to make a more detailed comparison to theoretical models of the thermal conductivity in the vortex state. In figure 7.5 a) we show the $\kappa_0(H)/T$ vs. H for the optimally doped ($T_c = 89$ K) sample fitted to the semi-classical theory of Kübert and Hirschfeld [114] (eq. 3.19). The model includes the semi-classical Volovik effect and the energy dependence of the quasiparticle scattering rate, but neglects any quasiparticle-vortex scattering. The model provides a reasonable fit to the data giving the fitting parameter $\rho\sqrt{H} = 3.3\mathrm{T}^{1/2}$. In the dirty limit ($\gamma > E_H$) the fitting parameter ρ in eq. 3.19 can be conveniently expressed (see eq. 3.21)in terms of the ratio of two energy scales, the impurity bandwidth, γ, and the average energy shift experienced by a quasiparticle due to the Volovik effect, E_H: $\rho = \sqrt{6/\pi}\gamma/E_H$. The latter energy scale, E_H, is given by $E_H = a\hbar\sqrt{2/\pi}v_F\sqrt{H/\Phi}$, which when evaluated using $v_F = 2.7 \times 10^7$ cm/s and $a = 1/2$ (square vortex lattice), is equal to $1.56\sqrt{H}$ (meV $\mathrm{T}^{1/2}$), or in units of temperature,

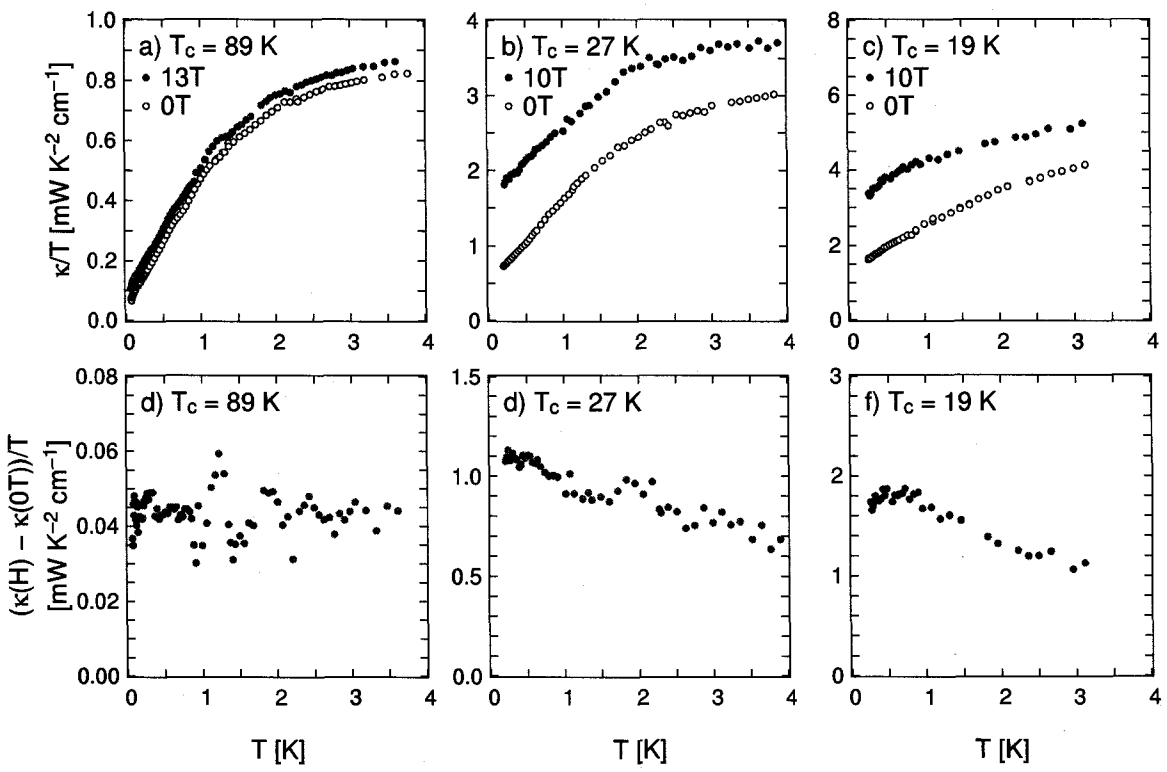

Figure 7.3: $\kappa(H)/T$ vs. T up to 4K for Tl2201 with a) $T_c = 89$ K, b) $T_c = 27$ K and c) $T_c = 19$ K.

$16.7\sqrt{H}$ (K/T$^{1/2}$). Thus, for the $T_c = 89$ K sample $\rho\sqrt{H} = 3.36\text{T}^{1/2}$ results in $\gamma = 3.79$ meV (44 K).

As a consistency check we can check to see if we are in the "dirty" limit, $\gamma > E_H$. For $H = 13$T, $E_H = 5.6$ meV (65 K) which is just greater than our value of γ. However, as we would like to avoid the need for a numeric calculation, as would be required to treat the crossover from the "dirty" to "clean" limits, we will satisfy ourselves that our fitted value of γ using the "dirty" limit expression for ρ, while approximate, is close to the correct value. Fitting to lower H gives a slightly smaller value of γ.

From our value of γ we can also calculate the normal state scattering rate by assuming strong (unitary) scattering. In the unitary limit γ is simply related to Γ by $\gamma \simeq 0.63\sqrt{\hbar\Gamma\Delta_0}$ [108]. Using $\Delta_0 = 73.6$ meV[2] from the 0T thermal conductivity (see ch. 6) $\hbar\Gamma = 0.493(5.7\text{K})$. The quasiparticle mean-free-path derived from this value of Γ is $l = v_F/\Gamma = 3600$ Å. Notably, this estimate agrees reasonably well with estimates

[2]This value of γ is based on $\kappa_0(0\text{T})/T = 0.45$ mW K^{-2} cm^{-1}. As noted above and in chapter 5, however, this value, and hence Δ_0, may vary by a factor of 2 due to error in the thickness of the sample.

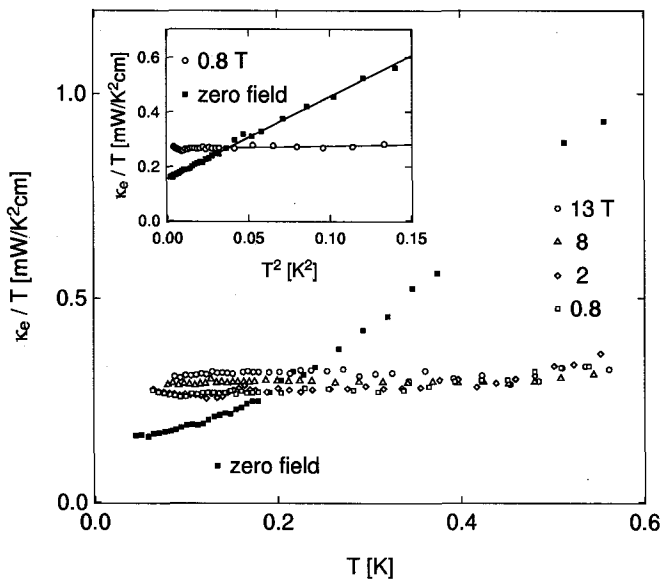

Figure 7.4: Electronic thermal conductivity in ultrapure YBCO from reference [166], plotted as κ_{el}/T vs. T for magnetic fields from zero to 13 T. The electronic contribution is extracted as discussed in reference [166]. Inset: The low field curves plotted against T^2.

of the quasiparticle mean-free-path in overdoped Tl2201 from low-temperature, normal state resistivity measurements, where l is estimated to be of the order of 10^3 Å [164]. Thus, it would appear that at least at optimal doping the semi-classical description of thermal transport in the vortex state provides a consistent picture, with scattering in the unitary limit. Furthermore, the large value of $\gamma = 3.79$ meV gives us confidence that the analysis of the previous chapter is appropriate. In the previous chapter we correctly assumed that at sub-Kelvin temperatures the thermal conductivity may be analyzed in the "universal" limit, ($T \ll \gamma$) and thus κ_{el} has a simple T linear temperature dependence (Note the condition $\gamma \ll \Delta$ is also satisfied at optimal doping.). Furthermore, if we go on to evaluate the leading order temperature correction to κ in the universal limit, the term that features so prominently in ultrapure YBCO, we find that this correction term is negligible with $\gamma = 3.79$ meV. From eq. 3.16, in the unitary limit and with $\gamma = 3.79$ meV, $\kappa/T = \kappa_0/T(1 + 0.0007T^2)$. At 4 K this correction term is negligible, consistent with our observation that $\kappa(H)/T - \kappa(0\mathrm{T})/T$ is T independent up to 4 K.

Despite this seemingly excellent agreement between experiment and theory we remark that in at least one measurement a value of $\gamma = 3.79$ meV appears too large. In penetration depth measurements, the penetration depth crosses over from having a T linear temperature dependence in the "clean" limit to T^2 dependence in the "dirty" limit at

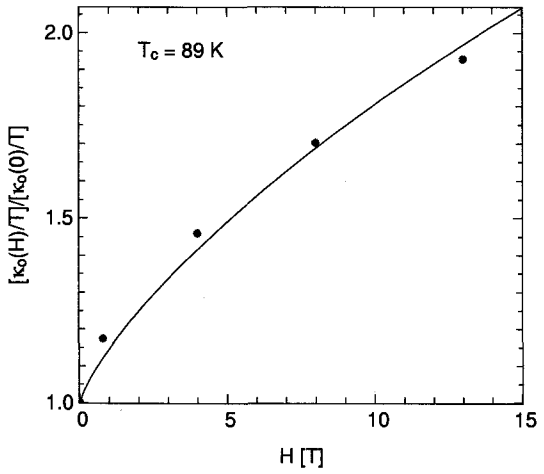

Figure 7.5: $\kappa_0(H)/\kappa_0(0)$ vs. H for optimally doped Tl2201 (T_c = 89 K). The solid line is a fit to eq. 3.21 yielding $\rho\sqrt{H} = 3.36T^{1/2}$.

a temperature $T^* \simeq 6\ln(2)\gamma/\pi$ [108]. Thus, for γ = 3.79 meV (44 K), T^* = 53 K and one would expect to observe $\lambda - \lambda_0 \propto T^2$ at low temperatures. In contrast, however, ρ_s has been measured in nearly optimally doped samples to have a T linear temperature dependence down to 5 K [149].

7.2.2 The Volovik effect vs. doping

We would like to evaluate γ and subsequently Γ for all of our samples. Unfortunately, extensive data at several fields is not available for all samples. However, given that eq. 3.19 is fit by only a single parameter, we can uniquely fit for $\rho\sqrt{H}$ with only two data points, and calculate γ as we have above for optimal doping. This will clearly be an approximation, particularly in the heavily overdoped samples where $H \sim H_{c2}$. As H approaches H_{c2}, the analytic equation (eq. 3.19) no longer applies. Additionally the bound states of the vortex cores must begin to contribute substantially to heat conduction. For instance, in measurements on heavily overdoped Tl2201 (T_c = 18 K) by Proust et al. [7], $H_{c2} \simeq$ 13 T. In this case, E. Boaknin [127] found that eq. 3.19 only fit the data reasonably to $H <$ 2T, yielding $\rho\sqrt{H}$ = 1.0 (γ = 1.13). Note that at higher H, $\kappa(H)/T$ is less than the naive extrapolation of eq. 3.19 from low H. Thus, fitting eq. 3.19 to high H will overestimate $\rho\sqrt{H}$ and the resulting value for γ, which we call γ^* and give in table 7.1, serves as an upper limit on γ.

We find from this analysis that γ^* varies from 1.7 to 3.8 meV. The largest value of γ is found for the optimally doped (T_c =89 K) sample. In the unitary scattering picture

Table 7.1: Upper limit of the impurity bandwidth, γ^*, from $\kappa(H)$ in Tl2201.

T_c (K)	p	κ_0/T (mW K^{-2} cm^{-1})	$\rho\sqrt{H}$ (T$^{1/2}$)	γ (meV)	Δ (meV)	$\hbar\Gamma$ (meV)
89	0.16	0.045	3.36	3.79	74	0.49
84 [a]	0.186	0.080 ± 17 %	2.70	3.05	40	0.58
76	0.202	0.145 ± 16 %	1.86	2.09	22	0.50
72 [b]	0.208	0.139 ± 15 %	1.67	1.89	23	0.38
68	0.213	0.115 ± 25 %	1.48	1.67	28	0.25
27	0.253	0.340 ± 24 %	2.30	2.90	9.5	2.2
26 [a]	0.252	0.48 ± 17 %	1.50	1.69	6.69	1.08
19 [b]	0.258	1.35 ± 15 %	2.38	2.69	2.4	7.6

[a]The same sample was measured both after annealing to $T_c = 84$ K and reannealing to $T_c = 26$ K.
[b]The same sample was measured both after annealing to $T_c = 19$ K and reannealing to $T_c = 72$ K.

this follows from the optimally doped sample having the highest gap, Δ, assuming the normal state scattering rate is comparable in all samples. Γ is shown to vary between 0.25 and 0.75 meV (neglecting the $T_c < 27$ K samples), which translates to a factor of 3 variation in the level of disorder. Given the different histories of our various samples, this factor of 3 variation does not seem unreasonable. Finally, we note that for our most heavily overdoped sample ($T_c = 19$ K) $\gamma^* > \Delta_0$[3]. It is apparent that the samples are sufficiently disordered that the universal limit calculations may no longer apply, as noted in ch. 6.

7.2.3 Comparison to other cuprates

The magnitude of the Volovik effect is in Tl2201 is of comparable magnitude to that observed in previous measurements on other cuprate materials. In fig. 7.6 we plot $\kappa(H)/\kappa(0\text{T})$ vs. H for optimally doped samples of YBCO, BSCCO and LSCO, along with our measurements of optimally doped Tl2201. The data presented here is for YBCO

[3]Even using the more accurate value of $\gamma = 1.13$ taken from the low field data on the $T_c = 18$ K by Boaknin, $\gamma \sim 0.5\Delta_0$.

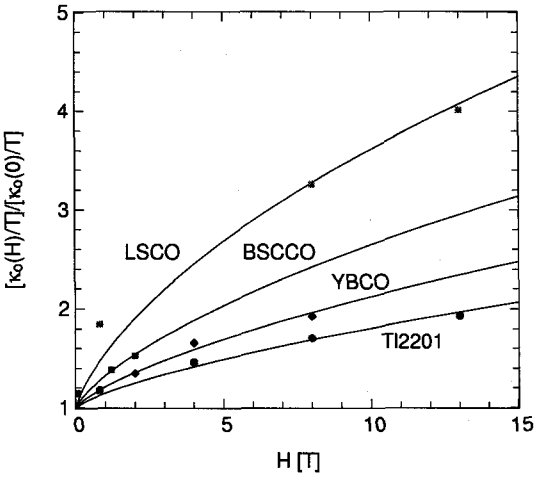

Figure 7.6: $\kappa_0(H)/\kappa_0(0)$ vs. H at optimal doping for representative samples of the four cuprate materials, Tl2201 (red), YBCO (black) from ref [9], BSCCO (blue) from ref [10], and LSCO x =0.17 (magenta). The solid lines are fits to eq. 3.21.

crystals is taken from reference [9] and for the BSCCO sample[4] from reference [10]. The LSCO x=0.17 data is discussed in further detail in ch. 8.

In all samples there is a qualitative agreement with the semi-classical theory. A comparison of the magnitude of the growth in κ gives us the relation between γ in typical samples of the various cuprates, the values of which are listed in table 7.2. As first noted by Chiao et al. [9] in a comparison of the field dependence in BSCCO and YBCO, there is a discrepancy between the value of γ extracted from the field dependence and what is otherwise known about the relative disorder levels of the various cuprate families. Assuming all else being equal (v_F, Δ_0, scattering phase shift), γ should be a function of the disorder level in the material.

It is a matter of fact that YBCO is the least disordered of the cuprates[5]. One demonstration of this fact is the height of the peak in κ below T_c, shown for YBCO and Tl2201[6] in fig. 6.1, is much larger in YBCO than in the other cuprate materials. In BSCCO the

[4]Aubin does not extrapolate to $T = 0$. Our own extrapolation of the published data using eq. 6.1 gives values of 0.42, 0.48, 0.58 and 0.64 mW K^{-2} cm^{-1} for 0T, 0.06 T, 1.2 T and 2 T, respectively. Note that 0.42 mW K^{-2} cm^{-1} is an anomalously large value of κ_0/T for optimally doped BSCCO indicating that this sample may in fact be an overdoped. Other measurements of optimally doped BSCCO give $\kappa_0/T \simeq 0.15$ mW K^{-2} cm^{-1} [15, 16].

[5]The YBCO sample presented in fig. 7.6 was grown in a YSZ stabilized crucible. While this is not the state of the art in terms of sample purity, samples grown in this fashion are considered to have a low level of disorder in relation to the other cuprate families.

[6]Although we have not measured the thermal conductivity at high temperature in the $T_c = 89$ K Tl2201 sample, the $T_c = 84$ K sample likely has a similar peak height.

Table 7.2: Impurity bandwidth, γ, from $\kappa(H)$ for optimally doped cuprates.

	$\rho\sqrt{H}$ ($T^{1/2}$)	γ (meV)
Tl2201 (T_c = 89 K)	3.36	3.79
YBCO	2.61	2.71
BSCCO	1.98	2.05
LSCO x=0.17	1.38	1.43

peak in κ below T_c [165] is slightly larger than that of the Tl2201, but still much less than YBCO. Yet, YBCO, with clearly the largest peak height has a comparatively large value of γ, as derived from the H dependence of κ. Also, it is interesting that LSCO has the smallest value of γ, perhaps a reflection of a smaller T_c and Δ, but still somewhat surprising given the level of disorder created in LSCO due to the cation substitution of Sr for La. Despite these seeming inconsistencies, we note that some consistency is observed between BSCCO and Tl2201. BSCCO has a larger value of γ than Tl2201, consistent with a peak height that is larger than the Tl2201 sample with T_c = 84 K.

Unfortunately, a more detailed quantitative analysis is not possible since high T and low T measurements have not been performed systematically using the same samples. This limits the conclusions we can draw from the comparison of the various cuprates. However, it remains plausible that the semi-classical theory can provide a consistent quantitative description of Tl2201 and BSCCO, despite the apparent inconsistency with YBCO.

Summary

- At $T = 0$ κ/T increases with H consistent with the Volovik effect. This behavior is qualitatively consistent with the field dependence expected for a d-wave superconductor.
- Up to $T = 4K$ temperature is not an important energy scale for thermal conductivity (ie $\gamma, E_H > 4K$).
- At high T a crossover to decreasing κ/T occurs reflecting the increasing importance of quasiparticle vortex scattering at higher temperatures.
- Good qualitative agreement between semi-classical theory of transport in the vortex state and the measured magnitude of the field dependence. YBCO stands out as

quantitatively inconsistent with the other cuprates.

8

Low T Thermal Conductivity in LSCO

In the two previous chapters we presented the case for generic agreement between the thermal conductivity in YBCO, Bi2212 and Tl2201 and mean-field theories of d-wave nodal quasiparticles in the superconducting and mixed states. In 0T we showed the quasiparticle gap, Δ_0, from thermal conductivity to agree with the gap measured in ARPES and tunneling. In the mixed state we found the thermal conductivity to increase with applied field in agreement with semi-classical theories based on the Volovik effect.

In this chapter we present low temperature thermal conductivity measurements on LSCO. In the superconducting state of underdoped LSCO at 0T we find that a finite electronic contribution to the thermal conductivity, κ_0/T, is observed but that unlike YBCO, BSCCO and Tl2201 its magnitude is too small to be accounted for solely by the mean-field theory of d-wave nodal quasiparticles. Moreover, with increasing doping, κ_0/T onsets abruptly at the non-superconductor-to-superconductor transition, tying the onset of delocalized quasiparticles to the onset of superconductivity.

The observation of a linear term at all dopings in underdoped LSCO is interesting when one considers that in underdoped LSCO resistivity measurements have revealed the field-induced normal state to be a charge insulator [80] (as discussed in chapter 2). Given that in all superconductors investigated to date (including cuprates) heat transport at $T \rightarrow 0$ is always seen to increase as one goes from the superconducting state to the field-induced normal state, these two observations point to a violation of the Wiedemann-Franz law in underdoped cuprates. Note that this universal law is violated in the electron-doped cuprate $Pr_{2-x}Ce_xCuO_{4+\delta}$ (PCCO) at optimal doping [167], in that low-temperature heat conduction was found to exceed the expected charge conduction by a factor of approximately two. However, the law is recovered in the strongly overdoped regime [7].

In this chapter we show that the natural assumption that heat conduction will increase upon going from the superconducting state to the field-induced normal state to

be incorrect in underdoped LSCO. Indeed, in the $T \rightarrow 0$ limit the thermal conductivity *decreases* in the vortex state and the residual linear term drops to a value below our resolution limit in the field-induced normal state. This argues for a thermally insulating normal state and reveals a novel thermal metal-to-insulator transition. Unfortunately, as transport in both charge and heat channels (in the normal state) show insulating behavior, it is not possible to make a strict test of the Wiedemann-Franz law.

This measurement of a field-induced thermal metal-to-insulator transition in underdoped LSCO is contrasted with the recent measurements of the normal state of heavily underdoped YBCO by Mike Sutherland [6]. A new generation of YBCO samples has been developed at the University of British Columbia that allow the low T_c underdoped region that has been heavily studied in LSCO to also be studied in YBCO. One of the results of this study is that the insulating behavior observed in LSCO is not observed in comparably doped YBCO. This indicates that the insulating behavior in LSCO is not generic, but representative of additional physics. We contrast the results on these two materials and speculate on the origin of the two main results in LSCO, namely the suppressed linear terms in the superconducting state (0T) and the field induced metal-to-insulator transition in LSCO.

These findings shed new light on the nature of the intriguing state of underdoped cuprates above H_{c2}, for which several proposals have been put forward recently, including stripe order [24], d-density wave order [19] and a Wigner crystal of d-wave hole pairs [168]. A compelling explanation is found when we consider competing superconducting and spin-density wave order (stripes) [54, 169, 51]. There is now clear evidence from neutron scattering measurements of a static spin density wave order (stripes) in LSCO. The static stripe order in LSCO exists both in the superconducting state up to $x \sim 0.14$ [59] and increases in intensity with increasing field [64, 53, 65, 68]. As such, a clear correlation exists between the intensity of the SDW order and the doping and field dependence of the thermal conductivity, κ_0/T. The absence of similar behavior in YBCO is attributed to the lack of clear evidence for static stripes in YBCO [69].

8.1 LSCO 0T

8.1.1 Fitting the low temperature thermal conductivity

The thermal conductivity measured at sub-Kelvin temperatures in LSCO is shown in fig. 8.1 at various Sr concentrations (hole doping) from the undoped, Mott insulator at

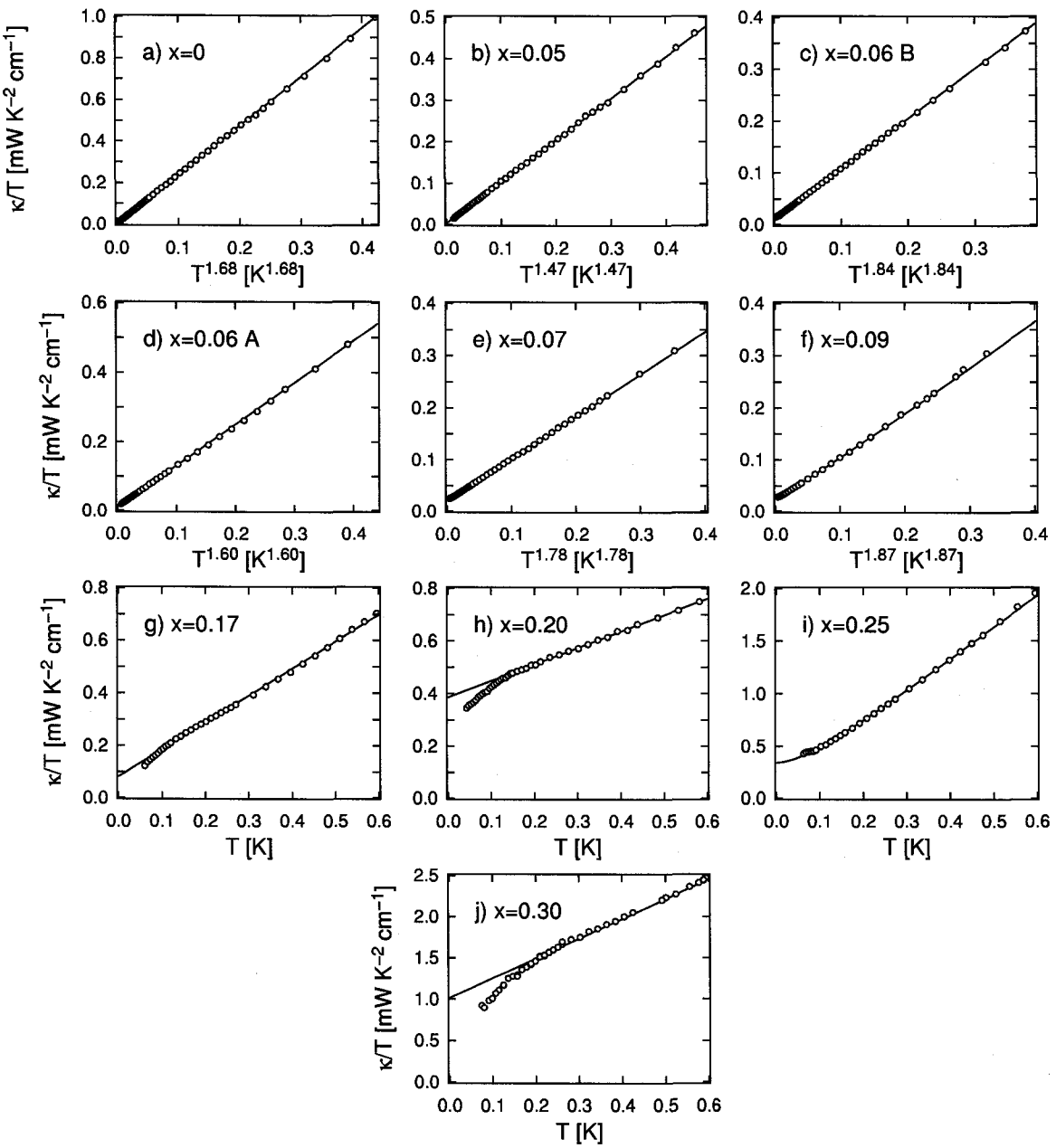

Figure 8.1: The thermal conductivity in zero field as a function of temperature for LSCO at various dopings from a) undoped $x = 0$ to j) heavily overdoped, non-superconducting $x = 0.30$. The data is plotted as κ/T vs. T^{α} up to a temperature of 600 mK. The lines are fits to the data as described in the text. The intercept provides a measure of the electronic contribution to the thermal conductivity, κ_0/T.

$x = 0$ to the non-superconducting, metal at $x = 0.30$. As we have done with Tl2201 in ch. 6, we will extract the electronic and phonon contributions to κ by extrapolating the data down to $T = 0$. Unlike Tl2201, however, in LSCO we have an added complexity in that the form of the phonon thermal conductivity evolves as a function of doping from having a power law T^{α} temperature dependence in underdoped samples to having a T^2 temperature dependence in overdoped samples, much like that observed in Tl2201. In this chapter we focus on the electronic contribution to κ, leaving the discussion of the phonon thermal conductivity, which is interesting in it's own right, to chapter 9.

For the overdoped samples ($x = 0.17$, 0.20, 0.25 and 0.30) the thermal conductivity is fit to the same expression used for Tl2201 (eq. 6.1): $\kappa/T = \kappa_0/T + AT$, a T linear electronic contribution plus a T^2 phonon contribution that we attribute of phonon-electron scattering (see ch. 9)[1]. The fitting parameters resulting from these fits are given in table 8.1. In addition, in the $x = 0.17$, 0.20 and 0.30 samples a noted downturn in the data is observed at 0.16 - 0.2 K, that is notably not present in the x=0.25 samples or in any of the underdoped samples. Like the downturns observed in some samples of Tl2201 (see ch. 6), we attribute these downturns to a decoupling of the electronic and phonon channels of heat conduction and in all cases extrapolated the data from above the downturn[2] to determine κ_0/T.

In contrast to the overdoped samples, in the underdoped samples ($0 < x < 0.09$) the phonon thermal conductivity has a higher power of temperature. The data is fit very well to the empirical form

$$\frac{\kappa}{T} = \frac{\kappa_0}{T} + BT^{\alpha}, \tag{8.1}$$

with co-efficient, B, and power law α given in table 8.1. We emphasize that eq. 8.1 provides an excellent fit to the data for the underdoped samples. The quality of the fit is seen most easily by the striking linearity of the data when plotted as κ/T vs. $T^{\alpha-1}$, as we have up to 600 mK for the underdoped samples in fig. 8.1. In these plots the y-axis intercept provides the electronic contribution κ_0/T and the slope is the phonon thermal conductivity. As discussed in section 3.1.2, this form for the phonon thermal conductivity

[1]In the x=0.25 sample we have added in a term in the phonon scattering rate that accounts for the small upturn in the data at low temperatures and fit the data to $\kappa/T = \kappa_0/T + 1/(1/(AT) + 1/(BT^2))$. This additional term ($BT^2$) accounts for the possibility that phonons reach the boundary scattering limit at very low temperatures in this sample.

[2]Unfortunately, the need to extrapolate from above the downturn ($\sim$ 160 mK), adds additional error to the determination of κ_0/T. This is particularly problematic for the x =0.17 sample. In this sample our extrapolation procedure provides what is a low end estimate of κ_0/T, the actual value may be up to 50% higher.

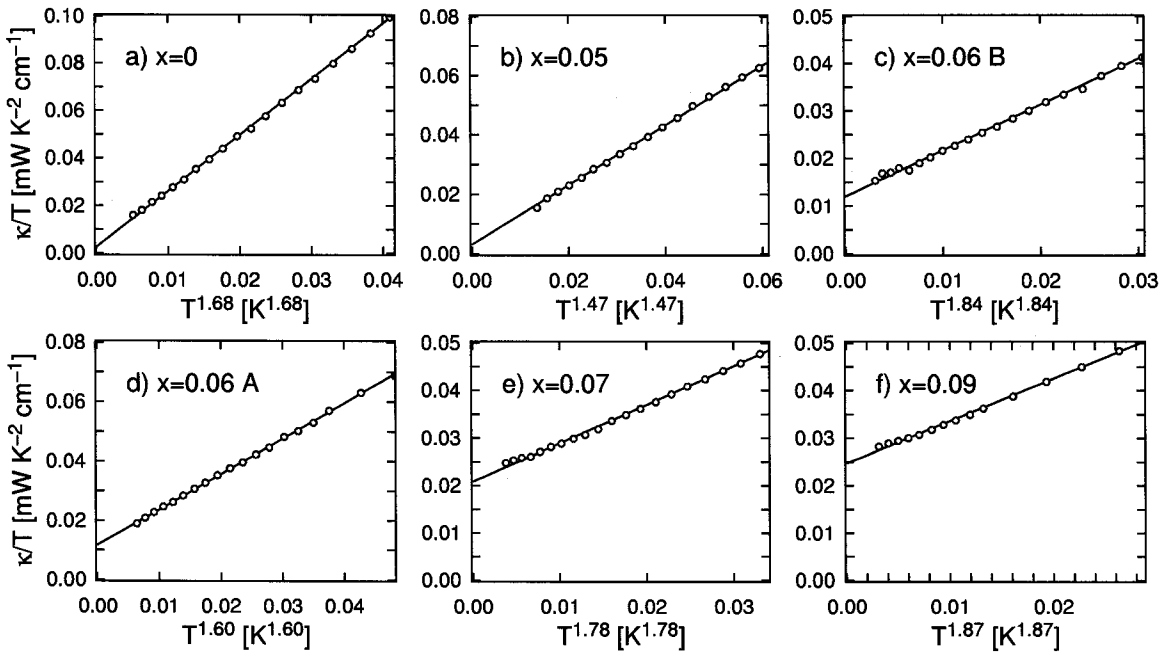

Figure 8.2: A zoom on the low temperature thermal conductivity in zero field in underdoped LSCO with Sr doping x from a) 0 to f) 0.09. The data is plotted as κ/T vs. T^{α} up to a temperature of 150 mK. The lines are fits to the data as described in the text. The intercept provides a measure of the electronic contribution to the thermal conductivity, κ_0/T.

is consistent with phonons that are scattered specularly (rather than diffusely) from the boundaries of the sample, as observed in many well-known insulators [91, 87, 90, 92, 93]. In fig. 8.2 we plot a blow up of κ_0/T vs. $T^{\alpha-1}$ below 150 mK on the underdoped samples to clearly show the extrapolated values of κ_0/T.

8.1.2 The doping dependence of κ_0/T in LSCO

Having described our analysis of the data, several observations can be made. First, we note that a finite residual linear term in $\kappa(T)$ is resolved for $x \geq 0.06$, co-incident with the non-superconductor to superconductor transition. Like YBCO, Bi2212 and Tl2201 the d-wave superconducting state is a thermal metal (has a finite linear in T electronic term) at all dopings but outside the superconducting region, *i.e.* below $x = 0.055$, the residual linear term becomes extremely small. The power-law fitting procedure described above to extrapolate to $T = 0$ yields a value of $\kappa_0/T = 3$ μW K^{-2} cm^{-1} for both the $x = 0$ and $x = 0.05$ samples. Now, even though the power-law fit does provide a good description of the data (see Figs. 8.1 and 8.2), all the way up to 0.4 K, the fact that κ_0/T is 5 times smaller than the value of κ/T at the lowest data point (40 mK) means that one

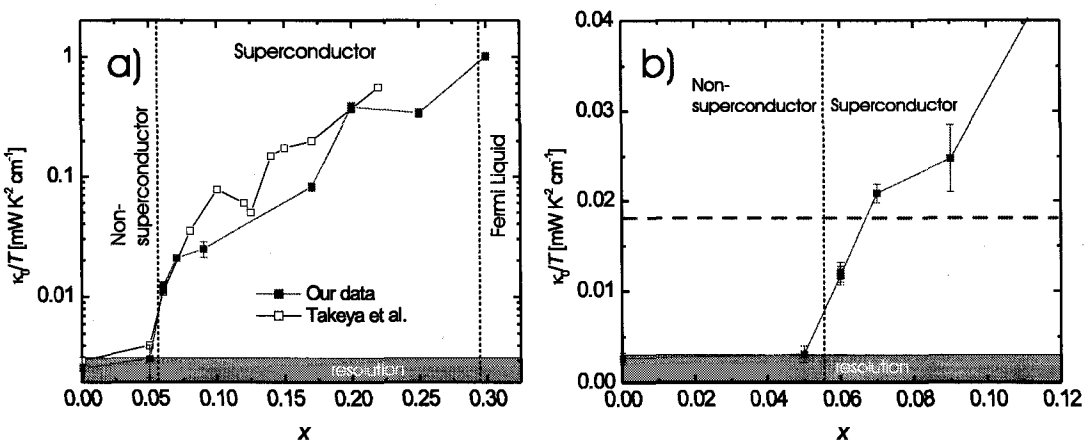

Figure 8.3: a) κ_0/T vs. x for LSCO on a semi-log plot from $x = 0$ to $x = 0.30$. The shaded region indicates the estimated resolution limit of our experiment (see text). Also shown is similar data from the Ando group [5]. b) A blowup of κ_0/T vs. x at low dopings. The red dashed line is the minimum value of κ_0/T allowed by the mean-field nodal quasiparticle formalism (eq. 3.14). Note the onset of κ_0/T with doping coincides with the insulator-superconductor transition at $x \simeq 0.05$.

has to view the extrapolated value with caution. The conservative position is to assume that the parent compound $x = 0$ is a heat insulator as well as a charge insulator, and regard this minute linear term of 3 μW K^{-2} cm^{-1} as the resolution limit of our technique[3] (when applied to this series of samples), and treat the $x = 0$ data as our reference (for an insulating state in LSCO crystals). We emphasize that the $x = 0.05$ sample is no more conductive than the parent compound (see Fig. 8.3), and hence is also taken to be a thermal insulator. By contrast, the linear term in the $x = 0.06$ sample (at zero field), of magnitude 12 μW K^{-2} cm^{-1}, is clearly above the reference limit (by a factor 4) and is thus unambiguously a thermal metal.

The coincidence of rise in κ_0/T and the non-superconductor to superconductor transition is also observed in measurements of the low-temperature thermal conductivity in LSCO by the Ando group [5] which is shown along with our data in fig. 8.3a. Their results are, overall, very consistent with our measurements, with the exception of our x

[3]In fitting the data using eq. 8.1 an extraneous contribution to κ_0/T will occur whenever the actual phonon thermal conductivity deviates from our model of BT^{α}. This is the likely origin of the minute linear terms in the x=0 and 0.05 samples. Note that an error of this sort provides an offset to κ_0/T but does not impair our ability to resolve field-induced changes in κ/T. The statistical error in the fit of κ_0/T is smaller than 3 μ W K^{-2} cm^{-1} and given as the error bars in figures 8.3, 8.5 and 8.7.

Table 8.1: The electronic contribution to the thermal conductivity, κ_0/T, and fitting parameters for the phonon thermal conductivity, α, B and A for LSCO in 0T.

Sr x	T_c [K]	κ_0/T $[\frac{\text{mW}}{\text{K}^2\text{cm}}]$	A^{a} $[\frac{\text{mW}}{\text{K}^3\text{cm}}]$	α^{b}	B^{b} $[\frac{\text{mW}}{\text{K}^{\alpha+1}\text{cm}}]$
0	-	0.0026 ± 24%	-	2.68 ± 0.01	2.36 ± 7%
0.05	-	0.0031 ± 30%	-	2.47 ± 0.02	1.00 ± 8%
0.06 A	5	0.0117 ± 8.6%	-	2.60 ± 0.02	1.20 ± 8%
0.06 B	8.5	0.0121 ± 9.1%	-	2.84 ± 0.01	0.963 ± 9%
0.07	19.3	0.0208 ± 5.0%	-	2.78 ± 0.01	0.810 ± 5%
0.09	15	0.0248 ± 15%	-	2.87 ± 0.01	0.890 ± 15%
0.17	34.5	0.082 ± 7.7%	1.03 ± 6.5%	-	-
0.20	33.5	0.386 ± 8.2%	0.626 ± 8.3%	-	-
0.25[c]	13.0	0.341 ± 7.6%	3.14 ± 7.1%	-	-
0.30	-	1.01 ± 7.1%	2.40 ± 7.1%	-	-

[a]From equation 6.1.
[b]From equation 8.1.
[c]This sample was also fit to an additional boundary-scattering term yielding $B = 28.9 \pm 3.5$ mW K^{-4} cm^{-1} (see text).

= 0.09 and 0.17 data[4].

Second, although there is a clear finite linear term in the superconducting state of underdoped LSCO, like YBCO, Bi2212 and Tl2201, the smallness of linear term is inconsistent the mean-field theory of Durst and Lee [109]. Indeed, for $x = 0.06$, $\kappa_0/T \simeq 12$ μW K^{-2} cm^{-1}, which is below the minimum value for LSCO from Eq. 3.14 is $\frac{k_B^2}{3\hbar}\frac{n}{c}(1+1) = 18.3$ μW K^{-2} cm^{-1}, shown as dashed line in figure 8.3b. In underdoped LSCO κ_0/T is finite, although it's magnitude is suppressed from the prediction for a mean-field d-wave superconductor. It is also particularly interesting to note that in Takeya's data (shown in fig. 8.3a) they observe a dip in κ_0/T observed at a doping of $x = 0.125$ (1/8), corresponding to the doping where T_c is suppressed and spin-density wave order in enhanced in the $La_{2-x}Re_xCuO_4$ family of materials. As we will discuss in

[4]This discrepancy may be due to a number of factors. First, a difference in the procedure to fit the data (they fit to $\kappa/T = \kappa_0/T + CT^3$) results in systematically higher values of κ_0/T than the power law fitting procedure described above. Second, it may reflect a slight difference in the doping of our samples. As noted in ch. 5, our samples of $x = 0.09$ and x=0.17 have transition temperatures that are lower than typical samples with these dopings.

Table 8.2: v_F/v_2 and Δ_0 for overdoped LSCO.

Sr x	T_c [K]	v_F/v_2 .	Δ_0 [meV]	$4k_BT_c$ [meV]
0.17	34.5	8.9 ± 7.7 %	70 ± 5	11.9
0.20	33.5	42 ± 8.2 %	14.8 ± 1.2	11.6
0.25	13.0	37.2 ± 7.6%	16.7 ± 1.3	4.5

section 8.4, this leads us to believe that the suppressed values of κ_0/T in LSCO is due to a competition between spin-density wave order and superconductivity.

At higher doping, κ_0/T exceeds the limit imposed by the d-wave mean field formalism and we can attempt to determine whether the mean-field d-wave theory describes the data at these dopings by extracting a value of Δ_0, as was done in ch. 6 in Tl2201. Using eq. 3.14 and the same values of v_F and k_F used for Tl2201 gives the values of Δ_0 for our overdoped samples shown in table 8.2. Also given in table 8.2 is the gap calculated from T_c assuming that the relation $\Delta_0 = 4k_BT_c$ applies to LSCO as it does reasonably well to Tl2201 (see ch. 6). For the x=0.17 and x=0.25 samples the disagreement between the estimates is substantial. At least for the $x = 0.25$ sample, this may simply be a reflection of the sample being heavily disordered, in which case the universal limit need not apply. This is evident when we consider the residual resistivity of this sample (see fig. 5.6. The extrapolated value of the resistivity in our sample of LSCO with $x = 0.25$ is $\simeq 50$ $\mu\Omega$ cm, almost an order of magnitude higher than the residual resistivity found in heavily overdoped Tl2201 ($\rho_0 = 6\mu\Omega$ cm) [164, 7] where it has been noted that the universal limit likely does not apply due to high disorder [7] (see also ch.'s 6 and 7). The large disorder is also reflected in a very small increase in κ with applied field in this sample, as shown in the following section.

Unlike the $x = 0.25$ sample, for the x =0.20 sample the gap extracted from thermal conductivity and the estimation from T_c differ by only a factor of 1.5 (note ρ_0 from fig. 5.6 is much smaller for this sample than the $x = 0.25$ sample). While this does not constitute excellent agreement between theory and experiment it may suggest that in LSCO over a narrow range of doping about $x = 0.20$, the d-wave mean-field theory provides an adequate description of the data.

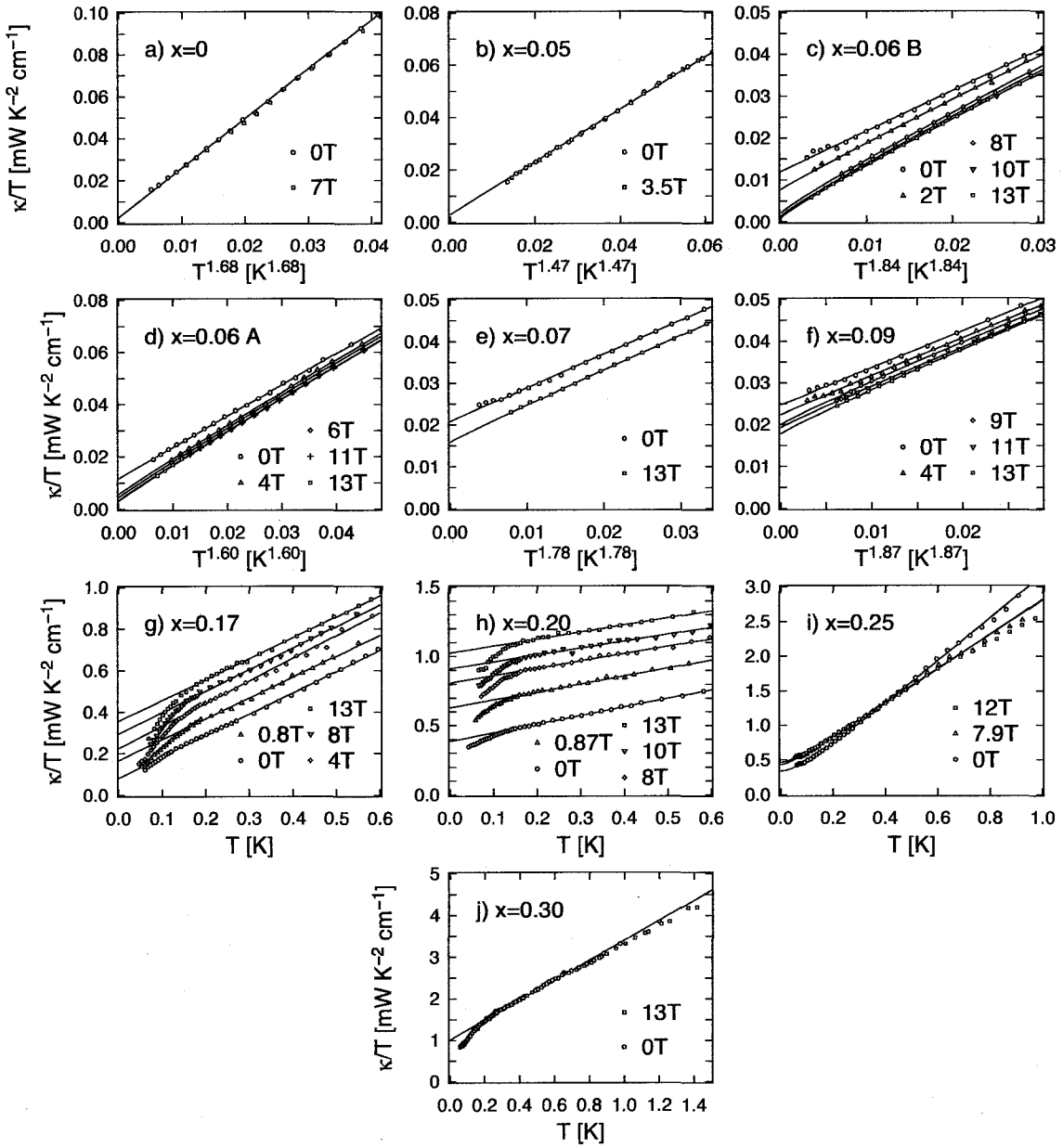

Figure 8.4: The thermal conductivity in the presence of an applied magnetic field as a function of temperature (as κ/T vs. T^{α}) for LSCO at various dopings from a) undoped $x = 0$ to j) heavily overdoped, non-superconducting $x = 0.30$. For the underdoped samples (a-f) the data is plotted up to 150 mK. The lines are fits to the data as described in the text. The residual linear term increases with an applied field for overdoped and optimally doped LSCO (g-j) but *decreases* with field for underdoped, superconducting samples (a-f). The non-superconducting samples (a, b and j) exhibit no field dependence.

8.2 Field-induced normal state in underdoped LSCO

In figure 8.4 κ_0/T vs. $T^{\alpha-1}$ is shown in 0T and in the presence of an applied field, H, for LSCO with Sr doping from $x = 0$ to $x = 0.30$. The principal observation is that *κ decreases with increasing field for the underdoped samples* ($x = 0.06$, 0.07 and 0.09). In Fig. 8.5, the field evolution of κ_{el}/T is shown at fields intermediate between 0 and 13 T, as $\kappa_o(H)/T$ normalized to $\kappa_o(0\text{T})/T$ for LSCO $x = 0.06$ A, 0.09, 0.17 and 0.20. By contrast to the underdoped samples, the electronic heat conductivity in the more highly doped samples ($x = 0.17$ and 0.20) increases with field, as it does in all known superconductors.

Note that κ is totally independent of magnetic field in our reference sample ($x = 0$), as in the other non-superconducting samples ($x = 0.05$ and 0.30). This shows that field dependence is a property of the superconducting state. We can therefore use this criterion to establish that the non-superconducting normal state is reached in the bulk by 11 T in sample $x = 0.06$ A. Indeed, as seen in Fig. 8.4 d), a further increase of the field to 13 T causes no further change in κ. This claim is supported by resistivity measurements, shown in Fig. 8.6 a), where the resistive onset of superconductivity is entirely absent for fields above 12 T (down to 40 mK). We take this as an additional indication that the field-induced (non-superconducting) normal state has been reached by 13 T at $x = 0.06$ (in the bulk) for sample A[5].

A zoom on the $x = 0.06$ data in sample A is shown in Fig. 8.7, where we can see that κ_0/T drops by a factor 4 from $H = 0$ to $H = 13$ T, ultimately reaching a value equal to that of the reference sample, namely $\kappa_0/T = 3$ μW K^{-2} cm^{-1}. We conclude that the field-induced normal state in underdoped LSCO is a thermal insulator. This implies the existence of an unprecedented kind of thermal metal-to-insulator transition. The superconducting state is a thermal metal by virtue of its delocalized nodal quasiparticles, while the field-induced normal state in the same sample is a thermal insulator, with either no Fermionic excitations or localized Fermionic excitations. The well-known crossover from charge metal to charge insulator, identified as the change from a positive $d\rho/dT$ at low T near and above optimal doping to a negative $d\rho/dT$ in underdoped LSCO [80, 76] (see fig. 2.7), now finds a parallel in the heat sector where the metal-insulator crossover is identified as the change from a positive $d\kappa/dH$ at low T to a negative $d\kappa/dH$ (see

[5]Similar measurements on $x = 0.06$ sample B, shown in fig.'s 8.6 b), indicate that the field-induced normal state is achieved at 16 to 18 T at 40 mK, unfortunately just beyond the fields at which thermal conductivity was measured.

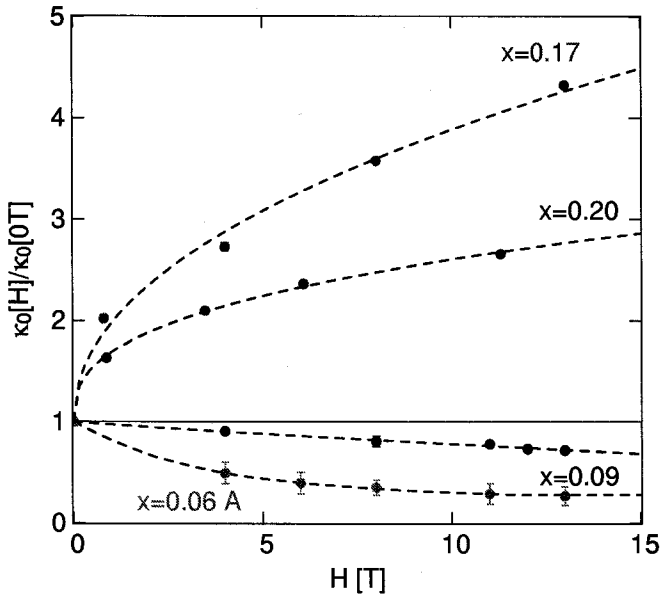

Figure 8.5: $\kappa_0(H)/T$ normalized to $\kappa_0(0\mathrm{T})/T$ and as a function of magnetic field H for LSCO with Sr doping $x = 0.06$ (A), 0.09, 0.17 and 0.20. The conductivity increases with applied magnetic field for the overdoped samples but *decreases* with field for the underdoped samples. The dashed lines are guides to the eye.

Fig. 8.5).

We mention that because of the insulating character of both heat and charge conduction in $x = 0.06$ at 13 T, it is technically not possible to perform a real test of the Wiedemann-Franz law. Consequently, the possibility that the two conductivities cease to be equal as they are in overdoped Tl-2201 [7] but rather diverge as they do in PCCO [167] is still an open question.

It should be carefully noted that the suppression of superconductivity to reach the field-induced normal state combined with the low temperature of our measurement distinguishes the decrease in κ with applied field observed here from other measurements that also show a field-induced decrease at notably higher temperatures. In particular recent measurements on LSCO [3], YBCO [170] and Bi2201 [171] by the Ando group also observe a decrease in κ with field, but at temperatures greater than 0.3 K. While the conclusions reached by the Ando group on LSCO are similar to our own, we view the low temperature of our measurement and the ability to reach the field-induced normal states as crucial elements of our arguments. This is highlighted by the fact that a decrease in κ at elevated temperatures is quite common and is observed not only in the cuprates [166, 120, 10] (see for instance our measurements on Tl2201 in fig. 7.1 or ultrapure YBCO

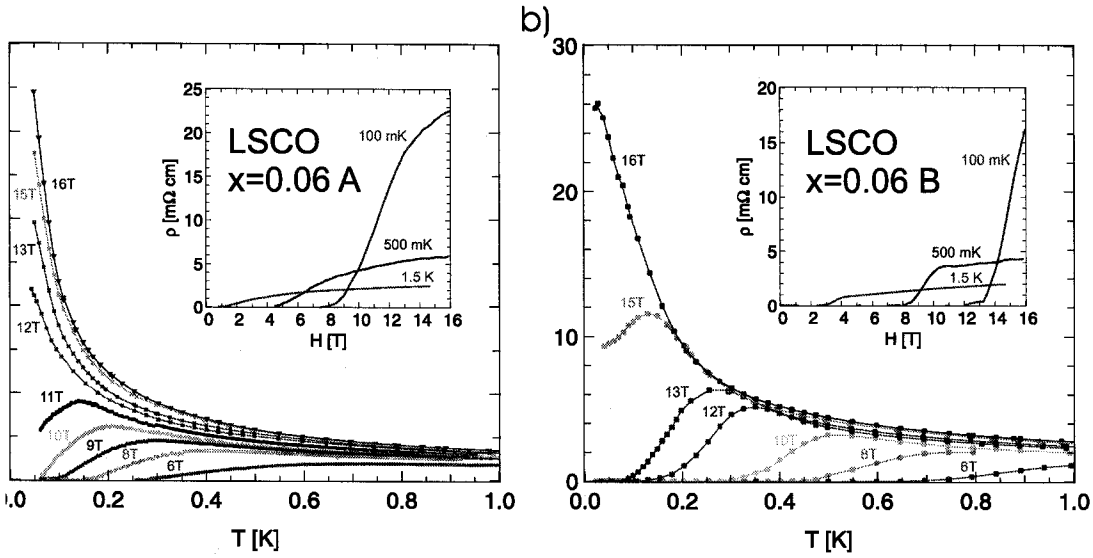

Figure 8.6: Low-temperature resistivity of LSCO with $x = 0.06$ in applied magnetic fields from 6 T to 16 T in sample a) A and b) B. By 12 T the superconducting transition has been suppressed to below 40 mK in sample A. Insets: Resistivity vs. magnetic field at 0.1, 0.5 and 1.5 K. In sample B a flux-flow and normal state regimes are clearly distinguished by a rapid rise in ρ followed by a plateau. In sample A the transitions are broader in magnetic field than sample B, indicating greater sample inhomogeneity.

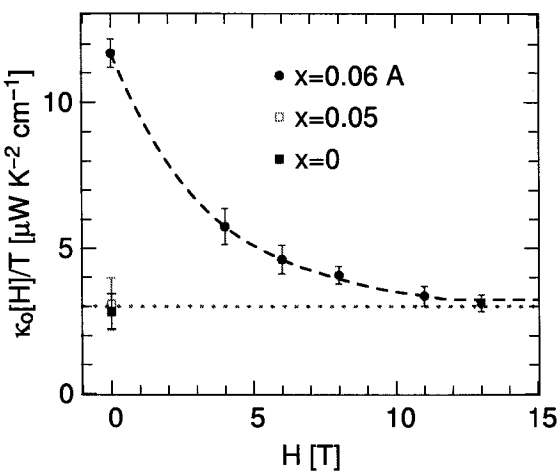

Figure 8.7: $\kappa_o(H)/T$ vs. H for LSCO $x = 0.06$ A. κ_o/T is also shown for $x = 0$ and 0.05 at zero field. The dotted line represents the estimated resolution of our experiment (see text). The error bars are statistical errors in the fitted values of κ_o/T and do not include errors in the geometric factors (which do not enter into the field dependence) or systematic errors in the fitting procedure (discussed in the text). The dashed lines are guides to the eye.

in fig. 7.1.) but also in conventional superconductors (see section 3.3.1) where the normal state is clearly metallic. In these cases the physics is not that of quasiparticle localization, but rather a combination of phonon-vortex scattering or quasiparticle-vortex scattering.

In conventional superconductors the phonon thermal conductivity at higher temperatures may decrease with increasing field due to enhanced phonon-quasiparticle scattering, as discussed in sec. 3.3.1 (in fact this is a sizeable effect in conventional superconductors, see measurements on Nb [104] shown in fig. 3.5). In our measurements at low temperatures, however, the linear in T contribution to κ, which is attributed to electronic conductivity, primarily decreases with H. The phonon thermal conductivity, which has a $T^{2.5-2.9}$ temperature dependence, is actually enhanced, albeit weakly, with the application of field. In this regard it is important to measure κ down to low T in order to extract κ_{ph} and κ_{el}.

In addition, in many cases in the cuprates, a decrease in κ may be accounted for by quasiparticle-vortex scattering [118, 119, 166, 115, 117, 116]. In this context, the other key feature of our measurement, namely that we have suppressed superconductivity with field, is very important. In conventional superconductors, vortices are no longer present in the field-induced normal state. On this basis one would not expect quasiparticle-vortex scattering to fully account for the decrease in κ in our heavily underdoped LSCO, although it may make some contribution.

Recent measurements of the Nernst co-efficient above T_c, however, have forced us to reconsider this notion. The Nernst effect measures a transverse voltage in the presence of a longitudinal thermal gradient. In the presence of mobile vortices, a contribution to the Nernst co-efficient results from the dissipation of vortices as they move in response to the thermal gradient. Several groups have now observed a Nernst signal above T_c in underdoped cuprates, arguing for the presence of vortices in the pseudogap state [47, 172, 173, 174, 175, 176]. In addition, according to the Nernst effect measurements, the field-induced normal state we are achieving in these underdoped samples results from the suppression of coherent superconductivity and not to mean-field H_{c2} of conventional superconductors. Rather the mean-field H_{c2} estimated from the Nernst effect is on the order of the pseudogap energy scale [176].

It is thus tempting to account for the decrease in κ at low temperatures in our samples as due a novel persistence of quasiparticle-vortex scattering into the field-induced normal state. However, if this were indeed the case, we would not expect the thermal conductivity to plateau precisely at H_{c2}, rather the thermal conductivity would continue to decrease in

the field-induced normal state. A more compelling argument may be made on the basis of recent measurements in heavily underdoped YBCO where no such field-induced decrease in κ is observed. These revealing measurements, which I will treat in the following section, point to an alternate scenario discussed in this chapters final section, namely that the metal-insulator transition in LSCO results from a field-tuned competition between superconductivity and static spin-density wave order.

8.3 Low temperature thermal conductivity in heavily underdoped YBCO

In this section we compare the thermal conductivity of heavily underdoped LSCO to recent measurements by Mike Sutherland in heavily underdoped $YBa_2Cu_3O_y$ (YBCO)[6]. YBCO has a higher maximum critical temperature (T_c^{max} = 93 K versus 40 K) and it can be prepared with much lower levels of disorder than LSCO. The effect of doping on the electron system is investigated by comparing LSCO and YBCO samples with doping on either side of the critical doping for the onset of superconductivity (p_{SC}).

The main finding is the observation of delocalized Fermionic excitations in the non-superconducting state of YBCO ($p < p_{SC}$) at $T \rightarrow 0$, thereby revealed it to be a metallic state. This result shows that upon doping, a clean Mott insulator may first becomes a metal before it turns into a superconductor, meaning that holes can be mobile without forming a condensate of Cooper pairs. Remarkably, in YBCO the conductivity of this metallic phase evolves continuously from that of the superconducting state just above p_{SC}, suggesting that the metallic normal state has the same nodal excitation spectrum as the d-wave superconductor. By contrast, as we have shown, in the LSCO system such delocalized low-energy excitations are not observed in the non-superconducting state, showing that these excitations are either localized or gapped.

We begin with non-superconducting samples, for which $p < p_{SC}$. In Figure 8.8, the thermal conductivity of YBCO is compared to our LSCO sample with x=0.05. Unlike LSCO, where $\kappa_0/T = 3 \pm 1 \mu$W K^{-2} cm^{-1}, in YBCO a distinct linear term is observed, of magnitude $\kappa_0/T = 36 \pm 5 \mu$W K^{-2} cm^{-1}, much larger than that obtained for an undoped crystal of YBCO [4] (y=0.0) where $\kappa_0/T = 0 \pm 1 \mu$W K^{-2} cm^{-1}. This observation points to a fundamental difference between the two systems. As one adds carriers to the

[6]The measurements on YBCO is the thesis work of Mike Sutherland. Details of the measurements not presented here may be found in references [6, 13].

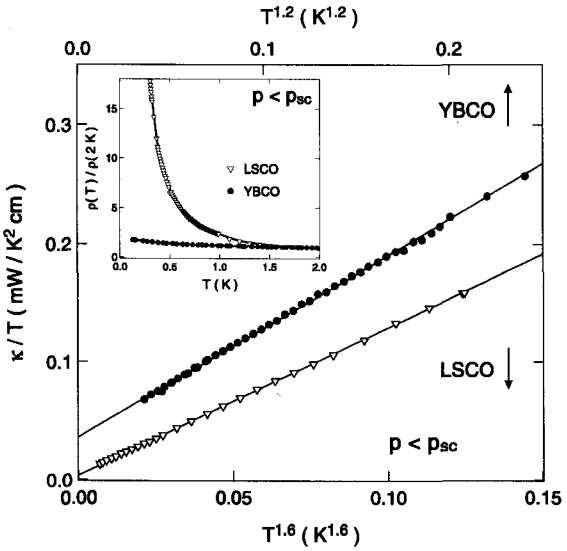

Figure 8.8: The thermal conductivity, κ, vs. T^{α} for heavily underdoped, non-superconducting YBCO and LSCO ($x = 0.05$). Both samples have a hole concentration p close to, but less than p_{SC}, the critical concentration for the onset of superconductivity. The YBCO sample shows a sizable residual linear term κ_0/T, indicating the presence of delocalized Fermionic carriers of heat. By contrast, the LSCO sample shows a vanishingly small value of κ_0/T, consistent with an insulating state. Inset: The electrical resistivity normalized to ρ(2K) for the same samples of YBCO and LSCO. The LSCO is insulating, consistent with a model of variable-range-hopping (see ch. 5), and exhibits a 100-fold increase in resistivity between 2 K an 0.1 K. In contrast the resistivity of YBCO is nearly flat.

parent insulator in clean samples of YBCO, the ground state becomes metallic before the emergence of superconductivity, while in LSCO the ground state is an insulator right up to p_{SC}.

Having uncovered a metallic phase in lightly-doped YBCO with no long-range superconducting order, we can explore some of the basic properties of its low-lying excitations. Specifically, we ask how they compare to the well-understood d-wave nodal quasiparticles of the superconducting state (at $p > p_{SC}$) and, of particular relevance to our measurements on LSCO, how they respond to a magnetic field.

We now compare the non-superconducting metallic phase encountered below p_{SC} with the coherent superconducting state, accessed by studying YBCO with a hole concentration beyond the critical doping at $p = p_{SC}$, as we have done in LSCO. The dependence of κ_0/T on doping in YBCO is shown in Figure 8.9 [4, 6, 13]. As can be seen, the magnitude of the residual conductivity evolves smoothly through this critical concentration and into the superconducting state. As discussed in ch. 3 and ch. 6, in a d-wave superconductor,

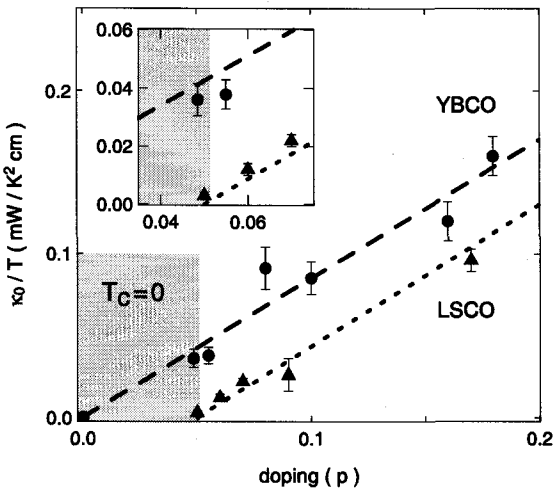

Figure 8.9: The residual thermal conductivity, κ_0/T, as a function of carrier density p for YBCO (circles) and LSCO (triangles). This Fermionic heat conductivity decreases with decreasing p in both cases, but at p_{SC} it goes to zero in LSCO while it remains finite in YBCO. Dashed lines are linear guides to the eye. Inset: Zoom on region close to p_{SC}. The smooth continuation across p_{SC} in YBCO suggests that the energy spectrum is the same (i.e. nodal) in both the superconducting phase and the non-superconducting, metallic phase.

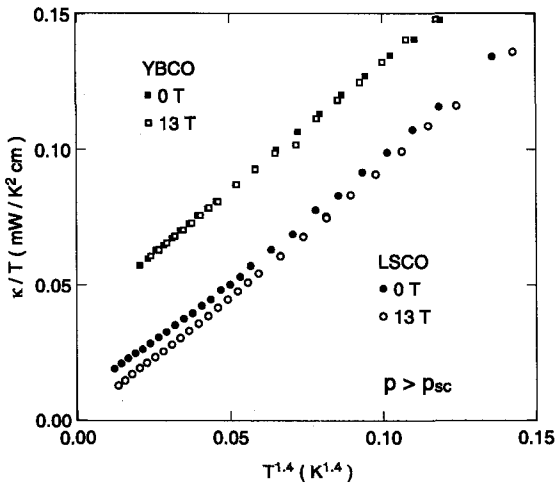

Figure 8.10: Temperature dependence of thermal conductivity for $p > p_{SC}$ in both YBCO and LSCO ($x = 0.06$ A), for two values of a magnetic field applied perpendicular to the CuO_2 planes (H=0 and H=13 T). The doping p is just above p_{SC} (p=0.055 and $T_c = 9$ K in YBCO; $x = p$=0.06 and $T_c = 5$ K in LSCO). In LSCO the thermal conductivity decreases with increasing field. In contrast, in YBCO the magnetic field has no effect on κ_0/T.

nodal quasiparticles are low-lying Fermionic excitations that give rise to a finite κ_0/T, the magnitude of which is given by eq. 3.14 and is governed entirely by their Dirac energy spectrum.

As discussed in ref. [4], the value one obtains for the gap in YBCO in this manner tracks the value measured by ARPES and tunneling well into the underdoped regime (see fig. 6.7). This shows that the overall decrease in κ_0/T with underdoping is caused by a monotonically increasing gap. For the highly-underdoped YBCO samples, the linear term of approximately 40 μW K^{-2} cm^{-1} implies a gap maximum of 160 meV, which suggests that the in-plane exchange coupling energy J of the Mott insulator, estimated to be 125 meV [177], sets the magnitude of Δ_0.

Two important points emerge from Figure 8.9. First, the monotonic decrease in κ_0/T with underdoping observed in YBCO persists smoothly through the quantum critical point at $p = p_{SC}$: there is no detectable change in the conductivity of YBCO in going from the d-wave superconductor into the non-superconducting metallic phase. Indeed, within error bars the residual linear term in a sample with p just below p_{SC}, $\kappa_0/T = 36 \pm 5$ μW K^{-2} cm^{-1}, is identical to that of a sample with p just above p_{SC}, $\kappa_0/T = 38 \pm 3$ μW K^{-2} cm^{-1}. (Both values are also compatible with the overall, roughly linear, trend.) Given that the residual linear term is solidly understood as arising from nodal quasiparticles in the superconducting state, its seamless evolution into the non-superconducting state below p_{SC} strongly suggests that a nodal spectrum is also a characteristic of that metallic phase in YBCO.

The second important conclusion one may draw from figure 8.9 is that LSCO appears to be qualitatively different from YBCO. While in LSCO the quantum phase transition at p_{SC} corresponds to a (thermal) metal-insulator transition, in YBCO it has no impact on the conductivity of the electron system. The very same situation was observed to occur as a function of applied magnetic field, for $p > p_{SC}$: in LSCO the transition from thermal metal (d-wave superconductor) to insulator is found to be simultaneous with the suppression of superconductivity, occurring right at the upper critical field H_{c2}, for LSCO x=0.06 A.

In YBCO, however, no such decrease is observed for p close to p_{SC}[7] (or anywhere as $T \rightarrow 0$), as shown in fig. 8.9. In fact, a field of 13 T has very little effect, whether $p < p_{SC}$

[7]Incidentally, as noted above, this result argues against quasiparticle-vortex scattering as the cause of the decrease in κ observed in LSCO. If quasiparticle-vortex scattering was predominant in LSCO one would expect a similar behavior in YBCO.

or $p > p_{SC}$. In the sample with $p < p_{SC}$, $\kappa_0/T = 38 \pm 5$ μW K^{-2} cm^{-1} in 13 T (compared to 36 ± 5 μW K^{-2} cm^{-1} in zero field). One can see that the thermal conductivity of the sample with $p > p_{SC}$ is entirely unaffected by a field, and the extrapolated value of $\kappa_0/T = 37 \pm 5$ μW K^{-2} cm^{-1} is obtained in both H=0 and H=13 T. Note that 13 T is a fair fraction of the field necessary to suppress bulk superconductivity at this doping, so that the field-induced normal state in this sample will clearly have the same conductivity as the superconducting state. The conclusion is, therefore, that in YBCO near p_{SC} the thermal conductivity does not change across the phase boundary, whether one reaches the non-superconducting state by decreasing p at fixed H=0 or by increasing H at fixed $p > p_{SC}$.

This is reminiscent of previous spectroscopic studies (ARPES [178] and tunneling [33]) which found the gap in underdoped cuprates to persist largely unchanged as the temperature was increased from below to above T_c. The observation of this "pseudogap" above T_c has been interpreted as the persistence of pairing amplitude (gap) once long-range superconducting order has been destroyed by thermal fluctuations of the phase (see for example Ref. [44]). Within such an interpretation, the fact that the measurements on YBCO are done essentially at T=0 would imply a quantum (rather than thermal) disordering of the phase with increasing magnetic field or decreasing doping. What our study shows is that this putative phase disordering would leave the system in a metallic ground state. Beyond this particular interpretation, several theoretical models have been proposed for the pseudogap state of underdoped cuprates (see for example Refs. [21, 46, 45]).

In light of these results on YBCO, the obvious question is why LSCO and YBCO exhibit different behavior around p_{SC}? If our interpretation of YBCO as a phase disordered d-wave superconductor is correct, then the thermal metal-to-insulator transition observed in LSCO seems to signal additional physics not present in YBCO. The difference between YBCO and LSCO may lie in the greater amount of disorder found in LSCO, which would cause the non-superconducting state of LSCO near $p = p_{SC}$ to be an insulator (thermally and electrically). However, if LSCO were merely a disordered version of YBCO, it is hard to see why the metal-to-insulator transition would be pinned to the onset of superconductivity (at p_{SC}). The latter fact points instead to another explanation, namely a scenario of competing phases where the other phase (e.g. with SDW order) is insulating.

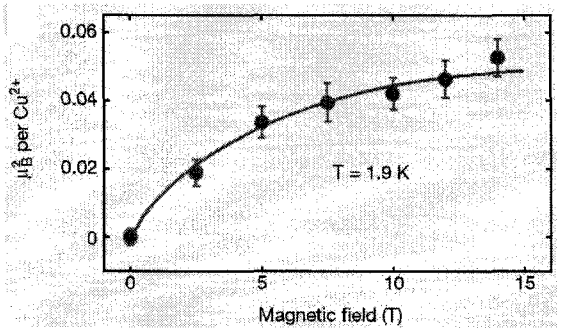

Figure 8.11: The intensity of field-induced, incommensurate SDW order, expressed as μ_B^2 per Cu atom, as a function of magnetic field, H, from the elastic neutron scattering measurements of Lake et al. [53]. Note, the intensity of the Bragg peak present in 0 T has been subracted.

8.4 Competing spin-density-wave order in LSCO

In LSCO there is well established evidence for static spin-density wave (SDW) order in underdoped samples from elastic neutron scattering measurements, as reviewed in section 2.2.3. As a general consideration one would expect the presence of order that competes with the superconductivity to affect the ground state excitations, and hence the thermal transport. Indeed, we find a compelling correlation between the appearance and intensity of spin-density wave order in neutron scattering measurements and the field and doping dependence of the thermal conductivity, with the spin-density wave state being less conductive than the superconducting state.

First, in elastic neutron scattering measurements, the incommensurate magnetic Bragg peak, that evidence the SDW order in underdoped LSCO, has been observed to be enhanced by the application of a magnetic field by a number of groups [53, 65, 64, 67, 66, 68]. In figure 8.11, the intensity of the field-induced, incommensurate magnetic Bragg peak, expressed in terms of μ_B^2, is shown as a function of magnetic field from measurements by Lake et al. [53].The enhancement of the static SDW order shown here correlates well with the decrease in the thermal conductivity with applied field depicted in figure 8.7.

Second, neutron scattering measurements observe static SDW order in zero field up to a Sr doping of $x \sim 0.13$, with a noted enhancement of the SDW intensity at $x = 1/8$ [58, 59]. This observation correlates well with the doping evolution of the thermal conductivity in zero field. For one, the 0T thermal conductivity is reduced from the universal limit expectation in underdoped LSCO. In addition, measurements of the 0T thermal conductivity by the Ando group [5], reproduced in fig. 8.3a, show a local mini-

mum in κ_0/T at $x = 1/8$. Furthermore, by optimal doping ($x = 0.17$) the ground state has undergone a quantum critical transition to a state with the only order being that of the d-wave superconductor. This accounts both for κ_0/T values in 0T that may be reconciled with the "universal' limit expectation, and for the recovery of the conventional increase in κ with field in overdoped samples. In fact, the field dependence of both the $x = 0.17$ and $x = 0.20$ samples is qualitatively consistent with the roughly $\sqrt{H}$ field dependence observed in other optimally doped cuprates [9, 10] and described by semi-classical models [114, 117, 179].

Two theory groups have since modeled the field dependence of the thermal conductivity in underdoped LSCO in the context of competing order [161, 180] with different approaches. Gusynin and Miransky calculated the thermal conductivity in the "universal" limit ($T \ll \gamma \ll \Delta_0$) of a d-wave superconductor in the presence of an additional order parameter that fully gaps the nodal region [161]. This calculation models a small gap from competing order, such as SDW or CDW, but is also is sufficiently general to describe a similar gap from another origin, such as a sub-dominant superconducting order parameter (is or id). The addition of the small gap modifies the "universal" limit (eq. 3.14) to give [161]

$$\frac{\kappa_0}{T} = \frac{k_B^2}{3}\left(\frac{n}{d}\right)\left(\frac{v_F}{v_2} + \frac{v_2}{v_F}\right)\frac{\gamma^2}{\gamma^2 + m^2}, \tag{8.2}$$

where m is the sub-dominant gap (The quasiparticle dispersion in this case is $E(\mathbf{k}) = \sqrt{v_F^2 k_1^2 + v_2^2 k_2^2 + m^2}$.). For $m \ll \gamma$, κ_0/T will be approximated well by the standard calculation of Durst and Lee [109]. However, for values of the sub-dominant gap, m, on the order of the impurity bandwidth ($m \sim \gamma$), the thermal conductivity will be suppressed relative to the standard result for a simple d-wave gap and as m grows beyond γ the thermal conductivity decreases rapidly.

Gusynin and Miransky also extend their calculation to include the affect of an applied field in an attempt to model our thermal conductivity data on LSCO. In these calculations they assume a general ansatz that the small gap m is present only for doping less than $x = 0.16$ and increases with decreasing doping and applied field. In addition, they include the usual enhancement of the thermal conductivity due to the Volovik effect in a fashion similar to calculations by Kübert and Hirschfeld [114] (described in sec. 3.4.4). The result of their calculations is reproduced in a plot of $\kappa_0(H)/T$ normalized to $\kappa_0(0\mathrm{T})/T$ vs. H (like our fig. 8.5) in fig. 8.12. While their calculations agree qualitatively with our experiments the decrease with H appears to be too rapid to fully account for our data.

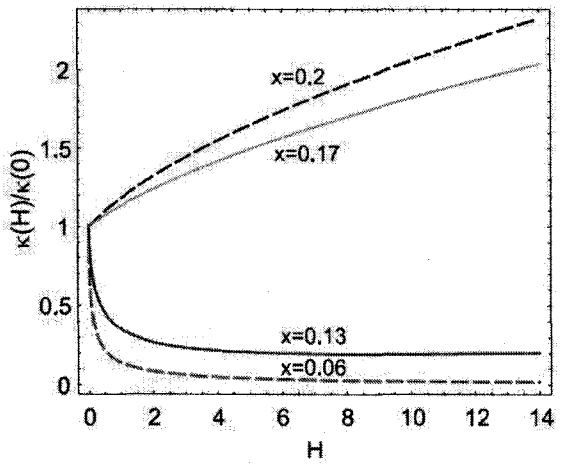

Figure 8.12: $\kappa_0(H)/T$ normalized to $\kappa_0(0\mathrm{T})/T$ vs. H calculated by Gusynin and Miransky [161]. They assume a subdominant gap, m, that grows with increasing H for Sr doping less than $x = 0.16$. Above $x = 0.16$ the H dependence is given by the Volovik effect.

Also, note that this is a weak coupling view of the SDW order, providing a gap at the Fermi surface rather than a drastic reshaping of the Fermi surface, as would occur in the strong coupling picture of microscopic phase separation.

This view is supported by recent ARPES [181] measurements, reproduced in fig. 8.13a, in LSCO showing a quasiparticle peak at the nodal position with Sr doping as low as $x = 0.03$ (non-superconducting and both thermally and electrically insulating). More recently, further APRES measurements in this region of the phase diagram have indicated a small gap (~ 7.5 meV) of nodal quasiparticles in heavily underdoped, non-superconducting samples [182] (see fig. 8.13b). It is plausible that in the absence of this gap heavily underdoped LSCO would appear metallic, like YBCO. In fact, it has already been argued based on optical conductivity [183] and resistivity [184] that underdoped LSCO has metallic behavior at higher energy (or temperature).

For larger doping, including superconducting samples, this small gap decreases to below the resolution of the ARPES measurements, but may in fact not be zero. If we assume that in LSCO γ is of the order of 1.5 meV, as indicated by the field dependence in LSCO with $x = 0.17$ (see ch. 7), then the gap needs to be of that order to have an effect on κ_0/T. Notably this is on the order of the energy resolution of the best ARPES measurements, so it is certainly possible that a small gap is present even in superconducting samples. If this is indeed the case, this gap is precisely the sort that enters into the theory of Gusynin and Miransky, explaining the field and doping dependence of our

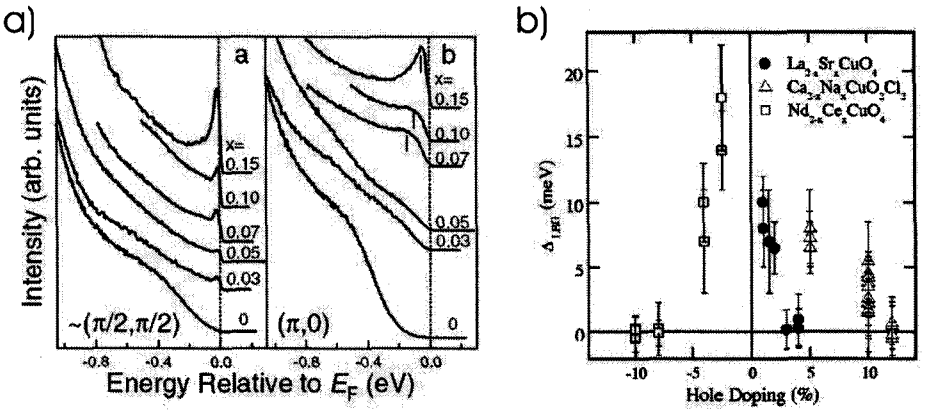

Figure 8.13: a) Energy distribution curves (EDC) from angle resolved photoemission on $La_{2-x}Sr_xCuO_4$ with various doping of Sr, x from Yoshida et al. [181]. The ARPES spectra along the nodal (π,π) direction (panel a) indicates a quasiparticle peak near the Fermi energy for Sr doping as low as $x = 0.03$. No such peak is observed along the anti nodal direction (panel b). b) The magnitude of the small gap along the nodal direction observed in ARPES on LSCO, Na-CCOC and NCCO from Shen et al. [182]. The small gap that is observed in heavily underdoped samples falls below the resolution of the technique at higher doping.

thermal conductivity data in LSCO. Moreover, although the origin of this gap is as yet unclear, it may also be the manifestation of the SDW order.

An alternate picture of competing SDW and superconducting order, that may equally describe our results on LSCO, is the situation where SDW order and superconductivity do not co-exist microscopically, but instead form mesoscopically phase separated regions of SDW and SC order [55, 65, 68] (as discussed in section 2.2.3). The application of magnetic field reveals SDW order in the vortex cores[8], and possibly outside of the cores [54]. In essence, the effect of field may be to tune the volume fraction of the thermally insulating SDW and thermally metallic d-wave superconducting phases. In this picture the electronic transport in underdoped samples is percolative transport between the thermally-metallic d-wave superconducting regions. The conductivity becomes insulating when the volume of the SDW order increases to the point where there is no longer a percolative path through the sample. This sort of view of competing SDW and SC order is discussed in the context of thermal conductivity by the theory of Takigawa et al. [180]. They associate the decrease in κ with applied field to a depletion in the local density of states in the vortex cores of underdoped cuprates. This depletion of the density of states is due to the normal state of underdoped cuprates being an insulating SDW state, rather

[8]In addition to the neutron scattering measurements, transverse-field μSR [185] and NMR [186] measurements of the mixed state indicate that static magnetism is indeed present in the vortex cores.

than a "normal" metal for overdoped samples.

Finally, we note that the absence of a similar competition between static SDW order and superconductivity in YBCO is likely attributed to the lack of observed *static* SDW in YBCO [69, 70]. However, although static SDW has not been found in YBCO, the dynamic spin fluctuations have been observed in both materials [56, 70], indicating that the materials are magnetically similar. This is evident in recent measurements of the dynamic spin susceptibility in LBCO [187] and YBCO [188], which show some qualitatively similar behavior. Ultimately, it may be that the characteristic that distinguishes LSCO and YBCO is disorder. The presence of static SDW order in LSCO may be related to disorder stabilizing stripes in LSCO: in this way disorder is not solely responsible for the field-induced M-I transition, yet is intimately connected to it.

8.5 Summary

In summary, we map out the ground state quasiparticle transport in LSCO as a function of field and doping across the doping phase diagram. In underdoped samples we find dramatic differences between the conductivity in LSCO and YBCO. While YBCO behaves as a phase disordered d-wave superconductor, LSCO exhibits suppressed electronic thermal conductivity in the superconducting state. The application of a magnetic field further suppresses the thermal conductivity at $T = 0$, unlike any previously measured superconductor. By measuring a sample in a magnetic field sufficient to suppress superconductivity we show the decrease in field to be associated with gapping or localization of quasiparticles in the field-induced normal state. Finally, by comparing our results to neutron scattering measurements we conclude that the novel suppression of the thermal conductivity in LSCO is due to a competition between superconducting and spin-density wave ground states in underdoped LSCO. Moreover, the qualitatively different behavior in YBCO at similar doping levels suggests that static spin density wave order plays a negligible role in governing the ground state excitations in YBCO.

9

PHONON THERMAL CONDUCTIVITY IN THE CUPRATES

In LSCO the phonon thermal conductivity displays a very unusual Sr doping dependence [11, 189, 190, 191]. In the parent compound, La_2CuO_4 there is a large phonon peak in the conductivity at $T \sim 30$ K. With Sr doping this peak is rapidly suppressed and between $x = 0.05$ and 0.25 no phonon peak can be resolved. However, at $x = 0.30$ the peak in κ reappears [11].

While the initial suppression of the peak can be explained in terms of scattering from the Sr dopant atoms, which act as point defects for phonon scattering, the same scattering mechanism cannot explain the re-emergence of the peak in κ_{ph} at large Sr doping. At first thought the re-emergence of the phonon-peak at large doping is also incompatible with the scattering of phonons from electrons. The argument for this is that the carrier density, and hence the quasiparticle density of states, $N(E_F)$, increases with increasing Sr content, and correspondingly so should the scattering of phonons by electrons. These contradictions, along with measurements on Eu and Nd doped LSCO, have led a number of authors to invoke novel scattering mechanisms such as scattering from fluctuating spin stripes [189, 190, 192] or from a soft optical phonon [191] present in LSCO.

In this chapter, we reconsider the role of the electron-phonon interaction in governing the phonon thermal conductivity and argue that electron-phonon scattering dominates the phonon thermal conductivity not only at intermediate temperatures, where the peak in κ is formed, but down to temperatures as low as 50 mK. This additional insight stems from the thermal conductivity in two systems, $La_{2-x}Sr_xCuO_4$ and $Tl_2Ba_2CuO_{4+\delta}$, measured over a wide range of doping ($0 \leq x \leq 0.30$ in LSCO, $0.16 \lesssim p \lesssim 0.26$ in Tl2201) and temperature (40 mK $< T <$ 150 K). We observe an intrinsic (not boundary scattered) T^2 temperature dependence of the phonon thermal conductivity in overdoped LSCO and Tl2201 that extends down to the lowest measured temperatures and which we interpret as resulting from phonon-electron scattering. Similar to the phonon thermal conductivity at intermediate temperatures, the magnitude of the low T phonon thermal

conductivity increases with increasing doping. We argue that this increase in κ_{ph} results from a decrease in the electron-phonon coupling, λ, with increasing doping.

This latter conclusion is consistent with angle-resolved photoemission (ARPES) experiments showing a decrease in the quasiparticle velocity renormalization with increasing doping [193, 155], a renormalization that has been interpreted, controversially, as resulting from the electron-phonon coupling, λ [193]. The parallel evolution of the decrease in electron-phonon coupling and the decrease in T_c with increasing doping in overdoped cuprates suggests that the electron-phonon interaction may play an important role in the mechanism for high temperature superconductivity.

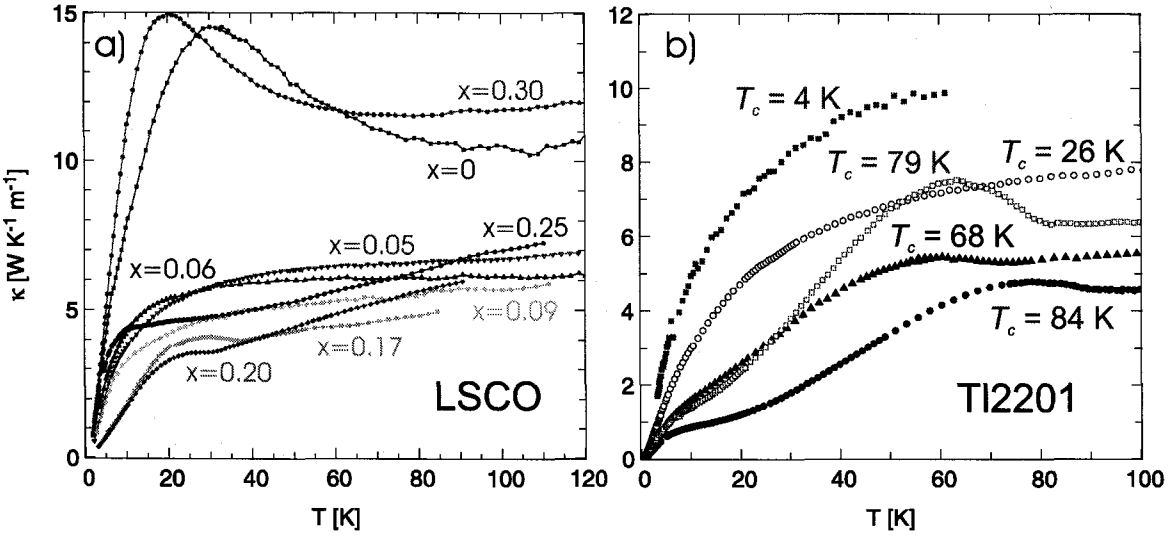

Figure 9.1: κ vs. T for a) $La_{2-x}Sr_xCuO_4$ at various Sr concentrations x from the Mott insulating parent compound $x = 0$ to heavily overdoped non-superconducting, $x = 0.30$. b) $Tl_2Ba_2CuO_{4+\delta}$ at various dopings from $\sim$ optimally doped $T_c = 84$ K to heavily overdoped $T_c = 4$ K. For Tl2201 a single sample was measured at two different dopings. The $T_c = 4$ K and 79 K (red) are measurements on one sample and the $T_c = 26$ K and 84 K (blue) are a second sample.

9.1 κ_{ph} at intermediate temperatures (4 K - 150 K)

In figure 9.1 we present the thermal conductivity at intermediate temperatures in LSCO and Tl2201. In underdoped LSCO, the general doping dependence of κ is that it first decreases with increasing doping, reaches a minimum at $x \sim 0.17-0.2$ and increases with increasing doping for overdoped samples. In Tl2201, for which only overdoped samples are available, the thermal conductivity increases with increasing doping for all samples. In addition to this general trend, in the LSCO samples with $x = 0.17$ and 0.20 and the

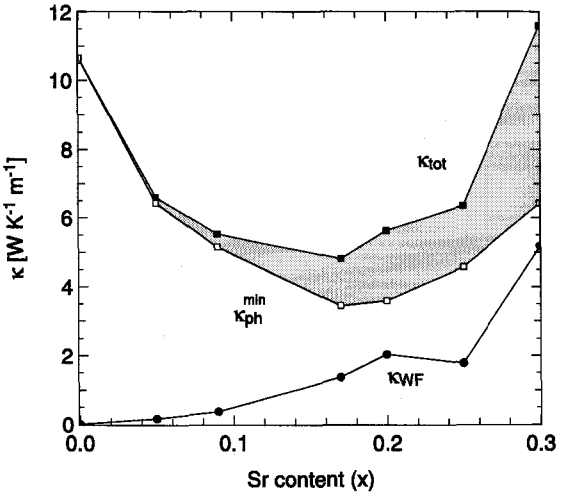

Figure 9.2: The total thermal conductivity, κ_{tot}, the Wiedemann-Franz law expectation for the electronic contribution, κ_{WF}, and the minimum phonon thermal conductivity $\kappa_{ph}^{min} = \kappa_{tot} - \kappa_{WF}$, in LSCO at 80 K vs. Sr doping, x. The actual phonon contribution will be in the shaded region between κ_{ph}^{min} and κ_{tot}. Note κ_{ph} has a minimum around optimal doping, $x = 0.17$.

Tl2201 samples with $T_c = 84$ K and 68 K, there is as a kink in the thermal conductivity at $T \sim T_c$ followed by a peak in κ at lower temperatures. We will defer discussion of this peak to section 9.1.1.

In overdoped samples, some of the increase in κ with increasing doping may be accounted for by the increase in the electronic contribution to κ. While in general there is no reliable means of extracting the electronic contribution to κ at these temperatures, we can make use of the Wiedemann-Franz law to provide a upper limit on the electronic contribution to the conductivity. (For inelastic scattering the Lorenz ratio, $\kappa_{el}/(\rho T)$, is less than the Sommerfeld value L_0.) Using the electrical resistivity, ρ, in LSCO[1] from figure 5.6, we calculate the Wiedemann Franz law expectation for electronic contribution to the thermal conductivity, $\kappa_{WF} = L_o T/\rho$ (L_o is the Sommerfeld value of the Lorenz number). This is shown along with the total conductivity, κ_{tot}, and the minimum value of the phonon thermal conductivity, given by $\kappa_{ph}^{min} = \kappa_{tot} - \kappa_{WF}$, at 80 K as a function of Sr doping in figure 9.2. The actual phonon thermal conductivity will have a value bounded by κ_{tot} and κ_{ph}^{min} shown as the shaded region in fig. 9.2. Note that κ_{ph} has a noted minimum around optimal doping, $x \sim 0.17$. Thus, although some of the doping

[1]In Tl2201 our resistivity data is not reliable enough to perform a similar comparison, although based on resistivity measurements from literature [144] we would predict a similar doping dependence and magnitude of the ratio of κ_{WF}/κ_{tot} as LSCO.

evolution of κ can be accounted for by κ_{el}, there is an underlying novel doping dependence of κ_{ph}. In particular it is clear that the peak in κ in the $La_{1.7}Sr_{0.3}CuO_4$ sample results from phonon conduction.

The reemergence of this phonon peak at large doping is puzzling and has led a number of authors to invoke novel scattering mechanisms such as scattering from fluctuating spin stripes [189, 190, 192] or from a soft optical phonon [191] present in low temperature orthorhombic phase of LSCO. As reviewed briefly in section 2.2.3 and references therein there is now plenty of evidence for static spin density wave order (stripes) in the LSCO. There is also evidence from inelastic neutron scattering measurements of spin fluctuations at temperatures and dopings where static order is not observed. Measurements of the dynamic spin density wave order in overdoped LSCO show the intensity of the incommensurate dynamic spin susceptibility to follow T_c and go to zero at the SC-M transition ($x = 0.30$) [67]. Thus, the observation of the peak in the phonon thermal conductivity coincides with the regions of the phase diagram where the material is either in the ordered antiferromagnetic state ($x = 0$) or where the SDW order vanishes.

Although there is presently no detailed theory, in principle fluctuating spin or charge stripes may couple to the lattice, providing a plausible source of phonon scattering, as argued in references [189, 190, 192]. Furthermore, it has been noted that the characteristic energy of the dynamic spin susceptibility from inelastic neutron scattering measurements ($\sim 6 - 10$ eV) is an appropriate energy scale to scatter acoustic phonons at intermediate temperatures [189].

Alternately, is has been proposed that the phonons may be scattered in LSCO by the soft optical phonon mode associated with the tetragonal-to-orthorhombic phase transition [191]. In this scenario, additional scattering associated with the soft phonon mode should occur only in the low temperature orthorhombic (LTO) phase ($x \lesssim 0.22$) and not in the low temperature tetragonal (LTT) phase, where the soft-phonon mode has hardened. For x greater than the LTO-LTT phase transition at $x = 0.22$ the phonon peak should recover. However, as the phonon peak remains suppressed in our sample with $x = 0.25$, which is well into the LTT phase, this interpretation is inconsistent with our measurements.

A common feature of both of these interpretations is that they invoke scattering from a dynamic excitation that has a characteristic energy applicable to phonon scattering at the intermediate temperatures where the phonon thermal conductivity forms a peak. These scattering mechanisms should not contribute strongly to scattering well below these temperatures, for instance down to 100 mK. Before discussing the phonon thermal

conductivity at low-T we will close this section by briefly discussing the peak in κ that occurs just below T_c.

9.1.1 The peak in κ below T_c

In samples near optimal doping there is as a kink in the thermal conductivity at $T \sim T_c$ followed by a peak in κ at lower temperatures. In YBCO, Bi2212 and Tl2201, this peak may be attributed to an enhancement of κ_{el} below T_c [147, 152]. The clearest evidence for this interpretation comes from microwave conductivity [148] and thermal Hall effect [150] measurements, both of which measure only electronic contribution to conductivity and yet observe a large increase in conductivity below T_c. This peak has been observed in microwave measurements on Tl2201 [149], Bi2212 [194] and YBCO [148]. The peak results from a collapse of the inelastic quasiparticle scattering rate in the superconducting state. This has a greater impact on the conductivity than the reduction in the density of states due to the opening of the superconducting gap. As the temperature is decreased the quasiparticle scattering rate continues to decrease until it becomes limited by the elastic impurity-induced quasiparticle scattering rate. In this way the height and temperature of the peak provide a measure of the relative contributions of elastic and inelastic scattering at $T \simeq T_c$.

In Tl2201 the difference in the peak height between the $T_c = 68$, 79 and 84 K samples reflects a difference in the impurity induced quasiparticle scattering rate, or in other words, the relative disorder of the samples. As a function of doping the peak can no longer be distinguished in the $T_c = 26$ K or 4 K samples. This may be an indication that the ratio of inelastic to elastic scattering at T_c decreases with increasing doping. Such a reduction could result from an intrinsic decrease in inelastic quasiparticle scattering with increasing doping. It may, however, simply reflect the lower T_c of overdoped samples; there is less inelastic scattering at lower temperature.

In LSCO it is not clear that the peak below T_c, observed only in the $x = 0.17$ and 0.20 samples is of the same electronic origin as Tl2201, YBCO and Bi2212. Evidence against an electronic origin comes from measurements of the c-axis thermal conductivity by Nakamura et al. [11]. Given the highly anisotropic charge transport in the cuprates, the c-axis thermal conductivity is expected to be entirely due to phonon conduction. However, Nakamura and co-workers observe the peak in κ below T_c to be present in both the c-axis and a-axis thermal conductivities. This points to a phonon origin to the peak below κ in LSCO. Moreover, this shows that the dominant phonon scattering mechanism

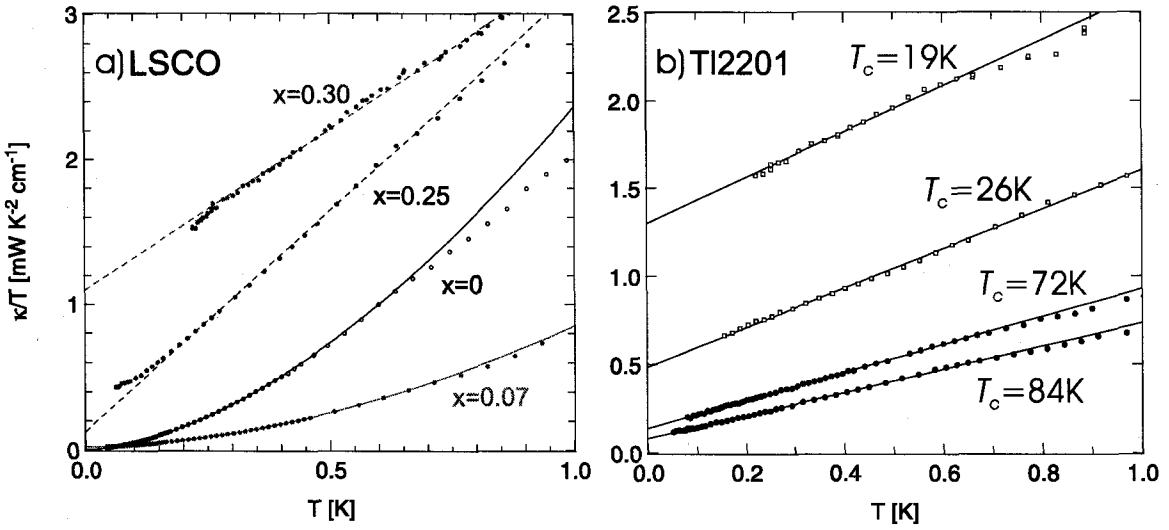

Figure 9.3: κ/T as function of temperature for a) $La_{2-x}Sr_xCuO_4$ at four Sr concentrations: $x =$ 0, 0.07, 0.25 and 0.30, and b) overdoped Tl2201 at $T_c = 84$, 72, 26 and 19 K. The solid lines are power law fits to the phonon thermal conductivity (eq. 8.1) for the underdoped LSCO samples. In contrast, the overdoped samples of LSCO and Tl2201 exhibit a substantial T^2 contribution to the phonon thermal conductivity (solid lines). Note for Tl2201, the data is for two samples, each measured to two different doping levels. The 72 K and 19 K measurements correspond to one sample and the 84 K and 26 K measurements correspond to the other sample.

is affected by the onset of superconductivity.

9.2 κ_{ph} at sub-Kelvin temperatures: phonon-electron scattering

In figure 9.3 we present the thermal conductivity (plotted as κ/T vs. T), at sub-Kelvin temperatures in LSCO and Tl2201 for select dopings. Here, unlike at higher temperatures, we can make more definitive extraction of the electronic and lattice contributions to the total thermal conductivity. The electronic contribution to κ is proportional to T and its magnitude is given by an appropriate extrapolation of κ/T to $T = 0$, as discussed in chapters 3, 6 and 8. The remaining T dependent term in fig. 9.3 is the phonon thermal conductivity, κ_{ph}[2].

There are a few observations to make about κ_{ph} in the low T limit. We will start first with the parent compound of LSCO, La_2CuO_4. La_2CuO_4 serves as a nice test case

[2]The T^3 electronic contribution to κ that is given by eq. 3.16 and is present in $YBa_2Cu_3O_7$ [166] is not present in LSCO or Tl2201, likely due to the larger quasiparticle scattering rates in LSCO and Tl2201 relative to ultrapure $YBa_2Cu_3O_7$.

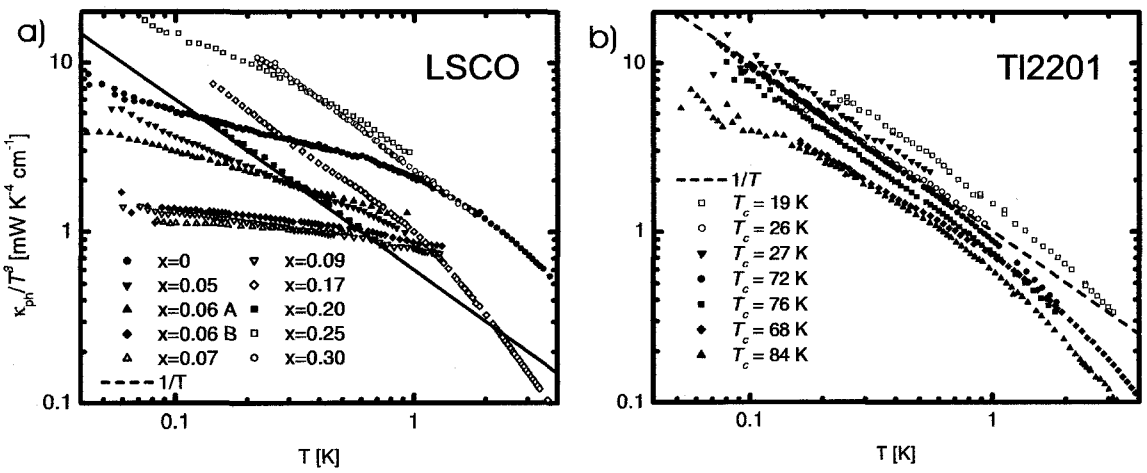

Figure 9.4: The phonon thermal conductivity in a) LSCO and b) Tl2201 as a several dopings. The data is plotted as κ_{ph}/T^3 vs. T on a log-log scale. Plotted in this fashion boundary scattering in the scattering diffuse limit will give a temperature independent curve. In the underdoped LSCO samples a single power law with α between 2.85 and 2.45 fits all of the data. In overdoped LSCO and Tl2201 the phonon thermal conductivity is qualitatively different, having a predominant T^2 temperature dependence. The boundary scattering limit is only achieved in some samples at very low temperatures.

for the phonon thermal conductivity as it is a Mott insulator and hence should have no electronic contribution to κ (zero intercept), and also presumably no electron-phonon scattering. As shown in chapter 8, the thermal conductivity of La_2CuO_4 fits very well to a single power law $\kappa = AT^{\alpha}$ with $\alpha = 2.67$, shown as the line through the data in figures 8.1 j) and 8.2 f). We take this as indication that the phonon thermal conductivity is in the boundary scattering limit, as discussed in ch. 3. Note that the power, α, is not 3, the result one gets for phonons scattered diffusely from the boundaries of a crystal, but rather a lower power law. This result is consistent with measurements on a number of insulators in the boundary scattering limit and can be attributed to the fact that phonons may scatter both diffusely and specularly from the surfaces of samples [4].

In the other underdoped LSCO samples we observe a similar power law T dependence to the phonon thermal conductivity (see chapter 8) and κ is fit very well below $T \simeq 0.5$ K to a form $\kappa/T = \kappa_0/T + AT^{\alpha-1}$ (eq. 8.1), where κ_0/T accounts for the low-temperature linear in T electronic contribution to κ.

In contrast to the underdoped samples, in both overdoped LSCO and Tl2201 the phonon thermal conductivity has a marked T^2 temperature dependence that extends down to very low temperatures. Most interestingly, the magnitude of this T^2 term *increases* with increasing doping. These two results are clearly shown in fig. 9.4 where

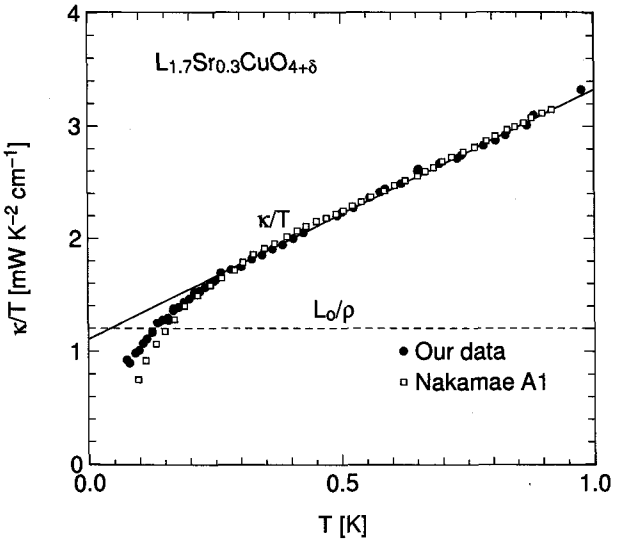

Figure 9.5: The thermal conductivity of overdoped, non-superconducting $La_{1.7}Sr_{0.3}CuO_4$ plotted as κ/T vs T. The line is a linear fit to the data. The extrapolated linear term from this fit agrees well with Wiedemann-Franz law, $\kappa_0/T = L_0/\rho_0$, using resistivity extrapolated from higher temperatures, as first shown by measurements by Behnia group on samples at the same doping level [79]. Also, plotted is the data from the Behnia group on their sample A1. There sample has a cross-sectional area 10 times that of our sample, yet has exactly the same phonon thermal conductivity. This rules out boundary scattering of the phonons over this range of temperatures. Note, a low-temperature downturn attributed to electron-phonon de coupling appears in both sets of data at a temperature of ~250 mK. Extrapolating the data from above the downturn provides agreement with the Wiedemann-Franz law.

we plot κ_{ph}/T^3 vs. T on a log-log scale[3]. With this presentation the Casimir limit for boundary scattering, a T^3 conductivity, gives a flat line while a T^2 conductivity is parallel to the red dashed line. Fig. 9.4 shows that κ_{ph} follows the general behavior of the phonon thermal conductivity at intermediate temperatures down to very low temperatures, namely the magnitude of κ_{ph} first decreases with doping for heavily underdoped samples and then increases with increasing doping in overdoped samples. Along the way the power of the temperature dependence of the phonon thermal conductivity changes from a high power close to the T^3 to a definite T^2 dependence in optimal doped to overdoped samples.

Moreover, we can show that the T^2 temperature dependence is intrinsic, ie not related to boundary scattering, for the overdoped samples. First, we compare our measurement

[3]To present the data in this fashion a linear in T term representing κ_{el} has been subtracted from all of the curves. In some samples this subtraction is difficult and we caution against over interpreting the details of fig. 9.4.

of $La_{1.70}Sr_{0.30}CuO_4$ to previous measurements of the same doping by the group of Kamran Behnia [79], shown in figure 9.5. Our sample has a comparable residual resistivity and electronic contribution to the thermal conductivity, κ_0/T, as their sample A1. However, the cross-sectional area of their sample is a factor of 10 larger than our sample and despite this difference, κ_{ph} is virtually identical in the two samples. In other words, κ_{ph} is not geometry dependent and not limited by boundary scattering.

Second, we note that in Tl2201 we have been able to perform measurements on the same sample at two different dopings by reannealing the samples. This procedure preserves the geometry of the sample while allowing one to vary the doping of the sample (see ch: 5). Two samples were measured in this fashion and both are plotted in fig.'s 9.3 and 9.4. In one case a sample was first measured at $T_c = 84$ K and then remeasured at $T_c = 26$ K and in the other case a sample was measured at $T_c = 19$ K and then remeasured at $T_c = 72$ K. Both of these samples show an increase in κ_{ph} with increasing doping (decreasing T_c), suggesting the evolution of κ_{ph} is intrinsic.

Incidentally, the measurements on the $La_{1.70}Sr_{0.30}CuO_4$ sample serve a secondary purpose. At this doping level, which is in the normal state, the Wiedemann-Franz law, relating charge and heat transport, has been verified [7, 79]. In fig. 9.5 the expectation for κ_{el}/T based on charge transport, L_o/ρ, is shown. This provides a useful check that we are correctly determining the electronic portion of the thermal conductivity and thereby shows that the additional T dependence is correctly attributed to the phonons.

To understand the origin of the scattering which gives rise to the low-temperature T^2 dependence of the phonon thermal conductivity, we draw inspiration from the fact that in a normal metal the scattering of phonons from electrons is also proportional to T^2 (see ch. 3). More specifically, Butler and Williams [94] calculate the thermal resistivity, W^{ph}_{ph-el}, in the case where phonon-quasiparticle scattering dominates the phonon scattering rate to be

$$W_{ph-el} = 0.42N(E_F)\Omega_a^{1/3}\left(\frac{\Theta_D}{T}\right)^2\lambda, \tag{9.1}$$

in units of K cm/W, where $N(E_F)$ is the electronic density of states at the Fermi energy in (spin states)/eV, Ω_a is the atomic volume in Å^3, Θ_D is the Debye temperature in K and λ is the electron-phonon coupling parameter. In our case, we are measuring the phonon thermal conductivity in a quasi-2D d-wave superconductor in the universal limit ($T \ll \gamma$),

so details of eq. 9.1 may not apply[4]. Nevertheless, W_{ph-el} will still be proportional to the electron-phonon coupling parameter, λ, and may depend in some fashion on $N(E_F)$. Assuming $N(E_F)$ increases with doping and Θ_D is only weakly doping dependent, eq. 9.1 at first thought predicts a trend with doping that is opposite to our measurements, namely $W^{ph} \propto 1/\kappa_{ph}$ increasing with increasing doping. Most importantly, however, we must account for the doping dependence of the electron-phonon coupling, λ.

λ is a physically interesting parameter that determines the electron-phonon mass enhancement and, in conventional superconductors, the superconducting transition temperature. In addition, λ renormalizes the bare quasiparticle velocity close to the Fermi energy, $v_F = v_F^{bare}/(1+\lambda)$ [197]. Recently, angle-resolved photoemission has directly measured the renormalization of the quasiparticle velocity at the Fermi energy. Although the origin of the quasiparticle velocity renormalization is currently controversial, one interpretation is that it arises due to coupling of the electrons to the phonons, and thus provides a measure of $(1+\lambda)$ [193]. Adopting this interpretation we note that the doping dependence of λ extracted from the nodal Fermi velocity is such that it decreases from $2.1 \pm 40\%$ to $0.3 \pm 25\%$, almost an order of magnitude decrease, upon doping from $x = 0.03$ to 0.30 in LSCO [155]. Such a decrease would overcome the doping dependence of $N(E_F)$ and account for the increasing phonon thermal conductivity observed in both LSCO and Tl2201. Our measurement complements the ARPES results, which measures the electrons interacting with the phonons, by providing a measure of the electron-phonon coupling from the perspective of the phonons interacting with the electrons.

The doping dependence of the electron-phonon coupling also explains another curious feature of our data. As shown in chapters 6, 7 and 8, in overdoped cuprates a downturn in the thermal conductivity is observed that we attribute to the thermal decoupling of the electrons and phonons. What is interesting is the doping evolution of this downturn. The downturn is seen in overdoped LSCO and Tl2201, but never in any of the underdoped LSCO samples. In addition, the onset temperature of the downturn seems to increase with increasing doping. Since the electron-phonon heat transfer rate is proportional to the electron-phonon coupling, in much the same way as it is in W_{ph-el} [154], the doping dependence of the onset of the downturn, and the lack of it's observance in underdoped samples, corroborates the doping dependence of λ from ARPES and κ_{ph}.

[4]A related quantity, the ultrasonic sound attenuation has been calculated in a d-wave superconductor in the appropriate limit, $T \ll \gamma$ [195, 196]. Interestingly they find that the sound attenuation is "universal" (independent of γ) for some phonon modes, like the electronic thermal transport.

While we have shown that a fairly consistent picture of the phonon thermal conductivity can be formed by considering electron-phonon scattering as the dominant phonon scattering mechanism there are two outstanding issues that stand in apparent conflict with our description. First, as we have outlined above, the phonon thermal conductivity in the underdoped samples has a T dependence, T^{α}, that we argue is consistent with scattering from the boundaries of the sample. However, we also note that the magnitude of the phonon thermal conductivity at low T in the underdoped samples is suppressed relative to that of the higher doped samples. This latter fact provides an argument for stronger electron-phonon scattering in underdoped samples that would dominate boundary scattering. Also note, that the Casimir limit is not reached in any of the underdoped samples.

One potential explanation that reconciles these two conflicting results is by considering the effects of phonon focusing [198]. Phonon focusing is where some phonon modes are scattered more strongly than others in the bulk of the sample. The remaining weakly scattered phonons are responsible for the majority of the heat conduction. The mean-free-path of these weakly scattered phonons may be limited by the boundaries of the sample and hence give a T dependence consistent with boundary scattering but a magnitude less than the Casimir limit. A hint that phonon focusing may be relevant phonon-electron scattering in the cuprates comes from recent sound attenuation measurements on Sr_2RuO_4, a material that is iso-structural to LSCO [199]. Here it was shown that the magnitude of the electron-phonon sound attenuation can differ by a factor of ~ 1000 between different phonon modes [199, 195]. Applied to the phonon thermal conductivity in LSCO, it may be that the scattering of some phonon modes is sufficiently strong in underdoped samples that these phonons make virtually no contribution to κ_{ph}. Rather the phonon conduction is via other weakly scattered phonon modes. These phonons that are weakly scattered by electrons may make it to the surface of the samples and be dominantly scattered by the boundaries of the sample, resulting in $\kappa_{ph} \propto T^{\alpha}$. As the doping increases the scattering of the strongly scattered modes decreases and they once again make a significant contribution to κ_{ph}.

A second puzzling issue is the field dependence of κ_{ph} in the mixed state in nearly optimally doped samples. As noted in ch. 7 and again shown for the sample with $T_c = 76$ K in fig. 9.6, the phonon thermal conductivity is essentially field independent below ~ 2 K, despite a factor of 3 increase in κ_0/T. The increase in κ_0/T results from the well studied increase in $N(E_F)$ due to the Volovik effect [112, 9, 114]. In contrast, in more

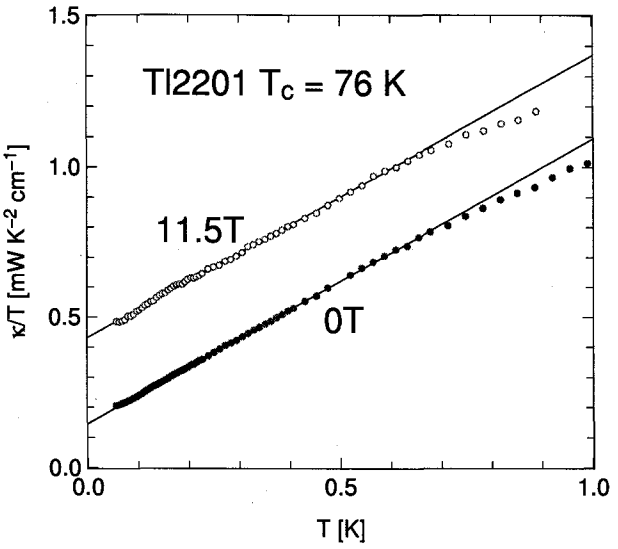

Figure 9.6: The thermal conductivity of Tl2201 with $T_c = 76$ K, plotted as κ/T vs. T, in 0T and 11.5T. A sizeable increase in the electronic contribution to κ, κ_0/T, is not accompanied by a change in κ_{ph}.

overdoped samples, where the applied field is closer to H_{c2}, κ_{ph} does decrease with the application of field, as shown in chapter 7 (see fig. 7.3) for Tl2201 with $T_c \leq 27$ K and in LSCO with a Sr content of $x = 0.25$ in chapter 8 (see fig. 8.4). The lack of H dependence in optimally doped samples is somewhat surprising. Naively, one would expect this increase in $N(E_F)$ from the Volovik effect to result in a significant decrease in κ_{ph}. One may speculate that this implies that for $H \ll H_{c2}$, the Volovik contribution to the quasiparticle density of states cancels out of the expression for the electron-phonon scattering, perhaps in the same spirit as the cancelation of the quasiparticle scattering rate in the "universal" expressions for the low temperature electronic conductivity [107, 111, 109]. Qualitatively, one may imagine a scenario whereby the field-induced quasiparticles that produce an increase in $N(E_F)$ also screen the electron phonon interaction by the same amount, ie $\lambda \propto 1/N(E_F)$. Hopefully a detailed theoretical treatment of the electron-phonon scattering will be able to add insight to this issue.

Finally, having described the phonon scattering at low temperatures in terms of electron-phonon scattering it seems natural that the same scattering mechanism also accounts for the novel doping dependence at intermediate temperatures. In short, the peak in κ_{ph} re-emerges at high doping because electron-phonon scattering, which washes out the peak, becomes very weak by this doping. We note, however, that we have not ruled out additional contributions from either scattering by the soft-optical phonon mode

in LSCO or from dynamic spin-stripes.

In conclusion, we reexamine the phonon thermal conductivity as a function of doping over a wide range of T in two different materials. We find notable T^2 dependence of κ_{ph} at low T, the magnitude of which increases with increasing doping. Correlating the T dependence with the quasiparticle velocity renormalization measured by ARPES we conclude that the electron-phonon coupling, λ, decreases with increasing doping in the cuprates.

9.3 Summary

In summary, find an intrinsic doping dependence to the phonon contribution to the thermal conductivity that extends down to the lowest measured temperatures and is present in both LSCO and Tl2201. κ_{ph} at low temperatures is found to have a similar evolution with doping to the peak in κ_{ph} observed in LSCO at higher temperatures by previous groups [11]. Namely, in both LSCO and Tl2201, the magnitude of κ_{ph} is initially suppressed at low doping in LSCO, however, with increasing doping in optimally doped to overdoped samples, tκ_{ph} increases with increasing doping. Moreover, in overdoped samples, κ_{ph} is shown to be independent of sample geometry, and is thereby intrinsic and to have a T^2 temperature dependence, which is notably the same as that expected for phonon-electron scattering in conventional metals.

We argue, based on the temperature and doping dependence of κ_{ph}, the low temperature to which the behavior extends, and the generic nature of these observations, that κ_{ph} can be explained if phonon-electron scattering is the dominant phonon scattering mechanism. In this scenario the increasing phonon thermal conductivity reflects a decrease in the electron-phonon coupling with increasing doping. The decrease in the electron-phonon coupling, which is parameterized by the electron-phonon coupling constant λ, is consistent with recent measurements of the quasiparticle velocity renormalization by angle-resolved photoemission, and the interpretation put forth by Lanzara et al. [193] that the quasiparticle velocity renormalization is due to the coupling of the electrons to the phonons. The resulting doping dependence of λ, observed from the perspective the electrons coupling to the phonons in the ARPES measurements, provides an explanation for the decrease in phonon scattering observed in our measurements of κ_{ph} in LSCO and Tl2201.

As the strength of the electron-phonon coupling, λ, is an important factor in determin-

ing the superconducting transition temperature in conventional BCS superconductors, the strong doping dependence of λ indicated here is consistent with the controversial notion that the electron-phonon interaction is the mechanism for superconductivity in the high-temperature superconductors. In this scenario, the decrease in T_c with increasing doping in optimally doped to overdoped cuprates simply follows from the decrease in the electron-phonon coupling with increasing doping. If this assertion is correct these results may have a profound impact on the understanding of the basic physics of high-temperature superconductors. Future efforts, both experimental and theoretical, will be required to fully explore these arguments and observations.

10

CONCLUSIONS

We have measured the low-temperature thermal conductivity in two families of the cuprates, LSCO and Tl2201, as a function of temperature, doping and magnetic field.

In Tl2201, we find the electronic contribution to the thermal conductivity increases with increasing doping, consistent with mean-field theories of thermal conductivity in a d-wave superconductor. We extract the quasiparticle gap from low temperature thermal conductivity and show that it agrees well with spectroscopic measurements of the gap from tunneling.

As further validation of the d-wave nodal quasiparticle description of the low-temperature thermal conductivity, we show in Tl2201 the field dependence of the thermal conductivity to agree well with semi-classical theories of transport in the vortex state based upon the Volovik effect.

In contrast, in underdoped LSCO we find qualitatively different behavior. In underdoped LSCO, we find the thermal conductivity to be too small to be accounted for by the mean-field theories of thermal conductivity in a simple d-wave superconductor. More striking, is the observation that the thermal conductivity decreases with an applied magnetic field, in striking contrast to all previously measured superconductors. In one sample where we are able to suppress superconductivity with an applied field, we show this decrease in thermal conductivity with applied field to be a novel thermal metal-to-insulator transition. This result is contrasted with measurements on YBCO at similar doping levels by Mike Sutherland. Here no decrease in the thermal conductivity is observed with applied magnetic field. Also, at higher doping in LSCO the field induced decrease in the thermal conductivity is no longer observed, rather the thermal conductivity increases consistent with the Volovik effect observed in other optimally doped and overdoped cuprates. By comparing our results to neutron scattering measurements we conclude that the novel suppression of the thermal conductivity in LSCO is due to a competition between superconducting and spin-density wave ground states in

underdoped LSCO.

In the last section of the thesis, we examine the phonon conductivity as a function of doping in both LSCO and Tl2201 at low temperatures. We find that in overdoped samples, the magnitude of the phonon conductivity increases with increasing doping down to low temperatures (50 mK), with a notable T^2 temperature dependence. We argue that the phonons are scattered predominantly by phonon-electron scattering at low temperatures. The phonon conductivity can thus be related to the electron-phonon coupling parameter, λ, which plays an important role in determining the superconducting transition temperature in conventional superconductors. The doping evolution of the phonon conductivity in our measurements is naturally explained by a decrease in electron-phonon coupling with increasing doping consistent with recent interpretations of the quasiparticle velocity renormalization measured by angle-resolved photoemission.

Finally, I will close with suggestions for future work that may build upon the results of this thesis. Two of the projects presented in this thesis stand out as open to additional exploration. First, we may continue to explore the role competing SDW and superconducting order plays in governing the low temperature quasiparticle transport. One interesting experiment in this regard is to measure a sample of LSCO at a doping, intermediate between the $x = 0.09$ and 0.17 samples already measured, that exhibits no static SDW order in zero field, but exhibits static SDW order in the presence of an applied magnetic field. We may then correlate the field at which SDW order emerges with the field dependence of the thermal conductivity and potentially provide very direct evidence for the influence of competing SDW and SC order on the low energy excitations.

A second project that will hopefully be advanced in future work beyond the preliminary work presented here is the investigation of the phonon contribution to the thermal conductivity at low temperatures. The observations and arguments presented in this thesis offer up some new ideas that if correct may have profound implications for the understanding of the mechanism of high temperature superconductivity. Much can be done to further explore the theoretical and experimental implications of electron-phonon interaction on the thermal conductivity, and in turn the results of thermal conductivity measurements on the field at large. In particular, measurements of additional overdoped LSCO samples, as a function of doping, but also as a function of other control parameters such as quasiparticle scattering rate and sample geometry, will aid in determining which factors influence the phonon contribution to the thermal conductivity.

In the underdoped region of the phase diagram, it will be interesting to investigate

the doping dependence of the phonon conductivity around the non-superconductor to superconductor transition, to investigate if and how closely the suppression of κ_{ph} is tied to the onset of superconductivity in this region of the phase diagram. In addition it will be important to assess the role of boundary scattering in underdoped crystals. In this regard it will be useful to measure samples of LSCO, and also YBCO, with carefully controlled doping and with varied cross-sectional area and/or surface treatments.

APPENDIX:SAMPLE CATALOG

A.1 LSCO

A.1.1 $x = 0$

- Sample growth: Grown by Shuichi Wakimoto in Spring 2002
- Annealing: Boule annealed in flowing Ar atomosphere at 700 °C for $\sim$ 24 hrs.
- Boule oriented using Laue x-ray diffraction. a-axis samples were subsequently cut and polished from the Boule using a diamond saw.
- Only one sample (sample 1) was prepared and measured thus far.

Sample dimensions

L (mm)	W (mm)	T (μm)	$\alpha = TW/L$ (cm)
0.98 ± 0.05	0.803 ± 8	167 ± 8	$1.37 \times 10^{-2} \pm 5\%$

Sample and contact resistance

- 4 contact pads put on using Ag epoxy.
- contact pads originally not annealed
- pads annealed in flowing Ar at 500 °C for 90 min.
- ρ(room T) = 83.2 mΩ cm (R = 6.08 Ω)

Measurement summary

- June 2002 – κ between 2 K and 150 K with contacts not annealed –measurement unsuccessfull due to large contact resistances
- July 2002 – κ between 2 K and 150 K and ρ between $\sim$ 20 K and 300 K with reannealed contacts
- August/September 2002 – κ between 40 mK and 2 K in the dilution refridgerator in 0T, 0.05T, 6T, 8T and 10T.

Published data

- – [1] – κ vs. T in the dilution refridgerator in 0T and 7T

A.1.2 $x = 0.05$

- Sample growth: 2 Boules grown by Shuichi Wakimoto
- Boule not post annealed.
- Boule oriented using Laue x-ray diffraction. a-axis samples were subsequently cut and polished from the Boule with a spark cutter (Summer 2000) and with a diamond saw (Jan. 2002).
- two samples, labeled 1 and 2, were prepared and measured.

Sample dimensions

Sample	L (mm)	W (mm)	T (μm)	$\alpha = TW/L$ (cm)
#1	3.5 $\pm$	0.52	100	1.48 $\times 10^{-3}$
#2 (side 1)	0.697 $\pm$ 0.05	0.545 $\pm$ 0.008	280 $\pm$ 8	2.19 $\times 10^{-2} \pm 8\%$
#2 (side 2)	1.235 $\pm$ 0.05	0.545 $\pm$ 0.008	280 $\pm$ 8	1.24 $\times 10^{-2} \pm 5\%$

Sample and contact resistance

- 4 contact pads put on sample #1 by Robert Hill
- 6 contact pads put on sample #2
- contacts pads made using Ag epoxy and diffused under flowing O_2 at 500 °C for $\sim$ 1 hr.

	ρ_{samp} [mΩ cm]	R_{samp} [Ω]	$R(I-)$ [Ω]	$R(I+)$ [Ω]	$R(V-)$ [Ω]	$R(V+)$ [Ω]
#1 (room T)	1.88	1.273	0.552	0.997	2.401	0.850
#1 (4.7K)	5.09	3.436	1.699	2.926	11.66	1.499

	ρ_{samp} [mΩ cm]	R_{samp} [Ω]	$R_{(I^-,V^-)}$ [Ω]	$R_{(I^-,V^+)}$ [Ω]	$R_{(I^-,I^+)}$ [Ω]	$R_{(V^+,V^-)}$ [Ω]
#2 (side 1, room T)	2.90	0.1323	1.327	0.575	0.588	1.587
#2 (side 2, room T)	2.85	0.2302	0.383	0.596	0.586	0.797

Measurement summary

- Nov. 2000 – sample 1 – ρ vs. T between 2 K and 300 K
- Dec. 2000 – sample 1 – κ vs. T between 2 K and 120 K
- Feb. 2001 – sample 1 – κ vs. T in dilution refridgerator between 40 mK and 0.6 K in 0T and 8T(potential heat-losses in measurement due to large sample thermal resistance (small cross-sectional area))
- April 2001 – sample 1 – ρ vs. T from 300 K down to 310 mK in the Heliox. R differs from Dec. 200 measurement by a factor of 1.15.
- Jan. 2002 – sample 1 – κ vs. T remeasured in dilution refridgerator between 40 mK and 0.6 K in 0T and 13T using a fridge mount that was modified to reduce heat losses.

- Feb. 2002 – sample 2 – measured ρ vs. T between 300 K and 300 mK in the Heliox
- Mar. 2002 – sample 2 – measured κ vs. T in dilution refridgerator between 40 mK and $\sim$ 1 K in 0T and 4T.
- Mar. 2002 – sample 2 – measured ρ vs. T in dilution refridgerator between $\sim$100 mK and $\sim$2 K.

Published data

- – sample #2 – [1] – κ vs. T at low T in 0T and 4T. ρ vs. T below 1 K.
- – sample #2 – [4] – κ vs. T at low T in 0T.

A.1.3 $x = 0.06$

- Sample growth: 2 Boules grown at McMaster University in the lab of Bruce Gaulin and Graeme Luke by David Hawthorn with instruction from Shuichi Wakimoto and Harry Zhang.
- All samples were cut from one of the Boule's (labeled Boule #1).
- Boule oriented using Laue x-ray diffraction. a-axis samples were cut from the Boule with a diamond saw and polished to an appropriate shape and size.
- four samples labeled 1, 2, 3 and 4 were prepared and measured.
- Note: samples #3 and #4 are labeled sample A and B respectively in publications.
-

sample	$T_c(\rho = 0)$
#1	6.5 K
#3	5.5 K
#4	8.5 K

Sample dimensions

Sample	L (mm)	W (mm)	T (μm)	$\alpha = TW/L$ (cm)
#1 (side 1)	1.195 $\pm$ 0.165	0.515 $\pm$ 0.008	182 $\pm$ 8	7.8 $\times 10^{-3} \pm 14\%$
#1 (side 2)	2.369 $\pm$ 0.13	0.515 $\pm$ 0.008	182 $\pm$ 8	3.96 $\times 10^{-3} \pm 7\%$
#2	0.705 $\pm$ 0.114	0.758 $\pm$ 0.008	180 $\pm$ 8	1.92 $\times 10^{-2} \pm 16\%$
#3	0.833 $\pm$ 0.05	0.758 $\pm$ 0.008	180 $\pm$ 8	1.65 $\times 10^{-2} \pm 7.5\%$
#4	0.659 $\pm$ 0.05	0.758 $\pm$ 0.008	183 $\pm$ 8	2.10 $\times 10^{-2} \pm 9\%$

Sample and contact resistance

- 6 contact pads put on sample #1. All other samples have only 4 contact pads
- sample #2 and #4 were annealed in flowing O_2 at 800 °C for $\sim$ 12 hrs. before (samp #2) and after (samp #4) putting contact pads on the sample. As shown below the contact resistances are poor for sample #2 and ρ(room T) does not agree well with the other samples. In contrast sample # 4 exhibits good contact resistance and good agreement with the other samples. We take this difference as indication that surface degradation results from the annealing process. Samples #1 and #3 were only annealed at 500 °C under flowing O_2 for 1 hr. to diffuse the contacts but were otherwise not post annealed.

	ρ_{samp} [mΩ cm]	R_{samp} [Ω]	$R_{(I^-,V^-)}$ [Ω]	$R_{(I^-,V^+)}$ [Ω]	$R_{(I^-,I^+)}$ [Ω]	$R_{(V^+,V^-)}$ [Ω]
#1 (face 1, room T)	1.697	0.218	0.548	0.7543	0.806	0.635
#1 (face 2, room T)	1.719	0.434	0.442	0.838	0.801	0.837
#2 (room T)	3.73	0.1939	5.61	5.75	6.21	4.00
#3 (room T)	1.646	0.1005	0.713	0.584	0.425	0.936
#3 (4K)	0	0	-	-	0.0366	-
#3 (310mK)	0	0	-	-	0.0378	-
#4 (room T)	1.63	0.0775	0.552	0.447	0.368	0.686
#4 (4K)	0	0	-	-	0.0109	-
#4 (310mK)	0	0	-	-	0.011	-

Measurement summary

- Dec. 2001 – sample 1 – ρ vs. T between 4 K and 300 K (side 1 and 2).
- Jan. 2002 – samples 3 and 4 – ρ vs. T between 320 mK and 300 K in Heliox. Measured T sweeps between 310 mK and 30 K in 15, 14, 13, 11, 10, 8, 6, 4 and 0T and H sweeps from 0 to 15T at 310 mK.
- Jan. 2002 – sample 3 – κ vs. T and ρ vs. T in the dilution refridgerator between 40 mK and 1 K at 0, 4, 6, 8, 10.5, 11 and 13 T.
- Mar. 2002 – sample 4 – κ vs. T and ρ vs. T in the dilution refridgerator between 40 mK and 1 K at 0, 2, 8, 10 and 13 T.
- Oct. 2002 – sample 3 and 4 – ρ vs. T in the "new" dilution refridgerator between 20 mK and 1 K at 0, 6, 8, 9, 10, 11, 12, 13, 15 and 16 T. H sweeps between 0 and 16T at 100 mK, 0.5 K and 1.5 K.
- Mar. 2003 – EPMA analysis on a piece of LSCO $x = 0.06$ from Boule #1.
- Aug. 2003 – sample 3 – κ and ρ vs. T measured from $\sim$ 2 K to 135 K
- Oct. 2003 – sample 4 – κ and ρ vs. T measured from $\sim$ 2 K to 110 K

Published data

- – samples #3 – [1] – κ vs. T at low T in 0T, 11 and 13 T and κ_0/T vs. H at intermediate fields. ρ vs. T below 1 K in various fields (from fridge data).
- – sample #3 and #4 (labeled A and B) respectively – [4] – κ vs. T at low T in 0T.
- – sample #3 – [6] – ??

A.1.4 $x = 0.07$

- Sample growth: Boule grown by Shuichi Wakimoto
- Boule oriented using Laue x-ray diffraction. a-axis samples were cut from the Boule with a diamond saw and polished to an appropriate shape and size.
- two samples, labeled #11b and #1, were prepared and measured.
-

sample	$T_c(\rho = 0)$
#1	
#11b	19 K

Sample dimensions

Sample	L (mm)	W (mm)	T (μm)	$\alpha = TW/L$ (cm)
#11a (side 1)	1.28 ± 0.05	0.530 ± 0.008	303 ± 8	1.255 $\times 10^{-2} \pm 5\%$
#11a (side 2)	1.86 ± 0.05	0.530 ± 0.008	303 ± 8	8.634 $\times 10^{-3} \pm 4\%$
#1 (side 1)	1.159 ± 0.146	0.540 ± 0.008	285 ± 8	1.295 $\times 10^{-2} \pm 13\%$
#1 (side 2)	1.736 ± 0.124	0.540 ± 0.008	285 ± 8	8.647 $\times 10^{-2} \pm 8\%$

Sample and contact resistance

- 6 contact pads put on both samples.
- both samples were annealed at 500 °C under flowing O_2 for 1 hr. to diffuse the contacts.
- sample #1 was annealed in flowing O_2 at 800 °C for $\sim$ 20 hrs. before before putting contact pads on the sample. Similar to LSCO $x = 0.06$ #2, the contact resistances are poor for this sample, indicative of surface degradation.

	ρ_{samp} [mΩ cm]	R_{samp} [Ω]	$R_{(I^-,V^-)}$ [Ω]	$R_{(I^-,V^+)}$ [Ω]	$R_{(I^-,I^+)}$ [Ω]	$R_{(V^+,V^-)}$ [Ω]
#11b (face 1, room T)	1.439	0.1147	0.861	0.782	0.541	1.259
#11b (face 2, room T)	1.433	0.166	0.372	0.571	0.541	0.625
#11b (face 1, 5.7K)	0	0	0.067	0.079	0.015	0.132
#11b (face 2, 5.7K)	0	0	0.027	0.055	0.015	0.067
#1 (face 1, room T)	1.807	0.1395	94.9	108.9	80.8	57.8
#1 (face 2, room T)	1.859	0.215	81.2	87.5	81.2	21.7

Measurement summary

- Oct. 2001 – sample 11b – ρ vs. T between 4K and 300 K in Heliox. And measured ρ vs. T in 15T between 1.3 K and 20 K.
- Nov. 2001 – sample 1 – ρ vs. T between 11 K and 300 K in Heliox.
- April 2002 – sample 11b – κ vs. T between 40 mK and 1 K in the dilution refridgerator in 0 and 13 T.
- May 2002 – ac susceptability on a piece of LSCO $x = 0.07$. Measured by Patrick Fournier at the University of Sherbrooke.
- Mar. 2003 – EPMA analysis on a piece of LSCO $x = 0.07$.

Published data

- – samples #11b – [4] – κ vs. T at low T in 0T.

A.1.5 $x = 0.09$

- Sample growth: Boule grown by Nigel Hussey and M. Nohara at the University of Tokyo in the lab of Hide Takagi.

- Boule oriented using Laue x-ray diffraction. a-axis samples were cut from the Boule with a diamond saw and polished to an appropriate shape and size.
- six samples, #1, #2, #3, #6, #7 and #8 were prepared and measured.
-

sample	$T_c(\rho = 0)$
#1	
#2	N/A
#3	17 K
#6	15 K
#7	16 K
#8	

Sample dimensions

Sample	L (mm)	W (mm)	T (μm)	$\alpha = TW/L$ (cm)
#1	2.00	0.450	100	2.25×10^{-3}
#2	0.649 ± 0.112	0.313 ± 0.008	60 ± 8	$2.90 \times 10^{-3} \pm 22\%$
#3	1.705 ± 0.160	0.424 ± 0.008	45.5 ± 8	$1.13 \times 10^{-3} \pm 20\%$
#6 (side 1)	1.86 ± 0.16	0.555 ± 0.008	45 ± 8	$1.34 \times 10^{-3} \pm 20\%$
#6 (side 2)	1.440 ± 0.137	0.555 ± 0.008	45 ± 8	$1.73 \times 10^{-3} \pm 20\%$
#7	0.435 ± 0.05	0.533 ± 0.008	83 ± 8	$1.02 \times 10^{-3} \pm 15\%$
#8 (side 1)	1.084 ± 0.116	0.244 ± 0.011	180 ± 8	$4.05 \times 10^{-3} \pm 12\%$
#8 (side 2)	1.748 ± 0.128	0.244 ± 0.011	180 ± 8	$2.51 \times 10^{-3} \pm 10\%$

Sample and contact resistance

- 6 contact pads put on samples 6 and 8. All other samples used a 4 wire configuration.
- Robert Hill put contacts on samples #1.
- sample #1 was repolished in Dec. 2000 to produce samples #2 and #3
- all samples were annealed at 500 °C under flowing O_2 for 1 hr. to diffuse the contacts.
- samples #2 was annealed in flowing O_2 at 900 °C for $\sim$ 50 hrs. before before putting contact pads on the sample. After annealing the edges of sample #2 were cracked, suggesting more severe sample degradation than simply the surface.

	ρ_{samp} [mΩ cm]	R_{samp} [Ω]	$R_{(I^-,V^-)}$ [Ω]	$R_{(I^-,V^+)}$ [Ω]	$R_{(I^-,I^+)}$ [Ω]	$R_{(V^+,V^-)}$ [Ω]
#1 (room T)	1.6	0.709	-	-	-	-
#2 (room T)	7.08	2.44	1.2	6.8	6.2	4.0
#3 (room T)	1.542	1.365	-	-	-	-
#7 (room T)	1.416	0.1388	0.6	0.8	0.7	1.0
#7 (10K)	0	0	-	-	0.0101	-
#6 (face 1, room T)	1.551	1.158	0.8	1.9	1.1	2.4
#6 (face 2, room T)	1.588	-	-	1.9	1.1	4.3

Measurement summary

- Feb. 2001 – sample 3 – κ and ρ vs. T between 2 K and 120 K.
- April 2001 – sample 3 – κ vs. T at 0, 8 and 13 T between 0 and 0.6 K in the dilution refridgerator
- May 2001 – sample 3 – ρ vs. T between 300 mK and 50 K in 0 and 15T in the Heliox.
- June 2001 – sample 2 – ρ vs. T between 2 K and 300 K. Full SC transition not observed in this sample.
- June 2001 – samples 6 and 7 – ρ vs. T between 2 K and 300 K. Measured T sweeps in 0T and 15T between 0.5 K and 30 K.
- July 2001 – sample 7 – κ vs. T at 0, 4, 8, 11, 12 and 13 T between 0 and 0.6 K in the dilution refridgerator.
- Dec. 2001 – sample 7 – ρ in pulsed fields up to 60T. Measured by Cyril Proust at the hight magnetic field lab in Toulouse, France. ρ measured at 0.39, 0.60, 0.95, 1.42, 2.1 and 4.9 K.
- May 2002 – ac susceptability on a piece of LSCO $x = 0.09$. Measured by Patrick Fournier at the University of Sherbrooke.
- Mar. 2003 – EPMA analysis on a piece of LSCO $x = 0.09$.

Published data

- – sample #7 – [4] – κ vs. T at low T in 0T.
- – sample #7 – [1] – κ vs. T at low T in 0T and 13 T and κ_0/T vs. H at intermediate fields.

A.1.6 $x = 0.17$

- Sample growth: Grown by T. Kimura (passed on to us by Prof. Phuan Ong)
- Sample arrived already cut to size with contact and wires attached by Prof. Ong's group
- $T_c(\rho = 0) = 34$ K

Sample dimensions

L (mm)	W (mm)	T (μm)	$\alpha = TW/L$ (cm)
0.97 ± 0.06	1.26 ± 0.01	212 ± 8	2.75 $\times 10^{-3}$ ± 7%

Sample and contact resistance

- 4 contact pads put on using Ag epoxy.

	ρ_{samp} [$\mu\Omega$ cm]	R_{samp} [mΩ]	$R_{(I^-)}$ [mΩ]	$R_{(V^-)}$ [mΩ]	$R_{(V^+)}$ [mΩ]	$R_{(I^+)}$ [mΩ]
room T	425	15.5	67	120	180	64
4K	0	0	8	7	4	12

Measurement summary

- Nov./Dec. 1999 – κ between 4 K and 80 K.
- Nov. 1999 – ρ between 4 K and 300 K.
- Feb. 2000 – κ between 40 mK and 0.6 K in the dilution refridgerator in 0T, 0.8T, 8T and 13T.
- May 2002 – *ac* susceptability. Measured by Patrick Fournier at the University of Sherbrooke.
- Dec. 2002 – κ remeasured between 40 mK and 4 K in the dilution refridgerator in 0T and 13T.

Published data

- – [1] – κ vs. T in the dilution refridgerator in 0T and 13T and $\kappa(60\text{mK})/T$ vs. H at intermediate fields.
- – [4] – κ vs. T in the dilution refridgerator in 0T and κ vs. T between 4 K and 70 K.

A.1.7 $x = 0.20$

- a-axis sample grown Nigel Hussey and M. Nohara at the University of Tokyo in the lab of Hide Takagi.
- originally recieved a single sample (sample 1). This sample was cut and polished to make two smaller a-axis samples (a and b).
-

sample	$T_c(\rho = 0)$
#1	31 K
a	32.5 K
b	33.5 K

Sample dimensions

Sample	L (mm)	W (mm)	T (μm)	$\alpha = TW/L$ (cm)
#1	1.447 ± 0.080	1.440 ± 0.017	287 ± 15	$2.86 \times 10^{-2} \pm 8\%$
a (side 1)	1.425	0.220	200	3.09×10^{-3}
a (side 2)	1.35	0.220	200	3.26×10^{-3}
b (side 1)	1.175 ± 0.05	0.227 ± 0.011	167 ± 8	$3.219 \times 10^{-3} \pm 8\%$
b (side 2)	1.485 ± 0.05	0.227 ± 0.011	167 ± 8	$3.549 \times 10^{-3} \pm 8\%$

Sample and contact resistance

- 4 contact pads put on sample 1. 6 contact pads put on samples a and b.
- all samples were annealed at 500 °C under flowing O_2 for 1 - 2 hrs. to diffuse the contacts.
- resistivity measurements on sample 1 are unreliable: room T resistance changed from 9.3 mΩ to 17.09 mΩ to 25 mΩ between measurements and heating on a hotplate to 200 °C for 10 min.

	ρ_{samp} [$\mu\Omega$ cm]	R_{samp} [mΩ]	$R_{(I^-,V^-)}$ [Ω]	$R_{(I^-,V^+)}$ [Ω]	$R_{(I^-,I^+)}$ [Ω]	$R_{(V^+,V^-)}$ [Ω]
#1 (room T)	217	9.63	1.4	1.0	0.8	1.4
a (face 1, room T)	229	74.1	0.432	0.485	0.250	0.687
a (face 2, room T)	296	90.7	0.532	0.624	0.250	0.955
b (face 1, room T)	261.7	81.3	-	-	0.294	-
b (face 2, room T)	263.3	103.3	-	-	0.294	-
b (30.5K)	0	0	-	-	0.0371	-

Measurement summary

- Aug. 2000 – sample 1 – κ between 4 K and 70 K.
- Aug. 2000 – sample 1 – ρ between 4 K and 300 K.
- Mar. 2001 – sample a – ρ between 4 K and 300 K. There is poor agreement between both sides of the sample, suggesting possible c-axis contanimation of the ab plane resistivity.
- Mar. 2001 – sample a – κ between 2 K and 80 K.
- July 2001 – sample b – ρ between 4 K and 300 K.
- Aug. 2001 – sample b – κ between 40 mK and 0.6 K in the dilution refridgerator in 0T, 1T, 4T, 7T and 13T.
- May 2002 – ac susceptability. Measured by Patrick Fournier at the University of Sherbrooke.

Published data

- – samples b – [4] – κ vs. T at low T in 0T.
- – samples b – [1] – κ vs. T at low T in 0T and 13 T and κ_0/T vs. H at intermediate fields.

A.1.8 $x = 0.25$

- Sample grown Harry Zhang at the University of Toronto.
- Boule oriented using Laue x-ray diffraction. a-axis samples were subsequently cut and polished from the Boule using a diamond saw.
- $T_c(\rho = 0) = 13$ K

Sample dimensions

Sample	L (mm)	W (mm)	T (μm)	$\alpha = TW/L$ (cm)
#1 (side 1)	1.55 $\pm$ 0.075	0.666 $\pm$ 0.008	106 $\pm$ 8	4.569 $\times 10^{-3} \pm 9\%$
#1 (side 2)	1.90 $\pm$ 0.100	0.666 $\pm$ 0.008	106 $\pm$ 8	3.716 $\times 10^{-3} \pm 9\%$

Sample and contact resistance

- 6 contact pads put on sample and annealed at 500 °C under flowing O_2 for 1 hrs. to diffuse the contacts.

	ρ_{samp} [$\mu\Omega$ cm]	R_{samp} [mΩ]	$R_{(I^-,V^-)}$ [Ω]	$R_{(I^-,V^+)}$ [Ω]	$R_{(I^-,I^+)}$ [Ω]	$R_{(V^+,V^-)}$ [Ω]
face 1 (room T)	321	70.2	0.442	0.335	0.356	0.498
face 2 (room T)	313	84.2	0.285	0.409	0.356	0.434
face 1 (6K)	0	0	0.027	0.019	0.045	0.030
face 1 (6K)	0	0	0.019	0.027	0.045	0.030

Measurement summary

- Mar. 2003 – EPMA analysis on a pieces of LSCO $x = 0.25$ from the top bottom and middle of the Boule.
- Apr. 2003 – ρ vetween 4 K and 300 K in 0T and 2 K to 100 K in 15 T.
- July 2003 – κ between 40 mK and 1 K in the dilution refridgerator in 0T, 7.92T and 12T.
- Oct. 2003 – κ between 2 K and 110 K.

A.1.9 $x = 0.30$

- Sample grown Harry Zhang at the University of Toronto.
- Boule oriented using Laue x-ray diffraction. a-axis samples were subsequently cut and polished from the Boule using a diamond saw.
- Sample annealed in 3 atm O_2 pressure at 900 °C for 150 hrs.

Sample dimensions

Sample	L (mm)	W (mm)	T (μm)	$\alpha = TW/L$ (cm)
#1 (face 1)	1.58 ± 0.05	0.508 ± 0.008	75.8 ± 8	2.438 $\times 10^{-3}$ ± 5%
#1 (face 2)	2.13 ± 0.05	0.508 ± 0.008	75.8 ± 8	1.808 $\times 10^{-3}$ ± 5%

Sample and contact resistance

- 6 contact pads put on sample and annealed at 500 °C under flowing O_2 for 1 hrs. to diffuse the contacts.

	ρ_{samp} [$\mu\Omega$ cm]	R_{samp} [mΩ]	$R_{(I^-,V^-)}$ [Ω]	$R_{(I^-,V^+)}$ [Ω]	$R_{(I^-,I^+)}$ [Ω]	$R_{(V^+,V^-)}$ [Ω]
face 1 (room T)	150.9	61.90	10.5	0.485	0.451	10.6
face 2 (room T)	147.5	81.59	0.794	0.432	0.451	0.927
face 1 (2K)	-	-	35.6	0.353	0.100	35.9
face 1 (2K)	-	-	0.832	0.207	0.100	0.955

Measurement summary

- Feb. 2003 – ρ between 4 K and 300 K in 0T and 2 K to 40 K in 13 T.
- Mar. 2003 – κ between 40 mK and 1.5 K in the dilution refridgerator in 0T and 13T.
- Oct. 2003 – κ between 2 K and 130 K. ρ between 4 K and 300 K
- Jan. 2004 – κ in the dilution refridgerator. Measured in Sherbrooke.

A.2 Tl2201

A.2.1 UBC #3

- Sample growth: Grown by Ruixing Liang and Darren Peets at the University of British Columbia
- Sample annealed under different conditions to produce different O doping.
- Sample annealed by Ruixing Liang at 400 °C and 60 atm O_2 for 14 days. For this annealing condition the samples is referred to as UBC3A (or from earlier work simply as UBC3).
- Sample annealed by Ruixing Liang at 480 °C and 50 atm O_2 for 14 days. For this annealing condition the samples is referred to as UBC3B.
- Sample annealed by Ruixing Liang at ??. For this annealing condition the samples is referred to as UBC3C.
- Geometric factor measured with optical microscope for L and W and SEM for T
-

sample	$T_c(\rho = 0)$
UBC3A	19 K
UBC3B	14 K
UBC3C	72 K

Sample Dimensions

L (mm)	W (mm)	T (μm)	$\alpha = TW/L$ (cm)
0.386 ± 0.053	0.447 ± 0.008	27 ± 5%	3.13 $\times 10^{-3}$ ± 15%

Sample and contact resistance

- 4 contact pads were made by evaporating gold onto sample. Wires were attached with Ag paint. The wires and paint were removed between each annealing.

	ρ_{samp} [$\mu\Omega$ cm]	R_{samp} [mΩ]	$R_{(I^-,V^-)}$ [Ω]	$R_{(I^-,V^+)}$ [Ω]	$R_{(I^-,I^+)}$ [Ω]	$R_{(V^+,V^-)}$ [Ω]
UBC3A (room T)	395.6	126.4	0.872	0.849	0.797	1.257
UBC3A (10K)	0	0	0.392	0.326	1.08	0.453
UBC3B (room T)	262.6	83.9	1.59	0.595	0.668	1.67
UBC3B (6.5K)	0	0	0.512	0.075	0.105	0.529
UBC3C (room T)	310	99.4	0.509	-	-	-
UBC3C (6K)	0	0	0.0928	-	-	-

Measurement summary

- Aug. 2003 – UBC3A – ρ between 4 K and 300 K in 0T.
- Aug. 2003 – UBC3A – κ between 40 mK and 3 K in the dilution refridgerator in 0T and 12T.
- Oct. 2003 – UBC3B – ρ between 4 K and 300 K in 0T.
- May 2004 – UBC3C – ρ between 4 K and 300 K in 0T. Measured in Sherbrooke by Shiyan Li and Ronan Larger.

A.2.2 UBC #4

- Sample growth: Grown by Ruixing Liang and Darren Peets at the University of British Columbia
- Sample annealed under different conditions to produce different O doping.
- Sample annealed by Ruixing Liang at 450 °C and 60 atm O_2 for 14 days. For this annealing condition the samples is referred to as UBC4A (or from earlier work simply as UBC4).
- Sample annealed by Ruixing Liang at ??. For this annealing condition the samples is referred to as UBC4B.
- Geometric factor measured with optical microscope for L and W and SEM for T
sample	$T_c(\rho = 0)$
UBC4A	5 K
UBC4B	76 K

Sample Dimensions

L (mm)	W (mm)	T (μm)	$\alpha = TW/L$ (cm)
0.450 ± 0.070	0.400 ± 0.008	39 ± 5%	3.47 $\times 10^{-3}$ ± 21%

Sample and contact resistance

- 4 contact pads were made by evaporating gold onto sample. Wires were attached with Ag paint. The wires and paint were removed between each annealing.

	ρ_{samp} [$\mu\Omega$ cm]	R_{samp} [mΩ]	$R_{(I^-,V^-)}$ [Ω]	$R_{(I^-,V^+)}$ [Ω]	$R_{(I^-,I^+)}$ [Ω]	$R_{(V^+,V^-)}$ [Ω]
UBC4A (room T)	173.5	50.0	0.700	0.691	0.440	0.821
UBC4A (7K)	-	2.25	0.112	0.026	0.064	0.142
UBC4B (room T)	260	74.9	0.312	-	-	-
UBC4B (6K)	0		0.0125	-	-	-

Measurement summary

- Sept. 2003 – UBC4A – ρ between 4 K and 300 K in 0T.
- Oct. 2003 – UBC4A – κ between 4 K and 100 K.
- May 2004 – UBC4B – ρ between 4 K and 300 K in 0T. Measured in Sherbrooke by Shiyan Li and Ronan Larger.

A.2.3 UBC #1

- Sample growth: Grown by Ruixing Liang and Darren Peets at the University of British Columbia (batch P7100)
- Sample annealed under different conditions to produce different O doping.
- Sample annealed by Dave Hawthorn at 350 °C in flowing O_2 for 2 hrs. to cure contacts and then annealed under vacuum (0.5 - 2 $\times 10^{-6}$ torr) at 500 °C and 60 atm O_2 for ~20 hours. For this annealing condition the samples is referred to as UBC1A (or from earlier work simply as UBC1).
- Sample reannealed by Dave Hawthorn at 480 °C in flowing Ar atmosphere for 3 hrs. Sample quench cooled from 480 °C to room T. For this annealing condition the samples is referred to as UBC1B.
- Geometric factor measured with optical microscope for L and W and SEM for T
-

sample	$T_c(\rho = 0)$
UBC1A	84 K
UBC1B	26 K

Sample dimensions

L (mm)	W (mm)	T (μm)	$\alpha = TW/L$ (cm)
0.724 ± 7%	0.377 ± 10%	36.35 ± 10%	1.90×10^{-3} ± 16%

Sample and contact resistance

- 4 contact pads were made by evaporating gold onto sample. Wires were attached with Ag paint. The wires and paint were removed between each annealing.

	ρ_{samp} [$\mu\Omega$ cm]	R_{samp} [mΩ]	$R_{(I^-,V^-)}$ [Ω]	$R_{(I^-,V^+)}$ [Ω]	$R_{(I^-,I^+)}$ [Ω]	$R_{(V^+,V^-)}$ [Ω]
UBC1A (room T)	594	313.0	3.26	3.03	1.65	4.8
UBC1A (5.7K)	0	0	7.33	6.95	0.916	12.5
UBC1B (room T)	368.6	194.0	9.25	0.750	0.814	9.298
UBC1B (20K)	0	0	1.61	0.0578	0.037	1.62

Measurement summary

- April 2003 – UBC1A – ρ between 4 K and 300 K in 0T.
- April 2003 – UBC1A – κ between 40 mK and 4 K in the dilution refridgerator at 0T and 10.4T.
- May/June 2003 – UBC1A – κ between 2 K and 140 K. ρ between 4 K and 300 K in 0T. κ also measured in 10.5 T 2 K and 100 K.
- Sept. 2003 – UBC1B – ρ between 4 K and 300 K in 0T.
- Sept. 2003 – UBC1B – κ between 4 K and 120 K in 0T.
- Oct. 2003 – UBC1B – κ between 40 mK and 4 K in the dilution refridgerator at 0T and 10T.

A.2.4 UBC #2

- Note: sample also labeled UBC60K in some lab notebooks and data files
- Sample growth: Grown by Ruixing Liang and Darren Peets at the University of British Columbia (batch P7100)
- Sample annealed by Ruixing Liang at 400 °C for 12 days under an oxgyen partial pressure created by CuO/Cu_2O at 500 °C.
- Geometric factor measured with optical microscope for L and W and SEM for T
- $T_c(\rho = 0) = 68$K

Sample dimensions

L (mm)	W (mm)	T (μm)	$\alpha = TW/L$ (cm)
0.374 ± 19%	0.463 ± 5%	46.0 ± 10%	5.69×10^{-3} ± 22%

Sample and contact resistance

- 4 contact pads were made by evaporating gold onto sample. Wires were attached with Ag paint.

	ρ_{samp} [$\mu\Omega$ cm]	R_{samp} [mΩ]	$R_{(I^-,V^-)}$ [Ω]	$R_{(I^-,V^+)}$ [Ω]	$R_{(I^-,I^+)}$ [Ω]	$R_{(V^+,V^-)}$ [Ω]
UBC2 (room T)	287.9	50.6	4.6	1.9	1.0	4.8
UBC2 (50K)	0	0	0.075	0.224	0.071	0.057

Measurement summary

- April 2003 – UBC2 – ρ between 4 K and 300 K in 0T.
- June 2003 – UBC2 – κ between 40 mK and 4 K in the dilution refridgerator at 0T and 13T.
- June 2003 – UBC2 – κ between 4 K and 110 K. ρ between 4 K and 300 K in 0T.

A.2.5 Mac #15

- Sample growth: Grown by Andrew Mackenzie at Cambridge University
- Sample annealed by Dave Hawthorn and Etienne Boaknin at 350 °C in flowing O_2 for 2 hrs. to cure contacts and then annealed under vacuum (0.5 - 2 $\times10^{-6}$ torr) at 500 °C for ~20 hours.
- Geometric factor measured with optical microscope for L and W and SEM for T
- $T_c(\rho = 0) = 89$K

Sample dimensions

L (mm)	W (mm)	T (μm)	$\alpha = TW/L$ (cm)
0.30 ± 22%	0.40 ± 5%	15.4 ± 10%	2.05×10^{-3} ± 25%

Sample and contact resistance

- 4 contact pads were made by evaporating gold onto sample. Wires were attached with Ag paint.

Mac #15 (Room T)

ρ_{samp}	1607 $\mu\Omega$ cm
R_{samp}	784 mΩ
$R(I-) + R_{samp}$ + wire	2.5 Ω
$R(V-) + R_{samp}$ + wire	3.15 Ω
$R(V+) + R_{samp}$ + wire	2.93 Ω
$R(I+) + R_{samp}$ + wire	3.25 Ω

Mac #15 (2 K)

R_{samp}	0
$R(I-) + R_{samp}$ + wire	0.475 Ω
$R(V-) + R_{samp}$ + wire	0.297 Ω
$R(V+) + R_{samp}$ + wire	0.458 Ω
$R(I+) + R_{samp}$ + wire	0.257 Ω

Measurement summary

- Sept./Oct. 2002 – ρ between 4 K and 300 K in 0T in Heliox.
- Nov. 2002 – κ between 40 mK and 4 K in the dilution refridgerator at 0, 0.8, 4, 8 and 13T.
- June 2003 – UBC2 – κ between 4 K and 110 K. ρ between 4 K and 300 K in 0T.
- Feb. 2003 – κ between 2.5 K and 100 K. (Note: measurement not reliable at high T due to potential heat losses.)

A.2.6 Mac #18 and #19

- Sample growth: Grown by Andrew Mackenzie at Cambridge University
- Both samples annealed at 350 °C in flowing O_2 for 2 hrs. to cure contacts and then annealed under vacuum (0.5 - 2 $\times 10^{-6}$ torr) at 500 °C for ~20 hours.
-

sample	$T_c(\rho = 0)$
Mac #18	88 K
Mac #19	85 K

Sample dimensions

Sample	L (mm)	W (mm)	T (μm)	$\alpha = TW/L$ (cm)
Mac #18	0.238 ± 0.043	0.209	15 ± 25%	1.32×10^{-3}
Mac #19	0.209 ± 0.043	0.157	14 ± 25%	1.05×10^{-3}

Sample and contact resistance

- 4 contact pads were made by evaporating gold onto sample. Wires were attached with Ag paint.

	ρ_{samp} [$\mu\Omega$ cm]	R_{samp} [mΩ]	$R_{(I^-,V^-)}$ [Ω]	$R_{(I^-,V^+)}$ [Ω]	$R_{(I^-,I^+)}$ [Ω]	$R_{(V^+,V^-)}$ [Ω]
Mac #18 (room T)	1830	1390	11.5	187	9.7	189
Mac #18 (4K)	0	0	7.7	212	7.8	242
Mac #19 (room T)	1770	1690	16.7	19.7	25.3	23.8
Mac #19 (4K)	0	0	6.1	7.7	11.4	9.1

Measurement summary

- Feb. 2002 – ρ between 4 K and 300 K in 0T.

BIBLIOGRAPHY

[1] D. G. Hawthorn, R. W. Hill, C. Proust, F. Ronning, Mike Sutherland, Etienne Boaknin, C. Lupien, M. A. Tanatar, Johnpierre Paglione, S. Wakimoto, H. Zhang, Louis Taillefer, T. Kimura, M. Nohara, H. Takagi, and N. E. Hussey. Field-induced thermal metal-to-insulator transition in underdoped $La_{2-x}Sr_xCuO_{4+\delta}$. *Phys. Rev. Lett.*, 90:197004, 2003. vii, 72, 80, 131, 133, 134, 137, 138, 139

[2] D. G. Hawthorn, R. W. Hill, F. Ronning, Mike Sutherland, Etienne Boaknin, M. A. Tanatar, Johnpierre Paglione, S. Wakimoto, H. Zhang, and Louis Taillefer. Field-induced thermal metal-to-insulator transition in underdoped LSCO. *Physica C*, 408-410C:725, 2004. vii

[3] X. F. Sun, Seiki Komiya, J. Takeya, and Yoichi Ando. Magnetic-field-induced localization of quasiparticles in underdoped $La_{2-x}Sr_xCuO_4$ single crystals. *Phys. Rev. Lett.*, 90:117004, 2003. vii, 101

[4] M. Sutherland, D. G. Hawthorn, R. W. Hill, F. Ronning, S. Wakimoto, H. Zhang, C. Proust, Etienne Boaknin, C. Lupien, Louis Taillefer, Ruixing Liang, D. A. Bonn, W. N. Hardy, Robert Gagnon, N. E. Hussey, T. Kimura, M. Nohara, and H. Takagi. Thermal conductivity across the phase diagram of cuprates: Low-energy quasiparticles and doping dependence of the superconducting gap. *Phys. Rev. B*, 67:174520, 2003. vii, viii, 1, 2, 9, 69, 70, 72, 76, 77, 104, 105, 107, 120, 133, 134, 135, 137, 138, 139

[5] J. Takeya, Yoichi Ando, Seiki Komiya, and X. F. Sun. Low-temperature electronic heat transport in $La_{2-x}Sr_2CuO_4$ single crystals: Unusual low-energy physics in the normal and superconducting states. *Phys. Rev. Lett.*, 88:077001, 2002. viii, 96, 109

[6] Mike Sutherland, D.G. Hawthorn, R.W. Hill, F. Ronning, M.A. Tanatar, J. Paglione, E. Boaknin, H. Zhang, Louis Taillefer, J. DeBenedictis, Ruixing Liang, D.A. Bonn, and W.N. Hardy. Nodal metallic phase in underdoped cuprates. unpublished (2004). viii, 1, 3, 92, 104, 105, 134

[7] Cyril Proust, Etienne Boaknin, R. W. Hill, Louis Taillefer, and A. P. Mackenzie. Heat transport in a strongly overdoped cuprate: Fermi liquid and a pure d-wave BCS superconductor. *Phys. Rev. Lett.*, 89:147003, 2002. viii, 2, 16, 19, 47, 69, 78, 79, 86, 91, 98, 101, 122

[8] D. G. Hawthorn, S. Li, M. Sutherland, Etienne Boaknin, R. W. Hill, C. Proust, F. Ronning, M. A. Tanatar, Johnpierre Paglione, N. N. Koleshnikov, Ruixing Liang, D. Peets, D. Bonn, W. Hardy, and Louis Taillefer. The quasiparticle gap in Tl2201 from low temperature thermal conductivity. unpublished (2004). viii

[9] M. Chiao, R. W. Hill, Christian Lupien, Bojana Popic, Robert Gagnon, and Louis Taillefer. Quasiparticle transport in the vortex state of $YBa_2Cu_3O_{6.9}$. *Phys. Rev. Lett.*, 82:2943, 1999. viii, 80, 88, 110, 124

[10] H. Aubin, Kamran Behnia, Shuuichi Ooi, and Tsuyoshi Tamegai. Evidence for field-induced excitations in low-temperature thermal conductivity of $Bi_2Sr_2CaCu_2O_8$. *Phys. Rev. Lett.*, 82:624, 1999. viii, 39, 80, 81, 88, 101, 110

[11] Y. Nakamura, S. Uchida, T. Kimura, N. Motohira, K. Kishio, K. Kitazawa, T. Arima, and Y. Tokura. In-plane and out-of-plane thermal conductivity of $La_{2-x}Sr_xCuO_4$ single crystals. *Physica C*, 185:1409, 1991. ix, 114, 118, 126

[12] J. G. Bednorz and K. A. Muller. Possible high T_c superconductivity in the Ba-La-Cu-O system. *Z. Phys. B*, 64:189, 1986. 1, 5

[13] Mike Sutherland. *Thermal conductivity in YBCO.* PhD thesis, University of Toronto, 2004. 1, 104, 105

[14] L. Taillefer, B. Lussier, R. Gagnon, K. Behnia, and H. Aubin. Universal heat conduction in $YBa_2Cu_3O_{6.9}$. *Phys. Rev. Lett.*, 79:483, 1997. xiv, 2, 8, 19, 69, 74, 75

[15] M. Chiao, R. W. Hill, Christian Lupien, Louis Taillefer, P. Lambert, R. Gagnon, and P. Fournier. Low-energy quasiparticles in cuprate superconductors: A quantitative analysis. *Phys. Rev. B*, 62:3554, 2000. 2, 19, 35, 69, 75, 77, 88

[16] S. Nakamae, K. Behnia, L. Balicas, F. Rullier-Albenque, H. Berger, and T. Tamegai. Effect of controlled disorder on quasiparticle thermal transport in $Bi_2Sr_2CaCu_2O_8$. *Phys. Rev. B*, 63:184509, 2001. 2, 19, 69, 75, 88

[17] M. K. Wu, J. R. Ashburn, C. J. Torng, P. H. Hor, R. L. Meng, L. Gao, Z. J. Huang, Y. Q. Wang, and C. W. Chu. Superconductivity at 93 K in a new mixed-phase Y-Ba-Cu-O compound system at ambient pressure. *Phys. Rev. Lett.*, 58:908, 1987. 5

[18] Jr. Charles P. Poole, editor. *Handbook of Superconductivity.* Academic Press, New York, 2000. 5, 7

[19] Sudip Chakravarty, R. B. Laughlin, Dirk K. Morr, and Chetan Nayak. Hidden order in the cuprates. *Phys. Rev. B*, 63:094503, 2001. 5, 11, 92

[20] T. C. Hsu, J. B. Marston, and I. Affleck. Two observable features of the staggered-flux phase at nonzero doping. *Phys. Rev. B*, 43:2866, 1991. 5

[21] Xiao-Gang Wen and Patrick A. Lee. Theory of underdoped cuprates. *Phys. Rev. Lett.*, 76:503, 1996. 5, 11, 108

[22] C. M. Varma. Pseudogap phase and the quantum-critical point in copper-oxide metals. *Phys. Rev. Lett.*, 83:3538, 1999. 5, 6, 11

[23] J. Zaanen and O. Gunnarson. Charged magnetic domain lines and the magnetism of high-T_c oxides. *Phys. Rev. B*, 40:7391, 1989. 5, 11

[24] E. W. Carlson, V. J. Emery, S. A. Kivelson, and D. Orgad. Concepts in high temperature superconductivity. In K. H. Bennemann and J. B. Ketterson, editors, *The Physics of Superconductors*, volume II. Springer-Verlag, 2004. (cond-mat/0206217). 5, 11, 12, 15, 92

[25] J. L. Tallon and J. W. Loram. The doping dependence of T^* - what is the real high-T_c phase diagram? *Physica C*, 349:53, 2001. 6

[26] J. Orenstein and A. J. Millis. Advances in the physics of high-temperature superconductivity. *Science*, 288:468, 2000. 6, 8, 12

[27] M. R. Norman and C. Pépin. The electronic nature of high temperature cuprate superconductors. *Rep. Prog. Phys.*, 66:1547, 2003. 6, 8

[28] M. A. Kastner, R. J. Birgeneau, G. Shirane, and Y. Endoh. Magnetic, transport, and optical properties of monolayer copper oxides. *Rev. Mod. Phys.*, 70:897, 1998. 8, 49

[29] C. C. Tsuei and J. R. Kirtley. Pairing symmetry in cuprate superconductors. *Rev. Mod. Phys.*, 72:969, 2000. 8

[30] N.E. Hussey. Low-energy quasiparticles in high-T_c cuprates. *Advances in Physics*, 51:1685, 2002. 8, 32, 33, 36

[31] W. N. Hardy, D. A. Bonn, D. C. Morgan, R. Liang, and K. Zhang. Precision measurements of the temperature dependence of lambda in $YBa_2Cu_3O_{6.95}$: Strong evidence for nodes in the gap function. *Phys. Rev. Lett.*, 70:3999, 1993. 8, 32, 33

[32] P. J. White, Z. X. Shen, C. Kim, J. M. Harris, A. G. Loeser, P. Fournier, and A. Kapitulnik. Rapid suppression of the superconducting gap in overdoped $Bi_2Sr_2CaCu_2O_{8+\delta}$. *Phys. Rev. B*, 54:R15669, 1996. 9, 77

[33] Ch. Renner, B. Revaz, J.-Y. Genoud, K. Kadowaki, and Ø. Fisher. Pseudogap precursor of the superconducting gap in under- and overdoped $Bi_2Sr_2CaCu_2O_{8+\delta}$. *Phys. Rev. Lett.*, 80:149, 1998. 9, 77, 108

[34] Y. J. Uemura, G. M. Luke, B. J. Sternlieb, J. H. Brewer, J. F. Carolan, W. N. Hardy, R. Kadono, J. R. Kempton, R. F. Kiefl, S. R. Kreitzman, P. Mulhern, T. M. Riseman, D. Ll. Williams, B. X. Yang, S. Uchida, H. Takagi, J. Gopalakrishnan, A. W. Sleight, M. A. Subramanian, C. L. Chien, M. Z. Cieplak, Gang Xiao,

V. Y. Lee, B. W. Statt, C. E. Stronach, W. J. Kossler, and X. H. Yu. Universal correlations between T_c and n_s/m^* (carrier density over effective mass) in high-T_c cuprate superconductors. *Phys. Rev. Lett.*, 62:2317, 1989. 9

[35] Tom Timusk and Bryan Statt. The pseudogap in high-temperature superconductors: an experimental survey. *Rep. Prog. Phys.*, 62:61, 1999. 9

[36] Jr. W. W. Warren, R. E. Walstedt, G. F. Brennert, R. J. Cava, R. Tycko, R. F. Bell, and G. Dabbagh. Cu spin dynamics and superconducting precursor effects in planes above T_c in $YBa_2Cu_3O_{6.7}$. *Phys. Rev. Lett.*, 62:1193, 1989. 9

[37] J. M. Harris, A. G. Loeser, D. S. Marshall, M. C. Schabel, and Z.-X. Shen. Anomalous superconducting state gap size versus T_c behavior in underdoped $Bi_2Sr_2Ca_{1-x}Dy_xCu_2O_{8+\delta}$. *Phys. Rev. B*, 54:R15665, 1996. 9, 10

[38] A. G. Loeser, Z.-X. Shen, D. S. Dessau, D. S. Marshall, C. H. Park, P. Fournier, and A. Kapitulnik. Excitation gap in the normal state of underdoped $Bi_2Sr_2CaCu_2O_{8+\delta}$. *Science*, 273:325, 1996. 9

[39] H. Ding, T. Yokoya, J. C. Campuzano, T. Takahashi, M. Randeria, M. R. Norman, T. Mochiku, K. Kadowaki, and J. Giapinzakis. Spectroscopic evidence for a pseudogap in the normal state of underdoped high-T_c superconductors. *Nature*, 382:51, 1996. 9

[40] C. C. Homes, T. Timusk, R. Liang, D. A. Bonn, and W. N. Hardy. Optical conductivity of c axis oriented $YBa_2Cu_3O_{6.70}$: evidence for a pseudogap. *Phys. Rev. Lett.*, 79:1645, 1993. 9

[41] B. Batlogg, H. Y. Hwang, H. Takagi, R. J. Cava, H. L. Kao, and J. Kwo. Normal state phase diagram of $(La,Sr)_2CuO_4$ from charge and spin dynamics. *Physica C*, 235:130, 1994. 9

[42] J. W. Loram, K. A. Mizra, J. M. Wade, J. R. Cooper, and W. Y. Liang. The electronic specific heat of cuprate superconductors. *Physica C*, 235:134, 1994. 9

[43] H. Alloul, T. Ohno, and P. Mendels. ^{89}Y NMR evidence for a fermi-liquid behavior in $YBa_2Cu_3O_{6+x}$. *Phys. Rev. Lett.*, 63:1700, 1989. 9

[44] V. Emery and S. Kivelson. Importance of phase fluctuations in superconductors with small superfluid density. *Nature*, 374:434, 1995. 10, 27, 108

[45] M. Franz and Z. Tĕsanović. Algebraic Fermi liquid from phase fluctuations: "topological" Fermions, vortex "berryons", and QED3 theory of cuprate superconductors. *Phys. Rev. Lett.*, 87:257003, 2001. 10, 108

[46] L. Balents, M. P. A. Fisher, and C. Nayak. Nodal liquid theory of the pseudo-gap phase of the high-T_c superconductors. *Int. J. Mod. Phys. B*, 12:1033, 1998. 10, 108

[47] Z. A. Xu, N. P. Ong, Y. Wang, T. Kakeshita, and S. Uchida. Vortex-like excitations and the onset of superconducting phase fluctuation in underdoped $La_{2-x}Sr_xCuO_4$. *Nature*, 406:486, 2000. 10, 103

[48] J. Corson, R. Mallozzi, J. Orenstein, J. N. Eckstein, and I. Bozovic. Vanishing of phase coherence in underdoped $Bi_2Sr_2CaCu_2O_{8+\delta}$. *Nature*, 398:221, 1999. 10

[49] V. J. Emery, S. A. Kivelson, and J. M. Tranquada. Stripe phases in high-temperature superconductors. *Proc. Natl. Acad. Sci. USA*, 96:8814, 1999. 11, 12

[50] S. A. Kivelson, E. Fradkin, V. Oganesyan, I. P. Bindloss, J. M. Tranquada, A. Kapitulnik, and C. Howald. How to detect fluctuating order in the high-temperature superconductors. *Rev. Mod. Phys.*, 75:1201, 2003. 11, 12, 14

[51] Subir Sachdev and Shou-Cheng Zhang. Tuning order in cuprate superconductors. *Science*, 295:452, 2002. 11, 12, 92

[52] J. M. Tranquada, B. J. Sternlieb, J. D. Axe, Y. Nakamura, and S. Uchida. Evidence for stripe correlations of spins and holes in copper-oxide superconductors. *Nature*, 375:561, 1995. 11, 12, 13

[53] B. Lake, H.M. Rønnow, N. B. Christensen, G. Aeppli, K. Lefmann, D. F. McMorrow, P. Vorderwisch, P. Smeibidl, N. Mangkorntong, T. Sasagawa, M. Nohara, H. Takagi, and T. E. Mason. Antiferromagnetic order induced by an applied magnetic field in a high-temperature superconductor. *Nature*, 415:299, 2002. 13, 14, 92, 109

[54] Eugene Demler, Subir Sachdev, and Ying Zhang. Spin-ordering quantum transitions of superconductors in a magnetic field. *Phys. Rev. Lett.*, 87:067202, 2001. 13, 14, 92, 112

[55] A. T. Savici, Y. Fudamoto, I. M. Gat, T. Ito, M. I. Larkin, Y. J. Uemura, G. M. Luke, K. M. Kojima, Y. S. Lee, M. A. Kastner, R. J. Birgeneau, and K. Yamada. Muon spin relaxation studies of incommensurate magnetism and superconductivity in stage-4 $La_2CuO_{4.11}$ and $La_{1.88}Sr_{0.12}CuO_4$. *Phys. Rev. B*, 66:014524, 2002. 13, 14, 112

[56] K. Yamada, C. H. Lee, K. Kurahashi, J. Wada, S. Wakimoto, S. Ueki, H. Kimura, Y. Endoh, S. Hosoya, G. Shirane, R. J. Birgeneau, M. Greven, M. A. Kastner, and Y. J. Kim. Doping dependence of the spatially modulated dynamical spin correlations and the superconducting-transition temperature in $La_{2-x}Sr_xCuO_4$. *Phys. Rev. B*, 57:6165, 1998. 13, 113

[57] A. R. Moodenbaugh, Youwen Xu, M. Suenaga, T. J. Folkerts, and R. N. Shelton. Superconducting properties of $La_{2-x}Ba_xCuO_4$. *Phys. Rev. B*, 38:4596, 1988. 13

[58] S. Wakimoto, R. J. Birgeneau, Y. S. Lee, and G. Shirane. Hole concentration dependence of the magnetic moment in superconducting and insulating $La_{2-x}Sr_xCuO_4$. *Phys. Rev. B*, 63:172501, 2001. 13, 109

[59] M. Fujita, K. Yamada, H. Hiraka, P .M. Gehring, S. H. Lee, S. Wakimoto, and G. Shirane. Static magnetic correlations near the insulating-superconducting phase boundary in $La_{2-x}Sr_xCuO_4$. *Phys. Rev. B*, 65:064505, 2002. 13, 92, 109

[60] T. Suzuki, T. Goto, K. Chiba, T. Shinoda, T. Fukase, H. Kimura, K. Yamada, M. Ohashi, and Y. Yamaguchi. Observation of modulated magnetic long-range order in $La_{1.88}Sr_{0.12}CuO_4$. *Phys. Rev. B*, 57:3229, 1998. 13

[61] Hiroyuki Kimura, Kazuma Hirota, Hiroki Matsushita, Kazuyoshi Yamada, Yasuo Endoh, Seung-Hun Lee, Charles F. Majkrzak, Ross Erwin, Gen Shirane, Martin Greven, Young S. Lee, Marc A. Kastner, and Robert J. Birgeneau. Neutron-scattering study of static antiferromagnetic correlations in $La_{2-x}Sr_xCu_{1-y}Zn_yO_4$. *Phys. Rev. B*, 59:6517, 1999. 13

[62] Y. S. Lee, R. J. Birgeneau, M. A. Kastner, Y. Endoh, S. Wakimoto, K. Yamada, R. W. Erwin, S.-H. Lee, and G. Shirane. Neutron-scattering study of spin-density wave order in the superconducting state of excess-oxygen-doped La_2CuO_{4+y}. *Phys. Rev. B*, 60:3643, 1999. 13, 14

[63] B. Lake, G. Aeppli, T. E. Mason, A. Schröder, D. F. McMorrow, K. Lefmann, M. Isshiki, M. Nohara, H. Takagi, and S. M. Hayden. Spin gap and magnetic coherence in a clean high-temperature superconductor. *Nature*, 400:43, 1999. 13

[64] S. Katano, M. Sato, K. Yamada, T. Suzuki, and T. Fukase. Enhancement of static antiferromagnetic correlations by magnetic field in a superconductor $La_{2-x}Sr_xCuO_4$ with x=0.12. *Phys. Rev. B*, 62:R14677, 2000. 14, 92, 109

[65] B. Khaykovich, Y. S. Lee, R. W. Erwin, S.-H. Lee, S. Wakimoto, K. J. Thomas, M. A. Kastner, and R. J. Birgeneau. Enhancement of long-range magnetic order by magnetic field in superconducting La_2CuO_{4+y}. *Phys. Rev. B*, 66:014528, 2002. 14, 92, 109, 112

[66] Y. S. Lee, F. C. Chou, A. Tewary, M. A. Kastner, S. H. Lee, and R. J. Birgeneau. Neutron scattering study of the effects of dopant disorder on the superconductivity and magnetic order in stage-4 La_2CuO_{4+y}. *Phys. Rev. B*, 69:020502, 2004. 14, 109

[67] S. Wakimoto, R. J. Birgeneau, Y. Fujimaki, N. Ichikawa, T. Kasuga, Y. J. Kim, K. M. Kojima, S.-H. Lee, H. Niko, J. M. Tranquada, S. Uchida, and M. v. Zimmermann. Effect of a magnetic field on the spin- and charge-density-wave order in $La_{1.45}Nd_{0.4}Sr_{0.15}CuO_4$. *Phys. Rev. B*, 67:184419, 2003. 14, 109, 117

[68] B. Khaykovich, R. J. Birgeneau, F. C. Chou, R. W. Erwin, M. A. Kastner, S.-H. Lee, Y. S. Lee, P. Smeibidl, P. Vorderwisch, and S. Wakimoto. Effect of a magnetic field on long-range magnetic order in stage-4 and stage-6 superconducting La_2CuO_{4+y}. *Phys. Rev. B*, 67:054501, 2003. 14, 92, 109, 112

[69] C. Stock, W. J. L. Buyers, Z. Tun, R. Liang, D. Peets, D. Bonn, W. N. Hardy, and L. Taillefer. Neutron scattering search for static magnetism in oxygen-ordered $YBa_2Cu_3O_{6.5}$. *Phys. Rev. B*, 66:024505, 2002. 14, 92, 113

[70] C. Stock, W. J. L. Buyers, R. Liang, D. Peets, Z. Tun, D. Bonn, W. N. Hardy, and R. J. Birgeneau. Dynamic stripes and resonance in the superconducting and normal phases of $YBa_2Cu_3O_{6.5}$ ortho-II superconductor. *Phys. Rev. B*, 69:014502, 2004. 14, 113

[71] H. Takagi, B. Batlogg, H. L. Kao, J. Kwo, R. J. Cava, J. J. Krajewski, and Jr. W. F. Peck. Systematic evolution of temperature-dependent resistivity in $La_{2-x}Sr_xCuO_4$. *Phys. Rev. Lett.*, 69:2975, 1992. xiii, 15, 16, 59

[72] H. Takagi, T. Ido, S. Ishibashi, M. Uota, S. Uchida, and Y. Tokura. Superconductor-to-nonsuperconductor transition in $(La_{1-x}Sr_x)_2CuO_4$ as investigated by transport and magnetic measurements. *Phys. Rev. B*, 40:2254, 1989. 16, 59

[73] Y. Nakamura and S. Uchida. Anisotropic transport properties of single-crystal $La_{2-x}Sr_xCuO_4$: Evidence for the dimensional crossover. *Phys. Rev. B*, 47:8369, 1993. 16, 59, 62

[74] B. Keimer, N. Belk, R. J. Birgeneau, A. Cassanho, C. Y. Chen, M. Greven, M. A. Kastner, A. Aharony, Y. Endoh, R. W. Erwin, and G. Shirane. Magnetic excitations in pure, lightly doped, and weakly metallic La_2CuO_4. *Phys. Rev. B*, 46:14034, 1992. 16, 17, 27, 59

[75] B. Ellman, H. M. Jaeger, D. P. Katz, T. F. Rosenbaum, A. S. Cooper, and G. P. Espinosa. Transport studies of $La_{2-x}Sr_xCuO_4$ near the insulator-metal-superconductor transition. *Phys. Rev. B*, 39:9012, 1989. 16, 17, 27, 59

[76] G. S. Boebinger, Yoichi Ando, A. Passner, T. Kimura, M. Okuya, J. Shimoyama, K. Kishio, K. Tamasaku, N. Ichikawa, and S. Uchida. Insulator-to-metal crossover in the normal state of $La_{2-x}Sr_xCuO_4$ near optimum doping. *Phys. Rev. Lett.*, 77:5417, 1996. 16, 17, 27, 59, 100

[77] Y. Ando, A. N. Lavrov, S. Komiya, K. Segawa, and X. F. Sun. Mobility of the doped holes and the antiferromagnetic correlations in underdoped high-T_c cuprates. *Phys. Rev. Lett.*, 87:017001, 2001. 16, 59

[78] Yoichi Ando, Seiki Komiya, Kouji Segawa, S. Ono, and Y. Kurita. Electronic phase diagram of high-T_c cuprates drawn by resistivity curvature mapping. cond-mat/0403032 (2004). 16, 59

[79] S. Nakamae, K. Behnia, N. Mangkorntong, M. Nohara, H. Takagi, S. J. C. Yates, and N. E. Hussey. Electronic ground state of heavily overdoped nonsuperconducting $La_{2-x}Sr_xCuO_4$. *Phys. Rev. Lett.*, 68:100502, 2003. 16, 75, 121, 122

[80] Y. Ando, G. S. Boebinger, A. Passner, Tsuyoshi Kimura, and Kohji Kishio. Logarithmic divergence of both in-plane and out-of-plane normal-state resistivities of superconducting $La_{2-x}Sr_xCuO_4$ in the zero-temperature limit. *Phys. Rev. Lett.*, 75:4662, 1995. 16, 91, 100

[81] N. F. Mott. *Metal-Insulator Transitions.* New York: Taylor and Francis, 2nd edition, 1990. 17

[82] E. Lai and R. J. Gooding. Unifying the phase diagrams of the magnetic and transport properties of $La_{2-x}Sr_xCuO_4$, $0 \leq x \leq 0.05$. *Phys. Rev. B*, 57:1498, 1998. 17

[83] J. M. Ziman. *Electrons and phonons.* Clarendon Press, Oxford, 1960. 21, 22, 25, 26

[84] R. Berman. *Thermal Conduction in Solids.* Clarendon Press, Oxford, 1976. 21, 25, 44

[85] P. G. Klemens. Thermal conductivity and lattice vibrational modes. *Solid State Physics*, 7:1, 1958. 21

[86] Peter Carruthers. Theory of thermal conductivity of solids at low temperatures. *Rev. Mod. Phys.*, 33:92, 1961. 21

[87] W. S Hurst and D. R. Frankl. Thermal conductivity of silicon in the boundary scattering regime. *Phys. Rev.*, 186:801, 1969. 21, 24, 95

[88] H. B. G. Casimir. *Physica*, 5:495, 1938. 24

[89] M. P. Zaitlin, L. M. Scherr, and A. C. Anderson. Boundary scattering of phonons in noncrystalline materials. *Phys. Rev. B*, 12:4487, 1975. 24

[90] P. D. Thacher. Effect of boundaries and isotopes on the thermal conductivity of LiF. *Phys. Rev.*, 156:975, 1967. 24, 95

[91] R. O. Pohl and B. Stritzker. Phonon scattering at crystal surfaces. *Phys. Rev. B*, 25:3608, 1982. 24, 25, 95

[92] E. P. Roth and A. C. Anderson. Interaction between thermal phonons and dislocations in LiF. *Phys. Rev. B*, 20:768, 1979. 24, 95

[93] R. Berman, F. E. Simon, and J. M. Ziman. The thermal conductivity of diamond at low temperatures. *Proc. Roy. Soc. (London)*, A220:171, 1953. 24, 95

[94] W. H. Butler and R. K. Williams. Electron-phonon interaction and lattice thermal conductivity. *Phys. Rev. B*, 18:6483, 1978. 25, 122

[95] A. B. Pippard. Ultrasonic attenuation in metals. *Phil. Mag.*, 46:1104, 1955. 26

[96] P. Lindenfeld and W. B. Pennebaker. Lattice conductivity of copper alloys. *Phys. Rev.*, 127:1881, 1962. 26

[97] A. F. Ioffe and A. R. Regel. *Semicond.*, 4:237, 1960. 27

[98] N. E. Hussey. The normal state scattering rate in high-T_c cuprates. *Eur. Phys. J. B*, 31:495, 2003. 27

[99] J. Bardeen, G. Rickayzen, and L. Tewordt. Theory of the thermal conductivity of superconductors. *Phys. Rev.*, 113:982, 1959. 27, 28, 29

[100] P. H. Kes, J. G. A. Rolfes, and D. de Klerk. Thermal-conductivity of niobium in purely superconducting and normal states. *J. Low Temp. Phys.*, 17:341, 1975. 28, 29

[101] C. B. Satterthwaite. Thermal conductivity of normal and superconducting aluminum. *Phys. Rev.*, 125:873, 1962. 29

[102] C. Caroli, P. G. De Gennes, and J. Matricon. Bound fermion states on a vortex line in a type-II superconductor. *Phys. Letters*, 9:307, 1964. 29

[103] Robert M. Cleary. Scattering of single-particle excitations by a vortex in a clean type-II superconductor. *Phys. Rev.*, 175:587, 1968. 29, 39, 81

[104] J. Lowell and J. B. Sousa. Mixed-state thermal conductivity of type ii superconductors. *Journal of Low Temperature Physics*, 3:65, 1970. 29, 30, 103

[105] L. P. Gor'kov and P. A. Kalugin. Defects and an unusual superconductivity. *Pis'ma Zh. Eksp. Teor. Fiz.*, 41:208, 1985. [JETP Lett. 41, 253 (1985).]. 32, 33

[106] Gianfranco Preosti, Heesang Kim, and Paul Muzikar. Density of states in unconventional superconductors: Impurity-scattering effects. *Phys. Rev. B*, 50:1259, 1994. 32, 33

[107] P. A. Lee. Localized states in a d-wave superconductor. *Phys. Rev. Lett.*, 71:1887, 1993. 32, 34, 75, 125

[108] Peter J. Hirschfeld and Nigel Goldenfeld. Effect of strong scattering on the low-temperature penetration depth of a d-wave superconductor. *Phys. Rev. B*, 48:4219, 1993. 32, 33, 34, 78, 84, 86

[109] A. C. Durst and P. A. Lee. Impurity-induced quasiparticle transport and universal-limit Wiedemann-Franz violation in d-wave superconductors. *Phys. Rev. B*, 62:1270, 2000. 32, 34, 35, 75, 97, 110, 125

[110] Eduardo Fradkin. Critical behavior of disordered degenerate semiconductors. II. spectrum and transport properties in mean-field theory. *Phys. Rev. B*, 33:3263, 1986. 34

[111] M. J. Graf, S-K. Yip, J. A. Sauls, and D. Rainer. Electronic thermal conductivity and the Wiedemann-Franz law for unconventional superconductors. *Phys. Rev. B*, 53:15147, 1996. 34, 35, 75, 82, 125

[112] G. E. Volovik. Superconductivity with lines of gap nodes - density-of-states in the vortex. *JETP Lett.*, 58:469, 1993. 36, 37, 80, 124

[113] C. Kübert and P. J. Hirschfeld. Vortex contribution to specific heat of dirty d-wave superconductors: Breakdown of scaling. *Solid State Commun.*, 105:459, 1998. 37

[114] C. Kübert and P. J. Hirschfeld. Quasiparticle transport properties of d-wave superconductors in the vortex state. *Phys. Rev. Lett.*, 80:4963, 1998. 37, 38, 39, 80, 81, 83, 110, 124

[115] F. Yu, M. B. Salamon, A. J. Leggat, W. C. Lee, and D. M. Ginsberg. Tensor magnetothermal resistance in $YBa_2Cu_3O_{7-x}$ via Andreev scattering of quasiparticles. *Phys. Rev. Lett.*, 74:5136, 1995. 38, 81, 103

[116] M. Franz. Mixed-state quasiparticle transport in high-T_c cuprates. *Phys. Rev. Lett.*, 82:1760, 1999. 38, 39, 81, 103

[117] I. Vekhter and A. Houghton. Quasiparticle thermal conductivity in the vortex state of high-T_c cuprates. *Phys. Rev. Lett.*, 83:4626, 1999. 38, 39, 80, 103, 110

[118] Wonkee Kim, F. Marsiglio, and J. P. Carbotte. Low-temperature thermal conductivity of high-purity $YBa_2Cu_3O_{6.99}$ in the vortex state: Analysis with arbitrary impurity scattering strength. *Phys. Rev. B*, 68:174513, 2003. 38, 39, 103

[119] Adam C. Durst, Ashvin Vishwananth, and Patrick A. Lee. Weak-field thermal hall conductivity in the mixed state of d-wave superconductors. *Phys. Rev. Lett.*, 90:187002, 2003. 38, 39, 81, 103

[120] Krishana K, Ong NP, Li Q, Gu GD, and Koshizuka N. Plateaus observed in the field profile of thermal conductivity in the superconductor $Bi_2Sr_2CaCu_2O_8$. *Science*, 277:83, 1997. 39, 81, 101

[121] M. Franz and Z. Tĕsanović. Quasiparticles in the vortex lattice of unconventional superconductors: Bloch waves or landau levels? *Phys. Rev. Lett.*, 84:554, 2000. 39

[122] A. A. Abrikosov and L. P. Gor'kov. Contribution to the theory of superconducting alloys with paramagnetic impurities. *Sov. Phys. JETP*, 12:1243, 1961. 40, 78

[123] Ye Sun and Kazumi Maki. Impurity effects in d-wave superconductors. *Phys. Rev. B*, 51:6059, 1995. 40, 78, 79

[124] Y. Sun and K. Maki. Transport-properties of d-wave superconductors with impurities. *Europhys. Lett.*, 32:355, 1995. 40, 78, 79

[125] W. A. Atkinson, P. J. Hirschfeld, and A. H. MacDonald. Gap inhomogeneities and the density of states in disordered d-wave superconductors. *Phys. Rev. Lett.*, 85:3922, 2000. 41

[126] W. A. Atkinson and P. J. Hirschfeld. Optical and thermal-transport properties of an inhomogeneous d-wave superconductor. *Phys. Rev. Lett.*, 88:187003, 2002. 41

[127] Etienne Boaknin. *Thermal Conduction in the Vortex State of Unconventional Superconductors.* PhD thesis, University of Toronto, 2003. 42, 44, 47, 64, 86

[128] G.K. White. *Experimental Techniques in Low Temperature Physics.* Clarendon Press, Oxford, 1968. 42

[129] Frank Pobell. *Matter and Methods at Low Temperatures.* Spinger-Verlag, Berlin - Heidelberg - New-York, 2nd edition, 1996. 42

[130] Etienne Boaknin, R. W. Hill, Cyril Proust, C. Lupien, Louis Taillefer, and P. C. Canfield. Highly anisotropic gap function in borocarbide superconductor $LuNi_2B_2C$. *Phys. Rev. Lett.*, 87:237001, 2001. 47

[131] Etienne Boaknin, M. A. Tanatar, Johnpierre Paglione, D. Hawthorn, F. Ronning, R. W. Hill, M. Sutherland, Louis Taillefer, Jeff Sonier, S. M. Hayden, and J. W. Brill. Heat conduction in the vortex state of $NbSe_2$: Evidence for multiband superconductivity. *Phys. Rev. Lett.*, 90:117003, 2003. 47, 48

[132] P. G. Radaelli, D. G. Hinks, A. W. Mitchell, B. A. Hunter, J. L. Wagner, B. Dabrowski, K. G. Vandervoort, H. K. Viswanathan, and J. D. Jorgensen. Structural and superconducting properties of $La_{2-x}Sr_xCuO_4$ as a function of Sr content. *Phys. Rev. B*, 49:4163, 1996. 49

[133] S. Wakimoto, H. Zhang, K. Yamada, I. Swainson, Hyunkyung Kim, and R. J. Birgeneau. Direct relation between the low-energy spin excitations and superconductivity in overdoped high-T_c superconductors. *Phys. Rev. Lett.*, 92:217004, 2004. 50

[134] K. Zhang, R. Mogilevsky, D. G. Hinks, J. Mitchell, A. J. Schultz, Y. Wang, and V. Dravid. Crystal growth of $(La,Sr)_2CuO_4$ by floating zone melting. *Journal of Crystal Growth*, 169:73, 1996. 50

[135] Chen Changkang. Phase diagram and its application to the crystal growth of high T_c oxide superconductors. *Prog. Crystal Growth and Charact.*, 36:1, 1998. 50, 51

[136] Hironao Kojima, Junichi Yamamoto, Yoshihiro Mori, M. K. R. Khan, Hideyoshi Tanabe, and Isao Tanaka. Single crystal growth of superconducting $La_{2-x}M_xCuO_4$ (M = Ca, Sr, Ba) by the TSFZ method. *Physica C*, 293:14, 1997. 50

[137] I. Tanaka and H. Kojima. Superconducting single crystals. *Nature*, 337:21, 1989. 50

[138] A. Revcolevschi and J. Jegoudez. Growth of large high-T_c single crystals by the floating zone method: A review. *Progress in Materials Science*, 42:321, 1997. 50

[139] S. Wakimoto, S. Ueki, Y. Endoh, and K. Yamada. Systematic study of short-range antiferromagnetic order and the spin-glass state in lightly doped $La_{2-x}Sr_xCuO_4$. *Phys. Rev. B*, 62:3547, 2000. 50

[140] N. E. Hussey, J. R. Cooper, J. M. Wheatley, I. R. Fisher, A. Carrington, A. P. Mackenzie, C. T. Lin, and O. Milat. Angular dependence of the c-axis normal state magnetoresistance in single crystal $Tl_2Ba_2CuO_6$. *Phys. Rev. Lett.*, 76:122, 1996. 62

[141] N. N. Kolesnikov, M. P. Kulakov, I. F. Schegolev, R. P. Shibaeva, O. M. Vyasilev, V. N. Molchanov, V. I. Simonov, and R. A. Tamazyan. Comparative study of Tl-2201 single crystals with $T_c = 30$ and 110 K by means of x-ray structural analysis and NMR. *Physica C*, 242:385, 1995. 62, 63, 71

[142] M. A. G. Aranda, D. C. Sinclair, J. P. Attfield, and A. P. Mackenzie. Cation distributions and possible phase separation in $Tl_2Ba_2CuO_{6+\delta}$ from synchrotron powder x-ray diffraction. *Phys. Rev. B*, 51:12747, 1995. 62, 63, 71

[143] C. Opagiste, G. Triscone, M. Couach, T. K. Jondo, J.-L. Jorda, A. Junod, A. F. Khoder, and J. Muller. Phase diagram of the $Tl_2Ba_2CuO_6$ compounds in the T, $p(O_2)$ plane. *Physica C*, 213:17, 1993. 62

[144] A. W. Tyler. *An Investigation into the Magnetotransport Properties of Layered Superconducting Perovskites.* PhD thesis, University of Cambridge, 1998. 62, 116

[145] D. C. Peets, Ruixing Liang, D. A. Bonn, W. N. Hardy, and M. Raudseep. cond-mat/0211028 (2002). 62, 63, 71

[146] M.R. Presland, J.L. Tallon, R.G. Buckley, R.S. Liu, and N.E. Flower. General trends in oxygen stoichiometry effects on T_c in Bi and Tl superconductors. *Physica C*, 176:95, 1991. 67

[147] R. C. Yu, M. B. Salamon, Jian Ping Lu, and W. C. Lee. Thermal conductivity of an untwinned $YBa_2Cu_3O_{7-\delta}$ single crystal and a new interpretation of the superconducting state thermal transport. *Phys. Rev. Lett.*, 69:1431, 1992. 71, 118

[148] D. A. Bonn, P. Dosanjh, R. Liang, and W. N. Hardy. Evidence for rapid suppression of quasiparticle scattering below T_c in $YBa_2Cu_3O_{7-\delta}$. *Phys. Rev. Lett.*, 68:2390, 1992. 71, 118

[149] D. M. Broun, D. C. Morgan, R. J. Ormeno, S. F. Lee, A. W. Tyler, A. P. Mackenzie, and J. R. Waldram. In-plane microwave conductivity of the single-layer cuprate $Tl_2Ba_2CuO_{6+\delta}$. *Phys. Rev. B*, 56:R11443, 1997. 71, 86, 118

[150] K. Krishana, J. M. Harris, and N. P. Ong. Quasiparticle mean free path in $YBa_2Cu_3O_7$ measured by the thermal hall conductivity. *Phys. Rev. Lett.*, 75:3529, 1995. 71, 118

[151] D. Duffy, P. J. Hirschfeld, and D. J. Scalapino. Quasiparticle lifetimes in a $d_{x^2-y^2}$ superconductor. *Phys. Rev. B*, 64:224522, 2004. 71

[152] P. J. Hirschfeld and W. O. Putikka. Effect of strong scattering on the low-temperature penetration depth of a d-wave superconductor. *Phys. Rev. Lett.*, 77:3909, 1996. 71, 118

[153] F. Yu, M. B. Salamon, V. Kopylov, N. N. Koleshnikov, H. M. Duan, and A. M. Hermann. Thermal conductivity of single crystal $Tl_2Ba_2CuO_6$ (Tl-2201) in applied magnetic fields. *Physica C*, 235-240:1489, 1994. 71, 81

[154] M. F. Smith, Johnpierre Paglione, and M. B. Walker. The origin of anomalous low-temperature downturns in the thermal conductivity of cuprates. unpublished (2004). 72, 73, 123

[155] X. J. Zhou, T. Yoshida, A. Lanzara, P. V. Bogdanov, S. A. Kellar, K. M. Shen, W. L. Yang, F. Ronning, T. Sasagawa, T. Kakeshita, T. Noda, H. Eisaki, S. Uchida, C. T. Lin, F. Zhou, J. W. Xiong, W. X. Ti, Z. X. Zhao, A. Fujimori, Z. Hussain, and Z.-X. Shen. High-temperature superconductors: Universal nodal Fermi velocity. *Nature*, 423:398, 2003. 75, 77, 115, 123

[156] A. Ino, C. Kim, M. Nakamura, T. Yoshida, T. Mizokawa, A. Fujimori, Z.-X. Shen, T. Kakeshita, H. Eisaki, and S. Uchida. Doping-dependent evolution of the electronic structure of $La_{2-x}Sr_xCuO_4$ in the superconducting and metallic phases. *Phys. Rev. B*, 65:094504, 2000. 76, 77

[157] H. Ding, M. R. Norman, T. Yokoya, T. Takeuchi, M. Randeria, J. C. Campuzano, T. Takahashi, T. Mochiku, and K. Kadowaki. Evolution of the Fermi surface with carrier concentration in $Bi_2Sr_2CaCu_2O_{8+\delta}$. *Phys. Rev. Lett.*, 78:2628, 1997. 76, 77

[158] N. E. Hussey, M. Abdel-Jawad, A. Carrington, A. P. Mackenzie, and L. Balicas. A coherent three-dimensional Fermi surface in a high-transition-temperature superconductor. *Nature*, 425:814, 2003. 76, 77

[159] N. Miyakawa, J. F. Zasadzinski, L. Ozyuzer, P. Guptasarma, D. G. Hinks, C. Kendziora, and K .E. Gray. Predominantly superconducting origin of large energy gaps in underdoped $Bi_2Sr_2CaCu_2O_{8+\delta}$ from tunneling spectroscopy. *Phys. Rev. Lett.*, 83:1018, 1999. 77

[160] J. Y. T. Wei, C. C. Tsuei, P. J. M. van Bentum, Q. Xiong, C. W. Chu, and M. K. Wu. Quasiparticle tunneling spectra of the high-T_c mercury cuprates: Implications of the d-wave two-dimensional van hove scenario. *Phys. Rev. B*, 57:3650, 1998. 77

[161] V. P. Gusynin and V. A. Miransky. Thermal conductivity and competing orders in d-wave superconductors. *Eur. Phys. J. B*, 37:363, 2004. xv, 78, 110, 111

[162] Y. J. Uemura. Superfluid density of high-T_c cuprate systems: implication on condensation mechanisms, heterogeneity and phase diagram. *Solid State Communications*, 126:23, 2003. 78

[163] Hyekyung Won and Kazumi Maki. d-wave superconductor as a model of high-T_c superconductors. *Phys. Rev. B*, 49:1397, 1994. 78

[164] A. P. Mackenzie, S. R. Julian, G. G. Lonzarich, A. Carrington, S. D. Hughes, R. S. Liu, and D. S. Sinclair. Resistive upper critical field of $Tl_2Ba_2CuO_6$ at low temperatures and high magnetic fields. *Phys. Rev. Lett.*, 71:1238, 1993. 81, 85, 98

[165] Yoichi Ando, J. Takeya, Yasushi Abe, K. Nakamura, and A. Kapitulnik. Temperature- and magnetic-field-dependent thermal conductivity of pure and Zn-doped $Bi_2Sr_2CaCu_2O_{8+\delta}$ single crystals. *Phys. Rev. B*, 62:626, 2000. 81, 89

[166] R. W. Hill, Christian Lupien, M. Sutherland, Etienne Boaknin, D. G. Hawthorn, Cyril Proust, F. Ronning, Louis Taillefer, Ruixing Liang, D. A. Bonn, and W. N. Hardy. Transport in ultraclean $YBa_2Cu_3O_7$: Neither unitary nor Born impurity scattering. *Phys. Rev. Lett.*, 92:027001, 2004. xv, 82, 85, 101, 103, 119

[167] R. W. Hill, Cyril Proust, Louis Taillefer, P. Fournier, and R. L. Greene. Breakdown of Fermi-liquid theory in a copper-oxide superconductor. *Nature*, 414:711, 2001. 91, 101

[168] Han-Dong Chen, Jiang-Ping Hu, Sylvain Capponi, Enrico Arrigoni, and Shou-Cheng Zhang. Antiferromagnetism and hole pair checkerboard in the vortex state of high T_c superconductors. *Phys. Rev. Lett.*, 89:137004, 2002. 92

[169] Steven A. Kivelson, Dung-Hai Lee, Eduardo Fradkin, and Vadim Oganesyan. Competing order in the mixed state of high-temperature superconductors. *Phys. Rev. B*, 66:144516, 2002. 92

[170] X. F. Sun, Kouji Segawa, and Yoichi Ando. Metal-to-insulator crossover in $YBa_2Cu_3O_y$ probed by low-temperature quasiparticle heat transport. cond-mat/0403683 (2004), 2004. 101

[171] Yoichi Ando, S. Ono, X. F. Sun, J. Takeya, F. F. Balakirev, J. B. Betts, and G. S. Boebinger. Quantum phase transitions in the cuprate superconductor $Bi_2Sr_{2-x}La_xCuO_{6+\delta}$. *Phys. Rev. Lett.*, 92:247004, 2004. 101

[172] Yayu Wang, Z. A. Xu, T. Kakeshita, S. Uchida, S. Ono, Yoichi Ando, and N. P. Ong. Onset of the vortexlike nernst signal above T_c in $La_{2-x}Sr_xCuO_4$ and $Bi_2Sr_{2-y}La_yCuO_6$. *Phys. Rev. B*, 64:224519, 2001. 103

[173] Yayu Wang, N. P. Ong, Z. A. Xu, T. Kakeshita, S. Uchida, D. A. Bonn, R. Liang, and W. N. Hardy. High field phase diagram of cuprates derived from the nernst effect. *Phys. Rev. Lett.*, 88:257003, 2002. 103

[174] C. Capan, K. Behnia, J. Hinderer, A. G. M. Jansen, W. Lang, C. Marcenat, C. Marin, and J. Flouquet. Anomalous dissipation in the mixed state of underdoped cuprates close to the superconductor-insulator boundary. *Phys. Rev. Lett.*, 88:056601, 2002. 103

[175] C. Capan, K. Behnia, Z. Z. Li, H. Raffy, and C. Marin. Entropy of vortex cores near the superconductor-insulator transition in an underdoped cuprate. *Phys. Rev. B*, 67:100507, 2003. 103

[176] Yayu Wang, S. Ono, Y. Onose, G. Gu, Yoichi Ando, Y. Tokura, S. Uchida, and N. P. Ong. Dependence of upper critical field and pairing strength on doping in cuprates. *Science*, 86:299, 2003. 103

[177] S. M. Hayden, G. Aeppli, T. G. Perring, H. A. Mook, and F. Dogan. High-frequency spin waves in $YBa_2Cu_3O_{6.15}$. *Phys. Rev. B*, 55:6905, 1996. 107

[178] J. M. Harris, P. J. White, Z.-X. Shen, H. Ikeda, R. Yoshizaki, H. Eisaki, S. Uchida, W. D. Si, J. W. Xiong, Z.-X. Zhao, and D. S. Dessau. Measurement of an anisotropic energy gap in single plane $Bi_2Sr_{2-x}La_xCuO_{6+\delta}$. *Phys. Rev. Lett.*, 79:143, 1997. 108

[179] H. Won and K. Maki. Nonlinear response and scaling law in the vortex state of d-wave superconductors. *Europhys. Lett.*, 54:248, 2001. 110

[180] Mitsuaki Takigawa, Masanori Ichioka, and Kazushige Machida. Quasiparticle heat transport in the mixed state of high T_c superconductors. cond-mat/0306492 (2003). 110, 112

[181] T. Yoshida, X. J. Zhou, T. Sasagawa, W. L. Yang, P. V. Bogdanov, A. Lanzara, Z. Hussain, T. Mizokawa, A. Fujimori, H. Eisaki, Z.-X. Shen, T. Kakeshita, and S. Uchida. Metallic behavior of lightly doped $La_{2-x}Sr_xCuO_4$ with a Fermi surface forming an arc. *Phys. Rev. Lett.*, 91:027001, 2003. 111, 112

[182] K.M. Shen, T. Yoshida, D.H. Lu, F. Ronning, N.P. Armitage, W.S. Lee, X.J. Zhou, A. Damascelli, D.L. Feng, N.J.C. Ingle, H. Eisaki, Y. Kohsaka, H. Takagi, T. Kakeshita, S. Uchida, P.K. Mang, M. Greven, Y. Onose, Y. Taguchi, Y. Tokura, Seiki Komiya, Yoichi Ando, M. Azuma, M. Takano, A. Fujimori, and Z.-X. Shen. Fully gapped single-particle excitations in lightly doped cuprates. *Phys. Rev. B*, 69:054503, 2004. 111, 112

[183] M. Dumm, Seiki Komiya, Yoichi Ando, and D. N. Basov. Anisotropic electromagnetic response of lightly doped $La_{2-x}Sr_xCuO_4$ with the CuO_2 planes. *Phys. Rev. Lett.*, 91:077004, 2003. 111

[184] Seiki Komiya, Yoichi Ando, X. F. Sun, and A. N. Lavrov. c-axis transport and resistivity anisotropy of lightly to moderately doped $La_{2-x}Sr_xCuO_4$ single crystals: Implications on the charge transport mechanism. *Phys. Rev. B*, 65:214535, 2002. 111

[185] R. I. Miller, R. F. Kiefl, J. H. Brewer, J. E. Sonier, J. Chakhalian, S. Dunsiger, G. D. Morris, A. N. Price, D. A. Bonn, W. H. Hardy, and R. Liang. Evidence for static magnetism in the vortex cores of Ortho-II $YBa_2Cu_3O_{6.50}$. *Phys. Rev. Lett.*, 88:137002, 2002. 112

[186] V. F. Mitrović, E. E. Sigmund, M. Eschrig, H. N. Bachman, W. P. Halperin, A. P. Reyes, P. Kuhns, and W. G. Moulton. Spatially resolved electronic structure inside and outside the vortex cores of a high-temperature superconductor. *Nature*, 413:501, 2001. 112

[187] J. M. Tranquada, H. Woo, T. G. Perring, H. Goka, G. D. Gu, G. Xu, M. Fujita, and K. Yamada. Quantum magnetic excitations from stripes in copper oxide superconductors. *Nature*, 429:534, 2004. 113

[188] S. M. Hayden, H. A. Mook, Pengcheng Dai, T. G. Perring, and F. Dogan. The structure of the high-energy spin excitations in a high-transition-temperature superconductor. *Nature*, 429:531, 2004. 113

[189] O. Baberski, A. Lang, O. Maldonado, M. Hücker, B. Büchner, and A. Freimuth. Stripe correlations of spins and holes and phonon heat transport in doped La_2CuO_4. *Europhys. Lett.*, 44:337, 1998. 114, 117

[190] X. F. Sun, Seiki Komiya, and Yoichi Ando. Heat transport of $La_{2-y}Eu_yCuO_4$ and $La_{1.88-y}Eu_ySr_{0.12}CuO_4$ single crystals. *Phys. Rev. B*, 67:184512, 2003. 114, 117

[191] C. Hess, B. Buüchner, U. Ammerahl, and A. Revcolevschi. Phonon thermal conductivity in doped La_2CuO_4: Relevant scattering mechanisms. *Phys. Rev. B*, 68:184517, 2003. 114, 117

[192] X. F. Sun, J. Takeya, Seiki Komiya, and Yoichi Ando. Thermal conductivity of lightly Sr- and Zn-doped La_2CuO_4 single crystals. *Phys. Rev. B*, 67:104503, 2003. 114, 117

[193] A. Lanzara, P. V. Bogdanov, X. J. Zhou, S. A. Kellar, D. L. Feng, E. D. Lu, T. Yoshida, H. Eisaki, A. Fujimori, K. Kishio, J.-I. Shimoyama, S. Uchida T. Noda, Z. Hussain, and Z.-X. Shen. Evidence for ubiquitous strong electron-phonon coupling in high-temperature superconductors. *Nature*, 412:510, 2001. 115, 123, 126

[194] Shih-Fu Lee, D. C. Morgan, R. J. Ormeno, D. M. Broun, R. A. Doyle, J. R. Waldram, and K. Kadowaki. $a-b$ plane microwave surface impedance of a high-quality $Bi_2Sr_2CaCu_2O_8$ single crystal. *Phys. Rev. Lett.*, 77:735, 1996. 118

[195] M. B. Walker, M. F. Smith, and K. V. Samokhin. Electron-phonon interaction and ultrasonic attenuation in the ruthenate and cuprate superconductors. *Phys. Rev. B*, 65:014517, 2002. 123, 124

[196] M. F. Smith and M. B. Walker. Phonon attenuation and quasiparticle–phonon energy transfer in d-wave superconductors. *Phys. Rev. B*, 67:214509, 2003. 123

[197] Neil W. Ashcroft and N. David Mermin. *Solid State Physics.* Saunders College, Toronto, 1976. 123

[198] A. K. McCurdy, H. J. Maris, and C. Elbaum. Anisotropic heat conduction in cubic crystals in the boundary scattering regime. *Phys. Rev. B*, 2:4077, 1970. 124

[199] C. Lupien, W. A. MacFarlane, C. Proust, L. Taillefer, Z. Q. Mao, and Y. Maeno. Ultrasound attenuation in Sr_2RuO_4: An angle-resolved study of the superconducting gap function. *Phys. Rev. Lett.*, 86:5986, 2001. 124